NATIONAL AERONAUTICS AND SPACE ADMINISTRATION

# *Space Programs Summary No. 37-41, Volume III*

*for the period July 1, 1966 to August 31, 1966*

## *The Deep Space Network*




JET PROPULSION LABORATORY
CALIFORNIA INSTITUTE OF TECHNOLOGY
PASADENA, CALIFORNIA

September 30, 1966

NATIONAL AERONAUTICS AND SPACE ADMINISTRATION

# *Space Programs Summary No. 37-41, Volume III*

*for the period July 1, 1966 to August 31, 1966*

## *The Deep Space Network*

JET PROPULSION LABORATORY
CALIFORNIA INSTITUTE OF TECHNOLOGY
PASADENA, CALIFORNIA

September 30, 1966

# Preface

The *Space Programs Summary* is a six-volume, bimonthly publication that documents the current project activities and supporting research and advanced development efforts conducted or managed by JPL for the NASA space exploration programs. The titles of all volumes of the *Space Programs Summary* are:

Vol. I. The Lunar Program (Confidential)

Vol. II. The Planetary–Interplanetary Program (Confidential)

Vol. III. The Deep Space Network (Unclassified)

Vol. IV. Supporting Research and Advanced Development (Unclassified)

Vol. V. Supporting Research and Advanced Development (Confidential)

Vol. VI. Space Exploration Programs and Space Sciences (Unclassified)

The *Space Programs Summary*, Vol. VI consists of an unclassified digest of appropriate material from Vols. I, II, and III; an original presentation of technical supporting activities, including engineering development of environmental-test facilities, and quality assurance and reliability; and a reprint of the space science instrumentation studies of Vols. I and II.

W. H. Pickering, *Director*
*Jet Propulsion Laboratory*

**Space Programs Summary No. 37-41, Volume III**



Prepared under Contract No. NAS 7-100, National Aeronautics & Space Administration

# Contents

# Contents (contd)

# I. Introduction

The Deep Space Network (DSN), established by the NASA Office of Tracking and Data Acquisition, is under the system management and technical direction of JPL. The DSN is responsible for two-way communications with unmanned spacecraft travelling from approximately 10,000 miles from Earth to interplanetary distances. Tracking and data-handling equipment to support these missions is provided. Present facilities permit simultaneous control of a newly launched spacecraft and a second one already in flight. In preparation for the increased number of U.S. activities in space, a capability is being developed for simultaneous control of either two newly launched spacecraft plus two in flight, or four spacecraft in flight. Advanced communications techniques are being implemented to make possible obtaining data from, and tracking spacecraft to, planets as far out in space as Jupiter.

The DSN is distinct from other NASA networks such as the Scientific Satellite Tracking and Data Acquisition Network (STADAN), which tracks Earth-orbiting scientific and communication satellites, and the Manned Space Flight Network (MSFN), which tracks the manned spacecraft of the *Gemini* and *Apollo* programs.

The DSN supports, or has supported, the following NASA space exploration projects: (1) *Ranger*, *Surveyor*, *Mariner*, and *Voyager* Projects of JPL; (2) *Lunar Orbiter* Project of the Langley Research Center; (3) *Pioneer* Project of the Ames Research Center, and (4) *Apollo* Project of the Manned Spacecraft Center (as backup to the Manned Space Flight Network). The main elements of the network are: the Deep Space Instrumentation Facility (DSIF), with space communications and tracking stations located around the world; the Ground Communications System (GCS), which provides communications between all elements of the DSN; and the JPL Space Flight Operations Facility (SFOF), the command and control center.

The DSIF tracking stations are situated such that three stations may be selected approximately 120 deg apart in longitude in order that a spacecraft in or near the ecliptic

plane is always within the field of view of at least one of the selected ground antennas. The DSIF stations are:

| Deep Space Communication Complex (DSCC) | Deep Space Station (DSS) | DSS serial designation[1] |
|---|---|---|
| Goldstone | Pioneer | 11 |
| | Echo | 12 |
| | Venus | 13 |
| | Mars | 14 |
| Canberra[2] | Woomera | 41 |
| | Tidbinbilla | 42 |
| | Booroomba[3] | 43 |
| | Johannesburg | 51 |
| Madrid[2] | Robledo | 61 |
| | Cebreros[4] | 62 |
| | Rio Cofio[3] | 63 |
| | Cape Kennedy (Spacecraft Monitoring) | 71 |
| | Ascension Island[4] (Spacecraft Guidance and Command) | 72 |

[1]As of June 1966, DSIF serial designations (e.g., DSIF-11) are no longer used.
[2]Planned.
[3]Station not yet authorized.
[4]Station not yet operational.

JPL operates the U.S. stations, and will operate the Ascension Island Station. The overseas stations are normally staffed and operated by government agencies of the respective countries, with the assistance of U.S. support personnel.

The Cape Kennedy Station supports spacecraft final checkout prior to launch, verifies compatibility between the DSN and the flight spacecraft, measures spacecraft frequencies during countdown, and provides telemetry reception from lift-off to local horizon. The other DSIF stations obtain angular position, velocity (doppler), and distance (range) data for the spacecraft, and provide command control to (up-link), and data reception from (down-link), the spacecraft. Large antennas, low noise phase-lock receiving systems, and high-power transmitters are utilized. The 85-ft diameter antennas have gains of 53 db at 2300 MHz, with a system temperature of 55°K, making possible the receipt of significant data rates at distances as far as the planet Mars. To improve the data rate and distance capability, a 210-ft diameter antenna has been built at the Goldstone Mars Station, and two additional antennas of this size are planned for installation at overseas stations.

In their present configuration, all stations with the exception of Johannesburg, are full S-band stations. The Johannesburg receiver has the capability for L- to S-band conversion. The Ascension Island Station will be basically full S-band when it becomes operational.

It is the policy of the DSN to continuously conduct research and development of new components and systems and to engineer them into the network to maintain a state-of-the-art capability. Therefore, the Goldstone stations are also used for extensive investigation of space tracking and telecommunications techniques, establishment of DSIF/spacecraft compatibility, and development of new DSIF hardware and software. New DSIF-system equipment is installed and tested at the Goldstone facilities before being accepted for system-wide integration into the DSIF. After acceptance for general use, it is classed as Goldstone Duplicate Standard (GSDS) equipment, thus standardizing the design and operation of identical items throughout the system.

The GCS consists of voice, teletype, and high-speed data circuits provided by the NASA World-Wide Communications Network between each overseas station, the Cape Kennedy Station, and the SFOF. Voice, teletype, high-speed data, and video circuits between the SFOF and the Goldstone stations are provided by a DSN microwave link. The NASA Communications Network is a global network consisting of more than 100,000 route mi and 450,000 circuit mi, interconnecting 89 stations of which 34 are overseas in 18 foreign countries. It is entirely operationally oriented and comprises those circuits, terminals, and switching equipments interconnecting tracking and data acquisition stations with, for example, mission control, project control, and computing centers. Circuits used exclusively for administrative purposes are not included.

During the support of a spacecraft, the entire DSN operation is controlled by the SFOF. All spacecraft command, data processing, and data analysis can be accomplished within this facility. The SFOF, located in a three-story building at JPL, utilizes operations control consoles, status and operations displays, computers, and data-processing equipment for the analysis of spacecraft performance and space science experiments, and communications facilities to control space flight operations. This control is accomplished by generating trajectories and orbits, command and control data from tracking and telemetry data received from the DSIF in near-real time. The SFOF also reduces the telemetry, tracking, command, and station performance data recorded by the DSIF into engineering and scientific information for analysis and use by scientific experimenters and spacecraft engineers.

# II. Tracking and Navigational Accuracy Analysis



## A. DSIF Two-Way Doppler Inherent Accuracy Limitations: III. Charged Particles

D. W. Trask and L. Efron

### 1. Introduction

This is the third in a series of articles (*SPS* 37-38, -39, Vol. III, pp. 8–12, 7–15, respectively) on the inherent accuracy limitations to the DSIF data type commonly referred to as two-way doppler. In practice the doppler is continuously counted and sampled at fixed intervals such that the observable used by the orbit determination program is the range difference between the observer and spacecraft, which is accumulated over a fixed count interval. Although the accuracy of these data types has consistently exceeded the quality necessary for the successful fulfillment of the current Earth-based radio guidance role to which it has been committed, an effort is continually in progress to improve the quality of these data so that needs of future missions may be met. This article discusses the effect of the charged particles which exist in the ionosphere and the space plasma between the spacecraft and the tracking station.

A set of standard data-taking conditions has been selected for this series of articles to illustrate the inherent accuracy limitations on two-way doppler ($f_2$). These errors[1] are expressed in terms of their contribution to the range difference derived from counting the doppler tone over $10^4$ sec. This relatively long count time ($T_c \approx 3$ hr) is chosen to show the advantage of continuously accumulating doppler in the presence of bounded errors such as spacecraft limit cycle motion, doppler counter quantization, and system phase jitter. These errors would look deceptively large (percentagewise) for small $T_c$. In addition, $T_c$ is also made large to reduce the correlations of successive data points. Examples of the occurrence of relatively long correlation widths include the deviation between the real universe and the fitters model of atmospheric corrections and of the relationships among station time tags, universal time, and ephemeris time. In addition, it is assumed that the count interval is centered about the zenith, i.e., maximum elevation angle. This has the effect of minimizing the effects of atmospheric refraction.

Both lunar and planetary missions are considered. For the lunar case the spacecraft is assumed to be at a lunar distance which results in a radio signal round-trip transit

[1]All statistics are quoted as 1-$\sigma$ values unless otherwise specified.

time ($\tau$) of 3 sec while the spacecraft distance is 1.5 AU ($\tau$ = 1,500 sec) for the planetary case. This influences, for example, the data sensitivity to transmitter oscillator stability and, in the case of the space plasma, the number of charged particles the radio signal encounters.

## 2. Discussion

*a. Electromagnetic wave propagation.* When an electromagnetic wave propagates through a region containing charged particles there is an interaction between the ionized particles and the electric and magnetic fields associated with the wave. Any external magnetic field will complicate the interaction. The motion of an ion of mass $m$ and charge $e^*$ is described by

$$m\ddot{\mathbf{r}} = e^*\mathbf{E} + \frac{e^*}{c}\dot{\mathbf{r}} \times \mathbf{H} - m\nu\dot{\mathbf{r}}$$

where

$\nu$ is the effective collision frequency

$\mathbf{H}$ is the magnetic field

$\mathbf{E}$ is the electric field vector

$c$ is the speed of light

$\mathbf{r}$ is the displacement of the ion

Magnetometer measurements aboard spacecraft have to date, shown that the magnetic fields encountered in the interplanetary medium are negligible with respect to their effects on radio tracking signals. The collision frequency may also be assumed to be near zero. Neglecting terms of order $(1/c)$ we have simply (Ref. 1).

$$m\ddot{\mathbf{r}} = e^*\mathbf{E}$$

For a plane $E$ $M$ wave of amplitude $E_0$ and angular frequency $\omega$ we will have $E = E_0\, e^{j\omega t}$ and

$$m\ddot{\mathbf{r}} = e^*E_0\, e^{j\omega t}$$

the solution of which is

$$r = -\left(\frac{e^*E_0}{m\omega^2}\right)e^{j\omega t} + At + B$$

Since $B$ merely specifies an origin and $A$ implies a constant component of velocity, they are usually both taken to be zero. This result is equally valid for electrons or heavy ionic particles. The mass of a proton or ion will be eighteen hundred times that of an electron. Thus, their amplitudes of motion will be very much smaller than those of electrons.

The conduction current, due to the presence of freely moving charged particles of density $N$, is given by

$$I = Ne^*\frac{dr}{dt} = -\frac{je^{*2}N}{m\omega}E_0e^{j\omega t}$$

The conductivity of the medium $\sigma$, is the ratio $I/E$ and is

$$\sigma = -\frac{je^{*2}N}{m\omega}$$

Since $\sigma$ is a purely imaginary quantity, it implies that the current and field waves are 90 deg out of phase with one another, and no power is consumed. Although, to these approximations, the wave is not damped, its velocity of propagation will be altered by the presence of the ions.

For a wave described by

$$E = a\cos(\omega t - kx)$$

the velocity of propagation, in a dispersive medium, is defined by the spatial variation of its phase. Surfaces of constant phase propagate at a velocity $v$, given by

$$v = \frac{\omega}{k}$$

We define the index of refraction $n$ of a medium by the relation

$$n = \frac{c}{v}$$

Taking the dielectric constant of free space to be unity, it can be shown that

$$n = \left(1 - \frac{Ne^{*2}}{mk\omega^2}\right)^{1/2}$$

At this point we note that $n \leq 1$ for both electrons or positive ions, and the phase velocity through the ionized region is greater than in free space. For any given electron density, it is also noted that the phase velocity decreases with the square of the signal frequency.

Since monochromatic waves exist in textbooks only, let us look at a signal composed of two waves of equal amplitude, but slightly different frequencies and propagation constants. If the two waves are given by

$$E_1 = \cos[\omega t - kx]$$

$$E_2 = \cos[(\omega + \delta\omega)t - (k + \delta k)x]$$

where $\delta\omega$ and $\delta k$ are small compared with $\omega$ and $\delta$, the sum $E = E_1 + E_2$ is given by

$$E = 2\cos\left[\frac{\delta\omega}{2}t - \frac{\delta k}{2}x\right]\cos\left[\left(\omega + \frac{\delta\omega}{2}\right)t - \left(k + \frac{\delta k}{2}\right)x\right]$$

The result is a wave exhibiting a beat frequency. The carrier is essentially the original frequency $E_1$, but the envelope is characterized by a wave for which planes of constant amplitude have a velocity of propagation $u$, given by

$$u = \frac{\delta\omega}{\delta k}$$

The quantity $u$ is referred to as the group velocity. Further analysis gives

$$uv = c^2$$

and we see that while the phase velocity may exceed $c$ in an ionized medium, the group velocity will be less than $c$.

For $N$ expressed in electrons per cubic meter and the signal frequency $f$ in Hz we have

$$n = \sqrt{1 - 80.6\frac{N}{f^2}}$$

The effect of a nonunity index of refraction on the doppler and ranging methods utilized in the radio tracking of a spacecraft is that the observed doppler will be advanced (the range difference accumulated by counting the doppler tone is decreased) by

$$\Delta\dot{f} = \frac{40.3}{f^2}\frac{d}{dt}\int N\,ds$$

and the ranging signal, which propagates at the group velocity, will be retarded (the extended travel time indicating a fictitious increase in the measured range) by an amount proportional to

$$\frac{40.3}{f^2}\int N\,ds.$$

The integration is along the entire signal ray path.

The integral may be broken down into two parts. One through the Earth's ionosphere and the other through the interplanetary medium. Additional planetary ionospheres encountered along the ray path would also bear consideration.

***b. Charged particle density and flux in the interplanetary medium.*** Plasma probes aboard *Mariners II* and *IV* and aboard *Pioneer VI* have measured or are measuring local values of charged particle density and flux in the interplanetary medium. The information gathered to date indicates that nearly all the charged particles detected are in the so-called solar wind which consists of a flow of electrons, protons and alpha particles moving radially outward from the Sun. The plasma flow seems to have three source mechanisms. The first is a perpetual general outflow from the solar corona while the second is the emission of intermittant jets of varying intensity. The duration of an individual jet may be several solar rotations. These latter give the solar wind a pinwheel streamer configuration. The final mechanism is anomaly effects such as plasma emissions due to solar flares. When viewed from along the Sun's axis of rotation, we see that the streamer regions of higher density take on a garden sprinkler appearance.

Under the assumption of local charge neutrality the electron density $N_e$ will be given by

$$N_e = N_p\left(1 + 2\frac{N_\alpha}{N_p}\right)$$

where $N_\alpha/N_p$ is the ratio of alpha particles to protons. From *Mariner II* (Ref. 2) results this ratio appears to be about 0.05. For a spherical outflow, conservation of mass requires $Nvr^2 =$ constant. This requires particle density flux to follow a $r^{-2}$ relation with respect to distance from the Sun (Fig. 1) (obtained from Ref. 3).

*Mariner II* measured proton densities in the interplanetary medium between the orbits of the Earth and Venus. Proton velocities varying from 300 to 800 km/sec (3-hr averages) have been recorded (Fig. 2; obtained from Ref. 3). At these velocities the gravitational deceleration between the orbits of Venus and the Earth would be negligible, and this is indicated to be so in that *Mariner II* detected no dependence of particle velocity on heliocentric distance. At a velocity of 500 km/sec a particle leaving the Sun would reach the vicinity of the Earth's orbit in 3½ days. During this time the Sun would have rotated approximately 45 deg. Fig. 3 illustrates how particles flowing radially outward near the Sun's equatorial plane would generate spiral streamers in the solar wind. The Sun's equator is inclined by 7 deg 15 min to the ecliptic, and hence all the interplanetary probes to date would have experienced the solar wind as described.

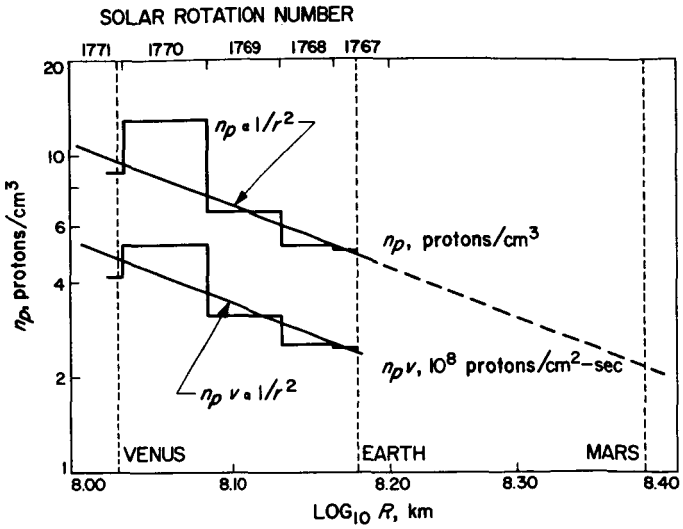


**Fig. 1. Logarithmic plot of proton density and flux vs distance from the Sun. The measurements have been averaged over a solar rotation. *Mariner II* (1962) (Ref. 3)**

The flux density in the solar wind is probably related to the solar sunspot cycle. *Pioneer VI*, which was launched into a heliocentric orbit between the Earth and Venus late in 1965, after the last minimum in the sunspot cycle (Fig. 4), has aboard two plasma probes from MIT and Ames. Recent telephone conversations with members of the experiment teams indicate it has detected the presence of only four or five dense streamers, while *Mariner II*, launched between the previous maximum and this minimum, detected the presence of many more and broader regions of high density. However, both spacecraft seem to be encountering very nearly the same average values of local electron density over a solar revolution. *Local* electron densities deduced from the proton density measurements, as shown in Fig. 2, range from 1–30 electrons/cm$^3$. An average near 10 electrons/cm$^3$ is indicated.

The Stanford dual frequency experiment aboard *Pioneer VI* consists of the transmission of two coherent signals at widely separated frequencies from Stanford to the probe (Ref. 4). Both signals are simultaneously modulated by a low frequency signal. The inverse square frequency dependence of phase and group velocities on electron density makes possible the detection of relative carrier phase and group envelope phase differences. From these measurements the total integrated electron density and its time rate of change along the entire signal ray path may be deduced. *Pioneer VI* is in an orbit having an aphelion and perihelion of 1 and 0.8 AU, respectively. In recent telephone conversations, Dr. Bruce Lusignan of Stanford indicated that preliminary results from the Stanford dual frequency experiment show average values over the entire interplanetary portion of the Stanford-*Pioneer VI* signal ray path that vary from 5–25 electrons/cm$^3$ with an average value over a solar revolution near 10 electrons/cm$^3$. This wide range may be accounted for by the presence of only a few dense streamers coupled with a geometry such that the ray path may at times lie entirely within or outside a streamer.

Subsequent *Pioneer* missions will explore the interplanetary medium beyond the orbit of the Earth out to a heliocentric distance of 1.2 AU. Referring to Fig. 1 we see that extrapolation of available data indicates that the effects on radio tracking signals due to the presence of the solar wind would be greater for a typical Venus mission than a typical Mars mission.

For a typical Mars mission near the minimum of the solar cycle we may expect an average electron density of 5 electrons/cm$^3$ along an S-band ray path through the interplanetary medium from Earth to Mars. Over 1.5 AU, this would produce a range error of approximately 11 m at S-band. The time rate of change of the integrated electron density would depend greatly on the number of streamers in the solar wind and the spacecraft-Sun-Earth geometry. A worst condition would occur when the geometry was such that the ray path went from almost entirely outside to almost entirely inside (or vice versa) a streamer. Assuming a linear variation over 3 days between extremes, 2 and 15 electrons/cm$^3$ could result in a phase advance of approximately 0.011 cm/sec ($\approx$0.0085 Hz) at 1.5 AU for an S-band signal. This would represent an error of 1.1 m in the change in range over $10^4$ sec.

References 2, 3, 5–8 are a source for further readings on solar wind research.

The Earth's ionosphere is also dependent on the state of solar activity, but the major source of ions seems to be primarily dependent on the ionizing radiation of the Sun in the upper atmosphere (Ref. 9 and 10). Particle flow from the Sun into the planetary atmosphere is negligible, if not nonexistent.

*c. Ionospheric effect on range measurements.* The ionospheric effect on range measurements is illustrated in Fig. 5 for the range nighttime (low sunspot index) to daytime (high sunspot index). This figure is based on an internal report by A. Liu and D. Cain which assumes a Chapman atmosphere and studies the variation of $\delta_I \rho$ with maximum electron density, height of maximum electron density, scale height, and temperature. The range

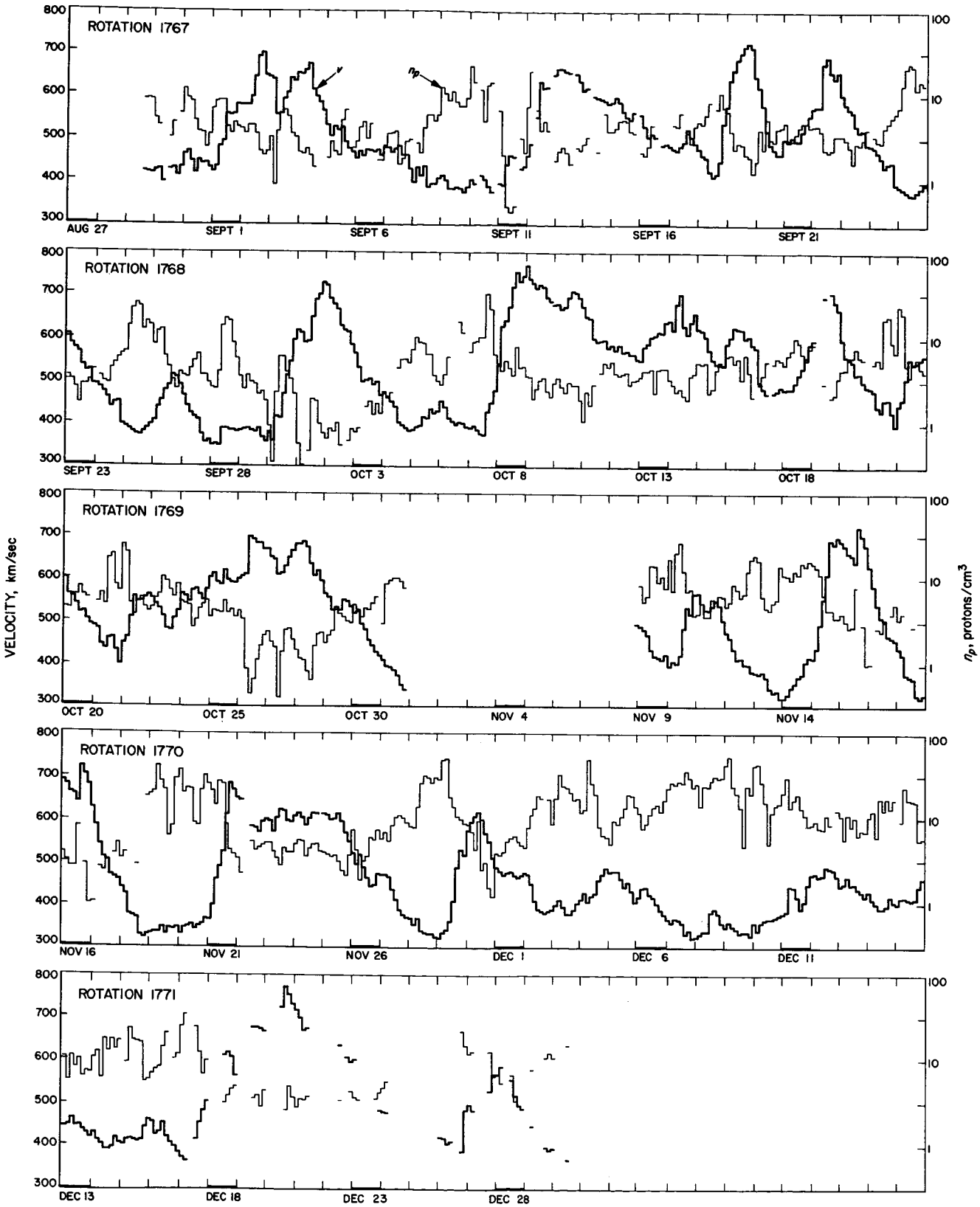


**Fig. 2. Calculated proton velocity and density (3-hr averages), *Mariner II* (1962) (Ref. 3)**

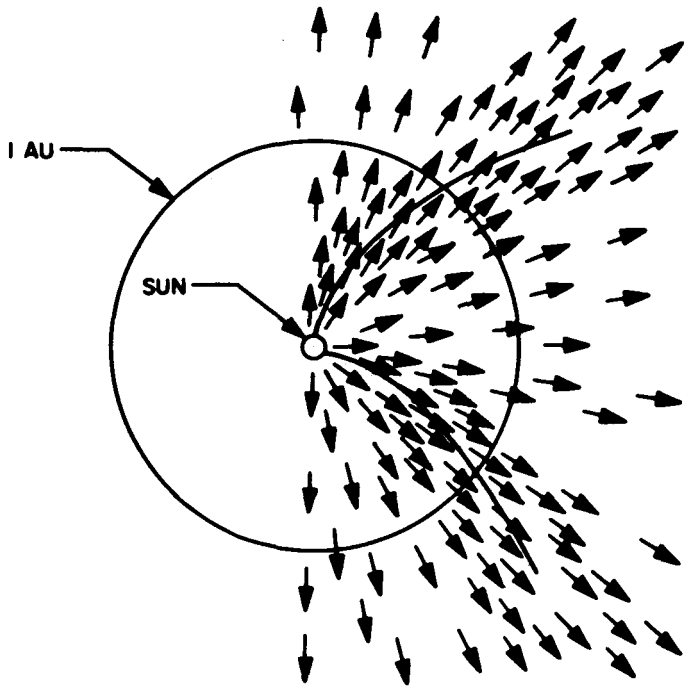


**Fig. 3. The pinwheel solar wind pattern illustrating two streamers formed by charged particles flowing everywhere radially outward from the Sun**

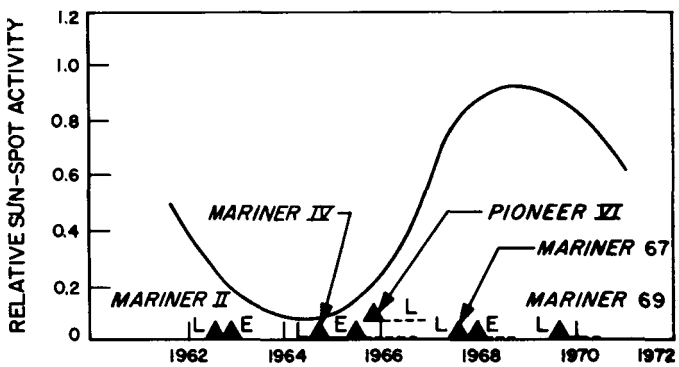


**Fig. 4. Solar activity cycle**

correction $\delta_I\rho$ varies linearly with the maximum electron density. This parameter causes the greatest variation in $\delta_I\rho$ and, in fact, differs by an order of magnitude for the conditions presented in Fig. 5. However, this effect is largely predictable from the sunspot index disseminated by the Bureau of Standards, Central Radio Propagation Laboratory, Boulder, Colorado, (Ref. 11 and 12) and a knowledge of the tracking geometry. In fact, the chief parameters determining the state of the ionosphere above any point on the Earth's surface appear to be the state of solar activity, geomagnetic latitude, time of day and time of year. The latter two are sometimes accounted for

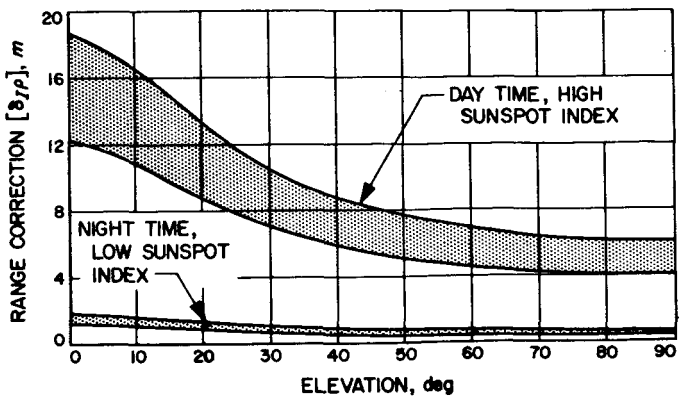


**Fig. 5. Effect of ionosphere on range measurements DSIF S-band system ($f = 2.3 \times 10^9$ Hz)**

by considering the solar zenith angle. Present ability to model the ionosphere for the purpose of predicting electron density profiles is very limited. Although it may be possible to predict the slope and level of the $\delta_I\rho$ vs elevation angle curve to about 10% on a day-to-day basis, at a particular location based on accumulated data,[2] the accuracy of long-range or world-wide predictions is very poor. The correlation between stations several hundreds of kilometers distant is often poor.

The correction to counted doppler accumulated over $T_c$ sec is essentially the difference between the two range corrections $T_c$ sec apart. In particular, the formula for this correction is

$$\epsilon_{CP_{\Delta\rho(t,T_c,\tau)}} = \frac{1}{2} E \{ [\delta_{CP}\rho(t) + \delta_{CP}\rho(t-\tau)] - [\delta_{CP}\rho(t-T_c) + \delta_{CP}\rho(t-T_c)-\tau] \}$$

where

$\epsilon_{CP_{\Delta\rho}}$ = effect of charged particles on the counted doppler range difference

$\delta_{CP}\rho$ = effect of charged particles on range

$t$ = time that accumulation of $\Delta\rho$ is completed at the receiving tracking station (in practice $t$ is the data time label)

$T_c$ = count (accumulation) time for $\Delta\rho$

$\tau$ = round trip signal transit time

$E\{\ \}$ = expected value operator

The above formula applies to the effect on accumulated doppler of charged particles in the ionosphere

[2]This represents extrapolation from a perfect knowledge. Otherwise it is probably no better than 20%.

and/or solar plasma. For the nominal conditions considered in this article, $\tau = 1500$ sec for 1.5 AU and $T_c = 10^4$ sec, and it is assumed that the elevation angle at the end points of the doppler accumulation interval is greater than 30 deg. A typical time history of elevation angle during the same lunar mission is shown in Fig. 6 for a deep space station (DSS) at Goldstone, California (latitude = +35.4 deg) and at Woomera, Australia (latitude = −31.4 deg). The maximum elevation angle ($\gamma_{max}$) is a function of the DSS latitude ($\phi$) and the local declination ($\delta_L$) of the probe. In particular

$$\gamma_{max} = 90 \text{ deg} - |\delta_L - \phi|$$

The majority of the DSS are located at either $\phi \approx +35$ deg or $\phi \approx -35$ deg. Therefore, for a distant probe $\gamma \geq 30$ deg for some of the DSS at the end points of the $T_c = 10^4$ sec doppler accumulation period. To minimize the effects of variations in elevation angle, it is assumed that the count interval is centered about the maximum elevation angle. This means that the range corrections which are being differenced will be at nearly identical elevation angles, and, therefore, errors in the predicted slope of the correction vs elevation angle will be minimized. It is assumed that with a reasonable model for the ionosphere $\epsilon_{I_{\Delta\rho}}$ will be good to 10% (although $\delta_I\rho$ is good only to 20%). The principal limitation is due to the fluctuations of $n$ with time.

In some instances the spacecraft will carry equipment which, along with ground based equipment, is sufficient to calibrate the total (ionosphere and space plasma) charged particle effect. Two approaches are available. The first is the dual frequency experiment of Stanford University (Ref. 4) which is aboard the *Pioneer VI* spacecraft and has been approved for the *Mariner* 67 mission.

The second approach also makes use of the fact that the charged particles retard the group velocity and advance the phase velocity. The DSIF two-way doppler experiences the phase velocity advance while the pulse

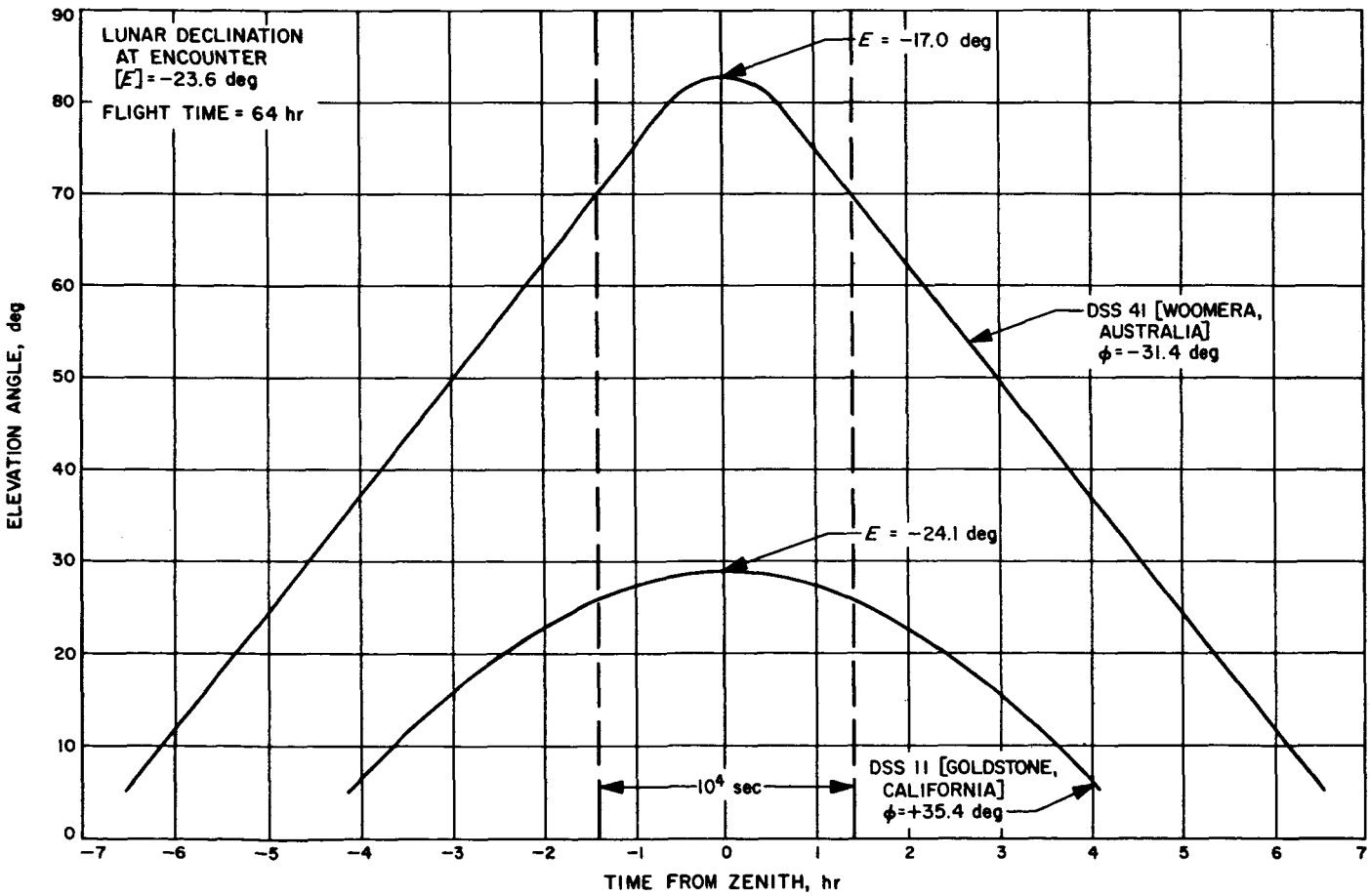


**Fig. 6. Typical elevation angle time history for a lunar mission**

code of the DSIF ranging system suffers the group velocity retardation. These two effects are nearly equal in magnitude and opposite in sign. Therefore, when the spacecraft carries a DSIF doppler/ranging transponder, the influence of the charged particles can be measured during the period when both range and $f_2$ are obtained. Missions (per present plans) which will be able to employ the phase-group velocity calibration technique include the *Lunar Orbiter, Apollo, Mariner* 67, *Mariner* 69, and the *Voyager* missions.

This method of calibration is limited by those errors (to the extent they cannot be measured or predicted) which do not have an equal effect on the range difference obtained by integrating the two-way doppler and the range increment obtained by differencing the range measurement at the start from the one at the end of the doppler accumulation interval.

The size of these combined errors is shown in Table 1 for the *Lunar Orbiter, Mariner* 67 Venus, and post 1970 missions. Time lags, tracking errors, and the resolution of the present ground handling system are the main sources of error. The measurement of charged particle effects was envisioned relatively recently. Specifications resulting from this requirement in several cases greatly exceed those imposed during the design of the spacecraft transponder and ground data handling system. Although this calibration technique will be exercised during the *Lunar Orbiter* mission the errors of the system will be large compared to the effect being measured. It should be noted that although bounds on the error sources considered in constructing Table 1 are reasonably well known, their actual variation over $10^4$ sec has not been rigorously tested. The *Lunar Orbiter* data will aid in analyzing some of these characteristics.

**Table 1. Limitations to range measurements: field performance**

| Mission | Uncertainty in $\rho(t_2) - \rho(t_1)$ ($t_2 - t_1 = 10^4$ sec), m | |
|---|---|---|
| | Spacecraft | Ground system |
| *Lunar Orbiter* | 1 – 6 | 1 – 7 |
| *Mariner 67* | | |
| Standard ground system | 0.5 – 5 | 1 – 7 |
| Research ground system | 0.5 – 5 | 0.1 – 1 |
| Post 1970 (Next generation spacecraft transponder) | 0.05 – 0.5 | 0.01 – 0.1 |

The *Mariner* 67 mission will be the first chance to measure a sizeable solar plasma effect. In addition, the calibration of the spacecraft transponder will be superior to that performed for the *Lunar Orbiter* and an improved ground system will be in operation at the 210-ft dish at Goldstone on an experimental basis. This system will provide data of sufficient quality to make meaningful comparisons with the measurements obtained by the Stanford University dual frequency experiment which is part of the *Mariner* 67 scientific payload.

The group/phase velocity requirements will be incorporated in the specifications of the next generation spacecraft transponders and ground data handling systems. It is anticipated that the charged particle effects will be measurable from 0.05 to 0.5 m during post 1970 missions.

Although such plans are being made for the future, charged particle effects are currently ignored at JPL when processing the two-way doppler data. The past plus the predicted history of the data processing is delineated in Table 2 for the case of the ionosphere and space plasma. This information is shown in a different form in Fig. 7 starting with the *Ranger III* mission and projecting into the 1970's. Event markers for the *Ranger III-IX* and *Surveyor 1* (lunar missions) as well as for the launch and target encounter of *Mariner II* (Venus), *Mariner IV* (Mars), and *Mariner* 67 (Venus) are superimposed on this figure. Both planetary (spacecraft at 1.5

**Table 2. Effect of charged particles on two-way doppler accumulated over $10^4$ sec[a]**

| Past and predicted history of data processing | | Source of charged particles | $\sigma_{CP_{\Delta\rho}}$, m |
|---|---|---|---|
| Time period | Conditions | | |
| 1962–1964 | Uncalibrated-L band | Ionosphere<br>Space plasma | 1.0 to 6.0<br>3.0 to 9.0 |
| 1964–1967 | Uncalibrated-S band | Ionosphere<br>Space plasma | 0.17 to 1.5<br>0.5 to 1.5 |
| 1967 | Modeled ionosphere uncalibrated | Ionosphere | 0.1 to 1.0 |
| 1967 | Phase-group velocity calibration | Total | 0.5 to 1.8 |
| 1970 | Modeled ionosphere | Ionosphere | 0.05 to 0.5 |
| 1970 | Phase-group velocity calibration | Total | 0.05 to 0.5 |

[a] $\rho = 1.5$ AU [Mars Mission] and the $10^4$ sec accumulation period is centered about the maximum elevation angle.

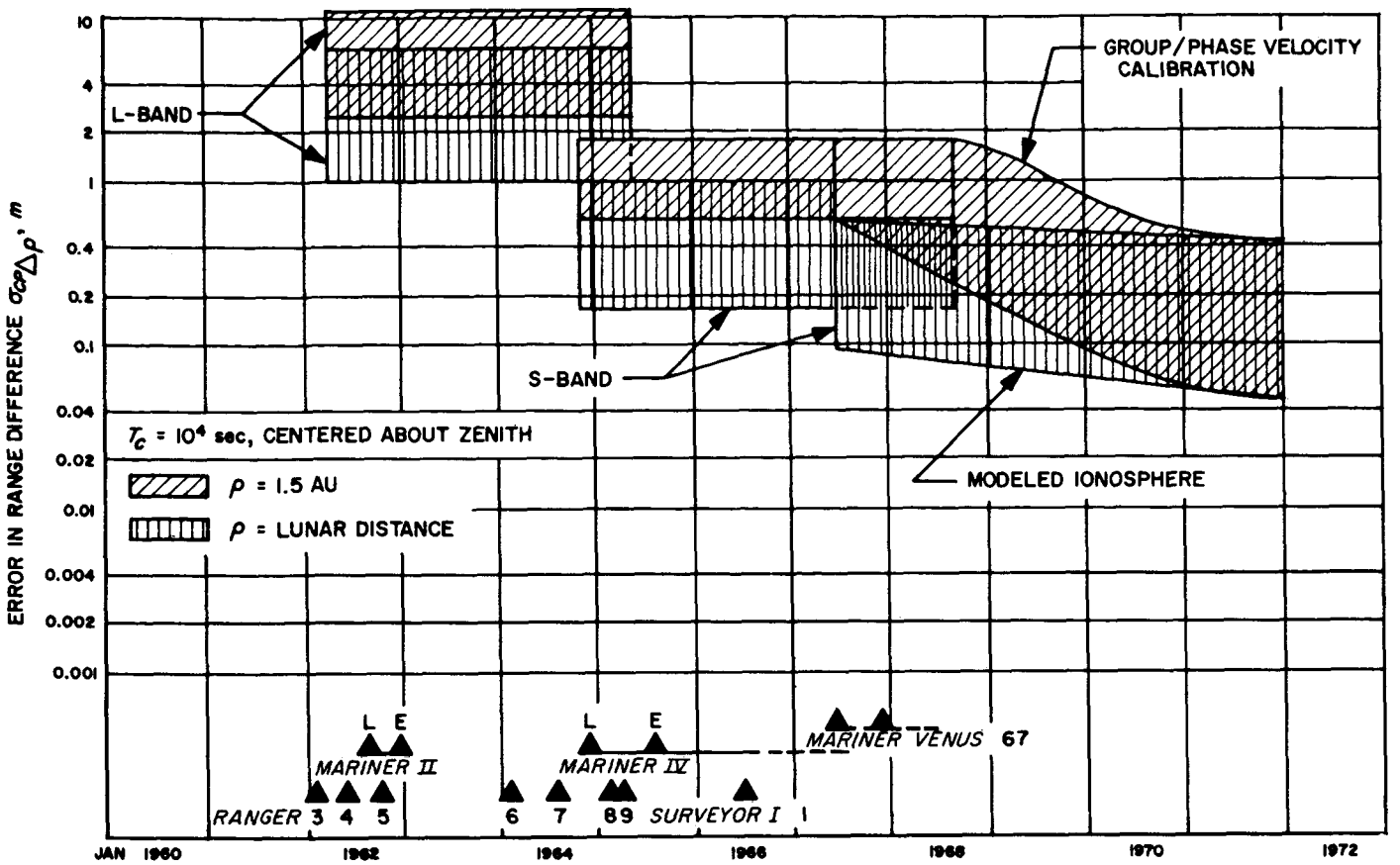


**Fig. 7. Effect of charged particles**

AU's) and lunar conditions are illustrated. The planetary missions include the ionospheric and space plasma effect while the lunar conditions illustrate only the effect of the ionosphere. (The space plasma effect is negligible.) Under favorable conditions a modeled but uncalibrated ionospheric correction will be accurate to 0.1 m. The calibration of the total charged particle effect for planetary distances to 0.1 m or less will not be available until the post *Mariner* 67 missions. These techniques, such as the phase-group velocity calibration, do not separate the contributions due to the ionosphere and space plasma but measure the total charged particle effect.

## 3. Summary

By 1970 the effects of charged particles will be measurable to less than 0.1 m by the group/phase velocity technique. That is, the charged particle effect on the phase velocity of DSIF doppler is nearly equal and opposite to its group velocity effect on the DSIF range code. Therefore, a comparison of the range difference obtained by accumulating doppler with the range difference obtained from direct range measurements at the ends of the doppler accumulation period will provide a measurement of the influence of the charged particles. This approach will be tried during the *Lunar Orbiter* mission. But the first chance to obtain meaningful space plasma measurements will come during *Mariner* 67. The *Mariner* 67 mission will also carry a Stanford University dual frequency experiment for comparing the two measuring techniques.

## 4. Acknowledgments

The authors wish to express their appreciation to Mr. T. W. Hamilton for the many helpful discussions on the topics included in this section and to Mr. M. Easterling for his help in ascertaining the current limitations associated with the DSIF ranging system. The cooperation of Mrs. Marcia Neugebauer in making the *Mariner II* solar plasma probe results available for our use is gratefully acknowledged.

# B. A Study of Planetary-Approach Orbit-Determination Policies Using *Mariner IV* Doppler Data

G. W. Null

## 1. Introduction

The *Mariner IV* spacecraft was launched November 28, 1964 and made its closest approach to Mars July 15, 1965 at 01:00:57 GMT. At the time of Mars encounter ($E$) the distance from Mars was 13201 km.

During the mission, highly accurate two-way doppler tracking data were taken by the DSN. During the period of $E-5$ days to E, four DSN tracking stations provided continuous coverage: Goldstone, California; Canberra, Australia; Woomera, Australia, and Johannesburg, South Africa. Goldstone and Canberra had regular S-band stations while Woomera and Johannesburg operated with L- to S-band conversion kits, which gave a factor of 3 poorer resolution. The Goldstone station was equipped with a "times 8" multiplier which multiplied the doppler frequency by 8 before counting, thus increasing the resolution. The limiting error source for all stations was instability in the rubidium standard. (See *SPS 37-39*, Vol. III, pp. 7–15 for a detailed description of the *Mariner IV* data noise and its causes.) This error source contributed a 1-$\sigma$ noise of 0.0005 m/sec for 60-sec sampled data or 0.00025 m/sec for 600-sec sampled data.

The accuracy of the tracking data for 60-sec data (expressed in range rate) at Mars distance was:

| | |
|---|---|
| For Goldstone | $\sigma_{\dot{r}} = 0.0005$ m/sec |
| For Canberra | $\sigma_{\dot{r}} = 0.001$ m/sec |
| For Woomera and Johannesburg | $\sigma_{\dot{r}} = 0.003$ m/sec |

When data are processed by counting over 600 sec, the error for all stations is $\sigma_{\dot{r}} \leq 0.0005$ m/sec.

For the time span of interest, 600-sec data were taken from $E-5$ days to $E-4$ hr (H) and 60-sec Goldstone data from $E-4$ hr to $E+4$ hr. Thus, each data point had an accuracy of 0.0005 m/sec 1$\sigma$. When assigning *a priori* standard deviations to the tracking, as used in orbit determination, the assumption was made (which will be substantiated by the results to follow) that low frequency, long correlation width noise external to the data was the predominant orbit error source. Therefore, for orbits, the 600-sec data are assigned a standard deviation which is a factor of $(10)^{1/2}$ smaller than the 60-sec data. The weights (standard deviations) for the results to be discussed are all quoted for a 60-sec sample rate.

This article will present the orbit determination target error results obtained by analyzing the tracking data from $E-5$ days to the following times:

$$(E-72\text{H}, E-48\text{H}, E-24\text{H}, E-17\text{H},$$
$$E-5\text{H}, E-1\text{H}, E-0.3\text{H}, E+0.25\text{H})$$

A weighted least squares single precision orbit determination program was used for the analysis. The quantities of interest are the predictions of the following closest approach quantities

$\mathbf{B}$ = a vector from the center of Mars normal to the incoming asymptote

$\mathbf{B} \cdot \mathbf{T}_c, \mathbf{B} \cdot \mathbf{R}_c$

where $\mathbf{T}_c$ is a unit vector in the plane of the ecliptic normal to the incoming asymptote $\mathbf{S}$. $\mathbf{R}_c$ makes up a right-handed RST coordinate system. For *Mariner IV*, $\mathbf{R}_c$ is very nearly normal to the elliptic plane. Finally, the errors in time of closest approach (TCA) are investigated. The evaluation of the target point prediction error, as a function of time, is accomplished by assuming that the "true" target point may be obtained by fitting data from $E-5$ days to $E+5$ days. A full discussion of this orbit and its accuracy is given in *SPS 37-39*, Vol. III, pp. 24–30. Summarizing these results, it was shown that the target point was accurate to at least 20 km. Since most of the errors to be discussed here are much greater than 20 km and since we are mainly interested in the deviations from the final predicted target point, it may be considered that the "true" target point is exact. The astronomical unit ($AU$) was determined to within $\pm 500$ km of 1$\sigma$ and the gravitational constant of Mars ($\mu$) to within $\pm 8$ km$^3$/sec$^2$.

The reason for fitting only the near-encounter tracking data for encounter operations, as was done for *Mariner II* and *Mariner IV*, has been the difficulty in obtaining good solutions over long tracking arcs. One particularly troublesome error source is small unpredictable disturbance accelerations from the attitude control system ($\cong 2 \times 10^{-7}$ cm/sec$^2$ for *Mariner IV* and 25 to 50 $\times$ $10^{-7}$ cm/sec$^2$ for *Mariner II*). Other important error sources are the planetary ephemerides and the $AU$. Although the use of longer tracking arcs in the presence of a determinate model should always give better and more reliable results, the actual nondeterminate errors negate this conclusion for current probes. Certain future missions including *Voyager* have such requirements for high accuracy as to necessi-

tate fitting over long arcs. This requires that the ephemeris errors and small force errors be held to a minimum. The work to control these errors is being planned such that by 1970 an accuracy of 100 km at $E-30$ days may be achieved.

Although it is hoped that such error sources will be reduced to a negligible amount by 1970, this is by no means certain. Therefore, it is important to examine carefully the accuracy attainable using only short arc encounter data, both for current spacecraft and for *Voyager* era spacecraft. The purposes of this study are:

(1) To compare, using the current single precision orbit determination program (SPODP), the actual real-time *Mariner IV* orbit determination errors with the errors which would have existed if alternative orbit determination policies had been adopted.

(2) To obtain a better indication of the accuracy obtainable using current software and present tracking data accuracies. This information is needed for planning for future missions in the following ways:
   (a) Demonstrating typical error patterns for the approach phase.
   (b) Giving a better background for "committing" orbit accuracy to the flight projects. Normally the committed accuracy will be at least as good as the current "state of the art" accuracy.
   (c) Showing which *a priori* statistical assumptions for data weighting and initial conditions are consistent with the actual errors. These assumptions may then be applied to study a wide range of trajectories for future missions.
   (d) Aiding the selection of an optimum orbit determination policy for future missions.

(3) To answer certain questions of general interest such as:
   (a) What accuracy in determining $AU$ and $\mu$ is possible as a function of time before encounter?
   (b) At what time does the smallest B plane uncertainty ($SMIA$) shift from being along $\mathbf{B} \cdot \mathbf{T}$ to being along the $\mathbf{B}$ vector, as predicted by orbit theory?

## 2. A Priori Statistics Used in Computer Runs

### a. Real time runs (plot symbol X).

(1) $\tilde{\sigma}_{\dot{r}}$ = 0.03 m/sec for 60-sec sample

(2) $\tilde{\sigma}_{position}$ = 500 km spherical distribution at $E-5$ days

(3) $\tilde{\sigma}_{velocity}$ = 0.1 m/sec spherical distribution at $E-5$ days

(4) $\tilde{\sigma}_{AU}$ = 2000 km

(5) $\tilde{\sigma}_{\mu}$ = 860 km$^3$/sec$^2$ = 2.0%

The errors in the *a priori* positions were $\cong$ 1000 km and the errors in the *a priori* velocities were $\cong$ 0.1 m/sec. The error in the *a priori* $AU$ was $\cong$ 1000 km and the error in $\mu$ was $\cong$ 100 km$^3$/sec$^2$.

### b. Postflight runs.

(1) Common characteristics
   (a) $\tilde{\sigma}_{\dot{R}}$ = 0.003 m/sec for 60-sec sampled data
   (b) $\tilde{\sigma}_{position}$ = $\infty$ at $E-5$ days
   (c) $\tilde{\sigma}_{velocity}$ = $\infty$ at $E-5$ days

(2) Runs solving for position and velocity only
   (a) Use true $AU$, $\mu$ (plot symbol 0)
   (b) Use true $AU$ but
   $\Delta\mu$ = 150 km$^3$/sec$^2$ (no plot since results were off scale $\cong$ 3000 km)
   (c) Use true $\mu$ but
   $\Delta AU$ = + 1500 km (plot symbol $\Delta$)

(3) Solve for position, velocity, $\mu$, and $AU$ with no *a priori* information (plot symbol ■)

## 3. Explanation of Plots

The various types of runs shown in the plots are discussed in Section 2. Also displayed on most plots are the 1-$\sigma$ limits which come from a no *a priori* solution for position and velocity with $\tilde{\sigma}_{\dot{R}}$ = 0.003 m/sec. The exception was Fig. 8 for $|\mathbf{B}|$ since SPODP does not compute $\sigma_B$. For most parameters the error is shown in two plots; one for the time span $E-5$ days to $E-5$ hrs and the other for the time span $E-5$ hrs to $E+0.25$ days.

Among the cases not shown was a set of runs defined by Section 2 (b) in which $\Delta\mu$ = 150 km$^3$/sec$^2$. The target error for this case was greater than 3000 km for the entire period $E-5$ days to $E+0.25$ hrs. Other cases not shown include a set using simulated data with no noise, solving for position and velocity with $\Delta AU$ = 500 km and $\Delta$ Earth–Mars ephemeris of 100 km spherical error. No significant differences were seen between this case and those displayed here.

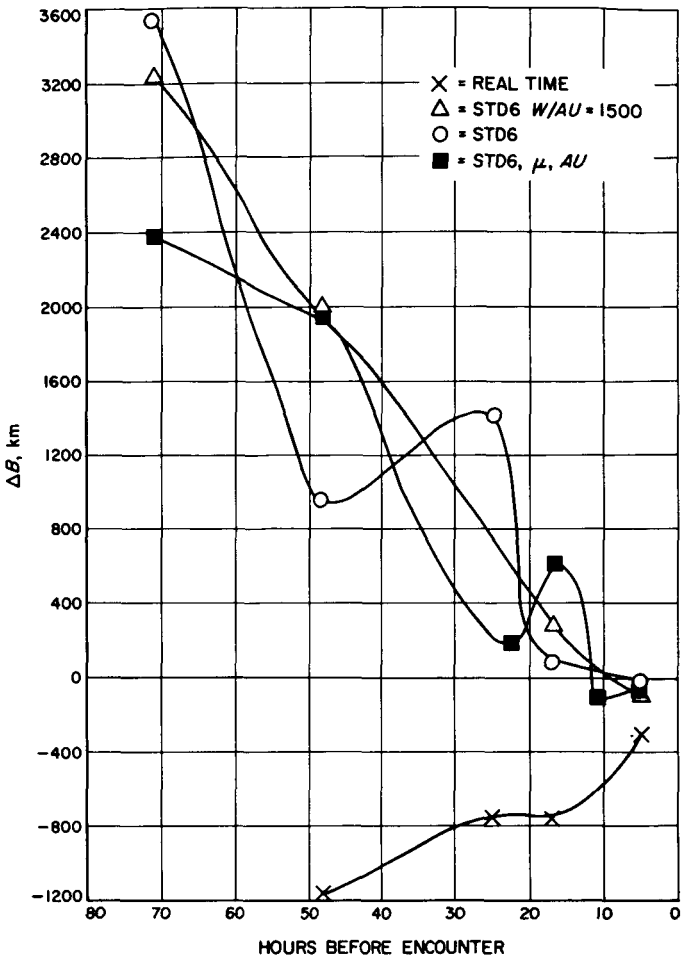


**Fig. 8. Vector magnitude error vs hours from *Mariner IV* encounter $E - 72$ H to $E - 5$ H**

The figures and their contents are listed as follows:

| *Fig.* | *Quantities* | *Time span, hrs* |
|---|---|---|
| 8 | $\Delta B$ | $E-72$ to $E-5$ |
| 9 | $\Delta B \cdot T$ | $E-72$ to $E-5$ |
| 10 | $\Delta B \cdot T$ | $E-5$ to $E$ |
| 11 | $\Delta\mu$ | $E-72$ to $E$ |
| 12 | $\Delta AU$ | $E-72$ to $E$ |
| 13 | Orientation angle of *SMIA* from **B** | $E-72$ to $E$ |
| 14 | $\Delta B \cdot R$ | $E-72$ to $E-5$ |
| 15 | $\Delta B \cdot R$ | $E-5$ to $E$ |
| 16 | $\Delta B$ | $E-5$ to $E$ |
| 17 | $\Delta TCA$ | $E-72$ to $E-5$ |
| 18 | $\Delta TCA$ | $E-5$ to $E$ |
| 19 | *SMAA* and *SMIA* | $E-72$ to $E-5$ |
| 20 | *SMAA* and *SMIA* | $E-5$ to $E$ |

*SMAA* and *SMIA* are the semimajor and semiminor axes of the 40% dispersion ellipse of the predicted target point in the *B* plane.

## 4. Significant Features Seen in the Plots

Comparing the 1-$\sigma$ limits with the actual errors, it may be seen that an *a priori* data weight of $\tilde{\sigma}_{\dot{r}} = 0.005$ m/sec for a 60-sec sample is consistent with the observed errors. Since simulated data showed similar errors, it is likely that software error is the major limiting error source and that a dramatic improvement in accuracy by perhaps a factor of five can be made with improved software. (High frequency noise on the data $\cong$ 0.0005 m/sec.) Limiting error sources such as ephemeris errors become proportionately more important for these higher accuracies.

The real-time runs tend to have larger errors and to show different patterns than the postflight runs because the *a priori* statistics used on position were too small in proportion to the errors in the *a priori* position. This was

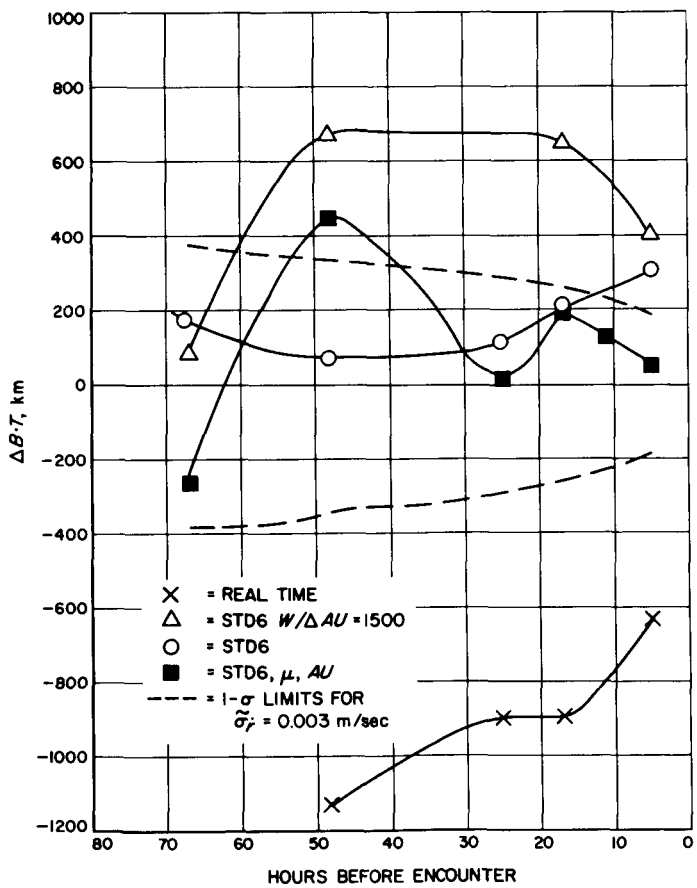


**Fig. 9. $B \cdot T_c$ error vs hours from *Mariner IV* encounter $E - 72$ H to $E - 5$ H**

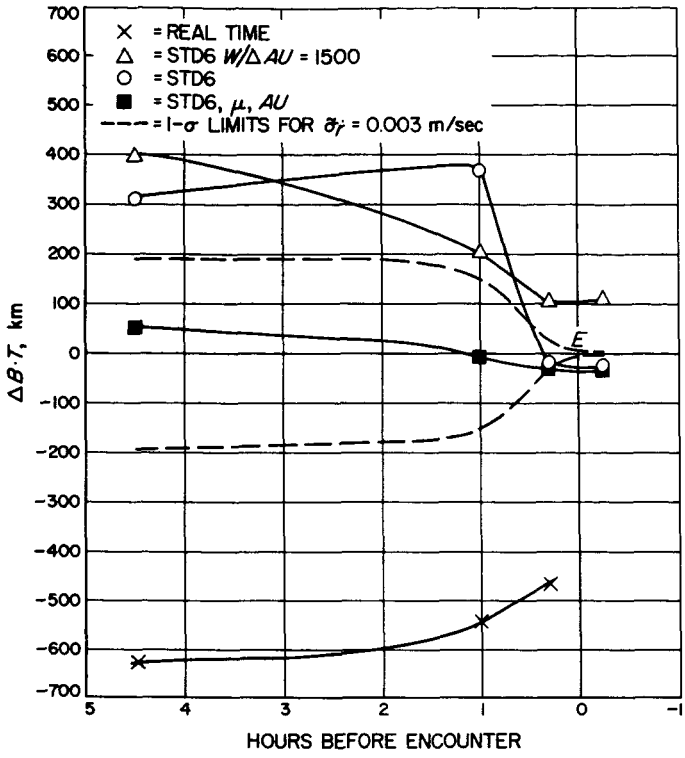


**Fig. 10. $B \cdot T_c$ error $E - 5$ H to $E + 0.25$ H**

especially true for $B \cdot T$ (Figs. 9 and 10) since the $Y$ *a priori* position had the largest *a priori* error and lay nearly along $B \cdot T$.

Based on the results of runs where $\Delta\mu = 150$ km³/sec² (not plotted), which resulted in target prediction errors of over 3000 km for the entire approach phase, it is mandatory to solve for the gravitational constant when a large uncertainty exists.

Strong $AU$ and $\mu$ solutions are obtained by $E-1$ day with the $AU$ being known to within a few hundred kilometers and $\mu$ to within 10 km³/sec². See Figs. 11 and 12.

As expected, the largest uncertainty in the $B$ plane (*SMAA*) fell along $\mathbf{B} \cdot \mathbf{R}$ prior to $E - 1$ day and then gradually shifted to be normal to the **B** (Fig. 13). Most of the shift occurred between $E-10$ hrs and $E-5$ hrs. The alignment of the *SMAA* normal to **B** can be shown to follow from the fact that for two-body motion with Earth and Mars fixed, there is an unobservable coordinate of the two-body orbit. This coordinate is the right ascension of the ascending node, where the reference plane for the orbit is the "plane of the sky" (a plane normal to the Earth-Mars line). A change of the ascending

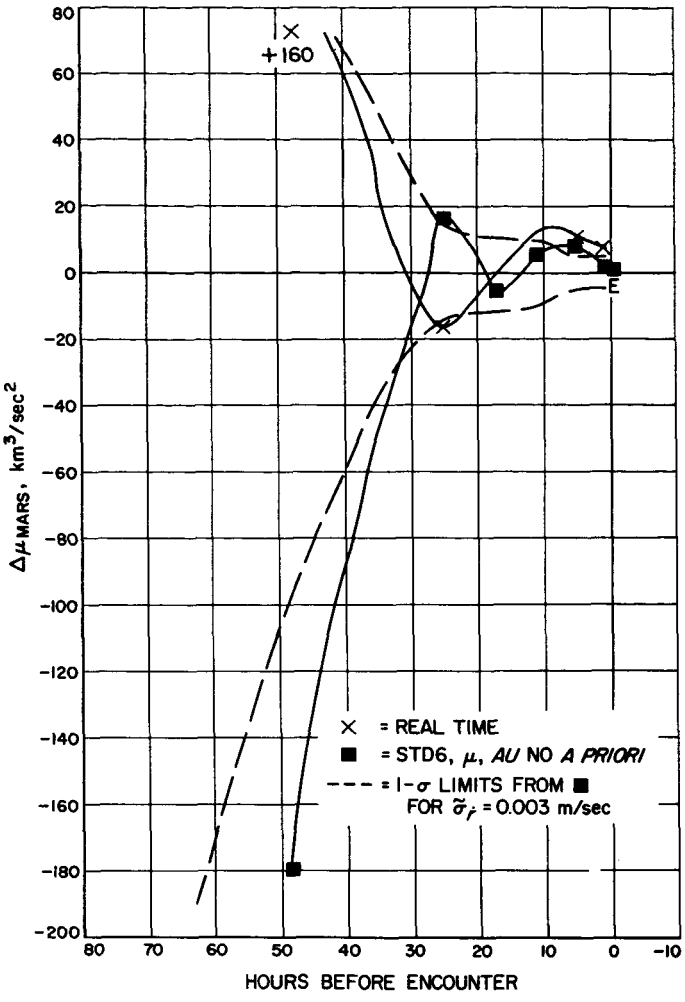


**Fig. 11. $GM_{Mars}$ errors vs hours from *Mariner IV* encounter**

node does not change the range or range rate as seen from the Earth, and thus the corresponding coordinate is unobservable with DSN tracking data. For *Mariner IV* the incoming and outgoing asymptotes lay very nearly along the Earth-Mars line, and thus the "unobservable" coordinate was essentially normal to the **B** and in the $B$ plane. This may be seen in Figs. 8–10 and 14–18 where $B$ and the time of closest approach are determined much faster than $\mathbf{B} \cdot \mathbf{T}$ and $\mathbf{B} \cdot \mathbf{R}$ which are components of **B**. The movement of the Earth-probe line in inertial space and the gravitational attraction of the Sun combine to make the "unobservable" coordinate slightly observable. The original work at JPL on this relationship was done by Carl Pfeiffer (Ref. 13).

Comparing the cases where $\mu$ and $AU$ are estimated (the ■ cases) with those where only position and velocity are estimated, there is a large difference in the *SMAA*

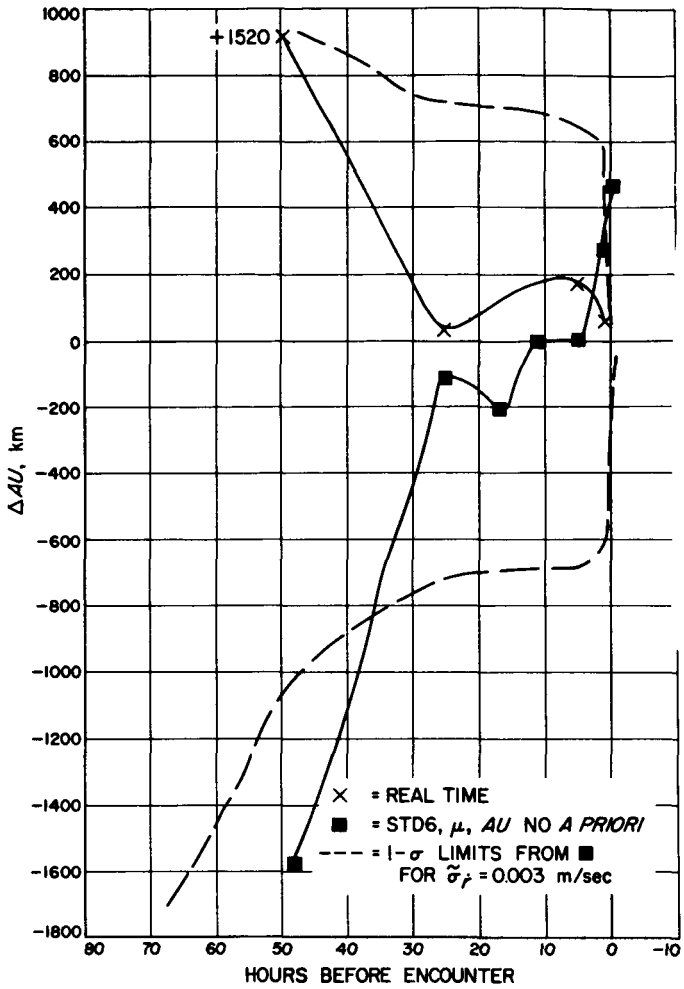


**Fig. 12. *AU* error vs hours from *Mariner IV* encounter**

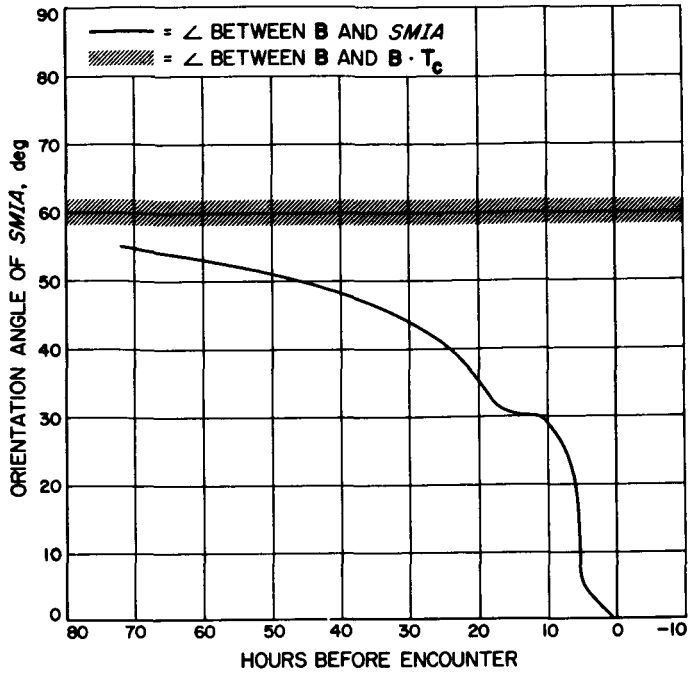


**Fig. 13. Orientation angle of semiminor axis (*SMIA*) vs hours from *Mariner IV* encounter (STD 6 solution with no *a priori*)**

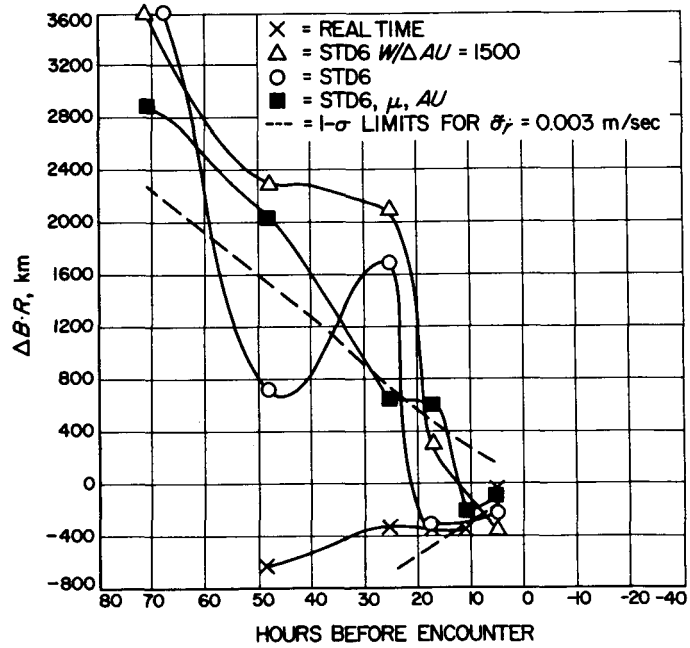


**Fig. 14. $B \cdot R_c$ error vs hours from *Mariner IV* encounter *E* − 72 H to *E* − 5 H**

versus time for the time span $E-30$ hr to $E-15$ hrs and again at $E-0.5$ hr to $E$ (Figs. 19 and 20).

These results indicate the accuracy of the orbit may be improved by several hundred kilometers (from 1000 to 600 km) at $E-20$ hrs if accurate and reliable values for the gravitational constant and *AU* are available before the flight. Also, there is a constant difference of 25 to 50 km between the two *SMIA*'s from $E-50$ hrs to $E-1$ hr, which amounts to a large percentage error at $E-1$ hr (1 km vs 25 km). The $E-5$ H to $E$ *SMIA* is essentially uncertainty in $B$ so that these results may be compared with the $B$ errors in Fig. 16. This figure indicates that *AU* and $\mu$ errors are important to the determination of $B$ in the $E-5$ to $E$ period.

The errors in the components of $B$ (Figs. 9, 10, 14 and 15) show that the results are insensitive to *AU* errors and to $\mu$ errors, provided $\mu$ is included in the solution, thus confirming the insensitivity of the *SMAA* to these factors.

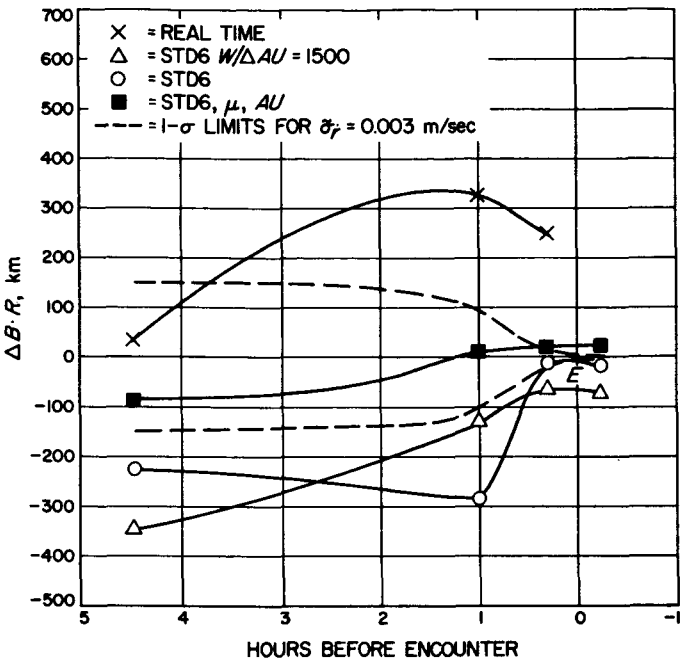


**Fig. 15. $B \cdot R_c$ error vs hours from *Mariner IV* encounter $E - 5$ H to $E + 0.25$ H**

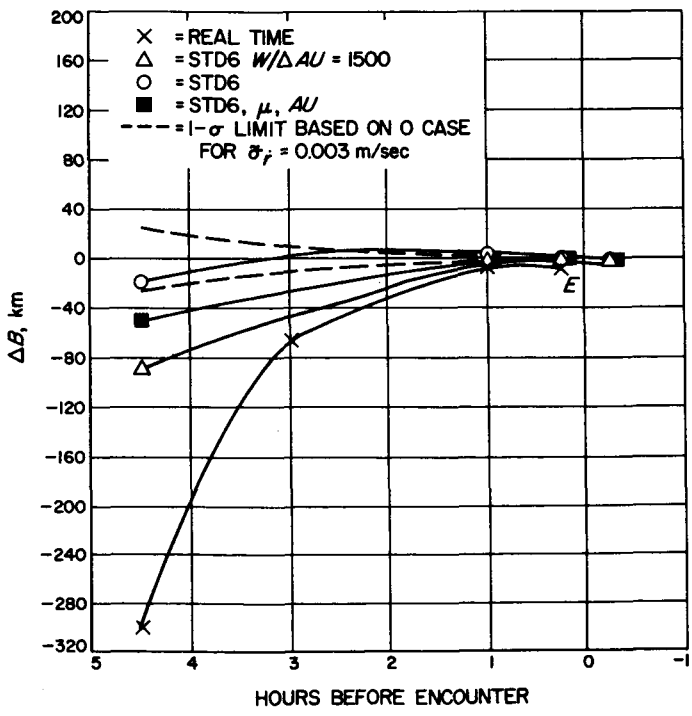


**Fig. 16. B vector magnitude error vs hours from encounter $E - 5$ H to $E + 0.25$ H**

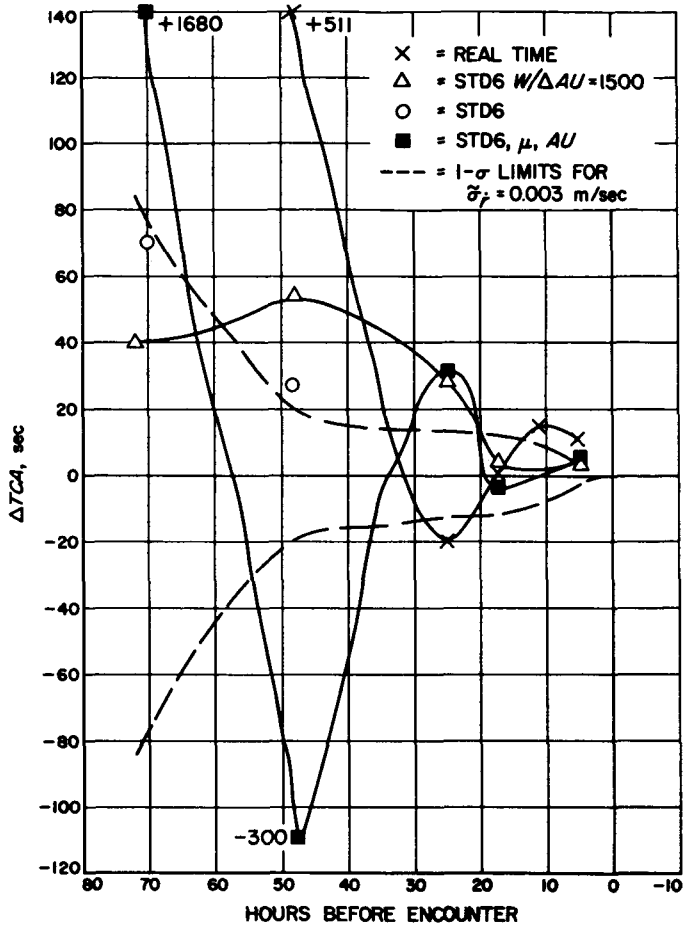


**Fig. 17. Time of closest approach error vs hours from *Mariner IV* encounter $E - 72$ H to $E - 5$ H**

## 5. Implication of the Results for Future Planetary Encounter Phases Before 1970

Data weights used for studies and real-time work should be no greater than 0.005 m/sec and could be considerably smaller depending on what software is available and how serious the limiting error sources are. All stations will be high resolution S-band for the future missions.

If it appears possible to achieve the necessary accuracy using encounter data with loose *a priori*, then information from preencounter should be used with extreme discretion to avoid the type of errors which occurred on *Mariner IV*. The single precision orbit program appears to give stable solutions for the approach phase.

If there is any serious doubt of the accuracy of the planetary gravitational constant, then this constant should definitely be included in the solution with fairly loose *a priori* statistics.

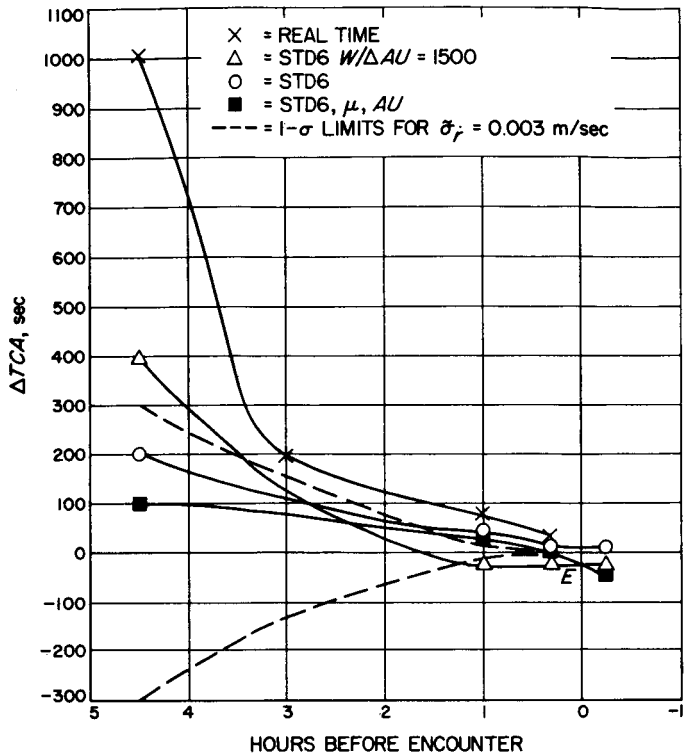


**Fig. 18. Time of closest approach error vs hours from *Mariner IV* encounter *E* − 5 H to *E* + 0.25 H**

The question of whether to estimate *AU* and perhaps the Earth-Mars ephemeris appears to be an open one since roughly equivalent answers are obtained in these cases or in the case where there is no *AU* error. This conclusion might change if better software were available, such as the double precision orbit program scheduled for completion in April 1967.

This study does not replace a thorough investigation of the encounter trajectories for each mission, especially with regard to the "unobservable coordinate" (normal to **B**). The variation of accuracy in this coordinate with trajectory geometry is not well understood at this time and deserves careful study. However, barring any unusual surprises, it may be expected that achieved accuracy on future missions, both to Mars and Venus, will be better than that shown here. Improved software will be available, ranging data will be taken starting with *Mariner* Venus 67, and for Venus missions the gravitational bending will be proportionally greater than Mars missions.

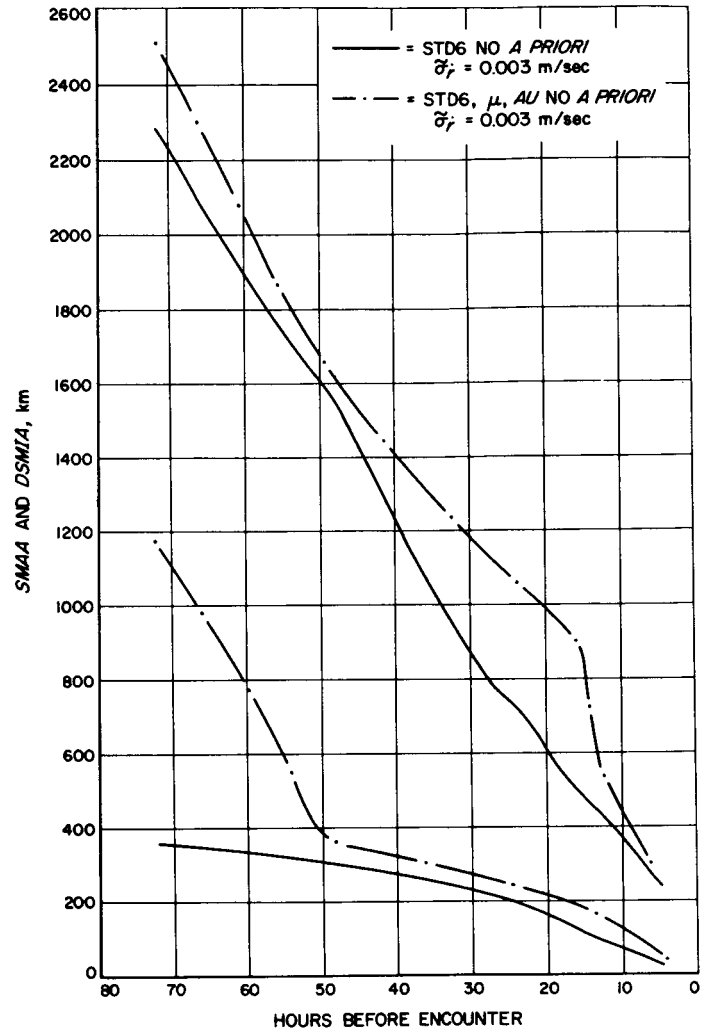


**Fig. 19. *SMAA* and *SMIA* vs hours from *Mariner IV* encounter *E* − 72 H to *E* − 5 H**



## C. Timing Data and the Orbit Determination Process at JPL

*P. M. Muller*

### 1. Introduction

JPL produces bimonthly summaries of time-data necessary to the *real-time* orbit determination program process. Samples of the published information are illustrated herein. Fairly adequate *predictions* of future

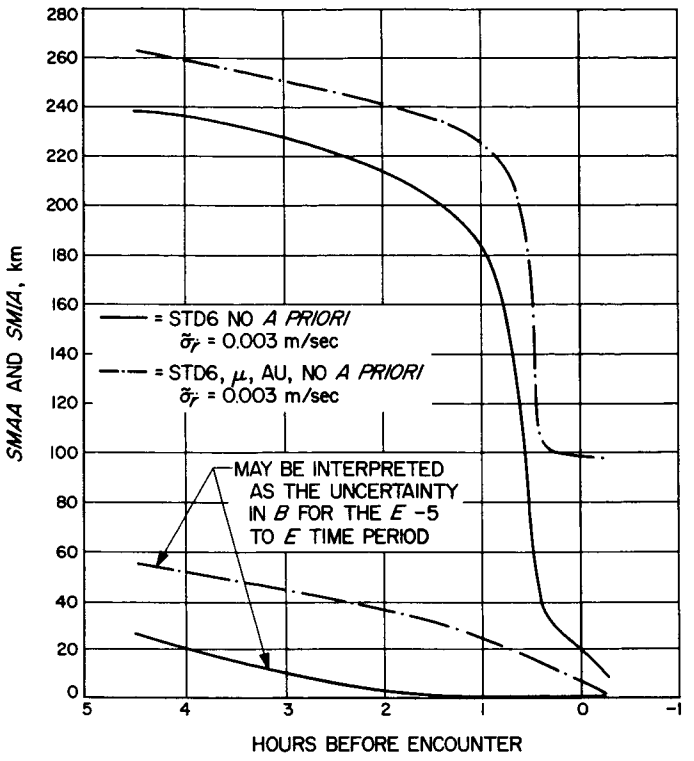


**Fig. 20. *SMAA* and *SMIA* vs hours from *Mariner IV* encounter $E - 5$ H to $E + 0.25$ H**

conditions are generated. Those faced with time problems will find the published summaries convenient and useful. We also recommend the references for background on this increasingly important geophysical and astrodynamical topic.

Ref. 14 documents the role of time in accurate orbit determination based on Earth-based radio guidance. Necessary time corrections require polynomial approximations to real UT1, UTC, and ET. The author has a computer program, TPOLY, which accepts U. S. Naval Observatory time-bulletin data. The program produces a convenient listing of raw data and auxiliary quantities, a set of polynomials which fit the data, and a punched deck which initializes the orbit determination program (ODP) with respect to timehandling.

The purpose of this article is to publicize this program and its regularly published output, which is available to all outside users of the JPL orbit determination program and any other interested people. A second purpose of this article is to outline the current methods of handling these timing problems, and to consider the direction of future effort.

## 2. Program Description

Input to the TPOLY program is obtained from the U.S. Naval Observatory, Washington, D.C. The Observatory takes no responsibility for our use of their data, and this fact must be emphasized. Readers who are not familiar with its service should write the Observatory for information. Ref. 15 documents its production of data bulletins and reprints of important journal articles. The N.B.S. in Boulder, Colorado, also participates in these activities (Ref. 16). The author takes responsibility for the material presented in this article, and for the TPOLY program outputs.

Refs. 14, 17, and 18 give substantial theoretical background for this material. Any of them will assist the reader. The input data includes the date of observation, UT1-UTC, UT2-UTC, and A.1-UTC on that date, and ET-UT1 for 1958.0. The program assumes that the difference $ET$ − atomic time is a constant.

The program computes various auxiliary quantities based upon the input [Fig. 21 (a)]. The title of Fig. 21 gives the dates identifying the run. Predictions are generated for approximately 6 mo ahead, as in Fig. 21 (b). Figs. 21 (c)–(e) illustrate the individual polynomial fits (least-squares quadratic to UT1, linear for UTC). Fig. 21 (f) is a summary of the polynomials produced, and their equations will be found at the top of the listing. Fig. 21 (g) is a daily print of the polynomial time-values and their residuals against the observed data, and against each other at the interval ends. The sum total of this output is duplicated and distributed by the author bimonthly, or on special order at other times. The January output contains listings for 1961 through the current date. Subsequent output listings are sufficient to make the data current. The use of recent polynomials and data is important to the more critical applications. Those interested in copies of these listings, or of Refs. 14 and 18, should write the author. Please ask separately for yearly TPOLY outputs, updates of same, copies of the punched polynomials, and the technical memoranda. Ref. 18 gives a detailed user's guide to the program, its printed outputs, and generally elaborates on the material presented herein.

The predictions of future UT1 are of special interest. Refs. 19 and 20, and their bibliography, are all concerned with finding a model for the irregularities of the Earth's rotation. We are also involved in this problem because our ODP must be able to use real-time data. It must have some overlap of polynomial coverage to

PROGRAM RUN TPOLY-1620 VERSION 7, DATED MARCH 1966

UPDATE OF TPOLY MAY 5, 1966 PREDICTS TO JAN 1, 1967

(a) COMPUTATION OF TPOLY FOR SPODP

INPUT DATA AND AUXILIARY QUANTITIES

| DATE | JD/1950 | J.D.NO. | (S/50)*E-6 | ET-UT1 | ET-UTC | A.1-UT1 | A.1-UT2 | A.1-UTC | UT1-UTC | UT2-UTC | UT2-UT1 | D(A1-UTC) | D(A.1-UT1) |
|---|---|---|---|---|---|---|---|---|---|---|---|---|---|
| 660105 | 5848 | 2439130.5 | 505.26720 | 36.6790 | 36.6110 | 4.4290 | 4.4230 | 4.3610 | -.0680 | -.0620 | .0060 | .0150 | .0150 |
| 660101 | 5844 | 2439126.5 | 504.92160 | OFFSET = | 300 STEP = | 0 | (FIT TO TIME) | | | | | | |
| 660112 | 5855 | 2439137.5 | 505.87200 | 36.6900 | 36.6290 | 4.4400 | 4.4420 | 4.3790 | -.0610 | -.0630 | -.0020 | .0180 | .0110 |
| 660119 | 5862 | 2439144.5 | 506.47680 | 36.7020 | 36.6470 | 4.4520 | 4.4550 | 4.3970 | -.0550 | -.0580 | -.0030 | .0180 | .0120 |
| 660126 | 5869 | 2439151.5 | 507.08160 | 36.7160 | 36.6660 | 4.4660 | 4.4680 | 4.4160 | -.0500 | -.0520 | -.0020 | .0190 | .0140 |
| 660202 | 5876 | 2439158.5 | 507.68640 | 36.7310 | 36.6840 | 4.4810 | 4.4820 | 4.4340 | -.0470 | -.0480 | -.0010 | .0180 | .0150 |
| 660209 | 5883 | 2439165.5 | 508.29120 | 36.7475 | 36.7020 | 4.4975 | 4.4970 | 4.4520 | -.0455 | -.0450 | .0005 | .0180 | .0165 |
| 660216 | 5890 | 2439172.5 | 508.89600 | 36.7650 | 36.7200 | 4.5150 | 4.5160 | 4.4700 | -.0450 | -.0460 | -.0010 | .0180 | .0175 |
| 660223 | 5897 | 2439179.5 | 509.50080 | 36.7830 | 36.7380 | 4.5330 | 4.5330 | 4.4880 | -.0450 | -.0450 | 0.0000 | .0180 | .0180 |
| 660302 | 5904 | 2439186.5 | 510.10560 | 36.8015 | 36.7560 | 4.5515 | 4.5480 | 4.5060 | -.0455 | -.0420 | .0035 | .0180 | .0185 |
| 660301 | 5903 | 2439185.5 | 510.01920 | OFFSET = | 300 STEP = | 0 | (FIT TO TIME) | | | | | | |
| 660309 | 5911 | 2439193.5 | 510.71040 | 36.8200 | 36.7740 | 4.5700 | 4.5640 | 4.5240 | -.0460 | -.0400 | .0060 | .0180 | .0185 |
| 660316 | 5918 | 2439200.5 | 511.31520 | 36.8370 | 36.7930 | 4.5870 | 4.5790 | 4.5430 | -.0440 | -.0360 | .0080 | .0190 | .0170 |
| 660323 | 5925 | 2439207.5 | 511.92000 | 36.8520 | 36.8110 | 4.6020 | 4.5910 | 4.5610 | -.0410 | -.0300 | .0110 | .0180 | .0150 |
| 660330 | 5932 | 2439214.5 | 512.52480 | 36.8690 | 36.8290 | 4.6190 | 4.6050 | 4.5790 | -.0400 | -.0260 | .0140 | .0180 | .0170 |
| 660406 | 5939 | 2439221.5 | 513.12960 | 36.8860 | 36.8470 | 4.6360 | 4.6200 | 4.5970 | -.0390 | -.0230 | .0160 | .0180 | .0170 |
| 660413 | 5946 | 2439228.5 | 513.73440 | 36.9070 | 36.8650 | 4.6570 | 4.6370 | 4.6150 | -.0420 | -.0220 | .0200 | .0180 | .0210 |
| 660420 | 5953 | 2439235.5 | 514.33920 | 36.9270 | 36.8830 | 4.6770 | 4.6540 | 4.6330 | -.0440 | -.0210 | .0230 | .0180 | .0200 |
| 660427 | 5960 | 2439242.5 | 514.94400 | 36.9455 | 36.9010 | 4.6955 | 4.6710 | 4.6510 | -.0445 | -.0200 | .0245 | .0180 | .0185 |
| 660504 | 5967 | 2439249.5 | 515.54880 | 36.9650 | 36.9200 | 4.7150 | 4.6880 | 4.6700 | -.0450 | -.0180 | .0270 | .0190 | .0195 |
| 660501 | 5964 | 2439246.5 | 515.28960 | OFFSET = | 300 STEP = | 0 | (FIT TO TIME) | | | | | | |

**Fig. 21. Program run TPOLY-1620 version 7, dated March 1966 update of TPOLY May 5, 1966 predicts to January 1, 1967**

(b) COMPUTATION OF TPOLY FOR SPODP

PREDICTS LISTING

| DATE | JD/1950 | J.D.NO. | (S/50)*E-6 | ET-UT1 | ET-UTC | A.1-UT1 | A.1-UTC | UT1-UTC | D(ET-UT1) | D(ET-UTC) | D(UT1-UTC) |
|---|---|---|---|---|---|---|---|---|---|---|---|
| 660501 | 5964 | 2439246.5 | 515.28960 | OFFSET = 300 | | STEP = 0 | | PREDICTS INTERVAL TIME | | | |
| | 5967 | 2439249.5 | 515.54880 | 36.9650 | 36.9200 | 4.7150 | 4.6700 | -.0450 | .0195 | .0190 | -.0005 |
| | 5974 | 2439256.5 | 516.15360 | 36.9819 | 36.9381 | 4.7319 | 4.6881 | -.0438 | .0169 | .0181 | .0011 |
| | 5981 | 2439263.5 | 516.75840 | 36.9980 | 36.9562 | 4.7480 | 4.7062 | -.0417 | .0160 | .0181 | .0020 |
| | 5988 | 2439270.5 | 517.36320 | 37.0135 | 36.9744 | 4.7635 | 4.7244 | -.0390 | .0154 | .0181 | .0026 |
| | 5995 | 2439277.5 | 517.96800 | 37.0288 | 36.9925 | 4.7788 | 4.7425 | -.0363 | .0153 | .0181 | .0027 |
| | 6002 | 2439284.5 | 518.57280 | 37.0442 | 37.0107 | 4.7942 | 4.7607 | -.0335 | .0153 | .0181 | .0027 |
| | 6009 | 2439291.5 | 519.17760 | 37.0596 | 37.0288 | 4.8096 | 4.7788 | -.0307 | .0153 | .0181 | .0027 |
| | 6016 | 2439298.5 | 519.78240 | 37.0746 | 37.0470 | 4.8246 | 4.7970 | -.0276 | .0149 | .0181 | .0031 |
| | 6023 | 2439305.5 | 520.38720 | 37.0882 | 37.0651 | 4.8382 | 4.8151 | -.0231 | .0136 | .0181 | .0044 |
| | 6030 | 2439312.5 | 520.99200 | 37.0991 | 37.0832 | 4.8491 | 4.8332 | -.0158 | .0109 | .0181 | .0072 |
| 660701 | 6025 | 2439307.5 | 520.56000 | OFFSET = 300 | | STEP = 0 | | PREDICTS INTERVAL TIME | | | |

D(0,-6) = .4460 D(-6,-12) = .3825 D(-12,-18) = .4206 D(+6,0) = .4055 DELD(+6,0) = .0230

(c) COMPUTATION OF TPOLY FOR SPODP

DATA USED IN POLY FIT

| DATE | JD/1950 | (S/50)*E-6 | ET-UT1 | ET-UTC | OFFSET | STEP |
|---|---|---|---|---|---|---|
| 660101 | 5844 2439126.5 | 504.92160 | | | 300 | 0 |
| | 5841 | 504.66240 | 36.6640 | 36.5960 | | |
| | 5848 | 505.26720 | 36.6790 | 36.6110 | | |
| | 5855 | 505.87200 | 36.6900 | 36.6290 | | |
| | 5862 | 506.47680 | 36.7020 | 36.6470 | | |
| | 5869 | 507.08160 | 36.7160 | 36.6660 | | |
| | 5876 | 507.68640 | 36.7310 | 36.6840 | | |
| | 5883 | 508.29120 | 36.7475 | 36.7020 | | |
| | 5890 | 508.89600 | 36.7650 | 36.7200 | | |
| | 5897 | 509.50080 | 36.7830 | 36.7380 | | |
| | 5904 | 510.10560 | 36.8015 | 36.7560 | | |
| 660301 | 5903 2439185.5 | 510.01920 | | | 300 | 0 |

Fig. 21. Cont'd.

(d) POLYNOMIAL CURVE FIT USING LEAST SQUARES METHOD

FIT OVER DATA FROM (660101,5844) TO (660301,5903) FOR INTERVAL (5841 TO 5904) ET-UT1

| TERM | COEFFICIENT |
|---|---|
| 0 | .596513845830E+03 |
| 1 | -.223155315486E-05 |
| 2 | .222368316125E-14 |

STANDARD DEVIATION= .0026

| SEC/50 | ET-UT1 | FIT | RESIDUAL |
|---|---|---|---|
| 504662400. | 36.6640E-00 | 36.6697E-00 | -.0057 |
| 505267200. | 36.6790E-00 | 36.6782E-00 | .0007 |
| 505872000. | 36.6900E-00 | 36.6885E-00 | .0014 |
| 506476800. | 36.7020E-00 | 36.7003E-00 | .0016 |
| 507081600. | 36.7160E-00 | 36.7138E-00 | .0021 |
| 507686400. | 36.7310E-00 | 36.7289E-00 | .0020 |
| 508291200. | 36.7475E-00 | 36.7456E-00 | .0018 |
| 508896000. | 36.7650E-00 | 36.7640E-00 | .0009 |
| 509500800. | 36.7830E-00 | 36.7840E-00 | -.0010 |
| 510105600. | 36.8015E-00 | 36.8056E-00 | -.0041 |

(e) POLYNOMIAL CURVE FIT USING LEAST SQUARES METHOD

FIT OVER DATA FROM (660101,5844) TO (660301,5903) FOR INTERVAL (5841 TO 5904) ET-UTC

| TERM | COEFFICIENT |
|---|---|
| 0 | .214480341136E+02 |
| 1 | .300099284775E-07 |

STANDARD DEVIATION= .0002

| SEC/50 | ET-UTC | FIT | RESIDUAL |
|---|---|---|---|
| 505267200. | 36.6110E-00 | 36.6110E-00 | 0.0000 |
| 505872000. | 36.6290E-00 | 36.6292E-00 | -.0002 |
| 506476800. | 36.6470E-00 | 36.6473E-00 | -.0003 |
| 507081600. | 36.6660E-00 | 36.6655E-00 | .0004 |
| 507686400. | 36.6840E-00 | 36.6836E-00 | .0003 |
| 508291200. | 36.7020E-00 | 36.7018E-00 | .0001 |
| 508896000. | 36.7200E-00 | 36.7199E-00 | 0.0000 |
| 509500800. | 36.7380E-00 | 36.7381E-00 | -.0001 |
| 510105600. | 36.7560E-00 | 36.7562E-00 | -.0002 |

**Fig. 21. Cont'd.**

permit practical operation. The consensus of these references is that we do not have a satisfactory model at the present time. We have, therefore, been forced to use an empirical method of prediction. It uses year-old UT1 data as *a priori* for the current predictions. Six-month averages in UT1 slope are used to estimate the expected average slope. Ref. 18 gives the details and equations, but the model is simply a linear polynomial added to year-old data.

The success of this method is due to the regular seasonal variations in UT1, and to the fact (Ref. 14, p. 109) that large, rapid (6-mo to 5-yr) changes in UT1 slope are fairly rare (generally decades apart). The author, and others, are actively investigating these problems from our own particular points of view. The plot, Fig. 22, gives some typical residuals between predictions and observations. It also includes some approximate statistical limits on this method. There is no certainty that our published

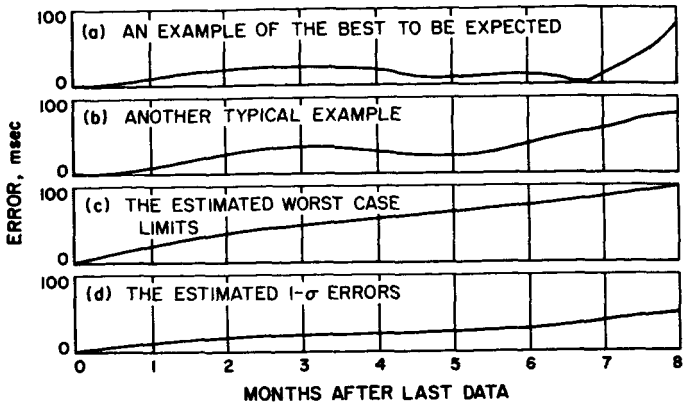


**Fig. 22. Typical prediction accuracies of UT 1**

predictions will fall within these limits. That they have done so over the entire period 1962 to the present gives some slight confidence in their future value. But Ref. 14 particularly points out how dangerous these assumptions can be.

N67 14425

# D. Theoretical Basis for the Double Precision Orbit Determination Program (DPODP): III. Probe Trajectory

*T. D. Moyer*

## 1. Introduction

This third article in the series describes the differential equations of motion of the probe which are integrated numerically in a rectangular coordinate system to give the probe ephemeris with ephemeris time (ET) as the independent variable. The $x$ axis is directed along the mean equinox of 1950.0, the $z$ axis is normal to the mean Earth equator of 1950.0, directed north, and the $y$ axis completes the right-handed system. The center of integration is located at the center of mass of the Sun, the Moon, or one of the nine planets. It may be specified as one of these bodies, or it may be allowed to change as the probe passes through the sphere of influence of a planet (relative to the Sun) or the Moon (relative to the Earth). For this case, the center of integration will be that body within whose sphere of influence the probe lies. At a change in center of integration, the position and velocity of the probe relative to the old center of integration are incremented by the position and velocity, respectively, of the old center relative to the new center. The injection position and velocity components may be referenced to any body (not necessarily the center of integration). The injection epoch is specified in the UTC time scale and must be transformed to ephemeris time.

The acceleration of the probe consists of:

(1) The Newtonian point mass acceleration relative to the center of integration.

(2) The direct oblate acceleration due to a near planet or the near Earth and Moon.

(3) Acceleration due to solar radiation pressure.

(4) Acceleration due to small forces, such as operation of the attitude control system and gas leaks.

(5) Acceleration due to motor burns.

The equations for computing each of these acceleration terms are given in Section 3. A motor burn of short duration or a spring separation may be represented alternatively as a discontinuity to the probe trajectory. The rectangular components of the velocity increment $\Delta\dot{\mathbf{r}}$ and the burn time $t_b$ are solved for parameters. The increment to the probe position is computed as $\Delta\mathbf{r} = \frac{1}{2}\,\Delta\dot{\mathbf{r}}t_b$.

The DPODP has available precomputed position and velocity ephemerides for the celestial bodies within the solar system. They consist of the heliocentric ephemerides of eight planets and the Earth-Moon barycenter, and the geocentric lunar ephemeris. The heliocentric ephemerides (with the exception of Mercury and Neptune) are obtained from a separate numerical integration for each body with epoch values chosen to obtain a least squares fit to source positions. The source positions, which represent astronomical observations, are obtained from an evaluation of certain general perturbation theories for the four inner planets, from a simultaneous integration of the motion of the five outer planets (corrected for motion of the inner planets) by W. J. Eckert, D. Brouwer, and G. M. Clemence, and from an evaluation of the Brown Improved Lunar Theory. The acceleration due to each perturbing body is computed from the source position or position from the fitted ephemeris for the perturbing body if previously computed. The fitted ephemerides are generated one at a time in the following order: preliminary Jupiter, Saturn, final Jupiter, Uranus, Pluto, Mars, Earth-Moon barycenter, and Venus. The ephemerides for Mercury, Neptune, and the Moon are obtained directly from the source positions with velocity obtained by numerical differentiation. A description of the JPL

(f) POLYNOMIAL SUMMARY FOR SPODP

ET-UTC = A+B*T  UT1-ET = C+D*T+E*T*T

| DATE FROM | DATE TO | JD/1950 FROM | JD/1950 TO | A | B | DEV. | C | D | E | DEV. |
|---|---|---|---|---|---|---|---|---|---|---|
| 640101 | 640401 | (5113,5204) | | .28444020E+02 | .14955802E-07 | .0002 | -.55873549E+02 | .11642456E-06 | -.15731393E-15 | .0004 |
| 640401 | 640710 | (5204,5304) | | .28535475E+02 | .14975058E-07 | 0.0000 | .14505182E+03 | -.77314012E-06 | .82727231E-15 | .0027 |
| 640710 | 640901 | (5304,5357) | | .28540733E+02 | .14963630E-07 | 0.0000 | -.21138099E+03 | .77793237E-06 | -.86013450E-15 | .0006 |
| 640901 | 641101 | (5357,5418) | | .28534666E+02 | .15192921E-07 | .0002 | -.23683174E+03 | .88906376E-06 | -.98143552E-15 | .0021 |
| 641101 | 650101 | (5418,5479) | | .28590095E+02 | .15074038E-07 | .0002 | -.91524256E+02 | .26298114E-06 | -.30709080E-15 | .0005 |
| 650101 | 650301 | (5479,5538) | | .28663622E+02 | .15131450E-07 | .0004 | .12955656E+03 | -.67170154E-06 | .68082041E-15 | .0009 |
| 650301 | 650501 | (5538,5599) | | .28796647E+02 | .15061314E-07 | .0002 | -.34246210E+03 | .13037586E-05 | -.13860726E-14 | .0014 |
| 650501 | 650701 | (5599,5660) | | .28884160E+02 | .14880915E-07 | 0.0000 | .20908441E+03 | -.98453356E-06 | .98736037E-15 | .0012 |
| 650701 | 650901 | (5660,5722) | | .28874081E+02 | .15106046E-07 | .0002 | -.33187949E+03 | .12209437E-05 | -.12605304E-14 | .0012 |
| 650901 | 651101 | (5722,5783) | | .29047903E+02 | .14956092E-07 | .0002 | -.35760054E+03 | .13229078E-05 | -.13615332E-14 | .0011 |
| 651101 | 660101 | (5783,5844) | | .29040792E+02 | .14971102E-07 | .0002 | .17628474E+03 | -.81812145E-06 | .78500217E-15 | .0011 |
| 660101 | 660301 | (5844,5903) | | .21448034E+02 | .30009928E-07 | .0002 | -.59651384E+03 | .22315531E-05 | -.22236831E-14 | .0026 |
| 660301 | 660501 | (5903,5964) | | .21444123E+02 | .30017464E-07 | .0003 | -.19667679E+03 | .65338382E-06 | -.66646551E-15 | .0014 |
| 660501 | 660701 | (5964,6025) | | .21420138E+02 | .30064327E-07 | .0002 | .21611250E+03 | -.95198937E-06 | .89439159E-15 | .0010 |
| 660701 | 660901 | (6025,6087) | | .21453549E+02 | .29999975E-07 | 0.0000 | -.29251458E+03 | .99615691E-06 | -.97104930E-15 | .0008 |
| 660901 | 661101 | (6087,6148) | | .21453537E+02 | .29999996E-07 | 0.0000 | -.45973219E+03 | .16305611E-05 | -.15727600E-14 | .0012 |
| 661101 | 670101 | (6148,6209) | | .21453543E+02 | .29999985E-07 | 0.0000 | .10812424E+03 | -.51435261E-06 | .45267764E-15 | .0005 |
| 670101 | 750101 | (6209,9131) | | .21453535E+02 | .30000000E-07 | 0.0000 | -.21434646E+02 | -.30000004E-07 | .32090686E-23 | 0.0000 |

(g) FIT OF POLYNOMIAL OVER PERIOD 660101 TO 660301 INCLUSIVE

PREVIOUS OFFSET = 150 THIS OFFSET = 300 NEXT OFFSET = 300 (PARTS IN 1.F+10)

| TYPE | DATE | JD/50 | J.D.NO. | (S/50)*E-6 | ET-UT1 | ET-UTC | A.1-UT1 | A.1-UTC | UT1-UTC | R(ET-UT1) | R(ET-UTC) |
|---|---|---|---|---|---|---|---|---|---|---|---|
| POLY1 | 660101 | 5844 | 2439126.5 | 504.92160 | 36.6731 | 36.6006 | 4.4231 | 4.3506 | -.0724 | | |
| POLY1 | | 5845 | 2439127.5 | 505.00800 | 36.6744 | 36.6032 | 4.4244 | 4.3532 | -.0711 | | |
| POLY1 | | 5846 | 2439128.5 | 505.09440 | 36.6756 | 36.6058 | 4.4256 | 4.3558 | -.0697 | | |
| POLY1 | | 5847 | 2439129.5 | 505.18080 | 36.6769 | 36.6084 | 4.4269 | 4.3584 | -.0684 | | |
| POLY1 | | 5848 | 2439130.5 | 505.26720 | 36.6782 | 36.6110 | 4.4282 | 4.3610 | -.0672 | | |
| DATA | | 5848 | 2439130.5 | 505.26720 | 36.6790 | 36.6110 | 4.4290 | 4.3610 | -.0680 | .0007 | 0.0000 |
| POLY1 | | 5849 | 2439131.5 | 505.35360 | 36.6796 | 36.6136 | 4.4296 | 4.3636 | -.0659 | | |
| POLY1 | | 5850 | 2439132.5 | 505.44000 | 36.6810 | 36.6162 | 4.4310 | 4.3662 | -.0648 | | |
| POLY1 | | 5851 | 2439133.5 | 505.52640 | 36.6824 | 36.6188 | 4.4324 | 4.3688 | -.0636 | | |
| POLY1 | | 5852 | 2439134.5 | 505.61280 | 36.6839 | 36.6214 | 4.4339 | 4.3714 | -.0625 | | |
| POLY1 | | 5853 | 2439135.5 | 505.69920 | 36.6854 | 36.6240 | 4.4354 | 4.3740 | -.0614 | | |
| POLY1 | | 5854 | 2439136.5 | 505.78560 | 36.6869 | 36.6266 | 4.4369 | 4.3766 | -.0603 | | |
| POLY1 | | 5855 | 2439137.5 | 505.87200 | 36.6885 | 36.6292 | 4.4385 | 4.3792 | -.0593 | | |
| DATA | | 5855 | 2439137.5 | 505.87200 | 36.6900 | 36.6290 | 4.4400 | 4.3790 | -.0610 | .0014 | -.0002 |
| POLY1 | | 5898 | 2439180.5 | 509.58720 | 36.7869 | 36.7407 | 4.5369 | 4.4907 | -.0462 | | |
| POLY1 | | 5899 | 2439181.5 | 509.67360 | 36.7900 | 36.7433 | 4.5400 | 4.4933 | -.0467 | | |
| POLY1 | | 5900 | 2439182.5 | 509.76000 | 36.7930 | 36.7458 | 4.5430 | 4.4958 | -.0471 | | |
| POLY1 | | 5901 | 2439183.5 | 509.84640 | 36.7961 | 36.7484 | 4.5461 | 4.4984 | -.0476 | | |
| POLY1 | | 5902 | 2439184.5 | 509.93280 | 36.7992 | 36.7510 | 4.5492 | 4.5010 | -.0481 | | |
| POLY1 | | 5903 | 2439185.5 | 510.01920 | 36.8024 | 36.7536 | 4.5524 | 4.5036 | -.0487 | | |
| POLY2 | 660301 | 5903 | 2439185.5 | 510.01920 | 36.7992 | 36.7536 | 4.5492 | 4.5036 | -.0456 | -.0032 | 0.0000 |

Fig. 21. Cont'd.

ephemeris tapes and the method by which they were generated is given in Refs. 21 and 22.

For three of these precomputed ephemerides, the orbital elements of an osculating conic at some epoch are solve for parameters. The ephemeris correction consists of the difference between the solve for conic and the osculating conic. Section 2 gives the formulas for correcting the basic ephemerides and for computing the corrected position and velocity of the Sun, Moon, or a planet relative to any other of these bodies. These quantities are required (1) to compute the above mentioned acceleration terms, (2) at phase changes, and (3) at the injection epoch, if the injection position and velocity are referred to a body other than the center of integration.

The probe ephemeris is represented by the three numerically integrated sum and difference (SAD) arrays. These arrays may be interpolated at any value of ET to give $\mathbf{r}$, $\dot{\mathbf{r}}$, $\ddot{\mathbf{r}}$, and $\dddot{\mathbf{r}}$ of the probe relative to the center of integration.

## 2. Planetary and Lunar Ephemerides

The corrected heliocentric position of a planet or Earth-Moon barycenter is given by

$$\mathbf{r}\,{}^{(S)}_{p}\,(\text{km}) = \mathbf{r}\,{}^{(S)}_{p}\,(\text{a.u.})A_E + \frac{\partial \mathbf{r}\,{}^{(S)}_{p}}{\partial \mathbf{E}_p}\,\Delta\mathbf{E}_p \qquad (1)$$

Similarly the corrected geocentric position of the Moon is given by

$$\mathbf{r}\,{}^{(E)}_{M}\,(\text{km}) = \mathbf{r}\,{}^{(E)}_{M}\,(\text{l.u.})R_E + \frac{\partial \mathbf{r}\,{}^{(E)}_{M}}{\partial \mathbf{E}_M}\,\Delta\mathbf{E}_M \qquad (2)$$

Each of these vectors has rectangular components referred to the mean Earth equator and equinox of 1950.0. The $x$ axis is along the mean equinox of 1950.0, the $z$ axis is normal to the mean Earth equator of 1950.0 directed north, and the $y$ axis completes the right-handed system. In Eqs. (1) and (2) above,

$\mathbf{r}\,{}^{(S)}_{p}$ (km) = corrected position vector of planet or Earth-Moon barycenter relative to Sun in units of kilometers

$\mathbf{r}\,{}^{(S)}_{p}$ (a.u.) = position vector of planet or Earth-Moon barycenter relative to Sun in astronomical units (a.u.), obtained directly from the ephemeris

$\mathbf{r}\,{}^{(E)}_{M}$ (km) = corrected position vector of Moon relative to Earth in units of kilometers

$\mathbf{r}\,{}^{(E)}_{M}$ (l.u.) = position vector of Moon relative to Earth in dimensionless units (l.u.), obtained directly from the lunar ephemeris

$A_E$ = conversion factor from astronomical units (a.u.) to kilometers

$R_E$ = conversion factor from dimensionless lunar units (l.u.), to kilometers

$\mathbf{E}$ = osculating two-body orbital elements for heliocentric ephemeris of planet or Earth-Moon barycenter, or geocentric lunar ephemeris

$\partial\mathbf{r}/\partial\mathbf{E}$ = partial derivatives of position on osculating conic with respect to orbital elements (Ref. 23, p. 241)

$\Delta\mathbf{E}$ = solve for corrections to osculating orbital elements

The position of the Moon relative to the Earth-Moon barycenter $B$ and of $B$ relative to the Earth is given by

$$\mathbf{r}\,{}^{(B)}_{M} = \frac{\mu}{1+\mu}\,\mathbf{r}\,{}^{(E)}_{M} \qquad (3)$$

$$\mathbf{r}\,{}^{(E)}_{B} = \frac{1}{1+\mu}\,\mathbf{r}\,{}^{(E)}_{M} \qquad (4)$$

where

$$\mu = \frac{\mu_E}{\mu_M} \qquad (5)$$

where

$\mu_E$ = gravitational constant of Earth, km$^3$/sec$^2$

$\mu_M$ = gravitational constant of Moon, km$^3$/sec$^2$

The following table lists sums of the position vectors Eqs. (1) to (4) to give the position vectors of the Earth (E), Moon (M), Sun (S), or planet (p) (other than the Earth) relative to the center of integration, with each of these bodies, respectively, as center.

Earth = Center

$$\mathbf{r}\,{}^{(E)}_{M} = \mathbf{r}\,{}^{(E)}_{M}$$

$$\mathbf{r}\,{}^{(E)}_{S} = \mathbf{r}\,{}^{(E)}_{B} - \mathbf{r}\,{}^{(S)}_{B}$$

$$\mathbf{r}\,{}^{(E)}_{p} = \mathbf{r}\,{}^{(E)}_{B} - \mathbf{r}\,{}^{(S)}_{B} + \mathbf{r}\,{}^{(S)}_{p}$$

Moon = Center

$$\mathbf{r}_{E}^{(M)} = -\mathbf{r}_{M}^{(E)}$$

$$\mathbf{r}_{S}^{(M)} = -\mathbf{r}_{M}^{(B)} - \mathbf{r}_{B}^{(S)}$$

$$\mathbf{r}_{p}^{(M)} = -\mathbf{r}_{M}^{(B)} - \mathbf{r}_{B}^{(S)} + \mathbf{r}_{p}^{(S)}$$

Sun = Center

$$\mathbf{r}_{E}^{(S)} = \mathbf{r}_{B}^{(S)} - \mathbf{r}_{B}^{(E)}$$

$$\mathbf{r}_{M}^{(S)} = \mathbf{r}_{B}^{(S)} + \mathbf{r}_{M}^{(B)}$$

$$\mathbf{r}_{p}^{(S)} = \mathbf{r}_{p}^{(S)}$$

Planet = Center

$$\mathbf{r}_{E}^{(p)} = -\mathbf{r}_{p}^{(S)} + \mathbf{r}_{B}^{(S)} - \mathbf{r}_{B}^{(E)}$$

$$\mathbf{r}_{M}^{(p)} = -\mathbf{r}_{p}^{(S)} + \mathbf{r}_{B}^{(S)} + \mathbf{r}_{M}^{(B)}$$

$$\mathbf{r}_{S}^{(p)} = -\mathbf{r}_{p}^{(S)}$$

$$\mathbf{r}_{p_j}^{(p)} = -\mathbf{r}_{p}^{(S)} + \mathbf{r}_{p_j}^{(S)}$$

All of the formulas in this section also apply when $\mathbf{r}$ is replaced by $\dot{\mathbf{r}}$, where the dot denotes differentiation with respect to ephemeris time.

The solve for parameters which affect the relative position and velocity between two celestial bodies are the: scaling factor $A_E$ for the heliocentric ephemerides; the scaling factor $R_E$ for the lunar ephemeris; corrections to osculating orbital elements $\Delta\varepsilon$ for any three of the ephemerides; and the gravitational constants of the Earth and Moon, $\mu_E$ and $\mu_M$. These are known as reference parameters.

In order to compute doppler observables, the relative acceleration $\ddot{\mathbf{r}}$ and jerk $\dddot{\mathbf{r}}$ between two celestial bodies are required. Given corrected $\mathbf{r}$, $\dot{\mathbf{r}}$ of a planet or Earth-Moon barycenter relative to the Sun or Moon relative to the Earth, $\ddot{\mathbf{r}}$ and $\dddot{\mathbf{r}}$ are computed from two-body formulas:

$$\ddot{\mathbf{r}} = -\mu\frac{\mathbf{r}}{r^3} \tag{6}$$

where

$\mu = \mu_S + \mu_p$ for the heliocentric ephemeris of a planet

$= \mu_S + \mu_E + \mu_M$ for the heliocentric ephemeris of the Earth-Moon barycenter

$= \mu_E + \mu_M$ for the geocentric lunar ephemeris

$$\dddot{\mathbf{r}} = \frac{3\mu\mathbf{r}}{r^4}\dot{r} - \frac{\mu\dot{\mathbf{r}}}{r^3} \tag{7}$$

where

$$\dot{r} = \frac{\mathbf{r}\cdot\dot{\mathbf{r}}}{r} \tag{8}$$

The values of $\ddot{\mathbf{r}}_{M}^{(B)}$ and $\ddot{\mathbf{r}}_{B}^{(E)}$ are computed from Eqs. (3) and (4) using $\ddot{\mathbf{r}}_{M}^{(E)}$. Given $\ddot{\mathbf{r}}_{p}^{(S)}$, $\ddot{\mathbf{r}}_{B}^{(S)}$, $\ddot{\mathbf{r}}_{M}^{(E)}$, $\ddot{\mathbf{r}}_{M}^{(B)}$, $\ddot{\mathbf{r}}_{B}^{(E)}$, the relative $\ddot{\mathbf{r}}$, $\dddot{\mathbf{r}}$ between two celestial bodies is computed from the table of vector sums where $\mathbf{r}$ is replaced by $\ddot{\mathbf{r}}$, $\dddot{\mathbf{r}}$.

## 3. Probe Acceleration

The equations for computing each term of the total probe acceleration relative to the center of integration are given in the following subsections.

*a. Newtonian point mass acceleration.*

$$\ddot{\mathbf{r}} = \sum_i \mu_i \left[\mathbf{h}(\mathbf{r} - \mathbf{r}_i) + \mathbf{h}(\mathbf{r}_i)\right] \tag{9}$$

where $i$ is summed over each planet, the Sun, and the Moon, including that body which is the center of integration, and

$\mu_i$ = gravitational constant of body $i$, km$^3$/sec$^2$

$\mathbf{r}$ = position of probe relative to center of integration in 1950.0 Earth equatorial rectangular coordinates

$\mathbf{r}_i$ = position of body $i$ relative to center of integration in 1950.0 rectangular coordinates

$\mathbf{h}(\mathbf{r})$ = vector function of $\mathbf{r} = -\mathbf{r}/r^3$

*b. Oblate body acceleration.* The acceleration of the probe due to the oblateness of a planet or the Moon is the direct acceleration of the probe due to the oblateness. The indirect acceleration of the center of integration due to the oblateness of a perturbing body is ignored in general. However, for the case where the Earth is the center of integration and the Moon is a perturbing body or vice-versa, an expression has been derived by F. Sturms

(*SPS 37-29*, Vol. IV, pp. 1–6) for the indirect acceleration, which accounts approximately for the oblateness of each body.

The direct acceleration of the probe due to oblateness of a body is derived from the generalized potential function (Ref. 24, pp. 173–174) for that body:

$$U = \frac{\mu}{r}\left[1 + \sum_{n=1}^{\infty}\sum_{m=0}^{n}\left(\frac{a_p}{r}\right)^n P_n^m(\sin\phi) \times \{C_{n,m}\cos m\lambda + S_{n,m}\sin m\lambda\}\right] \quad (10)$$

where

$\mu$ = gravitational constant of body, km$^3$/sec$^2$

$r, \phi, \lambda$ = radius, latitude, and longitude (positive east of prime meridian) of probe relative to body

$a_p$ = mean equatorial radius of body (an adopted constant used for $U$)

$P_n^m(\sin\phi)$ = associated Legendre function of the first kind. The argument $\sin\phi$ will be omitted here

$C_{n,m}$ and $S_{n,m}$ = numerical coefficients (tesseral harmonic coefficients)

The associated Legendre function $P_n^m$ is defined by

$$P_n^m = \cos^m\phi\,\frac{d^m}{d(\sin\phi)^m}P_n \quad (11)$$

where

$P_n$ = Legendre polynomial of degree $n$ in $\sin\phi$.

The zonal harmonic coefficient $J_n$ is defined as

$$J_n = -C_{n,o} \quad (12)$$

Eq. (10) may be written in three terms corresponding to the potential of a point mass, zonal harmonics, and tesseral harmonics

$$U = \frac{\mu}{r} - \frac{\mu}{r}\sum_{n=1}^{\infty}J_n\left(\frac{a_p}{r}\right)^n P_n + \frac{\mu}{r}\sum_{n=1}^{\infty}\sum_{m=1}^{n}\left(\frac{a_p}{r}\right)^n \times P_n^m\{C_{n,m}\cos m\lambda + S_{n,m}\sin m\lambda\} \quad (13)$$

with each term defined as

$$U = \frac{\mu}{r} + U(J) + U(C, S) \quad (14)$$

The inertial acceleration of the probe is computed in a rectangular coordinate system ($x'y'z'$) with the $x'$ axis directed outward along the instantaneous radius to the probe, the $y'$ axis directed east, and the $z'$ axis directed north. Fig. 23 shows these axes relative to body-fixed axes $x_by_bz_b$, where $x_b$ is along the intersection of the prime meridian and equator of the body, $z_b$ is directed north along the axis of rotation of the body, and $y_b$ completes the right-handed system. The transformation from body-fixed coordinates $\mathbf{r}_b = (x_b, y_b, z_b)$ to $\mathbf{r}' = (x', y', z')$ coordinates is given by

$$\mathbf{r}' = R\,\mathbf{r}_b \quad (15)$$

where

$$R = \begin{bmatrix} \cos\phi\cos\lambda & \cos\phi\sin\lambda & \sin\phi \\ -\sin\lambda & \cos\lambda & 0 \\ -\sin\phi\cos\lambda & -\sin\phi\sin\lambda & \cos\phi \end{bmatrix} \quad (16)$$

The position of the probe relative to the body in rectangular coordinates referred to the mean Earth equator and equinox of 1950.0 is given by $\mathbf{r} - \mathbf{r}_i$ where $\mathbf{r}$ and $\mathbf{r}_i$ are defined in Section a. Transformation from these inertial coordinates to body-fixed coordinates $\mathbf{r}_b$ is defined as

$$\mathbf{r}_b = T^T(\mathbf{r} - \mathbf{r}_i) \quad (17)$$

The overall transformation from $(\mathbf{r} - \mathbf{r}_i)$ to $\mathbf{r}'$ is thus

$$\mathbf{r}' = G(\mathbf{r} - \mathbf{r}_i) = RT^T(\mathbf{r} - \mathbf{r}_i) \quad (18)$$

The inverse transformation is

$$(\mathbf{r} - \mathbf{r}_i) = G^T\mathbf{r}' = TR^T\mathbf{r}' \quad (19)$$

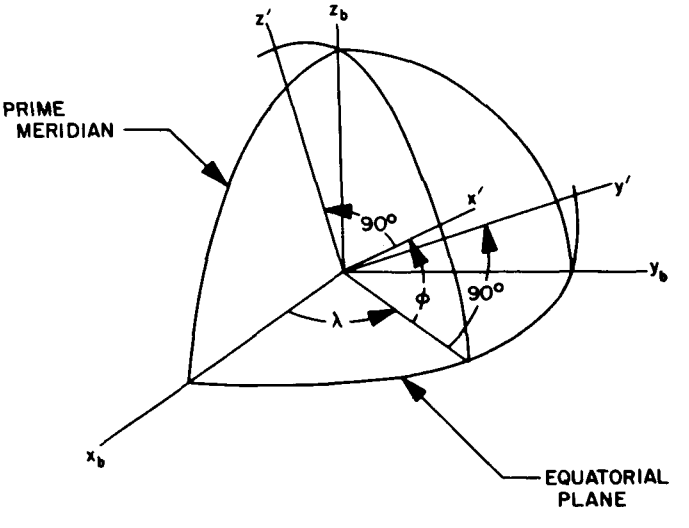


**Fig. 23. x', y' and z' axes relative to fixed body axes $x_by_bz_b$**

The transformation $T$ is specified in the DPODP for the Earth, the Moon, and Mars. Using body-fixed coordinates from Eq. (17), trigonometric functions of $\phi$ and $\lambda$ are given by

$$\sin\phi = \frac{z_b}{r} \tag{20}$$

$$\cos\phi = \frac{\sqrt{x_b^2 + y_b^2}}{r} \tag{21}$$

$$\sin\lambda = \frac{y_b}{\sqrt{x_b^2 + y_b^2}} \tag{22}$$

$$\cos\lambda = \frac{x_b}{\sqrt{x_b^2 + y_b^2}}$$

An expression will be developed for the inertial acceleration of the probe due to oblateness for any body with rectangular components along the instantaneous directions of $x'$ $y'$, and $z'$ axes, denoted $\ddot{\mathbf{r}}'$. This acceleration can be broken down into $\ddot{\mathbf{r}}'$ $(J)$ due to the zonal harmonics and $\ddot{\mathbf{r}}'$ $(C, S)$ due to the tesseral harmonics. With these terms, the contribution to the probe acceleration $\ddot{\mathbf{r}}$ relative to the center of integration in Earth equatorial rectangular coordinates due to the oblateness of any body is

$$\ddot{\mathbf{r}} = G^T\ddot{\mathbf{r}}' = G^T\{\ddot{\mathbf{r}}'(J) + \ddot{\mathbf{r}}'(C, S)\} \tag{23}$$

The components of $\ddot{\mathbf{r}}'$ are computed from

$$\ddot{x}' = \frac{\partial U}{\partial r} \tag{24}$$

$$\ddot{y}' = \frac{1}{r\cos\phi}\frac{\partial U}{\partial\lambda} \tag{25}$$

$$\ddot{z}' = \frac{1}{r}\frac{\partial U}{\partial\phi} \tag{26}$$

where the point mass term of $U$ has been accounted for in section *a.*, and is ignored here. Carrying out these derivatives gives

$$\ddot{\mathbf{r}}'(J) = \frac{\mu}{r^2}\sum_{n=1}^{n_1} J_n\left(\frac{a_p}{r}\right)^n \begin{bmatrix} (n+1)P_n \\ 0 \\ -\cos\phi\, P'_n \end{bmatrix} \tag{27}$$

$$\ddot{\mathbf{r}}'(C, S) = \frac{\mu}{r^2}\sum_{n=1}^{n_2}\sum_{m=1}^{n}\left(\frac{a_p}{r}\right)^n \times \begin{bmatrix} -(n+1)P_n^m\{C_{n,m}\cos m\lambda + S_{n,m}\sin m\lambda\} \\ m\sec\phi\, P_n^m\{-C_{n,m}\sin m\lambda + S_{n,m}\cos m\lambda\} \\ \cos\phi\, P_n^{m'}\{C_{n,m}\cos m\lambda + S_{n,m}\sin m\lambda\} \end{bmatrix} \tag{28}$$

where $n_1$ has a maximum value of 15, and $n_2$ has a maximum value of 8.

The Legendre polynomial $P_n$ is computed recursively from

$$P_n = \frac{2n-1}{n}\sin\phi\, P_{n-1} - \left(\frac{n-1}{n}\right)P_{n-2} \tag{29}$$

starting with

$$P_o = 1 \tag{30}$$

$$P_1 = \sin\phi$$

The first derivative of $P_n$ with respect to (wrt) $\sin\phi$, denoted $P'_n$, is given by

$$P'_n = \sin\phi\, P'_{n-1} + n\, P_{n-1} \tag{31}$$

starting with

$$P'_1 = 1 \tag{32}$$

The function $\sec\phi\, P_n^m$ is computed by first generating

$$\sec\phi\, P_m^m = (2m-1)\cos\phi\,[\sec\phi\, P_{m-1}^{m-1}] \tag{33}$$

starting with

$$\sec\phi\, P_1^1 = 1 \tag{34}$$

and then generating

$$\sec\phi\, P_n^m = \left(\frac{2n-1}{n-m}\right)\sin\phi\,[\sec\phi\, P_{n-1}^m] - \left(\frac{n+m-1}{n-m}\right)[\sec\phi\, P_{n-2}^m] \tag{35}$$

For each value of $m$ between 1 and $n_2$, $n$ is varied from $m+1$ to $n_2$. The general term $P_a^b$ is zero if $b > a$.

The function $\cos\phi\, P_n^{m'}$, where $P_n^{m'}$ is the derivative of $P_n^m$ wrt $\sin\phi$, is computed from

$$\cos\phi\, P_n^{m'} = -n\sin\phi\,[\sec\phi\, P_n^m] + (n+m)\,[\sec\phi\, P_{n-1}^m] \tag{36}$$

***c. Acceleration due to solar radiation pressure and attitude control.*** The acceleration of the probe due to solar radiation pressure and small forces such as gas

leaks from the attitude control system, noncoupled attitude control jets, etc., is represented by

$$\begin{aligned}\ddot{\mathbf{r}} = &\{[a_r + b_r(t - T_{AC1}) + c_r(t - T_{AC1})^2]\,[u(t - T_{AC1}) - u(t - T_{AC2})] \\ &+ \Delta a_r + \frac{C_1 A_p}{m r_{SP}^2}\,[G_r + G_r'\,(EPS) + \Delta G_r]\,u^*(t - T_{SRP})\}\,\mathbf{U}_{SP} \\ &+ \{[a_x + b_x(t - T_{AC1}) + c_x(t - T_{AC1})^2]\,[u(t - T_{AC1}) - u(t - T_{AC2})] \\ &+ \Delta a_x + \frac{C_1 A_p}{m r_{SP}^2}\,[G_x + G_x'\,(EPS) + \Delta G_x]\,u^*(t - T_{SRP})\}\,\mathbf{X}^* \\ &+ \{[a_y + b_y(t - T_{AC1}) + c_y(t - T_{AC1})^2]\,[u(t - T_{AC1}) - u(t - T_{AC2})] \\ &+ \Delta a_y + \frac{C_1 A_p}{m r_{SP}^2}\,[G_y + G_y'\,(EPS) + \Delta G_y]\,u^*(t - T_{SRP})\}\,\mathbf{Y}^*\end{aligned} \tag{37}$$

The terms in this equation are defined as

$\mathbf{U}_{SP}$ = unit vector from Sun to probe

$\mathbf{X}^*,\mathbf{Y}^*$ = unit vectors along spacecraft $x$ and $y$ axes ($\mathbf{X}^* \times \mathbf{Y}^* = \mathbf{U}_{SP}$)

$a_i,b_i,c_i$ where $i = r$, $x$, or $y$ = solve for coefficients for acceleration polynomials, km/sec$^2$, km/sec$^3$, km/sec$^4$

$t$ = ephemeris time

$T_{AC1},T_{AC2}$ = epochs at which the attitude control (AC) acceleration polynomials are turned on and off, respectively. The epochs may be specified in the UTC, S.T., or A.1 time scales

$u(t-T_{AC1})$ = 1 for $t \geq T_{AC1}$, 0 for $t < T_{AC1}$
$T_{AC1} \rightarrow T_{AC2}$

$\Delta a_r,\Delta a_x,\Delta a_y$ = input acceleration (not solve for), km/sec$^2$. The value for each $\Delta a_i$ will be obtained by linear interpolation between input points specified in any time scale

$$C_1 = \frac{JA_E^2}{c} \times \frac{1\ \text{km}^2}{10^6 m^2} = 1.031 \times 10^8\ \frac{\text{km}^3\text{kg}}{\text{sec}^2 m^2}$$

where

$J$ = solar radiation constant
= $1.383 \times 10^3$ watts/m$^2$
= $1.383 \times 10^3$ kg/sec$^3$

$A_E$ = $1.496 \times 10^8$ km

$c$ = $2.997{,}925 \times 10^5$ km/sec

$A_P$ = nominal area of spacecraft projected onto plane normal to Sun-probe line, $m^2$

$m$ = instantaneous mass of probe, kg

$r_{SP}$ = distance from Sun to probe, km

$T_{SRP}$ = epoch at which acceleration due to solar radiation pressure is turned on The epoch may be specified in the UTC, S.T., or A.1 time scales

$u^*(t-T_{SRP})$ = 1 for $t \geq T_{SRP}$ if spacecraft in sunlight, 0 for $t < T_{SRP}$ or if spacecraft in shadow

$G_r$ = solve for effective area for acceleration of spacecraft in radial direction due to solar radiation pressure, divided by nominal area $A_p$

$G_x$ = solve for effective area for acceleration of spacecraft in the direction of its positive $x$ axis (along $\mathbf{X}^*$ vector) divided by $A_p$

$G_y$ = solve for effective area for acceleration of spacecraft in the direction of its positive $y$ axis (along $\mathbf{Y}^*$ vector) divided by $A_p$

$G_r' G_x' G_y'$ = solve for derivatives of $G_r$, $G_x$, $G_y$ with respect to Earth-probe Sun angle, $EPS$

$EPS$ = Earth-probe Sun angle, radians

$\Delta G_r,\Delta G_x,\Delta G_y$ = increments to $G_r$, $G_x$, and $G_y$ obtained by linear interpolation of input points specified in any time scale

The unit Sun-probe vector $\mathbf{U}_{SP}$ is computed from

$$\mathbf{U}_{SP} = \frac{\mathbf{r} - \mathbf{r}_S^{(C)}}{\left\| \mathbf{r} - \mathbf{r}_S^{(C)} \right\|} \tag{38}$$

where

$\mathbf{r}$ = rectangular coordinates of probe relative to center of integration, referred to mean Earth equator and equinox of 1950.0

$\mathbf{r}_S^{(C)}$ = rectangular coordinates of Sun relative to center of integration C, referred to mean Earth equator and equinox of 1950.0

The spacecraft **X*** and **Y*** unit vectors are obtained as a rotation of the tangential **T** and normal **N** vectors through the angle $K$:

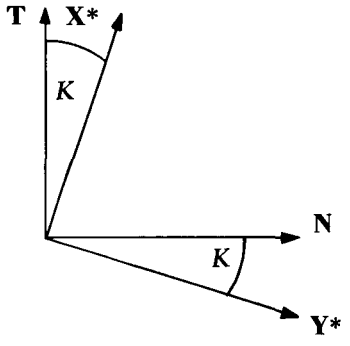


$$\begin{pmatrix} \mathbf{X}^* \\ \mathbf{Y}^* \end{pmatrix} = \begin{pmatrix} \cos K & \sin K \\ -\sin K \cos K \end{pmatrix} \begin{pmatrix} \mathbf{T} \\ \mathbf{N} \end{pmatrix} \tag{39}$$

The angle $K$ is an input (nonsolve for) constant. Computation of the unit vectors **T** and **N** requires the unit vector $\mathbf{U}_R$

$\mathbf{U}_R$ = unit vector from spacecraft to reference body which orients the spacecraft about the roll axis (Sun-probe line). The reference body may be a star, a planet, or the Moon.

If the reference body is a star

$$\mathbf{U}_R = \begin{bmatrix} \cos\delta\cos\alpha \\ \cos\delta\cos\alpha \\ \sin\delta \end{bmatrix} \tag{40}$$

where the right ascension $\alpha$ and declination $\delta$ are referred to the mean Earth equator and equinox of 1950.0. If the reference body $B$ is a planet or the Moon (normally the Earth),

$$\mathbf{U}_R = \frac{\mathbf{r}_B^{(C)} - \mathbf{r}}{\| \mathbf{r}_B^{(C)} - \mathbf{r} \|} \tag{41}$$

where

$\mathbf{r}_B^{(C)}$ = rectangular coordinates of reference body $B$ relative to center of integration $C$, referred to mean Earth equator and equinox of 1950.0

The unit normal vector **N** (normal to Sun-probe-reference body plane) is computed from

$$\mathbf{N} = \frac{\mathbf{U}_R \times \mathbf{U}_{SP}}{\| \mathbf{U}_R \times \mathbf{U}_{SP} \|} \tag{42}$$

The unit tangential vector **T** (tangent to Sun-probe-reference body plane) is

$$\mathbf{T} = \mathbf{N} \times \mathbf{U}_{SP} \tag{43}$$

The EPS angle may be computed from

$$\cos \text{EPS} = -\mathbf{U}_{SP} \cdot \mathbf{U}'_R \qquad 0 < EPS < 180° \tag{44}$$

where

$\mathbf{U}'_R$ is computed from Eq. (41) using $B$ = Earth.

*d. Acceleration due to motor burn.* The acceleration of the probe in 1950.0 Earth equatorial rectangular coordinates due to a motor burn is given by

$$\ddot{\mathbf{r}} = a\mathbf{U}\{\mu(t - T_o) - \mu(t - T_f)\} \tag{45}$$

where

$a$ = magnitude of $\ddot{\mathbf{r}}$ vs time

$\mathbf{U}$ = unit vector in direction of $\ddot{\mathbf{r}}$ vs time

$T_o$ = effective start time of motor, the ET value of the solve for UTC epoch, $T_0$ (UTC)

$T_f$ = effective stop time of motor, ET

$t$ = ephemeris time

$$\mu(t - T_o) = \begin{cases} 1 \text{ for } t \geq T_o \\ 0 \text{ for } t < T_o \end{cases} \qquad T_o \rightarrow T_f$$

The effective stop time $T_f$ is given by

$$T_f = T_o + T \tag{46}$$

where

$T$ = solve for burn time of motor, ET

The acceleration magnitude $a$ is given by

$$a = \frac{F(t)}{m(t)} C = \frac{F_o + F_1 t + F_2 t^2 + F_3 t^3 + F_4 t^4}{m_o - \dot{M}_o t - \tfrac{1}{2}\dot{M}_1 t^2 - \tfrac{1}{3}\dot{M}_2 t^3 - \tfrac{1}{4}\dot{M}_3 t^4} C \tag{47}$$

where

$F(t)$ = magnitude of thrust at time $t$. The polynomial coefficients of $F(t)$ are solve for parameters

$m(t)$ = spacecraft mass at time $t$

$C$ = 0.001 for $F$ in newtons and $m$ in kg. For $F$ in lb and $m$ in lbm, $C$ = 0.009,806,65

$m_o$ = spacecraft mass at $T_o$ (ET)

$\dot{M}_o, \dot{M}_1, \dot{M}_2, \dot{M}_3$ = polynomial coefficients for propellant mass flow rate (positive) at time $t$, $\dot{M}(t) = \dot{M}_o + \dot{M}_1 t + \dot{M}_2 t^2 + \dot{M}_3 t^3$ (not solve for parameters)

$t$ = E.T. $- T_o$ (ET), seconds

The unit vector **U** in the direction of thrust is given by

$$\mathbf{U} = \begin{Bmatrix} U_x \\ U_y \\ U_z \end{Bmatrix} = \begin{Bmatrix} \cos\delta \cos\alpha \\ \cos\delta \sin\alpha \\ \sin\delta \end{Bmatrix} \quad (48)$$

where

$\alpha$ = right ascension of **U**

$\delta$ = declination of **U**

given by

$$\alpha = \alpha_o + \alpha_1 t - \alpha_2 t^2 + \alpha_3 t^3 + \alpha_4 t^4 \quad (49)$$

$$\delta = \delta_o + \delta_1 t - \delta_2 t^2 + \delta_3 t^3 + \delta_4 t^4 \quad (50)$$

where the polynomial coefficients of Eqs. (49) and (50) are solve for parameters.



# E. Theoretical Basis for the Double Precision Orbit Determination Program (DPODP): IV. Light Time Solution

T. D. Moyer

## 1. Introduction

This fourth article in the series gives the formulation for the solution of the light time problem, which is the first step in the computation of all observable quantities. An electromagnetic signal is transmitted from a tracking station on Earth at time $t_1$. This signal is received by the probe and retransmitted at time $t_2$, arriving at the same or different tracking station on Earth at time $t_3$. Alternatively, the signal may be transmitted directly by the probe at time $t_2$. All observables are related to characteristics of this electromagnetic radiation, i.e., the angle of the incoming ray, the ratio of received to transmitted frequency, or the round trip transit time. The transmitting and receiving station(s) and the probe are referred to as direct participants, and $t_1$, $t_2$, and $t_3$ are the epochs of participation of each participant. The solution to the light time problem consists of the heliocentric position, velocity, acceleration, and jerk of each direct participant evaluated at its epoch of participation. The next articles in the series will give the formulation for computing doppler, range, and angular observables, starting with the solution to the light time problem.

The solution to the light time problem is obtained by solving the light time equation for each leg of the path of electromagnetic radiation from the transmitting to the receiving station. The light time equation relates the light time between two points to the heliocentric positions of each of the two participants evaluated at their epochs of participation. Starting with the known reception time $t_3$, the light time equation is solved by an iterative technique for the down leg of the light path to give the epoch of participation for the probe, $t_2$. Given $t_2$, the light time equation is solved iteratively for the up leg of the light path to give the transmission time $t_1$.

The light time equation is derived in Section 2 and accounts for the effects of general relativity. The method of computing the heliocentric position vector of each participant is given in Section 3. If a participant is a station, the position of the station relative to the center of the celestial body on which it is located must be computed. The formulation for doing so is given in Section 4.

## 2. Light Time Equation

Light moves along a geodesic path in the four-dimensional non-Euclidean geometry of space time. The geometry is embodied in the coefficients of the expression for the distance or interval $ds$ between two points (Ref. 25, p. 93)

$$ds^2 = \left(1 - \frac{2\mu}{c^2 r} + \frac{2\mu^2}{c^4 r^2}\right) c^2 dt^2 - \left(1 + \frac{2\mu}{c^2 r}\right)(dr^2 + r^2\, d\theta^2 + r^2 \sin^2\theta\, d\phi^2) \quad (1)$$

where

$r, \theta, \phi$ = Schwarzschild isotropic spherical coordinates of a point in a heliocentric nonrotating frame of reference

$t$ = uniform coordinate time in heliocentric frame of reference (ephemeris time)

$\mu$ = gravitational constant of Sun, $1.32715 \times 10^{11}$ km$^3$/sec$^2$

$c$ = speed of light at infinite distance from Sun, 299,792.5 km/sec

$ds$ = interval between two points with differentials $dr$, $d\theta$, $d\phi$, and $dt$ in the space-time coordinates

The departure from pseudo-Euclidean geometry in Eq. (1) is due to the mass of the Sun. The effects of the mass of each planet and the Moon have been ignored.

The square of the coordinate speed of light $\dot{s}$ is

$$\dot{s}^2 = \left(\frac{dr}{dt}\right)^2 + r^2\left(\frac{d\theta}{dt}\right)^2 + r^2 \sin^2\theta\left(\frac{d\phi}{dt}\right)^2 \qquad (2)$$

For the motion of light, the interval $ds$ between two points on the light path is zero (Ref. 1, p. 93). Setting $ds = 0$ in Eq. (1), substituting Eq. (2), and ignoring $1/c^4$ terms gives

$$\dot{s} = c\left(1 - \frac{2\mu}{c^2 r}\right) \qquad (3)$$

If light moved along a straight line at speed $\dot{s}$ relative to the Sun, the light time equation would be of the form

$$t_2 - t_1 = \frac{r_{12}}{c} + \frac{1}{c^3}(\quad) \qquad (4)$$

where $t_1$ is the time of emission of light from point 1; $t_2$ is the time of reception of light at point 2; and $r_{12}$ is the distance between point 1 at time $t_1$ and point 2 at time $t_2$, measured in a heliocentric nonrotating frame of reference. The $1/c^3$ term is due to the departure of the speed of light from the constant $c$.

For light passing by the Sun on a curved geodesic path with minimum radius $R$, the angle between the incoming and outgoing asymptotes is given by $4\mu/c^2R$, which has the well known maximum value of 1".75 when $R$ is set equal to the radius of the Sun, 700,000 km. The maximum angle between the straight line path between two points and the actual curved path is $4\mu/c^2R$. If the nominal length of the light path between two points is $L$, the difference in length $\Delta L$ between the straight line path and the curved geodesic path will be less than

$$\Delta L < \frac{L}{\cos\frac{4\mu}{c^2R}} - L = \frac{L}{2}\left(\frac{4\mu}{c^2R}\right)^2 \qquad (5)$$

which is of order $1/c^4$. Thus, the bending of light produces a term of order $1/c^5$ in the light time equation [Eq. (4)]. If all terms of order $1/c^5$ and greater are ignored in the derivation of the light time equation, the assumption of straight line motion at speed $\dot{s}$ given by Eq. (3) is valid.

Fig. 24 shows the geometry for straight line motion of light relative to the Sun S. Light is emitted from point 1 at ephemeris time $t_1$ and arrives at point 2 at ephemeris time $t_2$. The angles $\beta_1$ and $\beta_2$ are computed from

$$\cos\beta_1 = \frac{\mathbf{r}_1}{r_1} \cdot \frac{\mathbf{r}_{12}}{r_{12}} \qquad (6)$$

$$\cos\beta_2 = \frac{\mathbf{r}_2}{r_2} \cdot \frac{\mathbf{r}_{12}}{r_{12}} \qquad (7)$$

where $[\mathbf{r}_1 = \mathbf{r}_1^{(S)}(t_1)]$, $[\mathbf{r}_2 = \mathbf{r}_2^{(S)}(t_2)]$ = heliocentric position vectors of point 2 at ephemeris time $t_2$ and point 1 at ephemeris time $t_1$, with components referred to a nonrotating coordinate system. In the DPODP this coordinate system is referred to the mean Earth equator and

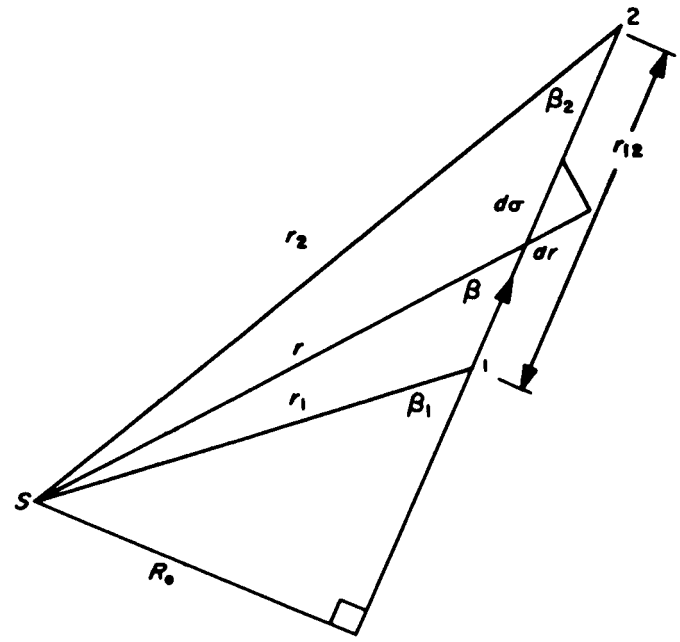


**Fig. 24. Geometry for straight line motion**

equinox of 1950.0. The $x$ axis is along the mean equinox of 1950.0, the $z$ axis is normal to the mean Earth equator of 1950.0 directed North, and the $y$ axis completes the right-handed rectangular coordinate system.

$$\mathbf{r}_{12} = \mathbf{r}_2 - \mathbf{r}_1 \tag{8}$$

$$r_{12} = \| \mathbf{r}_{12} \| \tag{9}$$

Noting the definitions of Eqs. (6) and (7), the angles $\beta_1$ and $\beta_2$ are in quadrants I and II and can be determined from their cosines. The time for light to travel from point 1 to point 2 at speed $\dot{s}$ given by Eq. (3) is

$$t_2 - t_1 = \int_0^{r_{12}} \frac{d\sigma}{\dot{s}} \approx \frac{1}{c} \int_0^{r_{12}} \left(1 + \frac{2\mu}{c^2 r}\right) d\sigma \tag{10}$$

From Fig. 24,

$$d\sigma = \frac{dr}{\cos\beta} = \frac{r\,dr}{\sqrt{r^2 - R_o^2}} \tag{11}$$

Substituting Eq. (11) into Eq. (10) gives

$$t_2 - t_1 = \frac{1}{c} \int_{r_1}^{r_2} \frac{r\,dr}{\sqrt{r^2 - R_o^2}} + \frac{2\mu}{c^3} \int_{r_1}^{r_2} \frac{dr}{\sqrt{r^2 - R_o^2}} \tag{12}$$

Evaluating the integrals gives

$$t_2 - t_1 = \frac{1}{c}\left[\sqrt{r_2^2 - R_o^2} - \sqrt{r_1^2 - R_o^2}\right] + \frac{2\mu}{c^3} \ln\left[\frac{r_2 + \sqrt{r_2^2 - R_o^2}}{r_1 + \sqrt{r_1^2 - R_o^2}}\right] \tag{13}$$

The $1/c$ term is simply $r_{12}/c$ and $\sqrt{r^2 - R_o^2}$ is $r \cos\beta$. Thus,

$$t_2 - t_1 = \frac{r_{12}}{c} + \frac{2\mu}{c^3} \ln\left[\frac{r_2(1 + \cos\beta_2)}{r_1(1 + \cos\beta_1)}\right] \tag{14}$$

But $r_2 \sin\beta_2 = r_1 \sin\beta_1 = R_o$ (15)

Substituting $r_2/r_1$ from Eq. (15) into Eq. (14) gives the final expression for the light time equation

$$t_2 - t_1 = \frac{r_{12}}{c} + \frac{2\mu}{c^3} \ln\left[\frac{\tan \tfrac{1}{2}\beta_1}{\tan \tfrac{1}{2}\beta_2}\right] \tag{16}$$

where $r_{12}$ is evaluated from Eqs. (8) and (9), and $\beta_1$ and $\beta_2$, which are in quadrants I and II, are evaluated from Eqs. (6) and (7). Note that $\beta_1$ is always greater than $\beta_2$. Since the right side of Eq. (16) is a function of $t_2$ and $t_1$, the equation must be solved by an iterative procedure.

The $1/c^3$ term in Eq. (16) is indeterminate for light traveling radially to or from the Sun. For light traveling radially from the Sun, $\beta_1 = \beta_2 = 0°$ and

$$\frac{\tan \tfrac{1}{2}\beta_1}{\tan \tfrac{1}{2}\beta_2} = \frac{\sin\beta_1}{1 + \cos\beta_1} \cdot \frac{1 + \cos\beta_2}{\sin\beta_2} = \frac{1 + \cos\beta_2}{1 + \cos\beta_1} \cdot \frac{r_2}{r_1} = \frac{r_2}{r_1} \tag{17}$$

where $r_2 > r_1$. For light traveling radially toward the Sun, $\beta_1 = \beta_2 = 180°$ and

$$\frac{\tan \tfrac{1}{2}\beta_1}{\tan \tfrac{1}{2}\beta_2} = \frac{1 - \cos\beta_1}{\sin\beta_1} \cdot \frac{\sin\beta_2}{1 - \cos\beta_2} = \frac{1 - \cos\beta_1}{1 - \cos\beta_2} \cdot \frac{r_1}{r_2} = \frac{r_1}{r_2} \tag{18}$$

where $r_1 > r_2$. Hence, for light traveling radially to or from the Sun with $r_{larger}$ and $r_{smaller}$ equal to the larger and smaller values of $r_1$ and $r_2$,

$$t_2 - t_1 = \frac{r_{12}}{c} + \frac{2\mu}{c^3} \ln\left[\frac{r_{larger}}{r_{smaller}}\right] \tag{19}$$

In Eq. (16), if $\beta_1 = 90°$, $r_1 = 0.7 \times 10^6$ km (radius of Sun), $r_2 = 1$ a.u. $= 1.5 \times 10^8$ km, $\beta_2 \approx 16'$ and

$$\frac{2\mu}{c^3} \ln\left[\frac{\tan \tfrac{1}{2}\beta_1}{\tan \tfrac{1}{2}\beta_2}\right] = (10^{-5}\ \text{sec}) \ln \frac{1}{1/430} = 6.1 \times 10^{-5}\ \text{sec}$$

In Eq. (19), if $r_1 = 0.7 \times 10^6$ km (radius of Sun) and $r_2 = 1$ a.u. $= 1.5 \times 10^8$ km

$$\frac{2\mu}{c^3} \ln \frac{r_{larger}}{r_{smaller}} = (10^{-5} \text{ sec}) \ln 215 = 5.4 \times 10^{-5} \text{ sec}$$

### 3. Heliocentric Position Vector of Each Participant

The light time equation is solved for each leg of the path of electromagnetic radiation from the transmitter to the receiver in reverse order starting with the known reception time at the receiving station. The solution consists of the epoch of participation $t_i$ and the heliocentric position, velocity, acceleration, and jerk of each participant evaluated at its epoch of participation. The components of each vector are referred to the 1950.0 Earth equatorial rectangular coordinate system.

The light time equation (Eqs. 16 or 19) relates the light time in ephemeris time (ET) for a given leg of light path to the heliocentric position vectors of the two participants evaluated at their ET epochs of participation. However, for a receiving station on Earth, the known epoch of participation is in station time (ST) and must be converted to ET. Furthermore, to compute the heliocentric position vectors of certain participants requires the epoch of participation in time scales other than ET, i.e., UT1 for an Earth station. Thus, the time transformations given in the second article [*SPS 37-39*, Vol. III, pp. 36–38, Eqs. (3), (7), (8), and (9)] must be used extensively in the solution of the light time problem.

For a station on the Earth (E), the position of the station relative to the Sun (S) at its epoch of participation $t_i$ is computed from

$$\mathbf{r}_{stn}^{(S)}(t_i, \text{ET}) = \mathbf{r}_{stn}^{(E)}(t_i, \text{ET}, \text{UT1}) + \mathbf{r}_{E}^{(S)}(t_i, \text{ET}) \tag{20}$$

For a station or landed spacecraft on another celestial body $B$,

$$\mathbf{r}_{stn}^{(S)}(t_i, \text{ET}) = \mathbf{r}_{stn}^{(B)}(t_i, \text{ET}) + \mathbf{r}_{B}^{(S)}(t_i, \text{ET}) \tag{21}$$

For the probe with center of integration $C$,

$$\mathbf{r}_{pr}^{(S)}(t_i, \text{ET}) = \mathbf{r}_{pr}^{(C)}(t_i, \text{ET}) + \mathbf{r}_{C}^{(S)}(t_i, \text{ET}) \tag{22}$$

Each of these vector sums in 1950.0 Earth equatorial rectangular coordinates applies also for $\mathbf{r}$ replaced by $\dot{\mathbf{r}}$, $\ddot{\mathbf{r}}$, and $\dddot{\mathbf{r}}$. The formulation for computing the heliocentric position, velocity, acceleration, and jerk of a celestial body is given on pp. 25 and 26 of this summary. The position, velocity, acceleration and jerk of the probe relative to the center of integration is obtained by interpolation of the probe ephemeris sum and difference arrays. The formulation for computing the position, velocity, acceleration, and jerk of a station in 1950.0 Earth equatorial rectangular coordinates centered at the body on which the station is located is given in Section 4 of this article.

### 4. Body-Centered Station Position, Velocity, Acceleration, and Jerk in 1950.0 Rectangular Coordinates

*a. Introduction.* This section gives the formulation for computing the position, velocity, acceleration, and jerk of a station in a 1950.0 Earth equatorial rectangular coordinate system centered at the body on which the station is located.

A fixed station may be located on the Earth, the Moon, or Mars with spherical or cylindrical coordinates. Although not discussed here, the DPODP can also account for the motion of a moving ship station on Earth.

For a fixed Earth station, two models are available to represent the station position. The simplest is to represent the station position by constant values of the coordinates relative to the true axis of rotation, equator, and prime meridian. However, due to wandering of the pole (axis of rotation) relative to the Earth, the actual position of a fixed station relative to the true pole, equator, and prime meridian is a variable quantity. Therefore, the alternate method of representing the station position is to use constant values of station coordinates relative to the mean pole, equator, and prime meridian of the period 1900-05. These constant coordinates are transformed to variable coordinates relative to the true pole, equator, and prime meridian of the date using the time-varying coordinates of the true pole of date relative to the mean pole of 1900-05 supplied by the U. S. Naval Observatory. This model is relatively simple, should provide a better fit to the data, and has the added advantage that solved for station locations obtained from missions covering a

long period of time should be the same, regardless of the wandering of the pole relative to the Earth which has occurred during this period of time.

Section *b.* gives the formulation for computing body-fixed rectangular coordinates $\mathbf{r}_b$ of a station where $x_b$ is along the intersection of the prime meridian (passing through the true axis of rotation) and true equator of date; $z_b$ is along the instantaneous axis of rotation directed north; and $y_b$ completes the right-handed rectangular system of coordinates. Section *c.* gives the formulation for transforming body-fixed rectangular coordinates to 1950.0 Earth equatorial position, velocity, acceleration, and jerk. The details of the transformations are given only for an Earth station.

***b. Body-fixed rectangular coordinates.*** Fixed stations on any body, using constant coordinates relative to true pole, equator, and prime meridian:

A fixed station may be represented by spherical or cylindrical coordinates. The spherical coordinates are

$r$ = radius from center of body to station, km

$\phi$ = body-centered latitude measured from true equator (plane normal to instantaneous axis of rotation and containing center of mass)

$\lambda$ = longitude measured east from prime meridian (passing through instantaneous axis of rotation)

The cylindrical coordinates are: $u = (r \cos \phi)$, $v = (r \sin \phi)$, $\lambda$.

For spherical coordinates, the body-fixed coordinates $\mathbf{r}_b$ are

$$\mathbf{r}_b = \begin{bmatrix} x_b \\ y_b \\ z_b \end{bmatrix} = \begin{bmatrix} r \cos \phi \sin \lambda \\ r \cos \phi \sin \lambda \\ r \sin \phi \end{bmatrix} \tag{23}$$

For cylindrical coordinates,

$$\mathbf{r}_b = \begin{bmatrix} x_b \\ y_b \\ z_b \end{bmatrix} = \begin{bmatrix} u \cos \lambda \\ u \sin \lambda \\ v \end{bmatrix} \tag{24}$$

Fixed Earth station using constant coordinates relative to mean pole, equator, and prime meridian of 1900-05:

The solve for coordinates are spherical or cylindrical relative to the mean pole, equator, and prime meridian of 1900-05. The spherical coordinates are $r$, $\phi_0$, $\lambda_0$; the cylindrical coordinates are $u_0$, $v_0$, $\lambda_0$. The coordinates relative to the true pole are denoted by the same quantities without the subscript. The transformations are

$$\phi = \phi_o + \Delta\phi \tag{25}$$

$$\lambda = \lambda_o + \Delta\lambda \tag{26}$$

$$u = u_o + \Delta u \tag{27}$$

$$v = v_o + \Delta v \tag{28}$$

With these quantities, body-centered coordinates $\mathbf{r}_b$ are computed from Eqs. (23) or (24).

Fig. 25 shows the latitude $\phi_o$ and longitude $\lambda_o$ of a station $S$ relative to the mean pole of 1900-05 ($P_o$), and the instantaneous latitude $\phi$ and longitude $\lambda$ relative to the true pole of date ($P$). The pole $P_o$ and associated grid of equator and meridians are rotated through the angle $\omega$ carrying $P_o$ to $P$. The angular coordinates of $P$ relative to $P_o$ are $x$ measured south along the Greenwich meridian of 1900-05 (strictly the 1900-05 meridian of zero longitude) and $y$ measured south along the 90 W meridian of 1900-05. Values of $x$ and $y$ are supplied weekly by the U. S. Naval Observatory. They are represented by linear polynomials in the DPODP with coefficients specified by time block. Since $x$ and $y$ are only a few meters in linear dimension, an approximate expression for $\Delta\phi = \phi - \phi_o$ is

$$\Delta\phi = x \cos \lambda_o - y \sin \lambda_o \tag{29}$$

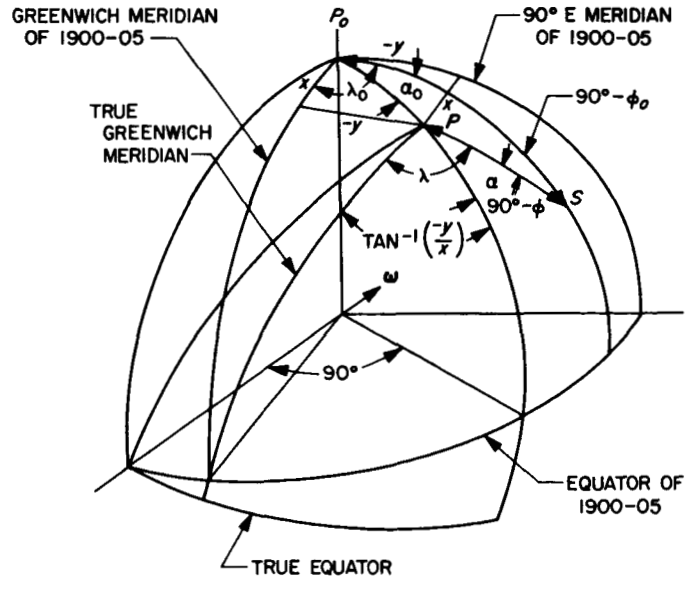


**Fig. 25. Latitude and longitude relative to mean pole of 1900-05 and to true pole of date**

Noting $\alpha_o$ and $\alpha$ on Fig. 24,

$$\lambda_o = \alpha_o + \tan^{-1}\left(\frac{-y}{x}\right) \tag{30}$$

$$\lambda = \alpha + \tan^{-1}\left(\frac{-y}{x}\right) \tag{31}$$

Thus,

$$\Delta\lambda = \lambda - \lambda_o = \alpha - \alpha_o \tag{32}$$

From the spherical triangle $P$, $P_o$, $S$,

$$\frac{\sin\alpha_o}{\cos\phi} = \frac{\sin\alpha}{\cos\phi_o} \tag{33}$$

Cross multiplying and using Eqs. (25) and (32) gives

$$\sin\alpha_o\cos\phi_o = \sin(\alpha_o + \Delta\lambda)\cos(\phi_o + \Delta\phi) \tag{34}$$

Expanding, noting that $\Delta\lambda$ and $\Delta\phi$ are very small angles, and ignoring the higher order term containing $\Delta\lambda\,\Delta\phi$, gives

$$\Delta\lambda = \tan\alpha_o\tan\phi_o\,\Delta\phi \tag{35}$$

From Eq. (30),

$$\tan\alpha_o = \frac{\tan\lambda_o + \frac{y}{x}}{1 - \frac{y}{x}\tan\lambda_o} \tag{36}$$

Substituting Eqs. (36) and (29) into Eq. (35) gives

$$\Delta\lambda = \tan\phi_o\,(x\sin\lambda_o + y\cos\lambda_o) \tag{37}$$

The cylindrical coordinates relative to the pole of 1900-05 and to the true pole of date are

$$u_o = r\cos\phi_o \qquad u = r\cos\phi = r\cos(\phi_o + \Delta\phi) \tag{38}$$

$$v_o = r\sin\phi_o \qquad v = r\sin\phi = r\sin(\phi_o + \Delta\phi) \tag{39}$$

Solving for $\Delta u = u - u_o$ and $\Delta v = v - v_o$ gives

$$\Delta u = -v_o\,\Delta\phi \tag{40}$$

$$\Delta v = u_o\,\Delta\phi \tag{41}$$

where $\Delta\phi$ is given by Eq. (29). Using cylindrical coordinates, $\Delta\lambda$ is computed from

$$\Delta\lambda = \frac{v_o}{u_o}(x\sin\lambda_o + y\cos\lambda_o) \tag{42}$$

*c. Transformation of body-fixed rectangular coordinates to 1950.0 position, velocity, acceleration, and jerk.* The position, velocity, acceleration, and jerk of a station in a 1950.0 Earth equatorial rectangular coordinate system centered at the body on which the station is located are denoted by $\mathbf{r}_{50}$, $\dot{\mathbf{r}}_{50}$, $\ddot{\mathbf{r}}_{50}$, and $\dddot{\mathbf{r}}_{50}$. The transformations from body-fixed coordinates $\mathbf{r}_b$ for a fixed station to $\mathbf{r}_{50}$, $\dot{\mathbf{r}}_{50}$, $\ddot{\mathbf{r}}_{50}$ and $\dddot{\mathbf{r}}_{50}$ are

$$\mathbf{r}_{50} = T\mathbf{r}_b \tag{43}$$

$$\dot{\mathbf{r}}_{50} = \dot{T}\mathbf{r}_b \tag{44}$$

$$\ddot{\mathbf{r}}_{50} = \ddot{T}\mathbf{r}_b \tag{45}$$

$$\dddot{\mathbf{r}}_{50} = \dddot{T}\mathbf{r}_b \tag{46}$$

where, for the Earth

$$T_E = (BNA)^T \tag{47}$$

$$\dot{T}_E = (\dot{B}NA + B\dot{N}A + BN\dot{A})^T \tag{48}$$

$$\ddot{T}_E \approx (\ddot{B}NA)^T \tag{49}$$

$$\dddot{T}_E \approx (\dddot{B}NA)^T \tag{50}$$

where the dots indicate differentiation with respect to ET. The matrices $A$, $N$, and $B$ are

$A$ = precession matrix, transforming from coordinates referred to the mean Earth equator and equinox of 1950.0 to coordinates referred to the mean Earth equator and equinox of date

$N$ = nutation matrix, transforming from coordinates referred to the mean Earth equator and equinox of date to coordinates referred to the true Earth equator and equinox of date

$B$ = rotation from coordinates referred to the true Earth equator and equinox of date to body-fixed coordinates $\mathbf{r}_b = (x_b, y_b, z_b)^T$, where $x_b$, $y_b$, $z_b$ is a right-handed rectangular coordinate system with $x_b$ and $y_b$ in the Earth's true equatorial plane, $x_b$ passing through the prime meridian, and $z_b$ directed North

The matrices $B$, $\dot{B}$, $\ddot{B}$, and $\dddot{B}$ are computed from

$$B = \begin{bmatrix} \cos\theta & \sin\theta & 0 \\ -\sin\theta & \cos\theta & 0 \\ 0 & 0 & 1 \end{bmatrix} \tag{51}$$

$$\dot{B} = \begin{bmatrix} -\sin\theta & \cos\theta & 0 \\ -\cos\theta & -\sin\theta & 0 \\ 0 & 0 & 0 \end{bmatrix}\dot{\theta} \tag{52}$$

$$\ddot{B} = \begin{bmatrix} -\cos\theta & -\sin\theta & 0 \\ \sin\theta & -\cos\theta & 0 \\ 0 & 0 & 0 \end{bmatrix} \dot{\theta}^2 \quad (53)$$

$$\dddot{B} = \begin{bmatrix} \sin\theta & -\cos\theta & 0 \\ \cos\theta & \sin\theta & 0 \\ 0 & 0 & 0 \end{bmatrix} \dot{\theta}^3 \quad (54)$$

where

$\theta$ = apparent (true) sidereal time = Greenwich hour angle of true equinox of date

The quantities of $\theta$ and $\dot{\theta}$ are computed from the following formulation

$$\theta = \theta_M + \delta\psi \cos\epsilon \quad \text{(rad)} \quad (55)$$

$$\dot{\theta} = \dot{\theta}_M + \delta\dot{\psi} \cos\epsilon - \dot{\epsilon}\delta\psi \sin\epsilon \quad \text{(rad/ephem sec)} \quad (56)$$

$$\epsilon = \bar{\epsilon} + \delta\epsilon \quad \text{(rad)} \quad (57)$$

$$\dot{\epsilon} = \dot{\bar{\epsilon}} + \delta\dot{\epsilon} \quad \text{(rad/ephem sec)} \quad (58)$$

(Ref. 26, p. 98)

$$\bar{\epsilon} = \frac{A + BT + CT^2 + DT^3}{206{,}264.80625} \quad \text{(rad)} \quad (59)$$

$A = 23°27'8''.26 = 84{,}428''.26$

$B = -46''.845$

$C = -0''.0059$

$D = 0''.00181$

$$\dot{\bar{\epsilon}} = \frac{B + 2CT + 3DT^2}{86{,}400 \times 36{,}525 \times 206{,}264.80625} \quad \text{(rad/ephem sec)} \quad (60)$$

$T$ = Julian centuries of 36,525 ephemeris days elapsed since 1900, January 0, $12^h$ ET

JED = Julian ephemeris date

$$T = \frac{\text{JED} - 241{,}5020}{36{,}525} \quad (61)$$

The parameters used in Eqs. (55) through (61) are defined as

$\theta_M$ = mean sidereal time = Greenwich hour angle of mean equinox of date

$\delta\psi$ = nutation in longitude

$\epsilon$ = true obliquity of ecliptic

$\bar{\epsilon}$ = mean obliquity of ecliptic

$\delta\epsilon$ = nutation in obliquity

The mean sidereal time is computed as a function of UT1 (See *SPS 37-39*, Vol. III, p. 36)

$$\theta_M = \text{UT1} + J + KT_U + LT_U^2 \quad (62)$$

where

$J = 6^h38^m45^s.836 = 23{,}925^s.836$

$K = 8{,}640{,}184^s.542$

$L = 0^s.0929$

$T_U$ = number of Julian centuries of 36,525 days of UT1 elapsed since 1900, January $0{,}12^h$ UT1

$$T_U = \frac{\text{JD (UT1)} - 241{,}5020}{36{,}525} \quad (63)$$

JD (UT1) = Julian date computed from UT1

The true sidereal time $\theta$ may be computed from Eqs. (55) and (62) as

$$\theta = \left[\left(\overline{\text{UT1}} + \frac{J + KT_U + LT_U^2}{86{,}400} + \frac{\delta\psi \cos\epsilon}{2\pi}\right)_{decimal\,part}\right] 2\pi \quad \text{(rad)} \quad (64)$$

where

$$\overline{\text{UT1}} = [\text{JD (UT1)} - 0.5]_{decimal\,part} \quad (65)$$

Differentiating Eq. (62) with respect to ET gives

$$\dot{\theta}_M = \frac{d\text{UT1}}{d\text{ET}}\left(1 + \frac{K + 2LT_U}{36{,}525 \times 86{,}400}\right)\frac{\pi}{43{,}200} \quad \text{(rad/sec)} \quad (66)$$

From *SPS 37-39*, Vol. III, p. 37,

$$\text{UT1} = \text{ET} - (\text{ET} - \text{A.1}) - (\text{A.1} - \text{UT1}) \quad (67)$$

and

$$\frac{d\text{UT1}}{d\text{ET}} = 1 + \frac{\Delta f_{cesium}}{9{,}192{,}631{,}770} - g - 2ht \quad (68)$$

where

$t$ = seconds past start of time block containing $f$, $g$, and $h$

Thus,

$$\dot{\theta}_M = \left(1 + \frac{K + 2LT_U}{36{,}525 \times 86{,}400}\right)\left(1 + \frac{\Delta f_{cesium}}{9{,}192{,}631{,}770} - g - 2ht\right)\frac{\pi}{43{,}200} \quad \left(\frac{\text{rad}}{\text{sec}}\right) \tag{69}$$

and $\dot{\theta}$ is computed from Eqs. (56) and (69).

N67 14427

# F. Range & Angle Corrections Due to the Ionosphere

A. Liu

## 1. Introduction

Radio waves passing through an ionosphere are not only deflected from a straight line, (refracted), but also the speed at which the wave is propagated is altered. The refraction due to the ionosphere for S-band frequencies can be as large as 12 sec of arc, although a more typical value is 6 sec of arc. The range correction can be as large as 20 m at low elevation angles. The ionospheric effects turn out to be more severe for missions to the inner planets than for missions to the outer planets. The reason is that for missions to Venus, for example, the observations are always taken more nearly in the direction of the Sun, and hence, through a much thicker ionosphere than for observations taken for a Mars mission, where for about half the duration of the mission, the measurements are taken at night (away from the Sun). Fig. 26 shows the ion density as a function of direction of Sun and altitude.

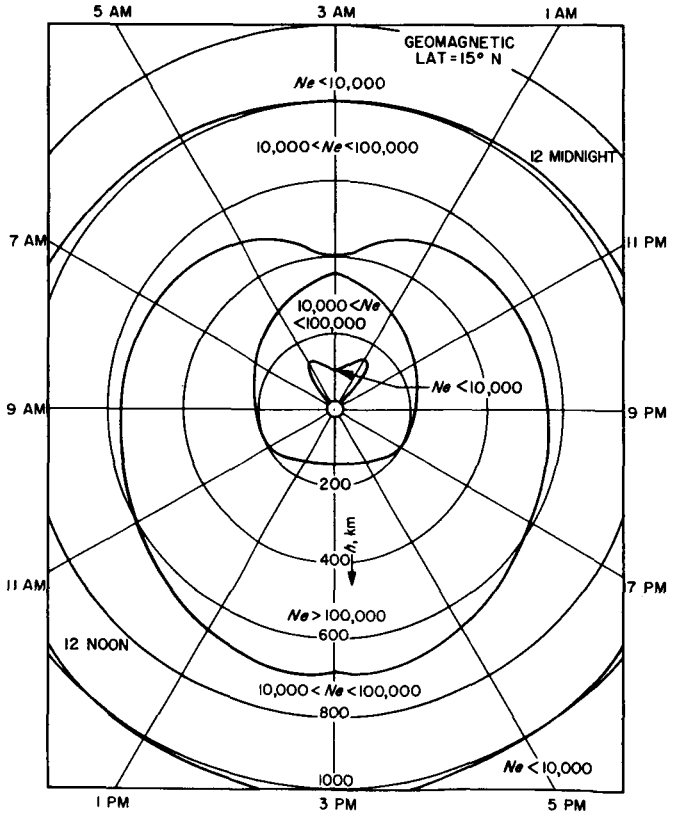


**Fig. 26. Ion density vs Sun direction and altitude**

A program was written to ray-trace through a Chapman ionosphere, and curves are presented to illustrate the effects of variations in the ionospheric model upon the range and angular measurements as a function of elevation angle.

## 2. Ray Tracing Formulae

(*SPS 37-28*, Vol. IV, pp. 1 and 2)

The assumptions made are

(1) The ionosphere is spherically layered, the density being given by a Chapman distribution.

(2) The ray path takes the shortest time route between two given points (Fermat's Principle).

Define the following

$c$ = speed of light in vacuum

$v$ = speed of light in medium

$\phi$ = polar angle

$n$ = index of refraction = $c/v$

The problem is to find the curve $C$ for which the travel time is at a minimum.

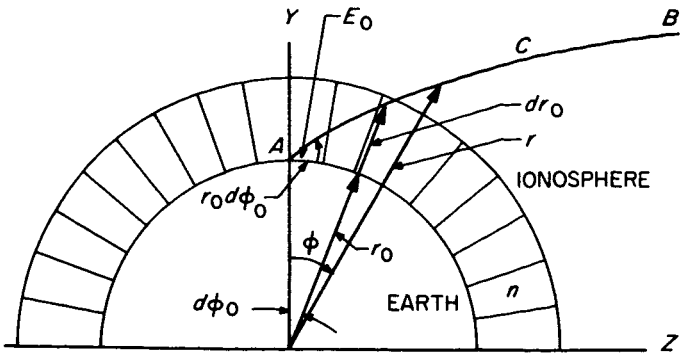


**Fig. 27. Ray path geometry**

Consider the situation illustrated in Fig. 27. A light ray is required to leave point $A$, pass through a medium with index of refraction $n$, and arrive at point $B$ in the least amount of time, $T$, i.e.,

$$T = \int_C \frac{ds}{v} \text{ is to be an extremal by finding the proper path } C, \text{ or} \tag{1}$$

$$T = \frac{1}{c}\int_C nds = \frac{1}{c}\int_C n\sqrt{1 + r^2\left(\frac{d\phi}{dr}\right)^2}\,dr \tag{2}$$

where $n$ is the index of refraction.

The path $C$ is determined by finding $\phi = \phi(r)$. A necessary condition for rendering $T$ an extremal is that the integral of Eq. (2) satisfy the Euler-Lagrange equation.

$$\frac{\partial F}{\partial \phi} - \frac{d}{dr}\left(\frac{\partial F}{\partial \phi_1}\right) = 0 \tag{3}$$

where

$$\phi_1 = \frac{d\phi}{dr} \tag{4}$$

and

$$F = n(\phi, r)\sqrt{1 + r^2\phi_1^2} = F(\phi, r, \phi_1) \tag{5}$$

At this point, we note that for the case where spherical symmetry exists,

$$\frac{\partial F}{\partial \phi} = 0 \tag{6}$$

The total bending to infinity can be found as

$$\phi = \int_{r_0}^{\infty} \frac{C_1}{(r\sqrt{n^2 r^2 - C_1^2})}\,dr \tag{7}$$

where

$$C_1 = r_0 n_0 \cos E_0 \tag{8}$$

*a. Angular refraction.* To evaluate the integral given by Eq. (7) make a change of variable to $u = rn$. It follows that,

$$du = (rn' + n)dr \tag{9}$$

where

$$n' = \frac{dn}{dr} \tag{10}$$

Integration by parts of Eq. (7) gives

$$\phi = \frac{\pi}{2} - C_1\int_{u_0}^{\infty}\left(\frac{rn'}{rn' + n}\right)\frac{du}{u\sqrt{u^2 - C_1^2}} \tag{11}$$

$$= \frac{\pi}{2} + \delta\phi \tag{12}$$

We note that $\delta\phi$ will have a singularity whenever $u = C_1$, and to remove this, singularity transform again the variable $u$ to $X$ by

$$\cos X = \frac{C_1}{u}, \tag{13}$$

yielding for $\delta\phi$,

$$\delta\phi = \int_{X = X_0}^{X} \frac{rn'}{(rn' + n)}\,dX \tag{14}$$

*b. "Range" or time of flight correction.* The path is now known, given by Eq. (14) and the transit time, $T$ or $R$, the measured range, is given by

$$R = cT = \int_{r_0}^{\infty} \frac{n^2 r}{\sqrt{n^2 r^2 - C_1^2}}\,dr \tag{15}$$

Changing variable $r$ to $u$ and integrating Eq. (15) by parts as before gives

$$\Delta R = \int_{u_0}^{\infty} -\frac{u}{\sqrt{u^2 - C_1^2}}\left(\frac{rn'}{rn' + n}\right)du - r_0\sin(E_0 - \delta\phi) + r_0 n_0 \sin E_0 \tag{16}$$

$$= \delta R - r_0\sin(E_0 - \delta\phi) + r_0 n_0 \sin E_0 \qquad (n_0 = 1) \tag{17}$$

We note again, that $\delta R$ suffers the same singularities as $\delta\phi$, for $u = C_1$ and to remove this singularity, a transformation to $X$ as before will give

$$\delta R = \int_{X=X_0}^{X} (rn)^2 \left(\frac{rn'}{rn' + n}\right) dX \qquad (18)$$

The actual numerical method for integrating Eqs. (14) and (18) depends upon the function in the integrand, which in turn depends upon the model atmosphere. The model atmosphere chosen is given by

$$Ne = N(\max) \exp\{\tfrac{1}{2}[1 - u - \exp(-u)]\}, \qquad (19)$$

where

$Ne$ = number of electrons/cm$^3$ at height $h$

$N(\max)$ = maximum number of electrons/cm$^3$ occurring at $h(\max)$

$h$ = altitude above Earth

$B$ = scale height and,

$u = [h - h(\max)]/B$

The index of refraction is related to $Ne$ by:

$$n = 1 - \tfrac{1}{2}\frac{K^2}{f^2} Ne, \qquad (20)$$

where

$f$ = transmitter frequency $= 2.3 \times 10^9$ Hz

$K^2 = 80.6$ for $Ne$ in units of electrons/m$^3$

### 3. Numerical Results

Eqs. (14) and (18), which give the angular and range refraction corrections[3], respectively, for a given Chapman ionosphere, have yielded numerical estimates for various assumed model atmospheres as a function of elevation angle. These estimates are summarized in Figs. 28–33.

Fig. 28 shows the variations in the range correction due to fluctuations of one order of magnitude in the maximum electron density. These corrections vary directly and linearly with the electron density and are the greatest variations in the corrections. The tropospheric range correction is superimposed for comparison purposes.

Fig. 29 shows the variations in the range correction due to changes in scale height, i.e., variations in temperature.

[3]The range corrections are in meters, and angular corrections are given in microradians (1 μrad ≈0.2 sec)

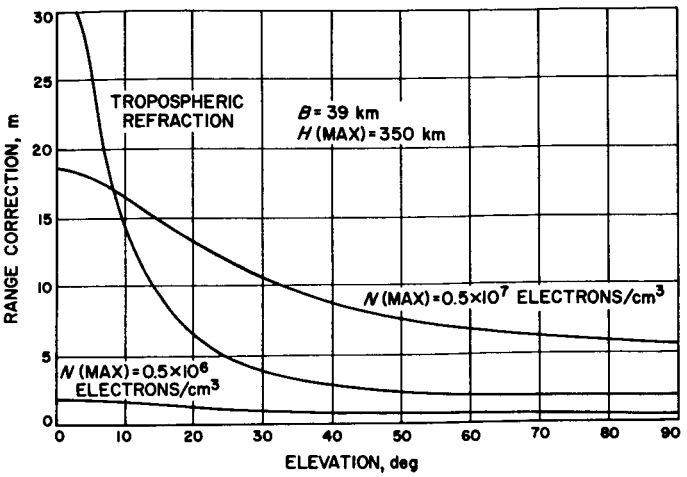


**Fig. 28. Range correction as a function of electron density**

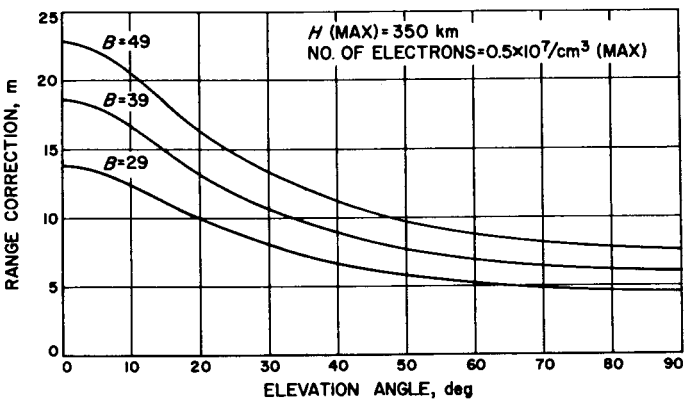


**Fig. 29. Range correction as a function of scale height**

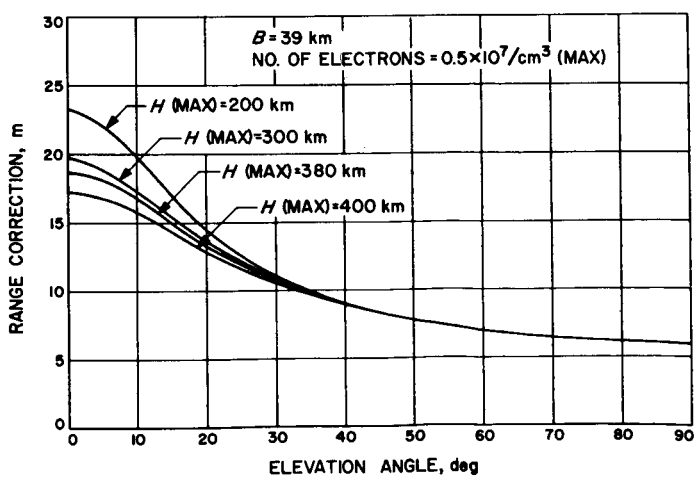


**Fig. 30. Range correction as a function of HMAX**

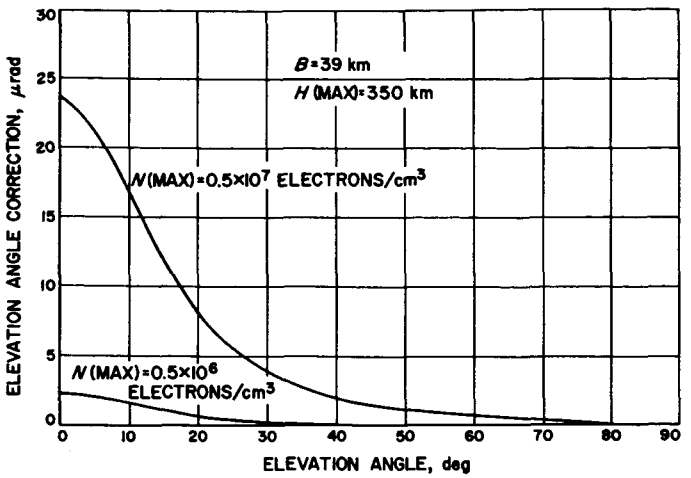


**Fig. 31. Elevation angle correction as a function of electron density**

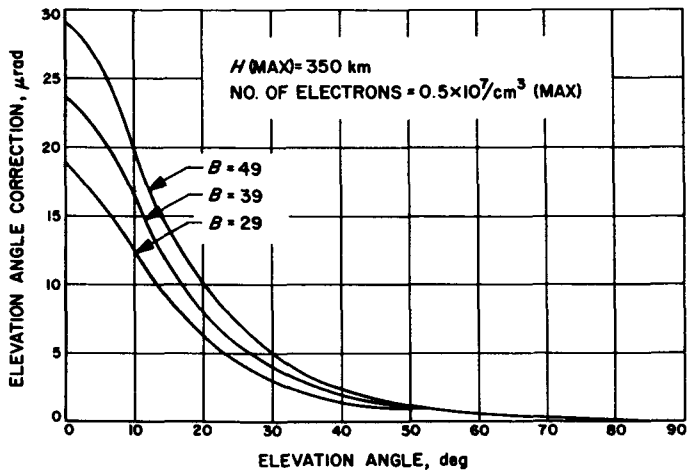


**Fig. 32. Elevation angle correction as a function of scale height**

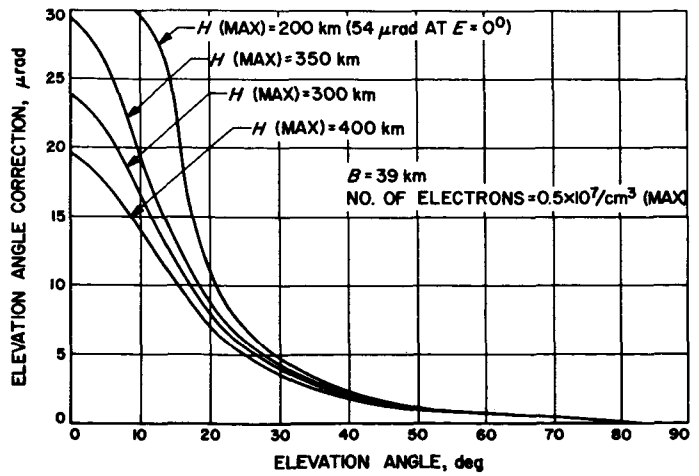


**Fig. 33. Elevation angle correction as a function of HMAX**

These changes produce the next greatest variations in the range corrections.

Fig. 30 shows the changes in the range correction due to variations in the height of maximum electron density (HMAX). HMAX will vary from 200 to 400 km during a day, and the curves illustrate the fact that the range corrections are relatively insensitive to changes in HMAX.

Figs. 31–33 show the angular corrections for the same set of parametric fluctuations. They may be summarized by saying that for the most part the corrections are on the order of 5″ of arc. The largest correction of this set is 12″ of arc (Fig. 33). From these curves, it appears that angular corrections are not important enough to warrant further study, other than the manner in which they interact with the range corrections.



## G. *Apollo* Project Support

*D. W. Curkendall*

The task reported here has as its objectives to provide the systems analysis effort to support the development of Unified S-band to be used in the *Apollo* program, to develop the capability of participating in the *Apollo* S-band qualification tests, and to assist the Manned Spaceflight Center (MSC) and Goddard Spaceflight Center (GSFC) in the planning and execution of the navigation aspects of the *Apollo* lunar landing mission. Specific items under this task will be selected each report period for further discussion.

The *Apollo* task includes, but only partially funds, items reported under Tracking and Navigational Accuracy found elsewhere in Sect. II of this volume. In Sects. H and I, D. Curkendall contributes two articles concerning the doppler data noise model and its relation to orbit accuracy. In the first of these, the influence of the oscillator stability on the data is analyzed assuming that the oscillator generates white frequency noise. Both two- and three-way doppler are investigated and it is shown that while the oscillator frequency noise is impressed directly onto the three-way data, a transformation to colored phase noise takes place when considering the two-way

configuration. The importance of this difference is discussed.

In the second article, an uncorrelated phase noise doppler model is applied to the three-dimensional navigation problem first analyzed by Hamilton and Melbourne using the white frequency noise model in *SPS 37-39*, Vol. III, pp. 18–23. The results obtained, which indicate a significant increase in accuracy over those obtained by Hamilton and Melbourne, are related to the oscillator error source equations and it is shown that the information content in a single pass of doppler data is inversely proportional to the round-trip light time to the probe when oscillator noise is the dominant error.

Also found in Sect. J is a paper entitled "Orbit Determination of Two Spacecraft Through the Use of Multiple Link Tracking Data." As the title implies, the article is a study of the navigational accuracy resulting when multiple-link doppler is obtained by coherently transmitting from the Earth to the first spacecraft, to the second, and finally back to the Earth. Three examples of performance are discussed.

The first example analyzes a direct LEM ascent to a rendezvous with the CSM. It is found that the addition of the multiple link data results in an orbital accuracy improvement of a factor of five over that using two- and three-way doppler alone. This is thought to be a marginal improvement considering the difficulty involved. However, if the three-way data is deleted, the improvement factor is approximately 50, suggesting that multiple-link data can supplant the function of three-way data for a rendezvous at interplanetary distances.

The second example analyzes the case of tracking a spacecraft which is behind the Moon using a lunar communications satellite as a coherent relay for the tracking signal. It is seen that entirely adequate orbital estimates can be obtained before direct contact is made with the spacecraft.

The final case examines the tracking of a released capsule-lander and its parent spacecraft for an interplanetary mission. It is found that the multiple link data cannot establish the orbits of the two spacecraft much better than two-way data alone at least in the time span 9 days to 1 day from encounter when the probes are experiencing nearly rectilinear motion. The *relative* orbits, however, are found to be precisely determined if the interspacecraft link is added.



# H. The Influence of Oscillator Instability on Orbit Accuracy

D. W. Curkendall

## 1. Introduction

In previous issues of this *Summary*, the ability of doppler tracking data corrupted by stationary-phase (bounded-range) errors to determine the radial velocity of a spacecraft was investigated. In *SPS 37-38*, Vol. III, pp. 20–24, the assumption was made that the noise consisted of white phase jitter; in *SPS 37-39*, Vol. III, pp. 30–34, this assumption was relaxed and the case of exponentially correlated noise was treated. Many of the error sources present in a doppler tracking system conform very well to this simple model and the results derived can be very useful in assessing the importance of such errors as counter truncation (*SPS 37-38*, Vol. III, pp. 8–13), atmospheric scintillation, and RF loop phase jitter. An error source of particular importance and whose noise characteristics contain significant departures from the simple models treated before is the frequency drift inherent in the master oscillator in the tracking station.

This article derives the statistical properties of the noise impressed on the data assuming that the frequency spectrum of the oscillator is flat. Both two-way (coherent) and three-way (non-coherent) tracking modes are considered. As before, application of the resulting noise model will be made to a simple one-dimensional tracking problem where it is desired to determine the velocity of a probe receding radially from the tracking station.

## 2. Noise Model for Two-Way (Coherent) Doppler

Figure 34(a) depicts a convenient visualization of a two-way doppler tracking system. The frequency transmitted is the sum from two oscillators; one whose output is a perfectly stable $f_0$, and a second noise generator whose output is time-dependent, or $f_\varepsilon(t)$. For this analysis, it is assumed that the spectrum of $f_\varepsilon$ is flat; i.e.,

$$E\,[f_\varepsilon(u)f_\varepsilon(v)] = \sigma_f^2\ \delta(u - v) \qquad (1)$$

where $E\,[\ ]$ denotes the expected value of $[\ ]$ and $\delta$ is the Dirac delta function. This sum frequency is transmitted to the spacecraft and returns $\tau$ seconds later, translated an amount proportional to the range-rate, $\dot{\rho}$, of the spacecraft. Upon return, the signal is beat with the current transmitter frequency as shown. Difference frequencies are then integrated producing range change data, $\Delta\rho$, and noise.

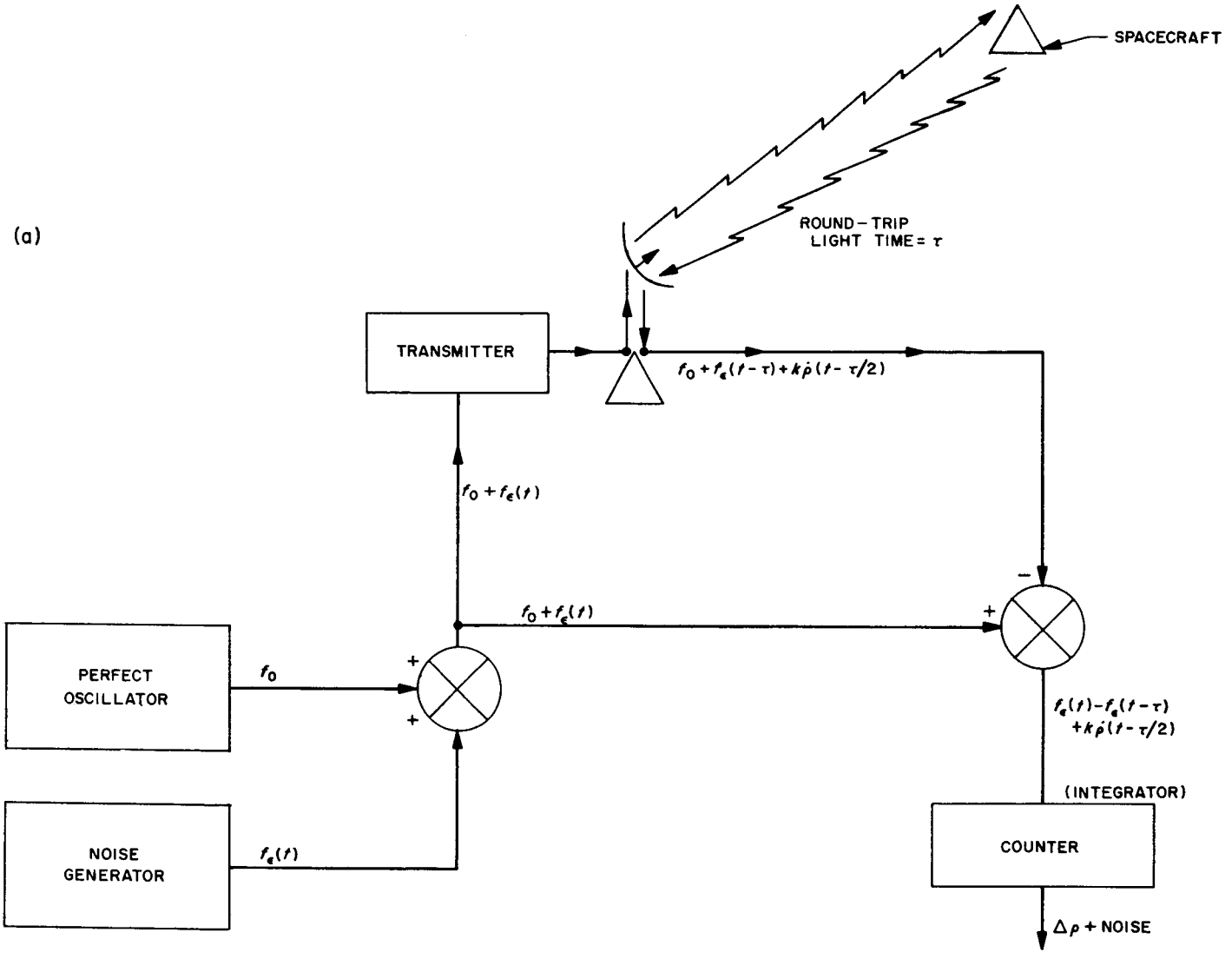


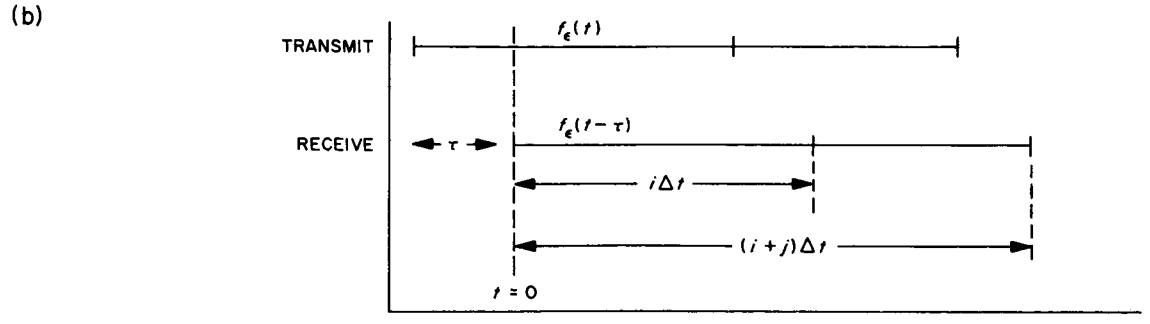


**Fig. 34. Simplified two-way coherent doppler measurement system**

Suppose we are taking a counter reading every $\Delta t$ seconds and treating the sequence of readings so obtained as the data vector (this is the total-count data-taking scheme discussed in *SPS* 37-38, Vol. III, pp. 20–24). Then, from Fig. 34(b) the error in the $i$th measurement is:

$$C_i = \int_0^{i\Delta t} f_\varepsilon(t) - f_\varepsilon(t-\tau)\,dt = \int_0^{i\Delta t} f_\varepsilon(t)\,dt - \int_{-\tau}^{i\Delta t-\tau} f_\varepsilon(u)\,du \tag{2}$$

then with the restriction that $i\Delta t \geq \tau$

$$C_i = -\int_{-\tau}^{0} f_\varepsilon(t)\,dt + \int_{i\Delta t-\tau}^{i\Delta t} f_\varepsilon(t)\,dt \tag{3}$$

Note that the left-hand term is not dependent on $i$ and will be present in all measurements on a single pass of data. It is thus possible to treat this term as a constant, subject to estimation; thus, we will re-define the $i$th error:

$$\xi_i = C_i - K = \int_{i\Delta t-\tau}^{i\Delta t} f_\varepsilon(t)\,dt \tag{4}$$

We may also compute the auto-covariance between the $i$th and the $(i+j)$th errors as:

$$E\,[\xi_i \xi_{i+j}] = E\left\{\int_{i\Delta t-\tau}^{i\Delta t} f_\varepsilon(u)\,du \int_{(i+j)\Delta t-\tau}^{(i+j)\Delta t} f_\varepsilon(v)\,dv\right\} \tag{5}$$

Interchanging the ordering of integration and the expectation operation and employing Eq. (1)

$$E\,[\xi_i \xi_{i+j}] = \sigma_f^2 \tau\left[1 - \frac{|j|\,\Delta t}{\tau}\right] \quad \text{for } |j|\,\Delta t \leq \tau$$
$$= 0 \quad \text{for } |j|\,\Delta t \geq \tau \tag{6}$$

In particular when $j = 0$

$$E\,[\xi_i^2] = \sigma_f^2 \tau \tag{7}$$

Fig. 35 illustrates the normalized auto-correction function obtained from Eq. (6), and assuming $j$ a continuous variable. Note that Eq. (7) shows the variance of the error to be stationary and not an increasing function with $i$.

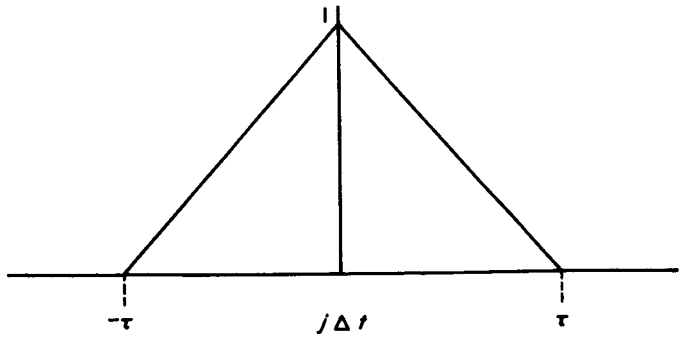


**Fig. 35. Normalized autocorrelation function for two-way coherent doppler**

### 3. Noise Model for Three-Way (Non-Coherent) Doppler

In the three-way configuration, the essential change from Fig. 34(a) is that a second oscillator is used to difference the incoming doppler signal. Thus, assuming that there is no unknown bias between the two oscillators, the error in the $i$th measurement is written:

$$C_i = \int_0^{i\Delta t} f_{1_\varepsilon}(t) - f_{2_\varepsilon}(t-\tau)\,dt \tag{8}$$

where the 1 and 2 subscripts refer to the independent oscillators. Then:

$$E\,[C_i\,C_{i+j}] = E\left\{\int_0^{i\Delta t}\int_0^{(i+j)\Delta t} (f_{1_\varepsilon}(u) - f_{2_\varepsilon}(u))\,(f_{1_\varepsilon}(v) - f_{2_\varepsilon}(v))\,du\,dv\right\}$$
$$= 2\sigma^2 i\Delta t \qquad j \geq 0$$
$$= 2\sigma_w^2 (i+j)\Delta t \qquad j \leq 0 \tag{9}$$

It is readily seen that the variance of the error grows linearly with time as contrasted with the stationary error found to be present in the previous case. For subsequent analysis, it will prove convenient to also obtain the statistics assuming that the data will be processed after differencing each counter reading with the previous readout and dividing the result by $\Delta t$, i.e.:

$$y_i = \frac{\Delta\rho_i - \Delta\rho_{i-1} + C_i - C_{i-1}}{\Delta t} \tag{10}$$

where the subscript $i$ refers to the $i$th measurement.

The statistics on the error

$$\mathcal{E}_i = C_i - C_{i-1}/\Delta t$$

are easily computed.

$$= \frac{1}{\Delta t^2} E \left\{ \int_{(j-1)\Delta t}^{j\Delta t} \int_{(i-1)\Delta t}^{i\Delta t} f_{1_\varepsilon}(u) f_{2_\varepsilon}(v) - f_1(v) f_2(u-\tau) - f_{1_\varepsilon}(u) f_{2_\varepsilon}(v-\tau) + f_{2_\varepsilon}(v-\tau)\, du\, dv \right\} \quad (11)$$

$$E[\mathcal{E}_i\, \mathcal{E}_j] = \frac{2\sigma_f^2}{\Delta t} \quad \text{if } i = j$$

$$= 0 \quad \text{if } i \neq j$$

The reader will now readily see the motivation for obtaining two equivalent descriptions of the three-way noise characteristics. By reverting to the differenced data type, we have obtained an uncorrelated model which will prove of distinct convenience when application is made to the tracking problem in Sect. 5.

## 4. Application of the Two-Way Model to a One-Dimensional Problem

Imagine that we are tracking a spacecraft moving radially from the station with constant but unknown speed $v$. The probe is tracked for $T$ seconds, and the integrated doppler is read-out every $\Delta t$ seconds for a total of $N$ measurements ($N\Delta t = T$). For two-way coherent tracking, the errors, $\xi_i$, in the measurements are described in Eq. (4). Relating the measurements, $y_i$, to the unknown velocity $v$ *and* the constant $K$ defined again by Eq. (4), we have:

$$\begin{bmatrix} y_1 \\ y_2 \\ \cdot \\ \cdot \\ \cdot \\ y_N \end{bmatrix} = \Phi = A \begin{bmatrix} v \\ K \end{bmatrix} + \xi \quad (12)$$

where $A$ is the partial derivative matrix of the $y$'s with respect to $v$ and $K$, i.e.,

$$A^T = \begin{bmatrix} \Delta t, & 2\Delta t, & \cdots & \cdots & \cdots & N\Delta t \\ 1, & 1, & \cdot & \cdot & \cdot, & 1 \end{bmatrix} \quad (13)$$

If $\Delta t > \tau$, then

$$E[\xi\, \xi^T] = \sigma_f^2\, \tau I = \Lambda_\varepsilon$$

where $I$ is the $N \times N$ identity (14)

If the data is then used to determine $v$ and $K$ and a minimum variance (MV) estimate is formed, the covariance ($2\times2$) of the errors in the estimate is given by

$$\Lambda_{v,K} = (A^T \Lambda_\varepsilon^{-1} A)^{-1} \quad (15)$$

This description of the problem is identical to that presented in *SPS 37-38*, Vol. III, pp. 20–24, which assumed that the noise on the data consisted of white phase errors in the read-out of the range-change. The one difference is that the phase error having variance $\sigma^2$ is replaced here by the term $\sigma_f^2 \tau$. We may quote the results of this reference directly then, and it is found that the variance of the error in the estimate of $v$ (we are not directly interested in how well we may determine $K$) is given as

$$Q(N) = \frac{12\sigma_f^2\, \tau N}{T^2(N^2-1)} \quad (16)$$

which for large $N$

$$Q(N) = \frac{12\sigma_f^2\, \tau}{T^2 N}$$

These results do not include the a-priori knowledge on $K$ (which is easily computed as $\sigma_{v_0}^2 \tau$); if this is included, we have:

$$Q(N) = \frac{12\sigma_f^2\, \tau N}{T^2(N+1)(N+2)} \quad (17)$$

which has the same asymptotic behavior as Eq. (14).

These results underscore the first important conclusion: *If the interval between samples is greater than the round-trip light time, the error variance in the estimate goes inversely with the number of samples. Moreover, the sample errors are uncorrelated producing a diagonal noise matrix (Eq. 14) and the MV estimate is easily formed.*

***Increasing the sampling density.*** If, in the above, $\Delta t < \tau$ it is no longer true that the noise co-variance matrix is uncorrelated and we have no previous analysis to quote in order to specify the error variance. In order to see the effect of sampling at a higher rate than once per round-trip light time, it is convenient to pick a single interval of $\tau$ and vary the number of samples taken in

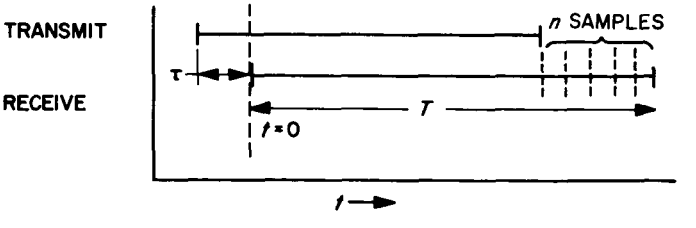


**Fig. 36. Observation schedule for high-density sampling**

that one-interval. Fig. 36 depicts the observation schedule which calls for measurements at

$$T,\ T-\frac{\tau}{n},\ T-\frac{2\tau}{n},\ \cdots,T-\frac{(n-1)\tau}{n}$$

or a total of $n$ measurements within this single $\tau$ interval. Here the small $n$ is to be differentiated from the total of $N$ samples for the entire data span.

Formulating the problem in this matter, the correlation between $\xi_i$ and $\xi_j$ is easily computed

$$E\left[\xi_{in}\xi_{jn}\right] = E\left\{\int_{T-\frac{i\tau}{n}}^{T+\tau-\frac{i\tau}{n}} f_\epsilon(u)du \int_{T-\frac{j\tau}{n}}^{T+\tau-\frac{j\tau}{n}} f_\epsilon(v)dv\right\} \tag{18}$$

$$= \sigma_f^2 \tau\left[\frac{n-(j-i)}{u}\right]$$

Using (18), the $n \times n$ covariance matrix of observation noise is given by:

$$\Lambda_\epsilon = \frac{\sigma_f^2 \tau}{n}\begin{bmatrix} n & n-1 & n-2 & \cdots & 1 \\ & n & n-1 & \cdots & 2 \\ \text{Symmetric} & & n & \cdots & 3 \\ & & & & \vdots \\ & & & & n-1 \\ & & & & n \end{bmatrix} \tag{19}$$

In order to form a MV estimate with these data, we have need of the inverse of this matrix. It is easily seen to be:[1]

$$\Lambda_\epsilon^{-1} = \frac{n}{\sigma_f^2 \tau}\begin{bmatrix} \frac{(n+2)}{(n+1)2} & -\frac{1}{2} & 0 & 0 & \cdots & 0 & \frac{1}{2(n+1)} \\ -\frac{1}{2} & 1 & -\frac{1}{2} & 0 & \cdots & & 0 \\ 0 & -\frac{1}{2} & 1 & -\frac{1}{2} & & & \vdots \\ 0 & & & & & & \\ \vdots & & & & & & \\ 0 & & & & & 1 & -\frac{1}{2} \\ \frac{1}{2(n+1)} & \cdots & & & & -\frac{1}{2} & \frac{(n+2)}{2(n+1)} \end{bmatrix} \tag{20}$$

This expression is valid for $n > 3$, the inverse for the $2 \times 2$ and $1 \times 1$ are of course easily computed directly.

[1] The author wishes to thank C. B. Solloway for obtaining the inverse of Eq. (19).

For simplicity, let us now assume that the constant $K$ has been sufficiently well-determined (from the rest of the data, perhaps) so that we may drop it from the estimate list and form a one-dimensional estimate of $v$. The $A$ matrix in Eq. (14) is now given by:

$$A^T = \left[T, T - \frac{\tau}{n}, T - \frac{2\tau}{n}, \cdots\cdots, T - \frac{(n-2)\tau}{n}, T - \frac{(n-1)\tau}{n}\right]$$

Inserting these expressions into (13) and performing the indicated summations, the final result becomes

$$= \frac{\sigma_f^2\ \tau}{T^2} \qquad \text{for } n = 1$$

$$\Lambda_v = Q(n) = \frac{9\sigma_f^2\ \tau}{4(3T^2 - T\tau)} \qquad \text{for } n = 2$$

$$= \frac{\sigma_f^2\ (n+1)}{n\ [2T^2 - 2T\tau + \tau^2] + 2T\tau - \tau^2} \quad \text{for } n \geqslant 3 \tag{21}$$

For $T >> \tau$, the general form of (21) reduces to

$$Q(n) = \frac{\sigma_f^2\ \tau(n+1)}{2T^2 n} \qquad \text{for } T >> \tau \tag{22}$$

and for large $n$

$$Q(n) = \frac{\sigma_f^2 \tau}{2T^2} \quad \text{for } T >> \tau \text{ and large } n \tag{23}$$

Comparing (23) and (21a), we see that as $n \to \infty$, the error variance reduces by only a factor of 2 over that obtained for $n = 1$. Thus, we reach the 2nd important conclusion: *Sampling faster than the round-trip light time brings but marginal improvement to the orbit estimate. Moreover, the noise covariance matrix is no longer diagonal and the MV estimate is difficult to form.*

## 5. Application of the Three-Way Model

In applying the three-way noise model to the same one-dimensional problem, it is convenient to assume the data type used is the differenced doppler (11) whose noise model is specified by (12). Thus,

$$\mathbf{y} = Av + \mathcal{E}$$

where $A^T = [1, 1, 1 \cdots, 1]$

and

$$E\left[\mathcal{E}\mathcal{E}^T\right] = \frac{2\sigma_t^2}{\Delta t} I$$

Application of (15) results in the mean-squared uncertainty in $v$:

$$Q(n) = \frac{2\sigma_f^2}{\Delta t N} = \frac{2\sigma_f^2}{T} \tag{24}$$

Eq. (24) is to be contrasted with (17) which shows the variance goes as $\tau/T^2N$. *Thus it is seen that the lack of coherence in the three-way data dramatically increases the effects of the oscillator instability.*

## 6. Concluding Remarks

The characteristics of the noise impressed on the doppler data have been obtained assuming a flat frequency spectrum present in the station's master oscillator. The important results of this analysis have been underscored in the main body of text and will not be repeated here. Although the models used are simple ones, it is argued that these conclusions apply to more complex circumstances. Found elsewhere in this volume is a second article contributed by the author which applies the bounded-range error model to a three-dimensional tracking problem first analyzed by Hamilton and Melbourne in *SPS 37-39*, Vol. III, pp. 18–23.



# I. Application of a Bounded Range Error Model to the Evaluation of the Information Content of a Single Pass of Doppler Data

D. W. Curkendall

## 1. Introduction

In *SPS 37-39*, Vol. III, pp. 18–23, Hamilton and Melbourne presented an analysis determining the information content of a single pass of doppler data from a distant spacecraft. It was shown that the range rate of the probe with respect to the observing tracking station could be approximated by:

$$\dot{\rho} = \dot{r} + r_s\omega \cos\delta \sin\omega t + \omega t_0 r_s \omega \cos\delta \cos\omega t \tag{1}$$

where

$\dot{r}$ = average geocentric range-rate during the pass

$r_s$ = distance of the station from the Earth's spin axis

$\omega$ = Earth's rotation rate

$\delta$ = declination of the probe

$t$ = time measured from the expected time that the probe will cross the meridian of the station

$t_0$ = actual time of meridian crossing.

By making successive observations of $\dot{\rho}$ and performing a regression analysis using Eq. (1), estimates of $\dot{r}$, cos $\delta$, and $t_0$ (which is related to the probe's right ascension) are obtained. The original analysis assumed that the noise in the successive observations of $\dot{\rho}$ was white, gaussian, and of zero mean. Using this assumption, results concerning the accuracy obtainable in the estimated parameters were obtained without explicit reference to the system which secured the observations.

It is our purpose here to make an explicit focus on the measurement system used and perform a similar analysis employing the noise model used in *SPS 37-38*, Vol. III, pp. 20–24. It was argued in this reference that when tracking a spacecraft in the two-way coherent mode, the primary error sources are better characterized as white *range* (as opposed to range rate) errors. This argument is pursued further in a separate article in this *Summary*, and here it is shown that the frequency drift inherent in the station's master oscillator produces doppler errors conforming to this model if the time between successive samples is greater than the round-trip light time to the probe.

As in the original article, calculations of estimation accuracy are made and it is shown that the white range error model produces significantly better estimates of performance.

## 2. Regression Analysis

To facilitate the application of the bounded range error model, it is convenient to use the total counted doppler as the basic data type. That is, the doppler frequency is integrated by means of an electronic counter, and its current reading minus the reading at the start of the tracking period is the observable. This quantity is interpreted as the change in the station-probe range. Thus using the definitions:

$$a = \dot{r}$$

$$b = r_s \cos \delta$$

$$c = \omega t_0 r_s \cos \delta$$

and integrating Eq. (1)

$$\Delta\rho(t_i) = \int_{t_s}^{t_i} \dot{\rho}(t)\, dt = a(t_i - t_s) - b(\cos \omega t_i - \cos \omega t_s) + c(\sin \omega t_i - \sin \omega t_s) \qquad (2)$$

where $t_s$ is the start of pass, and $t_i$ the time of read-out at the $i$th data time. The $i$th data point then will be the range change plus noise:

$$d_i = \Delta\rho(t_i) + n_i - n_0 \qquad (3)$$

where the $n_0$ is an error common to all measurements and is interpreted as the initial phase error at the start of the pass (or alternately, as a combination of the initial phase error and the oscillator induced error common to all measurement, that was discussed in the preceding article, Sect. H).

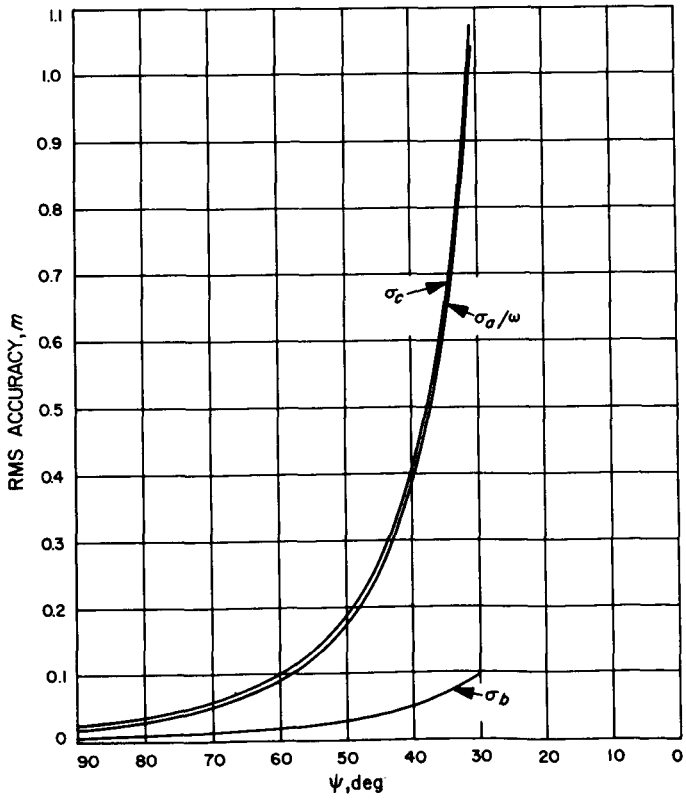


**Fig. 37. RMS estimation accuracy, $\sigma_a$, $\sigma_b$, $\sigma_c$ versus half-width of pass, $\psi$, for $\sigma_{\Delta\rho}$ = 0.06 m, 1-min samples**

Our objective is to determine the accuracy to which the constants $a$, $b$, and $c$ may be estimated if $n_i$ is assumed uncorrelated with $n_j$ and has stationary variance, $\sigma_{\Delta\rho}{}^2$. If a minimum variance estimate is performed, the covariance of uncertainty in the estimates is written

$$\Lambda = (A^T \Lambda_\varepsilon^{-1} A)^{-1} \tag{4}$$

where $A$ is the partial derivative of the data with respect to $t$ parameters to be estimated, and $\Lambda_\varepsilon$ is the covariance matrix of the noise on the data.

The $\Lambda_\varepsilon$ matrix is easily demonstrated to be diagonal if $n_0$ is treated as a parameter subject to estimation, thus making (4) a $4 \times 4$ matrix equation. Although we have no inherent interest in obtaining the value of $n_0$, formulating the problem in this manner greatly simplifies the computations:

We have

$$\Lambda^{-1} = A^T \Lambda_\varepsilon^{-1} A = \frac{1}{\sigma_{\Delta\rho}{}^2} A^T A =$$

$$\frac{N}{2\psi\sigma_{\Delta\rho}{}^2} \begin{bmatrix} \frac{8}{3}\frac{\psi^3}{\omega^2}, & -\frac{2}{\omega}(\psi \sin\psi - \psi^2\cos\psi), & \frac{2}{\omega}[(\sin\psi(2+\psi^2) - \psi\cos\psi], & \frac{2\psi^2}{\omega} \\ & \psi + \frac{\sin 2\psi}{2} - \psi\sin\psi\cos\psi + 2\psi\cos^2\psi, & -2[\sin^2\psi - \psi\sin\psi\cos\psi], & -2[\sin\psi - \psi\cos] \\ & & \psi - \frac{\sin 2\psi}{2} + 2\psi\sin^2\psi, & 2\psi\sin\psi \\ \text{Symmetric} & & & 2\psi \end{bmatrix} \tag{5}$$

where $\psi$ is the half-width of the pass (in degrees of Earth rotation), and $N$ is the number of measurements taken. Eq. (5) was written assuming that $N$ was large and that the indicated summations in $A^T A$ could be replaced by integrals. This equation is not conveniently inverted analytically; the dependence on $N$ and $\sigma_{\Delta\rho}$ can, however, be isolated from $\psi$, and Eq. (4) can be re-written as:

$$\Lambda = \frac{2\sigma_{\Delta\rho}{}^2}{N} \psi P(\psi) \tag{6}$$

Eq. (6) was solved numerically, and the results are plotted in Fig. 37. For this computation, it was assumed that data was obtained at the rate of 1 sample/min, and $\sigma_{\Delta\rho}$ was taken as 0.06 m (this is equivalent to the 0.001 m/sec figure used in *SPS* 37-38, Vol. III). Fig. 37 is to be compared to Fig. 36 in the original article, Sect. H. Note that the change to a bounded range error model results in an estimated accuracy improvement of approximately a factor of 50 for an entire pass of data ($\psi = 90$ deg).

As shown, for $\psi = 90$ deg, the following accuracies are obtained:

$$\sigma_{a/\omega} = 0.020 \text{ m}$$

$$\sigma_b = 0.007 \text{ m}$$

$$\sigma_c = 0.026 \text{ m}$$

### 3. Interpretation of Results

The numerical results quoted assume a sample rate of 1/min. Eq. (6) indicates that sampling at higher rates will result in even increased accuracy estimates by a factor of $1/N^{1/2}$, because $\sigma_{\Delta\rho}$ is assumed not to be a function of the sample spacing. As an aside, the original article derived a similar error variance equation proportional to $\sigma_{\dot\rho}^2/N$, but left concealed by this equation alone is the factor that $\sigma_{\dot\rho}^2$ is proportional to the sample rate when using the assumption of uncorrelated range rate noise. Thus the results quoted in the *SPS 37-38*, Vol. III, are insensitive to $N$ as long as it is large.

The formulation here, however, gives rise to the unrealistic result that we may drive the error variance to zero by simply taking samples at a fast enough rate. In order to keep the model realistic, let us assume that the data noise is entirely produced by the high-frequency drift in the oscillator and draw upon the result of the previous article (Sect. H) which shows that the data are uncorrelated only if the sample time is greater than the round-trip light time to the probe. Thus we must restrict $N$ to be

$$N_{\max} = \frac{2\psi}{\omega\tau} \tag{7}$$

where $\tau$ is the round trip light time. In addition, it has also been shown that the variance of the incremental range error is:

$$\sigma_{\Delta\rho}{}^2 = \sigma_f^2\,\tau \tag{8}$$

where $\sigma_f$ is a measure of the oscillator's performance. Substituting (7) and (8) into (6) we obtain

$$\Lambda = \frac{2\sigma_f^2\,\tau^2}{\omega} P(\psi) \tag{9}$$

Thus, we see that the performance degrades linearly with $\tau$, and Fig. 37 is reinterpreted to be the results obtainable for a 1-min light time and an oscillator whose rms frequency departure $\Delta f/f$ is approximately $5 \times 10^{-11}$ for a 1-sec averaging time. As an example, for a probe distance of 1 AU, the numbers given would be increased by a factor of 17.

The use of the estimates of $a$, $b$, and $c$ to obtain $\dot r$, $\delta$, and $r_s$, and the relationship between these estimates and errors in station longitude and Universal Time were discussed in the reference and will not be repeated here.

It should be cautioned, however, that the estimation procedure implied by this analysis is very sensitive to modeling errors or omissions. We have assumed that we can measure the *range change* to 0.06 m, a figure that is below our current knowledge of ionospheric effects and is probably below the perturbations on the spacecraft due to random non-gravitational forces. This assumption is to be contrasted with that made in the reference which implied that at any time during the pass the *velocity* could be measured to 0.001 m/sec accuracy.

As a final comment, it is noted that in order to achieve the accuracies quoted, continuous RF lock must be maintained with the spacecraft throughout the pass. In practice, each time lock is lost and then regained, a new $n_0$ is created and its estimation must be re-initiated. This (even assuming the data loss to be negligible) will degrade the estimation performance. In the limit, if lock is lost between each sample, the situation will revert to that characterized by independent range-rate noise, and the analysis of the reference applies.



## J. Orbit Determination of Two Spacecraft Through the Use of Earth-Based Multiple-Link Doppler Tracking Data

D. W. Curkendall

### 1. Introduction

The high accuracy of Earth-based doppler tracking data and its ability to produce precision orbits for a wide spectrum of lunar and planetary missions is well known and has recently been discussed in several *SPS* articles. In certain future missions, involving more than one spacecraft (or a spacecraft and a capsule), it may be useful to extend the basic concept of two-way doppler, i.e., tracking station to spacecraft to tracking station, to include an additional spacecraft-to-spacecraft link. With this scheme, provisions are made to transmit the received signal from the first vehicle to the second before its return to Earth. Phase coherence with the original transmission is maintained in all three links and, upon its return to the tracking station, the signal would contain a doppler shift proportional to the algebraic sum of the three relative range rates involved:

$$d = \dot\rho_{s1} + \dot\rho_{12} + \dot\rho_{2s} \tag{1}$$

where $s$ refers to the station, and the numbers identify the two spacecraft.

The qualitative motivation for such a data type is that orbital elements which are unobservable from Earth, or that are observed so obliquely as to be poorly determined, may come solidly into view. Of course, there is nothing new in the notion of spacecraft-to-spacecraft doppler links; the performance of these measurements from an Earth-based system, however, would seem to offer the important benefits of increased accuracy with a minimum of complexity of the on-board equipment. This article explores the utility of obtaining such a data type by constructing three navigation problems, each involving two spacecraft, and calculating the resultant navigation accuracy using the inter-spacecraft link as a data type.[1]

## 2. Numerical Results: Three Examples

The numerical results presented in this section were obtained from a computer study program specifically constructed to analyze the ability to determine the orbits of two vehicles simultaneously when data is available which relates to the state of both vehicles.[1]

In this program, the capability to obtain five different data types at each of a series of data times was mechanized; two of these data types have an associated bias. The five data types are

(1) Two-way doppler from Spacecraft No. 1.

(2) Two-way doppler from Spacecraft No. 2.

(3) Three-way doppler from Spacecraft No. 1 (this data type has a bias associated with it).

(4) Three-way doppler from Spacecraft No. 2 (with a bias).

(5) Multiplier-link (or stereo) doppler from the Station to Spacecraft No. 1, to Spacecraft No. 2, and back to the Station.

All of the physical constants, including the station locations, were considered known. Because of this, these numerical results may not be taken too literally; the comparisons, however, of the relative power of the different data configurations should be valid.

[1]For a description of the mathematical development involved, the reader is referred to AAS preprint 66-110, a paper having the same title as this article which is to be published in *Advances in the Astronautical Sciences*.

## 3. A Rendezvous Problem, Example 1

The first example treats a rendezvous situation and, for illustration, the trajectories used were taken from an *Apollo* mission profile of direct Lunar Excursion Module (LEM) ascent to the Command and Service Module (CSM). Fig. 38 shows the basic geometry and tracking pattern. Ref. 27 was the source for and describes in detail the trajectory used, but briefly the LEM rises from approximately zero degrees latitude and longitude and injects into a slightly elliptical orbit of 1820-km semi-major axis. The CSM is in a well-established circular lunar orbit of 1886-km semi-major axis. The orbits have nearly zero degrees inclination relative to the lunar equator and are inclined with respect to one another by 0.5 deg. From LEM injection, the two vehicles are co-visible to one another and the Earth for about 30 min before LEM occultation. Rendezvous occurs some 52 min

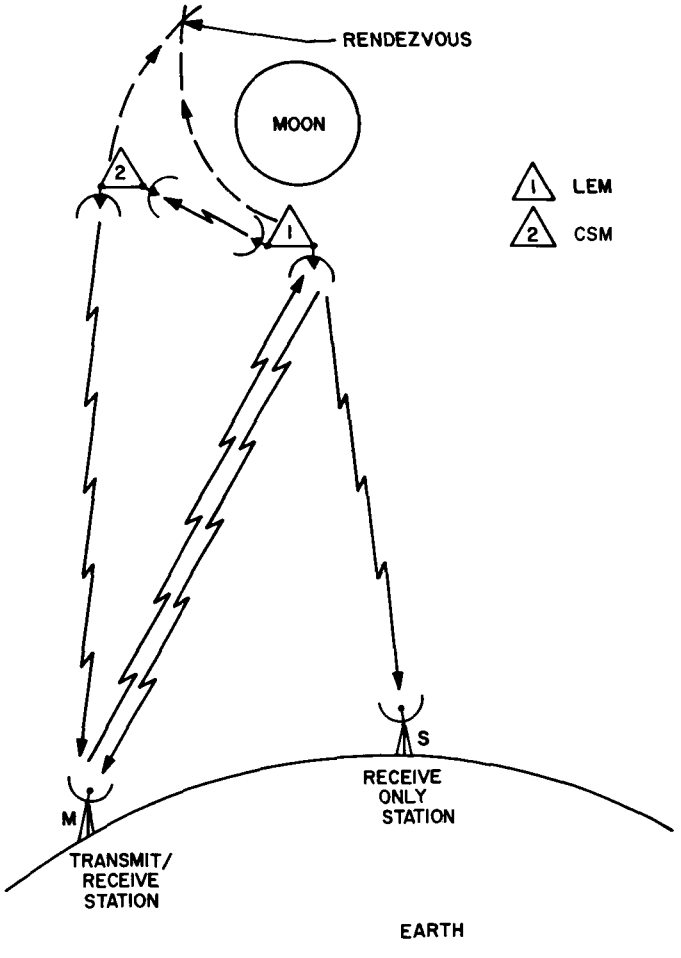


**Fig. 38. Basic geometry and tracking pattern, including inter-spacecraft doppler links for a rendezvous situation**

after LEM injection as a point in space not visible from the Earth. For simplicity, it was assumed that no mid-course maneuvers, interrupting the tracking and corrupting the orbit, were performed.

For the basic case, data types 1 to 5 were used, and then a second case for comparison was run omitting the stereo data. The two-way tracking originates from the Madrid station, and the Ascension Island station was used to obtain three-way data. These were picked to effect a large latitude difference between the stations, which is the direction found by Ref. 27 to be the more critical for tracking low-inclination lunar orbits. The noise on the doppler was assumed to be 0.03 m/s for 1-min samples, a highly conservative number based on present experience but used to offset the neglect in the uncertainties in the physical constants. The three-way data contain a bias arising from an unknown offset in the frequency of the oscillators in the master and slave tracking stations. This was taken as 0.03 m/s, representing an unknown offset of two parts in $10^{-10}$. The *a-priori* knowledge of the CSM orbit was assumed to be 1 km in position and 0.5 m/s in each of the three directions; the LEM's initial uncertainty was assumed to be 10 km in position and 1 km/s in velocity.

Fig. 39 plots the results from both of these cases. This figure shows the rms uncertainties in the prediction of the *difference* of the rendezvous conditions, both position and velocity, plotted as a function of tracking time. Although the relative performance between the two data configurations varies considerably over the time span considered, adding the stereo linkage improves the tracking accuracy significantly, if not spectacularly. After 29 min of tracking, the rms error in predicting both the final position and velocity is approximately reduced by a factor of 5.

The prediction accuracy of the LEM's absolute final position and velocity is not shown here, but after the full 29 min, the figures are 0.7 km and 0.6 m/s using the stereo linkage, and 1.5 km and 1.5 m/s without. Thus, a good portion of the factor of 5 shown on the graphs is realized, not by better absolute prediction capability, but by the ability of the spacecraft-to-spacecraft link to relate the two orbits in question to each other.

A second factor investigated was the effect of removing three-way doppler as a data-type from each of the two data configurations. The importance of the three-way doppler is that, similar to the stereo linkage, it affords

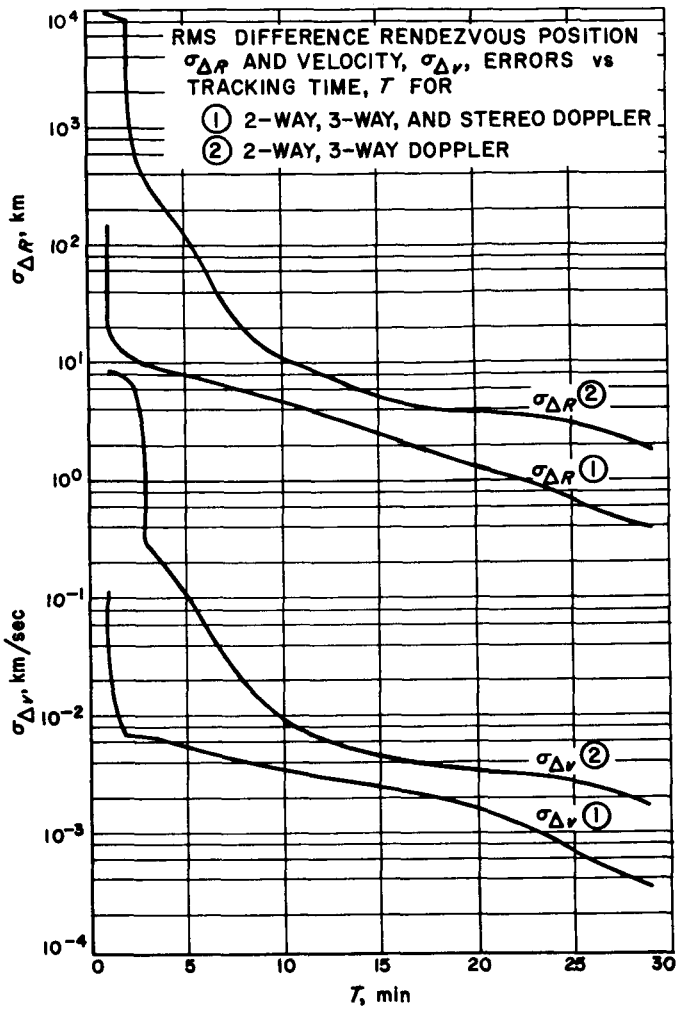


**Fig. 39. RMS rendezvous position and velocity errors**

the observer a second line-of-sight with which to view the orbit. The two tracking stations considered are displaced by 4500 km, which when viewing objects at lunar distance, results in pointing directions nearly 0.7 deg apart. The effect on the removal of this second line-of-sight is dramatically shown in Fig. 40, which plots the same information as before, except that no three-way doppler data are taken. The accuracy produced by two-way doppler alone increases to a final value of 21 km and 56 m/s. By way of contrast, the accuracy produced by the data configuration which includes the stereo linkage degrades but slightly to 0.5 km and 0.4 m/s. The implication is clear: at lunar distances, three-way doppler data are nearly as powerful as the more difficultly obtained multiple-link data and the performance gain is little more than nominal. At interplanetary distances, however, little parallax can be achieved by tracking from two Earth-bound stations; in this circumstance, obtaining

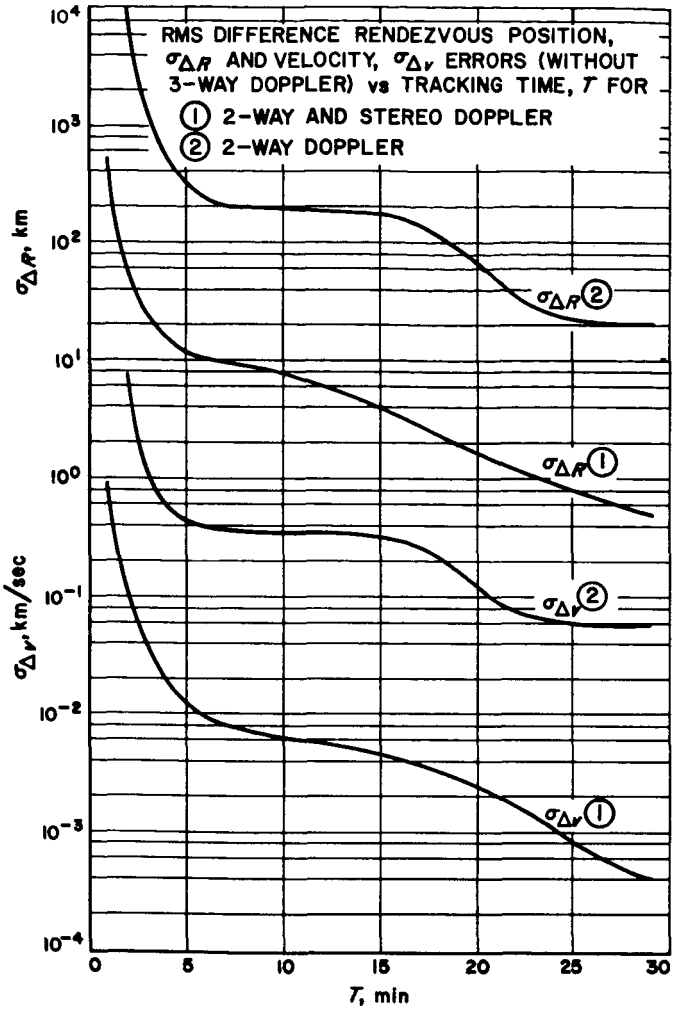


**Fig. 40. RMS rendezvous position and velocity errors without three-way doppler**

directly or indirectly inter-spacecraft range-rate data can easily supplant the function served by the three-way data.

### 4. *Tracking an Occulted Spacecraft, Example 2*

In our second example we shall use the same multiple-link concept to track and obtain navigation data from a spacecraft that is normally not visible to Earth-bound tracking stations. In this problem, we again borrow from the *Apollo* mission profile and inspect the ability to track the CSM/LEM just after de-boost into lunar parking orbit by means of a communications satellite in a well-established lunar orbit which is visible to both the Earth and the CSM.

As is shown in Fig. 41, the tracking station on the Earth broadcasts directly to the communications satellite, which in turn sends the received signal to the CSM; this

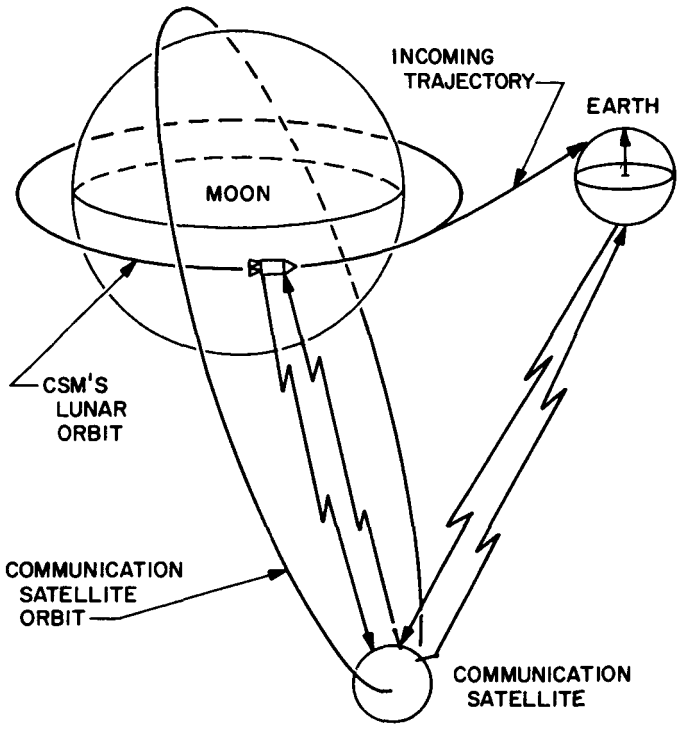


**Fig. 41. Tracking geometry for behind-the-Moon tracking**

is retransmitted back to the satellite and finally to the original station on Earth. The resulting doppler shift on the return signal can then be equated to:

$$d = 2\dot{\rho}_{sc} + 2\dot{\rho}_{cl} \qquad (2)$$

where $s$ is the station, $c$ is the communications satellite and $l$ refers to the CSM. This configuration could be used to monitor the de-boost maneuver itself, but this feature is not analyzed here. It was assumed that tracking commenced immediately after the end of the burn and continued for the approximately 30 min that the spacecraft was behind the Moon. The spacecraft is in a circular orbit lying nearly in the lunar equatorial plane and has an altitude of 150 km, as is specified by Ref. 27. The communications satellite was placed in an orbit inclined 45 deg to the lunar equator with the longitude of the descending node at the zero meridian. Its radius was two lunar radii, and at the start of tracking was at −90 deg longitude, −45 deg latitude. The relatively high inclination was specified in order that the out-of-plane components of the spacecraft's orbit would be clearly visible from the satellite. In this situation, only one data-type is possible, the modification of data-type 5, which is specified by Eq. (2). Again, data were taken at 1-min intervals, and it was assumed the measurements were corrupted by 0.03 m/s rms noise. The *a-priori*

knowledge of the initial position and velocity of the communications satellite was assumed to be 0.1 km and 0.05 m/s, respectively, in each of three axes. The corresponding numbers for the spacecraft were taken to be 10 km and 1 km/s.

In this problem, we are not interested in determining the relative orbits, as was the case in the rendezvous example, but in establishing the absolute orbit of the CSM/LEM combination. Fig. 42 plots the rms uncertainty in the three orbital elements of primary interest: (1) the semi-major axis, $a$, (2) the inclination, $i$, and (3) the radius of closest approach, $r_{ca}$.

It is seen that, after the end of 30 min, the uncertainties in these elements have been reduced to: $\sigma_a = 4.5$ km, $\sigma_i = 0.23$ deg, and $\sigma_{rca} = 17$ km. The $\sigma_{rca}$ is probably the most relevant of the three quantities plotted, for it is on the basis of the predicted closest approach altitude that a hypothetical *safe orbit* computation would be made. The performance shown for this quantity in Fig. 42 is not as good as perhaps could be desired, but the data

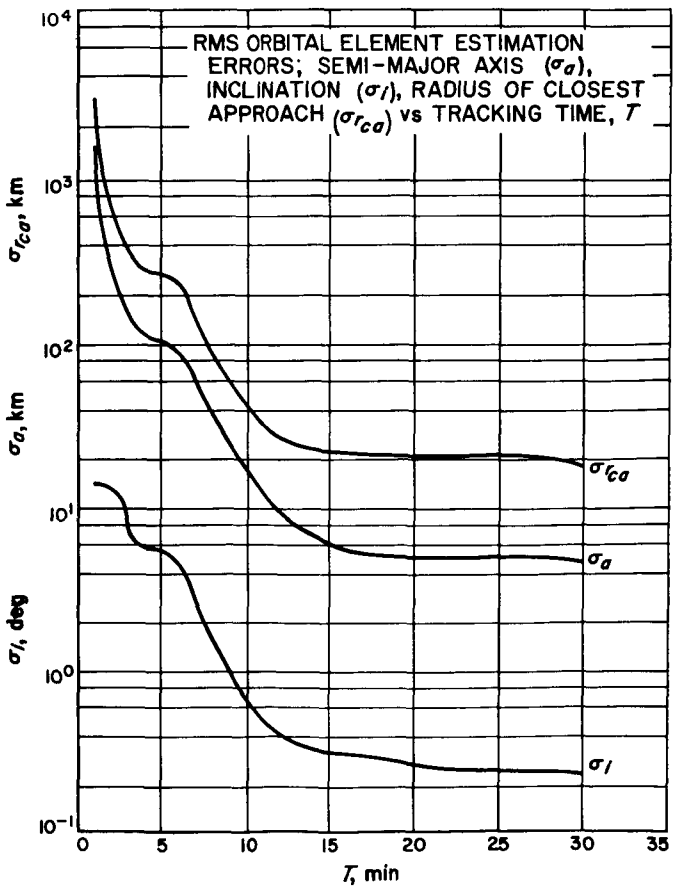


**Fig. 42. RMS orbital element estimation errors**

noise we have assumed is quite conservative and the *a-priori* uncertainty of the spacecraft's position is probably needlessly large. Even as computed, an adequate safe orbit decision could be made after 15 min of tracking.

It is interesting, for comparison, to assume for the moment that the Moon is transparent and that two-way tracking data from the spacecraft can be obtained. If 30 min of two-way data alone are processed, the resulting $\sigma_{r,ca}$ is 28 km, a factor of 1.6 larger than previously attained. This degradation occurs in spite of the fact that the communications satellite has an orbit nowhere near as precisely determined as is the location of the tracking station (in fact, it was assumed here that the station location is precisely known). The superior tracking geometry afforded by the satellite appears to more than compensate for its imprecise location and velocity.

If we now process both data-types, there is a dramatic reduction in $\sigma_{rca}$ to 0.25 km, illustrating the effectiveness, in general, of viewing an orbit from more than one tracking station. This also suggests that in the physically realizeable example, the orbit can be quickly determined very precisely as soon as the spacecraft becomes visible to the Earth.

## 5. An Interplanetary Bus/Capsule-Lander Problem, Example 3

The third and last example deals with a situation that might occur on an interplanetary mission, either to Mars or Venus. The specific situation analyzed is that the main spacecraft (or bus) is travelling on a trajectory that will fly by the planet Mars. At 10 days out from encounter, a capsule is split off from the bus and is placed on an impacting trajectory with the planet. At the time of capsule ejection, the orbit of the bus is imperfectly known and the capsule's orbit, which has the same position error, is further corrupted in velocity by the execution errors of the ejection. Both craft are to be tracked until 1 day from encounter, at which time definitive orbits of both will be determined.

For illustration, in this example, we shall capitalize on a feature of the multiple-link concept that has not been mentioned previously. Let us suppose that we are obtaining the three data types as previously listed, each of which is corrupted by noise:

$$d_1 = 2\dot{\rho}_{SB} + n_1$$
$$d_2 = 2\dot{\rho}_{SC} + n_2 \qquad (3)$$
$$d_5 = \dot{\rho}_{SB} + \dot{\rho}_{BC} + \dot{\rho}_{CS} + n_5$$

where $B$ and $C$ refer to the bus and capsule, respectively. If we now form a new data type from a linear combination of the first three, we may obtain:

$$d_n = d_5 - (d_1/2) - (d_2/2) = \dot{\rho}_{BC} + n_5 - 1/2(n_1 + n_2) \quad (4)$$

An analysis of the origin of the data noise will reveal that it is primarily composed of (1) uncorrected atmospheric effects and (2) instability of the oscillator in the tracking station.

It will be recognized that the signals used to obtain the three data types listed will traverse the same atmospheric path and have nearly the same propagation time. The major errors, and several others of less significance, will be nearly identical in all three sets of data; thus, Eq. (4) specifies a derived data-type equivalent to the inter-spacecraft range rate that should be unaffected by these major error sources. We shall use this technique, in this example, and assume that direct measurements of $\rho_{BC}$ are made which contain smaller errors than either of the two-way doppler measurements made to the bus and the capsule.

The bus was placed on a trajectory having a **B** distance of 8150 km;[2] the components **B**•**T** and **B**•**R** were 5480 and 6016 km, respectively. The components of the capsule were a **B**•**R** of 996 km and a **B**•**T** of 5926 km, which yields a trajectory inside the capture radius of 6350 km resulting from the specified hyperbolic excess velocity of 3.16 km/s. Starting at 1 day past capsule ejection, the data were taken at 1 sample/hr with an rms noise of 0.004 m/s (this is effectively the same figure used in the two previous examples: the noise is assumed to be inversely proportional to the square root of the integration time between samples) on the two-way measurements from the probe and the capsule. A noise ⅓ that figure was assumed on the $\dot{\rho}_{BC}$ measurement.

The *a-priority*, assumed on the bus injection conditions, was a pessimistic 1000 km in position and 1 m/s velocity, 1 $\sigma$, in each of the three axes. The capsule was given identical position uncertainties but positively correlated with a coefficient of 0.98. A unity correlation is more realistic, but the orbits were uncoupled somewhat in their *a-priori* position so that the subsequent navigation characteristics could better be studied. An additional 5 m/s velocity uncertainty was added to the capsule's *a-priority*, and this was loosely correlated with the velocity of the bus.

Fig. 43 shows the navigation accuracy results obtained, as a function of tracking time, from the two-way measurements alone and then inclusion of the stereo data. Plotted here are the uncertainties in the determination of the **B** vector,

$$\sigma_B = (\sigma^2_{\mathbf{B}\cdot\mathbf{R}} + \sigma^2_{\mathbf{B}\cdot\mathbf{T}})^{1/2}$$

for both the bus and the capsule. It is seen that the addition of a stereo link improves the knowledge of the target parameters of the bus by only a very small margin. Initially, the capsule's orbit is improved by the addition of $\dot{\rho}_{BC}$ data, in fact, the uncertainty falls by a factor of 3 and quickly becomes nearly identical to the bus uncertainty, but by the end of the 8 days of tracking, this gain has disappeared.

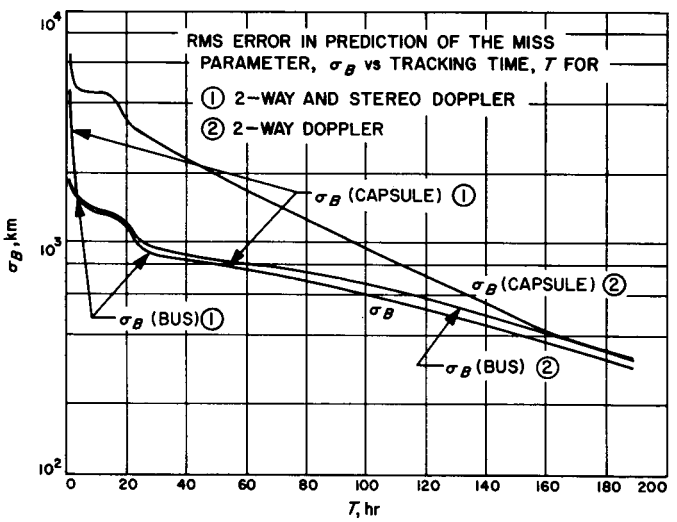


**Fig. 43. RMS error in prediction of the miss parameters**

Fig. 44 explains this behavior by plotting the rms difference errors in the estimation of the miss parameters, $\sigma_{\Delta B}$. Without the $\dot{\rho}_{BC}$ data, $\sigma_{\Delta B}$ falls to 300 km at the end of the tracking period; the corresponding figure using $\dot{\rho}_{BC}$ is 5 km, or a factor of 60 improvement. Even with only 2 days of tracking, the relative **B** estimation errors are only 70 km. Thus, the conclusion is reached that the inter-spacecraft link results in establishing the *relative* orbits of the two vehicles almost immediately even when the probes are experiencing rectilinear motion. Referring back to Fig. 43, the lower $\sigma_B$ on the capsule's absolute

[2] The **B** is the hypothetical vector from the center of the planet to the probe at closest approach assuming the planet has no mass. As such, **B** is perpendicular to the direction of the incoming asymptote, **S**. Normally **B** is broken into two components, **B** • **R** and **B** • **T** where **T** is a unit vector perpendicular to **S** and lying in the ecliptic plane and **R** is the unit vector which completes the **RST** orthogonal system.

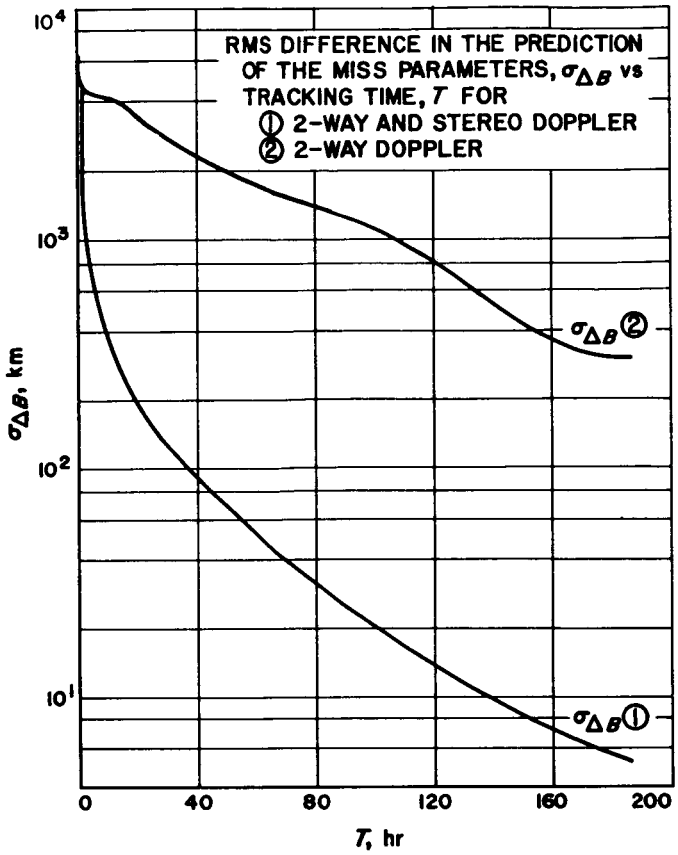


**Fig. 44. RMS difference in the prediction of the miss parameters**

orbit is achieved by *passing through* the well-determined bus to capsule orbit, the better knowledge of the orbit of the bus.

This leads us to observe that with an initially well-determined bus/capsule orbit, the capsule could be ejected and its new orbit quickly redetermined to the accuracy of the parent spacecraft.

## 6. Conclusions

On the basis of the three numerical examples presented, it may be concluded that establishing an inter-spacecraft doppler link can be very effective in determining the relative orbits of two vehicles. Even with otherwise very weak tracking geometry (Example 3), precise relative orbits can be determined with dispatch. In Example 1, the stereo data were found to be somewhat more powerful than three-way data at lunar distances. This was true even when the relative inclination between the two orbits was 0.5 deg; with larger relative inclinations one would expect a further improvement in the stereo data's ability to determine the out-of-plane components of the orbit.

However, it seems equally clear that, at least over short data arcs or in weak tracking geometry situations, the absolute orbits are not significantly improved with the addition of the multiple-link data. Thus, the usefulness of this, or related techniques, is only particularly attractive when: (1) the orbit of one vehicle is accurately known, (2) the objective of the tracking is to establish the relative orbits, as in Example 1, or (3) direct Earth-based tracking is unobtainable, as in Example 2.

*Acknowledgment.* The author is indebted to Dianne Wimp for providing the programming and computing support needed to obtain the numerical results presented in this article.



# K. *Pioneer* Project Support

*D. Curkendall*

The *Pioneer* Project consists of a series of probes whose purpose is to gather scientific information concerning the deep space environment in the region near the ecliptic plane and at a distance from the Sun varying from 0.8 to 1.2 AU. The DSN is committed to track the *Pioneer* spacecraft, obtain engineering and scientific telemetry, determine the orbit of each probe, and provide facilities within the SFOF and DSIF to the project for the conduct of the mission and reduction of data. Specific items under this task will be selected each reporting period for discussion in the *SPS*.

For this issue, Motsch, Chaney, and Curkendall have contributed an article (Section L) analyzing a sinusoidal periodicity discovered in the *Pioneer VI* doppler tracking data. It is found that this periodicity arises from a slight offset of the spacecraft antenna from the axis of rotation This phenomena is used to make a very accurate determination of the spacecraft rotation rate and, incidentally, to determine magnitude of the offset itself.

A second article (Section M) by Gallagher presents an analysis which relates injection dispersions due to launch-vehicle guidance errors to the initial tracking station's acquisition. Two of the parameters most critical to early acquisition are selected, and upper bounds on the variations of these parameters with injection errors are computed.

Lastly, Ball presents (in Section N) the second of a series of articles analyzing and tracing the effects of the observed *Pioneer VI* gas leak on the orbit. For this analysis, the tracking data were obtained from March 1 to June 20, 1966. It is concluded that the gas leak, while diminishing, is still significantly affecting the spacecraft orbit determination.



# L. *Pioneer VI* High-Frequency Data Analysis

*R. Motsch, D. Chaney, and D. Curkendall*

## 1. Introduction

During the analysis of the *Pioneer VI* high-resolution tracking data, a periodicity was discovered in the data noise. This periodicity arose from a slight offset of the spacecraft antenna from the spin axis. The resulting simple harmonic motion in the station–spacecraft range dominated the autocorrelation function of the noise; thus, it was necessary to remove the periodicity in order to determine the amount of random phase jitter in the doppler signal and the high-frequency drift characteristics of the rubidium oscillators.

Analysis of the problem showed that, in the process of removing the periodicity, one could obtain two parameters of interest: (1) the spacecraft rotation rate, and (2) the distance of the spacecraft antenna from the spin axis. This analysis, when applied to the *Pioneer VI* data, led to:

(1) Measurement of the approximately 58-rev/min spacecraft rotation rate and the change in this rate with a minimal accuracy of 0.01 rev/min.

(2) Measurement of an apparent antenna offset of approximately 1.5 cm.

## 2. Spacecraft Rotation and Antenna Offset Analysis

The spacecraft geometry pertinent to this study is portrayed in Fig. 45. We have considered the spacecraft antenna as a point source located a distance $d$ off the spin axis of the spacecraft.

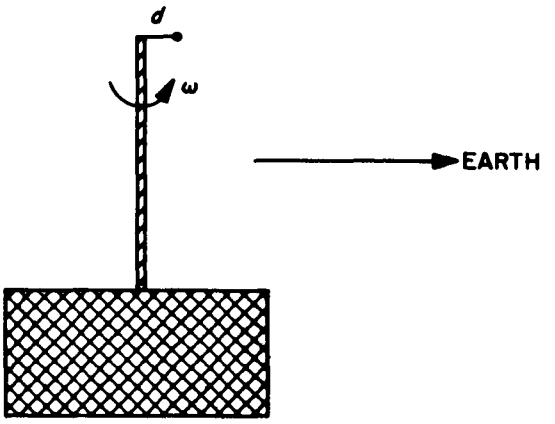


**Fig. 45. Spacecraft geometry**

It can be shown that, for a sampled data system, the autocorrelation function of the range-rate error due to antenna displacement and spacecraft rotation is given by:

$$R(\tau) = 2d^2 \sin^2 (\omega/2f_d) \cos \omega\tau$$

where $d$ is the apparent offset of the antenna when considered as a point source, $\omega$ is the angular velocity (rad/sec) with respect to the spacecraft spin axis, and $f_d$ is the data sampling rate. This expression for $R(\tau)$ was obtained under the assumption that, over any one pass, $\omega$ is essentially constant; i.e.,

$$2d^2 \sin^2 (\omega/2f_d) = A$$

$$R(\tau) = A \cos \omega\tau$$

Consider Fig. 46, where $R(\tau)$ is shown as the dashed curve. If the data sampling rate is more than twice the frequency of the autocorrelation curve, $R(\tau)$ can be constructed directly. However, if the data sampling rate is less than twice the frequency of the autocorrelation curve, some pseudo-autocorrelation $\hat{R}(\tau)$ will be obtained with amplitude of $A$, but with a period greater than that

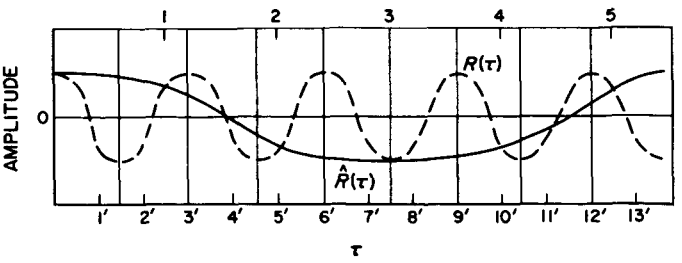


**Fig. 46. Amplitude vs time for the true autocorrelation function $R(\tau)$ and the pseudo-autocorrelation function $\hat{R}(\tau)$**

of $R(\tau)$. This situation is demonstrated in Fig. 46 by the unprimed numbers and the solid curve.

Let $f_s$ be the spacecraft rotation rate and $f_d$, the data sampling rate. Then, for $f_s \neq f_d$, there exists a time interval $T$ such that:

$$f_s T \pm 1 = f_d T$$

Thus, every $T$ sec it will *appear* that the spacecraft has gone through one rotation, as measured by the period of $\hat{R}(\tau)$ using a data sampling rate $f_d$. From the above equation, we obtain:

$$f_d - f_s = \pm 1/T$$

Since $T$ is necessarily positive, the above equation can be written:

$$|f_d - f_s| = 1/T, \quad f_s \neq n f_d, \quad n = 1, 2, \cdots$$

It has been shown above that any spacecraft rotation rate that is less than one half the data sampling rate can be determined uniquely, and any other spacecraft rotation rate that is not an integral multiple of the data sampling rate can be restricted to several possible choices. An example pertaining to these statements is shown in Fig. 47. In general, one will need *a priori* information to

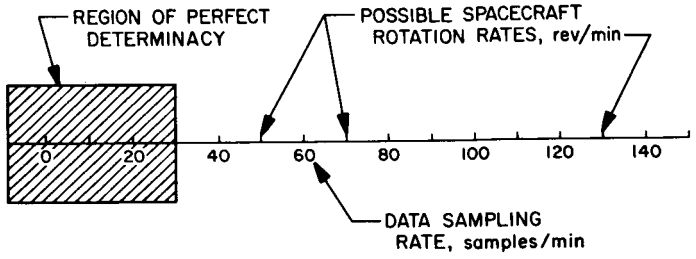


**Fig. 47. Possible spacecraft rotation rates for data sampling rate of 60 samples/min**

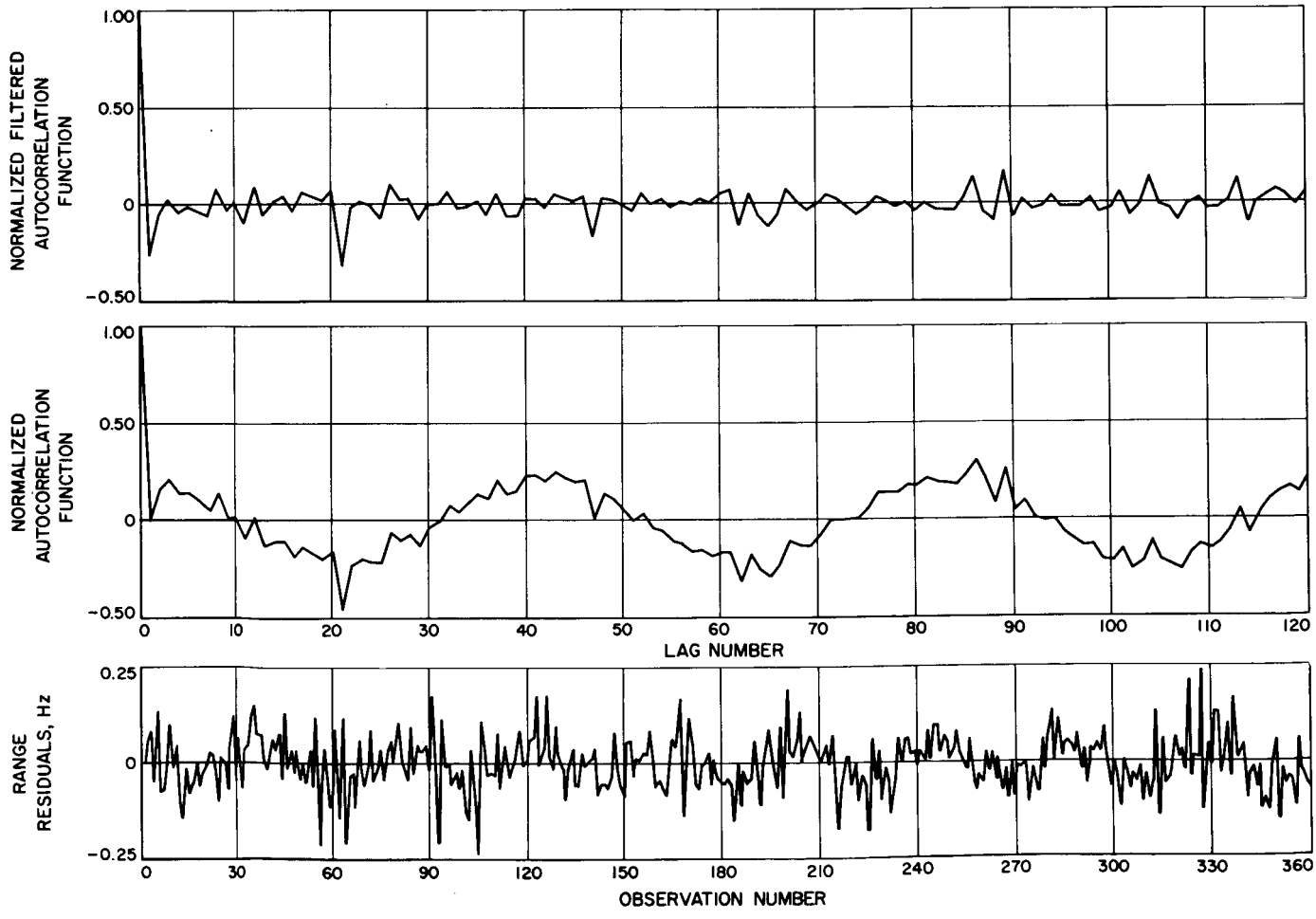


**Fig. 48. Range residuals, normalized autocorrelation function, and normalized filtered autocorrelation function for *Pioneer VI* on January 5, 1966, using Echo DSS 12 data**

resolve the ambiguity in the pseudo-autocorrelation $\hat{R}(\tau)$. If such information is available, $f_s$ can be uniquely determined, and, since $\omega = 2\pi f_s$, the apparent offset $d$ can be obtained from the equation:

$$2d^2 \sin^2 (\omega/2f_d) = A$$

where $A$ is the autocorrelation amplitude.

### 3. Results from Pioneer VI Data Analysis

The techniques described above were applied to data collected from the *Pioneer VI* probe. The Earth rate was removed from the data, a seventh-order polynomial was fitted to the resulting numbers, and residuals about the fit were formed. From these residuals, the autocorrelation function was produced, and a curve of the form $A \cos(\omega t)$ was fit to the autocorrelation data. Fig. 48 displays the range residuals, the normalized autocorrelation function, and the normalized filtered autocorrelation function obtained using the above processes on data for January 5, 1966. Information from a spin counter on the spacecraft was utilized to uniquely determine $f_s$ from $\omega$, and $d$ was determined from A. Table 3 lists the results for several passes of *Pioneer VI*.

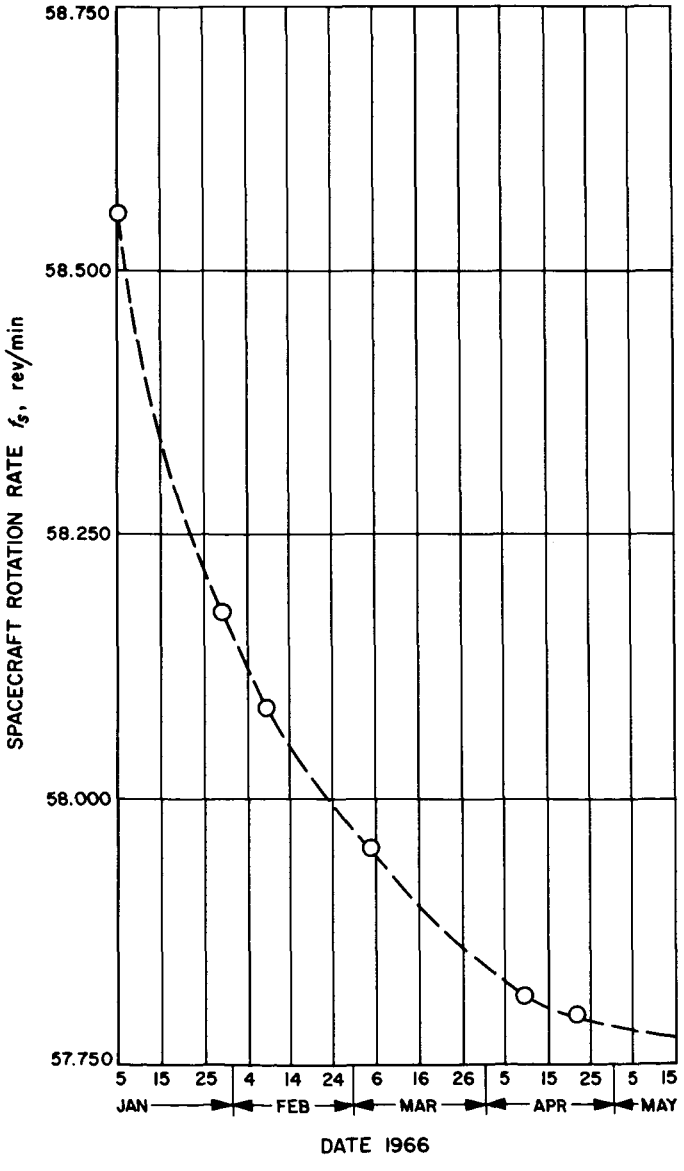


**Fig. 49. *Pioneer VI* rotation rate vs date 1966**

**Table 3. Results of *Pioneer VI* data analysis**

| Date | $\omega$, rad/sec | $A$, cps$^2 \times 10^{-4}$ | $f_s$, rev/min | | $d$, cm |
|---|---|---|---|---|---|
| | | | Computed | Measured | |
| 1- 5-66 | 0.1518 | 5.85 | 58.555 | 58.40 | 1.47 |
| 1- 5-66 | 0.1513 | 7.97 | 58.550 | — | 1.72 |
| 1-30-66 | 0.1909 | 10.93 | 58.177 | 58.04 | 1.60 |
| 2- 8-66 | 0.2003 | 11.75 | 58.087 | — | 1.58 |
| 3- 4-66 | 0.2141 | 15.92 | 57.956 | 57.72 | 1.72 |
| 4- 9-66 | 0.2292 | 17.95 | 57.811 | — | 1.71 |
| 4-21-66 | 0.2305 | 18.37 | 57.799 | — | 1.72 |

It is apparent that the *Pioneer VI* rotation rate is decreasing. This rate decrease is plotted in Fig. 49. It is known that *Pioneer VI* experienced a gas leak, and quite probably the decreasing rotation rate is associated with this leak.

N67 14434

## M. *Pioneer B*[6] Trajectory Dispersions and DSN Initial Acquisition

J. F. Gallagher[7]

### 1. Introduction

During mission operations, it is important to the orbit-determination process that the spacecraft be acquired in two-way lock as soon as possible. This is true because the slant-range rate from Johannesburg DSS 51 during

[6] *Pioneer B* was launched on August 17, 1966, at which time its designation became *Pioneer VII*.

[7] The author wishes to express his appreciation to D. Hubiak, W. Ross, and F. Borncamp of JPL Technical Section 337 for information furnished on the DSN.

the first 10 or 12 min after injection varies rapidly, and the doppler data during this early period is therefore powerful. The slant-range-rate curve from DSS 51 for the nominal *Pioneer B* trajectory is shown in Fig. 50.

For DSS 51 to acquire as early as possible, the station must be prepared to track the spacecraft on not only a nominal trajectory but also various off-nominal trajectories which might occur. The off-nominal trajectories referred to here are those resulting from such things as $3\sigma$-high or -low thrust performance of the third stage, but not "catastrophes" such as a failure of the third-stage motor to ignite.

There are two important quantities involved in early acquisition by DSS 51: rise azimuth, and the time at which the slant-range acceleration from DSS 51 first falls within the doppler capability of the spacecraft and ground station. This time is the earliest time at which initial RF acquisition for two-way lock can occur. The doppler capability of the spacecraft and ground station is rather complicated, depending upon many parameters, including bandwidth, sensitivity, and selectivity of the ground station and spacecraft receivers. This doppler capability also changes with time as improvements are made in the equipment. Personnel of JPL Technical Section 337 chose as a *working definition* of the doppler capability for the *Pioneer B* mission the following: the time at which the slant-range acceleration from DSS 51 falls below 40 m/sec$^2$.

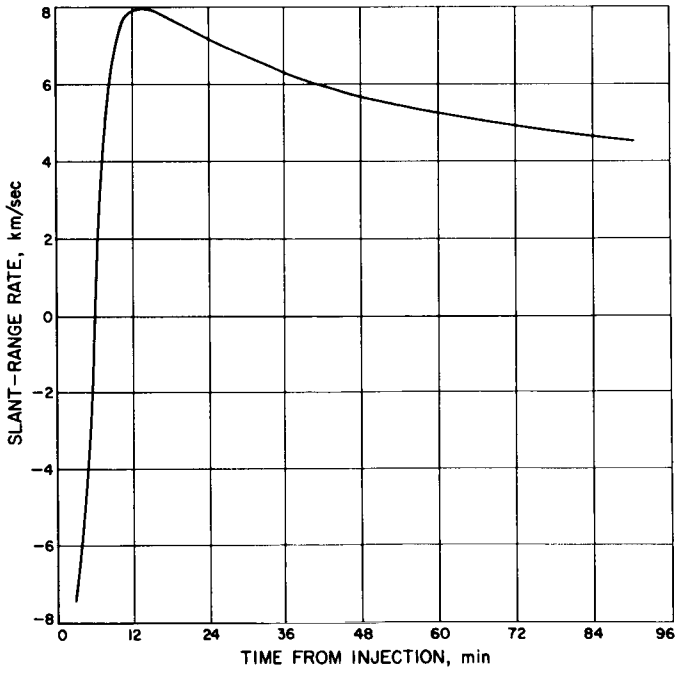


**Fig. 50. Slant-range rate from DSS 51 for the nominal *Pioneer B* trajectory**

Knowledge of the rise azimuth and its dispersions is important because, if these dispersions fall outside the beamwidth of the acquisition-aid antenna, a more difficult and time-consuming search for the spacecraft may be necessary and much early data valuable to orbit determination may be lost. On the other hand, if the dispersions in rise azimuth fall well within the beamwidth of the acquisition-aid antenna, the chances for very quick two-way acquisition are greatly improved. Knowledge of the time at which the slant-range acceleration from DSS 51 falls below 40 m/sec$^2$ and the dispersions on this time is important because with this information it is possible to work out a procedure for tuning the transmitter and receiver which will improve the chances of quick two-way acquisition and thereby maximize the amount of strong doppler data.

It is sufficient for the DSN to have advance knowledge of the nominal trajectory and two off-nominal trajectories which are loosely termed $3\sigma$-high and $3\sigma$-low. These off-nominal trajectories are those which result from a "worst-case" combination of the dispersions in each of the six injection conditions. In this case, the term "worst case" means worst with respect to launch azimuth and the time at which the slant-range acceleration curve falls below 40 m/sec$^2$.

## 2. Method

To determine these worst-case trajectories, the following method was used: First a nominal trajectory was computed beginning at injection and running out to 2 hr past injection. All of the station quantities for DSS 51 were obtained for this nominal trajectory. Then the $3\sigma$ dispersions in each of the six Earth-fixed spherical injection conditions were applied, one at a time, to the corresponding nominal injection conditions; the trajectories were computed to 2 hr; and the DSS 51 quantities were obtained along the trajectory. Trajectories using both positive and negative increments in the injection conditions were calculated to check for linearity. This procedure allows one to see the effect of a dispersion in any one of the six injection conditions upon any station quantity. A worst-case combination of injection conditions can be gotten simply by picking that set of plus-and-minus increments in the six injection conditions which results in all-positive or all-negative changes in the station quantity. If linearity holds, then we are guaranteed that the combination thus arrived at does, in fact, result in the greatest change in the station quantity, and that

we have a pair of off-nominal trajectories which brackets the trajectories we can actually expect to track.

## 3. Results

The Earth-fixed spherical injection conditions and their $3\sigma$ dispersions are shown in Table 4. One at a time, these $3\sigma$ dispersions were added to and subtracted from their corresponding nominal quantities, and the trajectories were calculated. The results for the rise azimuth at DSS 51 are shown in Table 5. Here we see that the smallest change in rise azimuth at DSS 51 is caused by the $3\sigma$ dispersion in $V$ and the largest change, by the $3\sigma$ dispersion in $\sigma$, the injection azimuth. The worst-case combination of injection conditions to maximize the value of the rise-azimuth angle at DSS 51 would be obtained by using positive increments in $R$, $\phi$, $\theta$, $V$, and $\gamma$ and a negative increment in $\sigma$. Increments with opposite signs would be used to minimize the rise azimuth, and this pair of trajectories should bracket the trajectory actually flown, at least as far as rise azimuth is concerned. Referring to Table 5, it appears that a rise-azimuth spread of 3 deg on either side of the nominal value should cover virtually all of the possibilities. Since the beamwidth of the acquisition-aid antenna is about 16 deg, the rise-azimuth dispersions should cause no trouble in acquisition.

**Table 4. Earth-fixed spherical injection conditions and their $3\sigma$ dispersions**

| Condition | Nominal value | $3\sigma$ Dispersion |
|---|---|---|
| Geocentric radius $R$, km | 6791.6385 | 22.5 |
| Geocentric latitude $\phi$, deg | −14.052728 | 0.258 |
| Longitude $\theta$, deg | 352.65549 | 0.384 |
| Earth relative velocity $V$, km/sec | 10.546620 | 0.075 |
| Relative path angle $\gamma$, deg | 2.5642066 | 1.05 |
| Relative azimuth angle $\sigma$, deg | 131.08955 | 1.05 |

**Table 5. Effects of injection-conditions dispersions upon rise azimuth at DSS 51**

| Trajectory | Resulting rise azimuth, deg | Difference, deg |
|---|---|---|
| Nominal | 270.47687 | — |
| $+\Delta R$ | 270.87919 | 0.40232 |
| $-\Delta R$ | 270.05910 | −0.41777 |
| $+\Delta\phi$ | 271.11444 | 0.63757 |
| $-\Delta\phi$ | 269.83581 | −0.64106 |
| $+\Delta\theta$[a] | 269.65577[a] | −0.82110 |
| $-\Delta\theta$ | 269.96299 | −0.51388 |
| $+\Delta V$ | 270.50748 | 0.03061 |
| $-\Delta V$ | 270.44529 | −0.03158 |
| $+\Delta\gamma$ | 271.05562 | 0.57875 |
| $-\Delta\gamma$ | 269.83356 | −0.64331 |
| $+\Delta\sigma$ | 269.60717 | −0.86970 |
| $-\Delta\sigma$ | 271.33660 | 0.85973 |

[a]The input for the $+\Delta\theta$ trajectory was incorrect; however, a check for linearity showed that the variation in rise azimuth with injection longitude is very linear for the small changes in the longitude used.

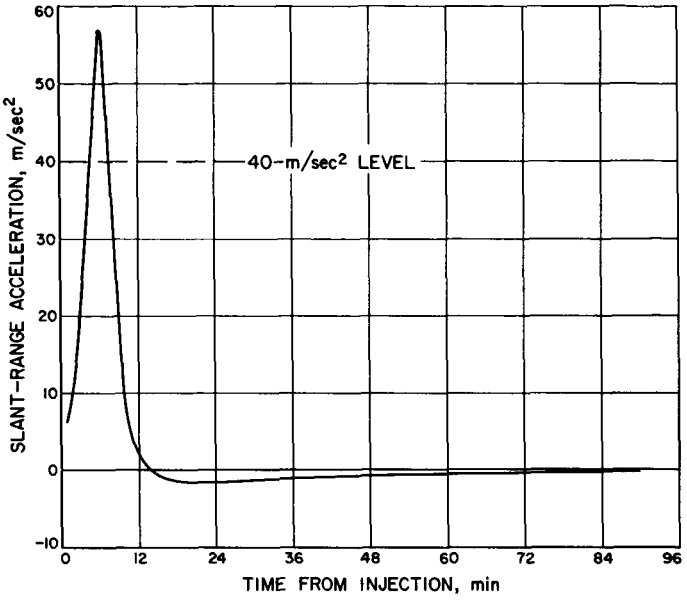


**Fig. 51. Slant-range acceleration from DSS 51 for the nominal *Pioneer B* trajectory**

Fig. 51 is a plot of the slant-range acceleration of the probe as seen from DSS 51. It can be seen that the slope of the curve is very steep in the neighborhood where the curve falls below 40 m/sec². The trajectory program does not compute the time at which the slant-range acceleration from a station takes on a given value. However, for the purposes of the study, it was sufficient to assume a straight-line variation in the slant-range acceleration between 7 and 8 min after injection. To find the time of this crossing, linear interpolation was done graphically for the nominal trajectory and for each of the six pairs of off-nominal trajectories. Fig. 52 is a sample of this graphical linear interpolation for the dispersions in the crossing time caused by dispersions in flight-path angle. Observe that the line labelled "nominal" in Fig. 52 is a linearized and magnified version of the portion of the curve of Fig. 51 which lies between 7 and 8 min after injection.

The effects of the dispersions in the six injection conditions upon the time of crossing the 40-m/sec² level are given in Table 6. In Table 6, we see that dispersions in $\gamma$

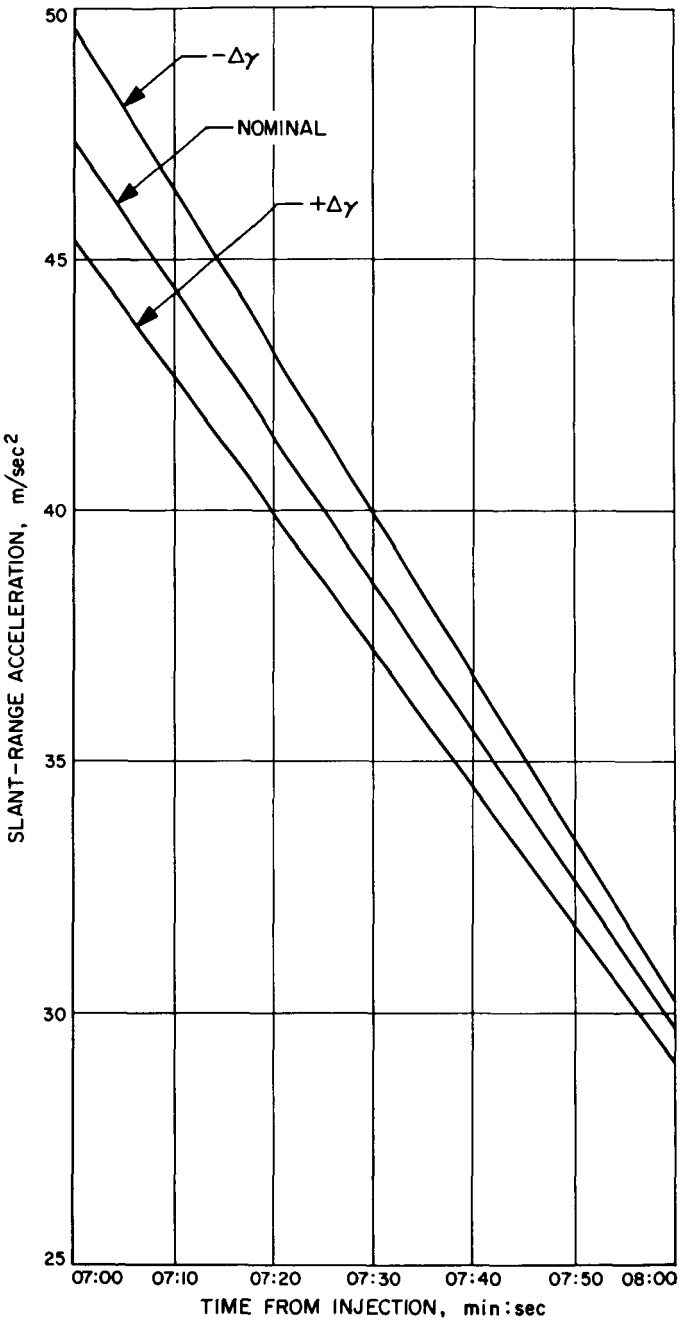


**Fig. 52. Sample plot showing the graphical linear interpolation for the dispersions in crossing time caused by dispersions in flight path angle**

are most influential here. The worst-case combination of injection conditions which causes the crossing time to be as early as possible would be a positive increment in $R$, negative in $\phi$, and positive in $\theta$, $V$, $\gamma$ and $\sigma$. This trajectory and its opposite (i.e., the one for which the crossing time is latest) should bracket the actual trajectory as far as the crossing time is concerned. From this information, the tuning procedure mentioned earlier can be worked out.

**Table 6. Effects of injection-conditions dispersions upon the time of the slant-range acceleration curve falling below 40 m/sec²**

| Trajectory | Resulting crossing time, min:sec after injection | Difference, sec |
|---|---|---|
| Nominal | 07:25.0 | – |
| $+\Delta R$ | 07:24.2 | −0.8 |
| $-\Delta R$ | 07:25.7 | 0.7 |
| $+\Delta\phi$ | 07:26.8 | 1.8 |
| $-\Delta\phi$ | 07:23.0 | −2.0 |
| $+\Delta\theta$[a] | 07:28.1[a] | 3.1 |
| $-\Delta\theta$ | 07:26.9 | 1.9 |
| $+\Delta V$ | 07:23.4 | −1.6 |
| $-\Delta V$ | 07:26.5 | 1.5 |
| $+\Delta\gamma$ | 07:19.7 | −5.3 |
| $-\Delta\gamma$ | 07:29.7 | 4.7 |
| $+\Delta\sigma$ | 07:21.5 | −3.5 |
| $-\Delta\sigma$ | 07:28.2 | 3.2 |

[a]The input for the $+\Delta\theta$ trajectory was incorrect; however, a check for linearity showed that the variation in crossing time with injection longitude is very linear for the small changes in the longitude used.



## N. The Effect of the Gas Leak on the *Pioneer VI* Orbit, Part II

*J. E. Ball*

*Pioneer VI*, launched on December 16, 1965, has been in a heliocentric orbit for the last 7 mo. The one anomaly that occurred during this time was a gas leak somewhere in the pneumatic system of *Pioneer VI*. Since 90% of the gas carried on the spacecraft was depleted 90 days after launch (March 16, 1966), JPL's single-precision orbit-determination program (SPODP) attempted to fit a trajectory over the arc of the spacecraft orbit from March 1 to June 20, 1966. Fig. 53 is a plot of the difference between the observed Echo DSS 12 two-way doppler values and the calculated two-way doppler values (residuals) for a portion of that arc. These residuals have a similar signature to the residuals of the fit over the arc of the spacecraft orbit from December 1965 to January 1966 (*SPS 37-39*, Vol. III, pp. 42–45). However, in this instance, the data covers approximately 4 mo. Earlier in the mission,

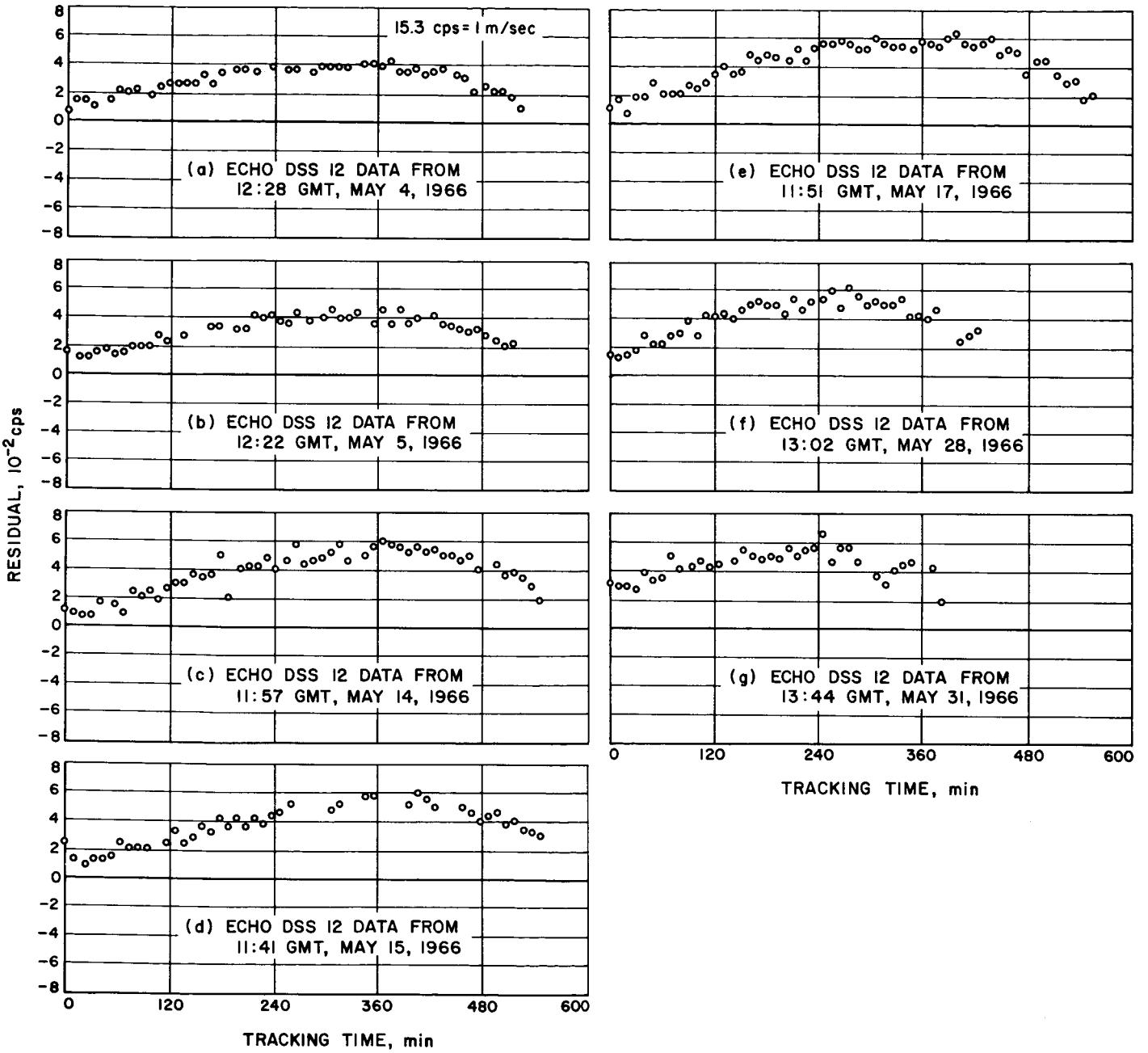


**Fig. 53. Residuals vs tracking time for a portion of the *Pioneer VI* trajectory fit for March through June 1966**

the data arc could not be extended much more than 1 mo before excursions in the residuals considerably exceeded those shown here. Thus, our relative ability to fit the data is improving with time, as would be predicted from the fact that the gas flow rate is following a decreasing exponential curve.

Table 7 compares the values of the spacecraft's position and velocity for December 18, 1965, as computed from the fit over the arc of the orbit from December to January to the values as computed from the fit over the arc of the orbit from March through June. The change in the injection conditions obtained is larger than the theoretical uncertainties computed, assuming no gas leak to be present. This may be seen by comparing the values of $\Delta Q$ in Table 7 to the values for $\sigma$. The version of the SPODP used to fit portions of the *Pioneer VI* orbit did not have the capability of estimating an exponential type of force such as that occurring in *Pioneer VI* from the gas leak.

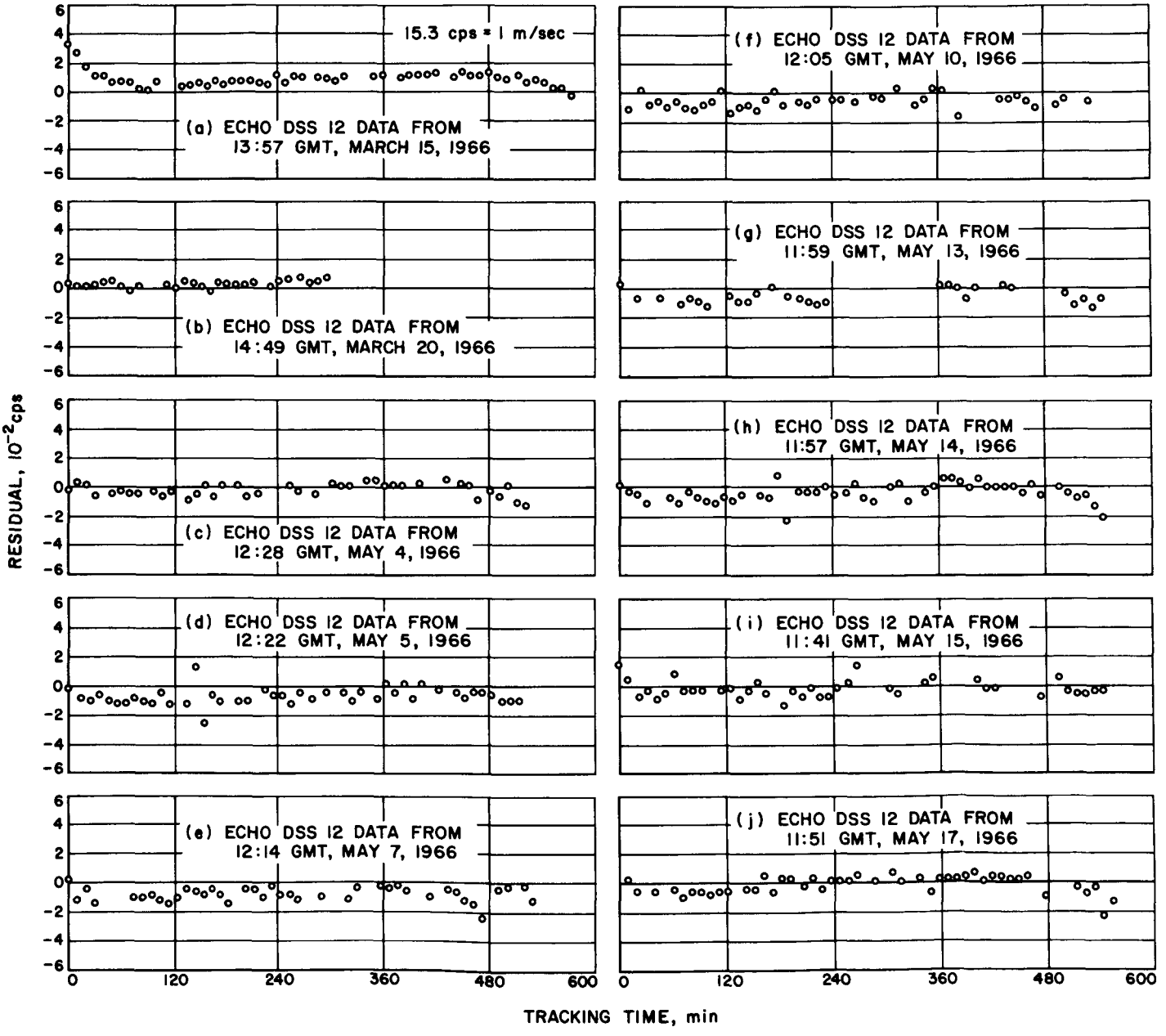


**Fig. 54. Residuals vs tracking time for a portion of the *Pioneer VI* trajectory fit for March through June 1966, using estimated values for the AU and the deep space stations' geocentric radius and longitude**

**Table 7. Comparison of *Pioneer VI* position and velocity as computed from two fits of data (Epoch: December 18, 1965)**

| Q | Fit from December 1965 to January 1966 | 1σ Value | Fit from March through June 1966 | 1σ Value[a] | ΔQ |
|---|---|---|---|---|---|
| X, km | 430843.04 | 78 | 430809.56 | 82 | 33 |
| Y, km | −24759.184 | 120 | −24011.667 | 121 | 748 |
| Z, km | −40436.293 | 240 | −42300.775 | 233 | 1864 |
| $\dot{X}$, km/sec | 2.1548440 | 0.0001 | 2.1566785 | 0.00009 | 0.00016 |
| $\dot{Y}$, km/sec | 0.02582071 | 0.00002 | 0.02623449 | 0.00006 | 0.00041 |
| $\dot{Z}$, km/sec | −0.10912526 | 0.00007 | −0.11013935 | 0.00015 | 0.00101 |

[a]These uncertainties are the values calculated, assuming no gas leak to be present.

In addition to the information desired from the prime experiments of *Pioneer VI*, it was hoped that, from analysis of the *Pioneer VI* orbit, a better determination of certain astronomical constants could result. Therefore, a determination of the astronomical unit (AU) was attempted over that portion of the orbit from March through June when the gas leak was small. In addition to solving for the AU, the deep space stations' geocentric radius and longitude were estimated to help improve the fit, as shown in Fig. 54.

Since the residuals from Fig. 54 are smaller and distribute themselves in a linear fashion along the zero residual line, as compared to the residuals in Fig. 53, improvements to the AU and deep space station locations are suggested when the additional parameters of the AU and station locations are estimated. However, a comparison of these values to the values determined from previous sources (Table 8) indicates that small unmolded and unknown forces acting on the spacecraft can produce erroneous station location results and other parameter estimation errors. Thus, it is concluded that the effects of the *Pioneer VI* gas leak, while diminished, are still significantly affecting the orbit of *Pioneer VI*. Future plans include continued processing of the tracking data as the gas leak continues to diminish and attempts to model the leak in the SPODP to obtain reliable estimates of the AU and certain other astronomical constants.

**Table 8. Comparison of values for the AU and tracking station longitudes as estimated from *Pioneer VI* orbit to those estimated previously**

| Q | Estimates from *Pioneer VI* orbit | 1σ Value | Previous estimates | 1σ Value | ΔQ |
|---|---|---|---|---|---|
| AU, km | 149,598,760 | 957 | 149,598,500 | 500 | 266 |
| Deep space station longitudes | | | | | |
| Echo DSS 12 | 243.19530 deg | — | 243.19428 deg | 40 m | 102 m |
| Tidbinbilla DSS 42 | 148.98208 deg | — | 148.98132 deg | 40 m | 76 m |
| Johannesburg DSS 51 | 27.686081 deg | — | 27.685513 deg | 40 m | 57 m |
| Robledo DSS 61 | 355.75172 deg | — | 355.75083 deg | 40 m | 89 m |

# References


1. Harnwell, G. P., *Principles of Electricity and Electromagnetism,* McGraw-Hill Book Co., New York, 1949.
2. *Solar Wind,* Ed. by Mackin, R. J., and Neugebauer, M. M., Pergamon Press, 1966.
3. Neugebauer, M. M., and Snyder, C. W., *Mariner II Observations of the Solar Wind I Average Properties,* Technical Report No. 32-991, Jet Propulsion Laboratory, Pasadena.
4. Pioneer Program Document No. PC-046-01, NASA, Ames Research Center, Moffett Field, California, February 1965.
5. Snyder, C. W., and Neugebauer, M. M., *J. Geophys. Res.* 68, 6361-6370, 1963.
6. Neugebauer, M. M., and Snyder, C. W., *J. Geophys. Res.* 70, 1587-1591, 1965.
7. Wolfe, J. H., Silve, R. W., and Myers, M. A., *J. Geophys. Res.* 71, 1319–1340, 1966.
8. Strong, I. B., et al., *Phys. Rev. Let.,* 16, 631-633, 1966.
9. Kelso, J. M., *Radio Propagation in the Ionosphere,* McGraw-Hill Book Co., New York, 1964.
10. Johnson, F. S., *Satellite Environment Handbook,* Stanford University Press, 1965.
11. Central Radio Propagation Laboratory, "Ionospheric Predictions," National Bureau of Standards, Boulder, Colorado.
12. Central Radio Propagation Laboratory, "Compilations of Solar Geophysical Data," National Bureau of Standards, Boulder, Colorado.
13. Pfeiffer, C. G., *On the Accuracy of Earth-Based Radio Tracking During the Approach Phase of a Mission,* Technical Memorandum No. 312-611, Jet Propulsion Laboratory, Pasadena, November 11, 1965.
14. Trask, D. W., and Muller, P. M., *Space Programs Summary 37-39,* Vol. III, Jet Propulsion Laboratory, Pasadena, pp. 7–16, 1966.
15. Reprints of U.S. Naval Observatory, Time Services Division, Washington, D. C.
16. Time and Frequency Service Bulletins from the National Bureau of Standards, Marian S. Cord, Ed., Boulder, Colorado.
17. Anderson, J. D., and Muller, P. M., *Timekeeping and the Orbit Determination Process,* Technical Memorandum No. 312-570, Jet Propulsion Laboratory, Pasadena, July 6, 1965.
18. Muller, P. M., *Timing Polynomials for the SPODP, Program TPOLY, and Other Related Discussion,* Technical Memorandum No. 312-722, Jet Propulsion Laboratory, Pasadena, August 1, 1966.
19. Munk, W. H., and Macdonald, G. J. F., *Rotation of the Earth,* Cambridge University Press, 1960.

# References (Cont'd)


20. Marsden, B., and Cameron, A. G. W., *Earth Moon System,* Plenum Press, New York, pp. 52–92, 1966.

21. Peabody, P. R., Scott, J. F., Orozco, E. G., *JPL Ephemeris Tapes E9510, E9511, and E9512,* Technical Memorandum No. 33-167, Jet Propulsion Laboratory, Pasadena, March 2, 1964.

22. Peabody, P. R., Scott, J. F., Orozco, E. G., *Users' Description of JPL Ephemeris Tapes,* Technical Report No. 32-580, Jet Propulsion Laboratory, Pasadena, March 2, 1964.

23. Brouwer, D., and Clemence, G. M., *Methods of Celestial Mechanics,* Academic Press, New York, 1961.

24. "Proceedings of the Eleventh General Assembly," Transactions of the International Astronomical Union, Vol. XIB, Berkeley, 1961.

25. Eddington, A. S., *The Mathematical Theory of Relativity,* Cambridge University Press, 1960.

26. *Explanatory Supplement to the Ephemeris,* Her Majesty's Stationery Office, London, 1961.

27. Apollo Navigation Working Group, *Apollo Missions and Navigation Systems Characteristics,* TR 65-AN-1.0, NASA, February 5, 1965.

# III. Communications Research and Development



## A. Wide Band Receiver System Frequency Divider

K. Schreder

### 1. Introduction

The wide band receiver system (WBRS) is currently in the module checkout phase with less than 30% of the modules remaining to be checked. One of the modules designed, built, and checked out is a frequency divider from 66 MHz. The module is shown in the block diagram of the transmitter section of Fig. 39, p. 101, *SPS 37-33*, Vol. III.

### 2. Circuit Description

The circuit is a locked oscillator divider. Fig. 1 shows the circuit configuration. The input circuit is designed for a 50% bandwidth to provide a low input voltage standing wave ratio (VSWR) over a wide 1-db bandwidth. The first stage, Q1, is an emitter-follower stage which is necessary for maintaining a low VSWR for greater than a 5% bandwidth. The next stage, Q2, provides limiting and insures proper isolation between the divider and the emitter follower. The divider stage, Q3, is a regenerative divider whose output circuit is tuned to the output frequency. Minimum power is taken from the divider which allows the divider to remain locked over a wide power range. The output stages, Q4 and Q5, amplify the signal to an output power greater than +13 dbm. (The FT-45 transistor was used instead of the more common 2N915 or 2N918 because of the higher current gain cutoff frequency $F_\beta$. The FT-45 has a lower current gain $\beta$, than the other two transistors, but a gain-bandwidth product $F_T$, about the same as a 2N918 which produces the higher $F_\beta$.)

### 3. Performance Characteristic

For a +13 dbm input signal, the output power was +13.6 dbm for a power drain of 600 mw from a +30 vdc supply. The input VSWR was less than or equal to 1.10 for a 5-MHz bandwidth and input power variations from +7 to +19 dbm.

The locking bandwidth was greater than 7.4 MHz. The percentage of locking bandwidth was 11.2%. (The locking bandwidth is defined as the bandwidth in which the output signal is synchronous with the input signal.)

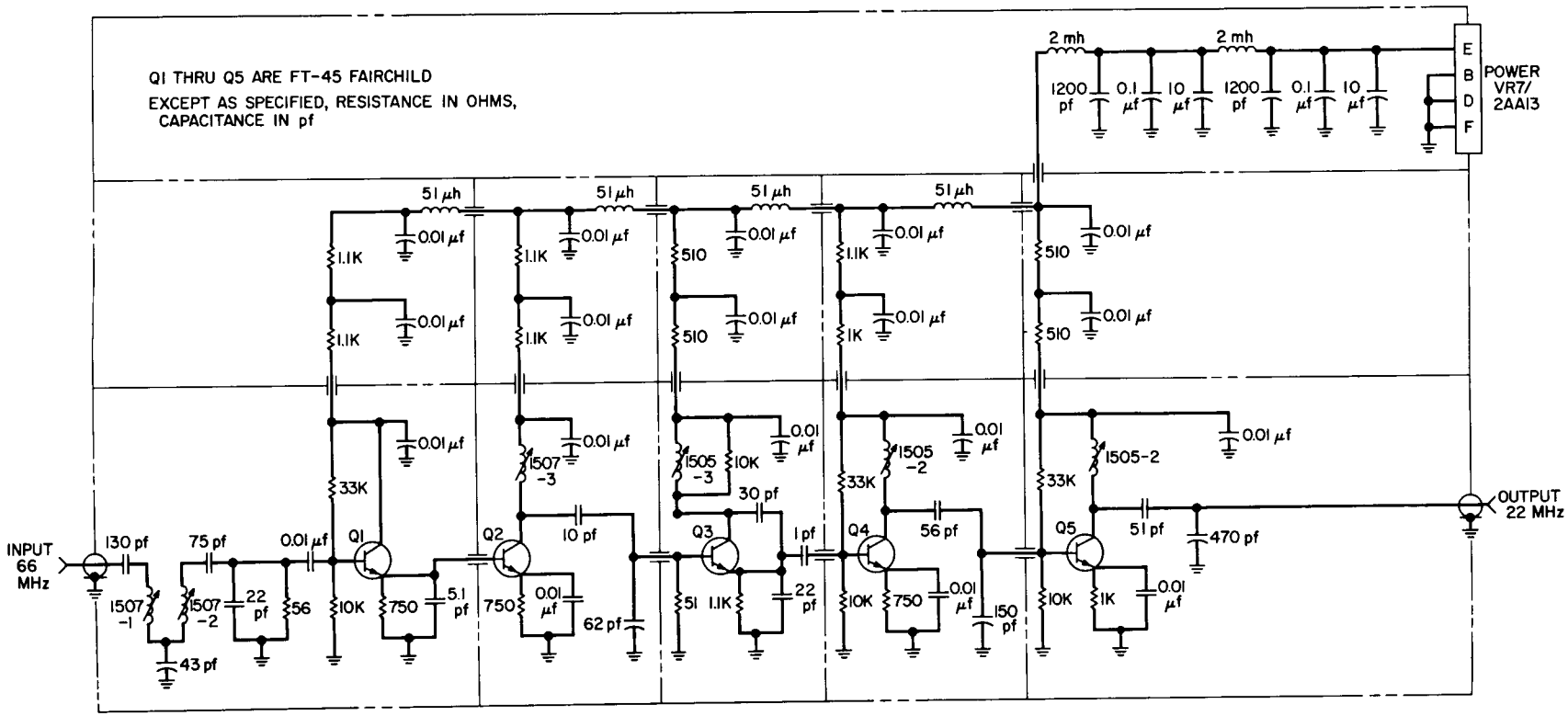


**Fig. 1. Schematic of ÷3 frequency divider**

The limiting curve is shown in Fig. 2. When the input signal is below —18 dbm, the locked oscillator stops. For a ±10% power supply variation, the output power varied ±0.9 db. Fig. 3 shows the output power variation for power supply variations from 40 to 14.5 vdc. For a supply voltage of 14.5 vdc or less, the oscillator stopped. The total output harmonic distortion was 1.88% with the 9th harmonic being the last measurable product.

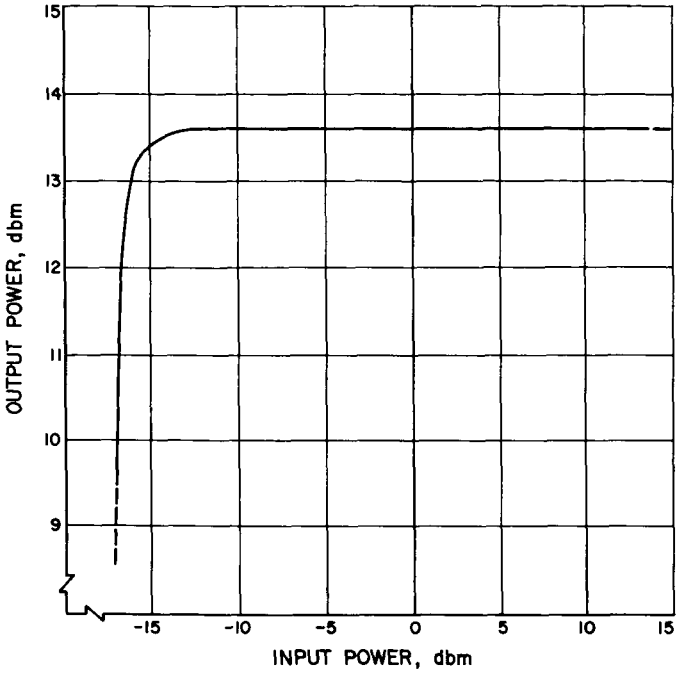


**Fig. 2. Limiting curve for ÷3 frequency divider**

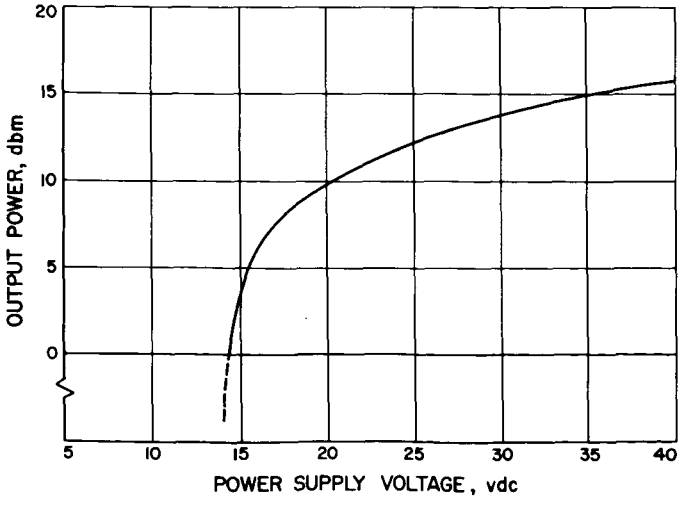


**Fig. 3. Output power variations due to power supply changes**



# B. Ephemeris Controlled Oscillators: Modification of Mod V Programmed Oscillator

*G. Thompson*

The Mod V programmed oscillator (PO) at the Mars DSS has been modified to increase its reliability. Because of this modification, the Mod V PO gain constant $K_0$, is no longer unity when used in a closed-loop, phase-locked receiver system (Fig. 4).

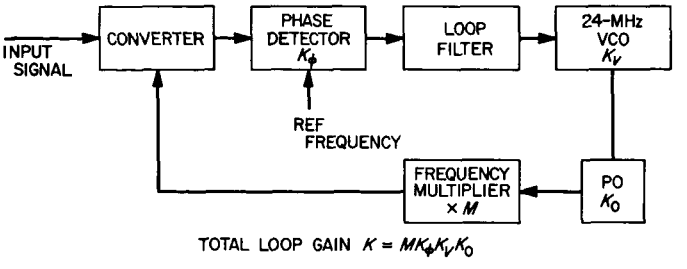


**Fig. 4. Phase-locked loop receiver using a PO**

The modification involves the 24-MHz voltage-controlled oscillator (VCO) as used in conjunction with the Hewlett-Packard (H-P) 5100A/5110A synthesizer. As previously reported (*SPS* 37-32, Vol. III, pp. 36–38) the 24-MHz VCO provides a means of voltage controlling the output frequency of the H-P synthesizer at frequencies from 1 to 50 MHz. The original system design (*SPS* 37-32) substituted the 24-MHz VCO for the 24-MHz reference in the 100-kHz decade of the H-P synthesizer (Fig. 5). This configuration made the VCO-synthesizer

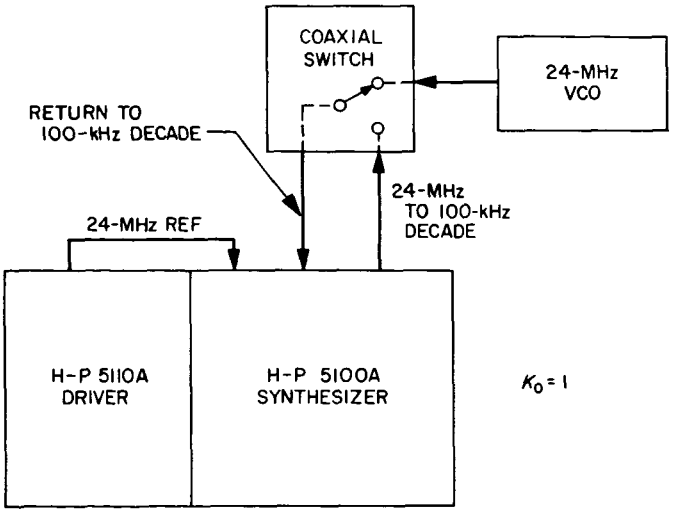


**Fig. 5. Original 24-MHz substitution in Mod V PO**

combination have the sensitivity of the VCO, $K_v$, with $K_0 = 1$ (Fig. 4).

The modification in Fig. 6 substitutes the 24-MHz VCO for the 24-MHz reference from the 5110A driver. Therefore, voltage control of the frequency can occur in the eight least significant digits of the synthesizer output frequency. The gain of the VCO is multiplied by 1.1111111, or in other words, $K_0 = 1.1111111$.

The modification was made because problems had been found with the substitution of the VCO in the 100-kHz decade. The modification requires a 24-MHz VCO operating at 100-mv rms into 50 Ω. The modification is simple to implement and provides a more reliable system.

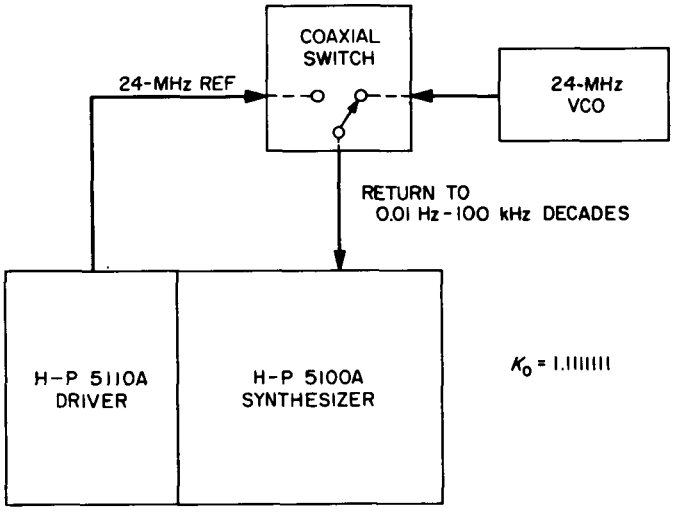


**Fig. 6. Present 24-MHz substitution in Mod V PO**

N67 14438

# C. Information Systems: Error Correction for High-Speed Data Transmission

*E. C. Posner and G. Solomon*

## 1. *Mariner* Spacecraft High-Speed Data Transmission, *E. C. Posner*

***a. Introduction.*** This report describes a coding-decoding scheme suitable for use with *Mariner* 1964, 1967, and 1969 spacecraft data transmitted over a high-speed data line. The method uses a (15,7) double error-correcting code and a very simple majority logic decoding. The probability of failing to decode correctly is reduced by a factor of more than 200.

Data from *Mariner* 1964, and ultimately from the *Mariner* 1967 and 1969 spacecraft, come to the SFOF over a 1200-bps commercial grade high-speed data line. The bit rate for *Mariner* 1964 spacecraft is at most 25 bps; for *Mariner* 1967 spacecraft is at most 33⅓ bps; and for *Mariner* 1969 is at most 66⅔bps. Of the 1200 bps, 450 bits are sync bits required by the telephone company and are not at the disposal of the user. Thus, 750 bps are all that are available to the Ground Communications System (GCS). Since, at most, 10 data words (a data word has 7 spacecraft information bits) arrive per second, the channel has space for other bits. These other bits are timing bits, station AGC bits, etc. There are 150 bps left for the spacecraft data. Figuring 10 spacecraft data words per minute, each spacecraft data word can be allotted 8 bps for error-correcting purposes, yielding coded words of length at most 15.

Fig. 7 shows the present method of error correction. An eighth data bit is put into the block — a sync information bit having nothing to do with the spacecraft data. These 8 bits are blocked into a 4 × 2 rectangular array. A third column is added as even parity on the four rows. A fifth row of three bits is now added as vertical parity on the three columns. The resulting 5 × 3 array of 15 bits is transmitted in a top-to-bottom, left-to-right serial scan.

This (15,8) coding scheme yields a code of minimum distance 4, which can correct single errors and still detect double errors. The purpose of this note is to propose a (15,7) code of minimum distance 5 which can correct double errors. The coding of more than one word at a time is not considered acceptable at the present time for the *Mariner* missions.

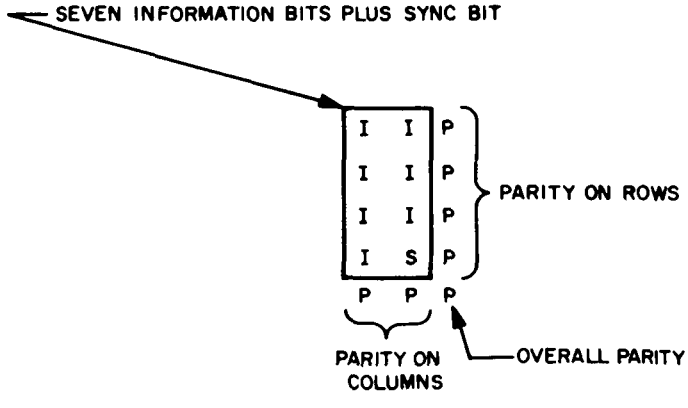


**Fig. 7. Present method of error correction**

*b. The Code.* We propose that the special sync bit S in Fig. 1 be moved to another portion of that 75-bit block which comes in with every word received from the spacecraft. For example, there is space in the portion of the block reserved for station AGC. Thus, we can add 8 check bits to the 7 spacecraft data bits to obtain coded words of length 15.

We can now use a (15,7) code instead of a (15,8) code. The (15,7) code which suggests itself is the famous double-error-correcting quasiperfect Bose-Chaudhuri (15,7) code. The definitions need not concern us here; the important point is that the code has minimum distance 5, and thus can correct all double errors, instead of just all single errors. The code is generated from the recursion polynomial $x^7 = x^3 + x + 1$, addition being modulo 2. This will be explained in the next section. A (14,7) double-error-correcting code does not exist (Ref. 1).

*c. Encoding.* Encoding would be done on the SDS 920 TDH computer at the DSIF sites. This high-speed data line will not go through the NASCOM communications processor at the Goddard Space Flight Center, and so no special formatting problems will arise. (This contrasts with the case for teletype. See *SPS 37-35*, Vol. III and Sect. D following.

To encode, regard the seven information bits $a_0$, $a_1$, $a_2$, $a_3$, $a_4$, $a_5$, $a_6$ as elements of the 2-element field. That is, each $a_i$ is 0 or 1, addition being modulo 2. The 8 check bits are generated by the rule

$$a_{i+7} = a_{i+3} + a_{i+1} + a_i, \qquad 0 \leq i \leq 7. \tag{1}$$

Extra storage space required in the 920 is minimal (less than ten words), and the running time is less than a millisecond.

Because the polynomial $x^7 + x^3 + x + 1$ divides $x^{15} + 1$ over the 2-element field, it can be shown that the bits $a_{15+i}$, $i \geq 0$, if computed by the rule in Eq. (1), would just repeat $a_0$ through $a_{14}$ in the same order. This fact is needed in the decoding process.

*d. Decoding.* We present a "majority logic" decoding scheme which is especially easy to implement on an IBM 7044, the computer used as the SFOF communications processor. Little extra storage (40 locations at most) is required to accommodate the (15,7) decoding scheme, and the running time is a few milliseconds.

The relation in Eq. (1) implies that $a_7 = a_3 + a_1 + a_0$, or better, $a_0 = a_1 + a_3 + a_7$. Let $i = 8$ in Eq. (1) to obtain $a_{15} = a_{11} + a_9 + a_8$. Since as observed $a_{15} = a_0$, we have $a_0 = a_{11} + a_9 + a_8$. Similarly, by letting $i = 12$ and $i = 14$ in Eq. (1) we obtain $a_0 = a_4 + a_{12} + a_{13}$ and $a_0 = a_2 + a_6 + a_{14}$. (In fact, these are the only check equations involving $a_0$.)

Consider the five expressions below, which are all equal to the original transmitted bit $a_0$ in the absence of errors:

$$\begin{cases} a_0 \\ a_1 + a_3 + a_7 \\ a_2 + a_6 + a_{14} \\ a_4 + a_{12} + a_{13} \\ a_8 + a_9 + a_{11}\,. \end{cases} \tag{2}$$

Compute the five quantities in Eq. (2) from the received word. If two or fewer errors have been made, at most two of the five quantities are changed, since no index occurs in more than one expression in Eq. (2). Hence, decode $a_0$ as $\hat{a}_0$, where $\hat{a}_0$ is 0 if the majority of the five expressions of Eq. (2) are zero; similarly, $\hat{a}_0$ is 1 if the majority are 1.

By the cyclic property of the (15,7) code, we can cycle the received word around one to the left, and decode $\hat{a}_1$ as $a_1$ in the same way. That is, the original $a_1$ becomes the new $a_0$ after the shift, the original $a_2$ becomes $a_1, \cdots$, $a_{14}$ becomes $a_{13}$, whereas $a_0$ becomes $a_{14}$. By repeating this process out to $a_6$, we can decode all the information bits. In fact, this shows that the (15,7) code is double-error correcting.

However, we always produce output in this fashion, even when more than two errors are made. Since the (15,7) code does not always make an error if more than two errors are made, we wish to detect whether such detectable errors have occurred. To do this, generate an $\hat{a}_7, \cdots, \hat{a}_{14}$ by the recursion of the previous section. Count the number of disagreements of the word $\hat{a}_0, \cdots, \hat{a}_{14}$ with the original received word. If the number of disagreements is 2 or less, we assume a double error, single error, or no error has been made, and declare the decoded information bits $\hat{a}_0, \cdots, \hat{a}_6$ as correct. If, however, there are 3 or more disagreements, then we declare that a detectable but uncorrectable error has occurred.

*e. Performance improvement.* The main improvement in performance comes from the fact that double errors, which are merely detected by the (15,8) double-parity

code, are corrected by the (15,7) cyclic code. Thus, when the bit error probability in the channel is $10^{-3}$, which is hopefully the worst encountered, the (15,8) code yields as output a detected but uncorrected error with probability about

$$\binom{15}{2}(10^{-3})^2 \approx 10^{-4}.$$

The (15,7) code has for this probability

$$\left[\binom{15}{3} - 180\right](10^{-3})^3 \approx 2.75 \times 10^{-7}$$

The 180 represents the number of triple-error patterns which are confused with double errors and decoded incorrectly. Thus, the mean time between failures to produce correct decoded output is increased by a factor of 220, from 2.8 hr to 26 days. This is a worthwhile improvement.

The probability of error (probability that the decoder outputs a word in error) is low in both systems, the present (15,8) and the proposed (15,7). For example, when the input bit error probability is $10^{-3}$, and burst errors are not occurring, the output word error probabilities are less than $2 \times 10^{-7}$. Burst errors could be avoided by dispersing the 15 bits of the code word throughout the transmitted block of 75 bits.

A computer program is now being written to incorporate this coding-decoding scheme in the *Mariner* spacecraft format for the GCS.



# D. Information Systems: Error Detection Equipment

G. Solomon

## 1. Modification of NASCOM Error-Detection Equipment for Error Correction

*a. Introduction.* An error detector will be installed at the DSN stations as part of the NASCOM high-speed data modem to be supplied to the DSN. It is suggested that through simple modification, greater and more efficient use of the projected coding system can be obtained. In particular, most of the data to be discarded can be recovered and used. In noisy situations, this will mean the difference between having a good channel and having no channel at all. The data is ordinarily spacecraft telemetry data from the Deep Space Stations received at the SFOF.

The basic code used by the NASCOM is a shortened (1023,990) BCH code with minimum distance 8, giving the code a capability of detecting up to 7 errors, correcting 1 and detecting 6, correcting 2 and detecting 5, or correcting 3 errors and detecting 4. As furnished, the equipment will detect errors and add to the received word of length 597 a 3-bit indicator of error status, i.e., it will tell whether the word was correctly received or not. The incorrect words would not be decoded. However, a computer program can be set up to correct up to 3 errors in the received word via an algebraic mechanization – a variant of Berlekamp-Solomon decoding procedures for cyclic codes (1) which is capable of decoding the word as fast as the word is received. As a sample result, for a probability of bit error of 0.001, which is considered very noisy for high-speed data lines, a double error-correcting procedure can expect to recover 0.95 of such words which are detected in error; a triple error-correcting procedure will recover 0.992 of these words. This triple error-correcting code will still detect 4 errors; the probability of letting an undetected error through in the block of 567 information bits would be less than $10^{-4}$.

Without error correction, 0.45 of the received words will be in error and would not be used; by using the triple error-correcting, quadruple error-detecting procedure as proposed, only 0.003 of the words would be thrown out. The output word error probabilities for bit error probabilities of 0.005, $10^{-3}$, $10^{-4}$ and $10^{-5}$ are given in Tables 1 and 2. The estimate of erroneous decoding is very conservative. Work is continuing to obtain a more exact figure (the problem is one of finding the distribution of words of weight 8 in the shortened BCH code). The statistics given make the proposed modification a worthwhile one, considering the economy and simplicity of the modifications.

*b. Error-correction procedures.* The (597,564) shortened code used by the NASCOM is encoded using the procedure in Ref. (9). To the information bits $a_0, a_1, a_2, \cdots a_{563}$) is assigned the polynomial

$$\sum_{i=0}^{563} a_i x^{564-i} = M(x).$$

**Table 1. $p(n)$, the probability of making $n$ errors $0 \leq n \leq 8$**

| | $p(n)$ as a function of $n$ | | | | | | | | |
|---|---|---|---|---|---|---|---|---|---|
| Input Bit Error Probability $P$ | $p(0)$ | $p(1)$ | $p(2)$ | $p(3)$ | $p(4)$ | $p(5)$ | $p(6)$ | $p(7)$ | $p(8)$ |
| 0.005 | 0.0494 | 0.1490 | 0.2242 | 0.2246 | 0.1688 | 0.1009 | 0.0503 | 0.0214 | 0.0127 |
| $10^{-3}$ | 0.5487 | 0.3295 | 0.0988 | 0.0197 | $2.944 \times 10^{-3}$ | $3.514 \times 10^{-4}$ | $3.488 \times 10^{-5}$ | $2.963 \times 10^{-6}$ | $7.576 \times 10^{-8}$ |
| $10^{-4}$ | 0.9418 | 0.0565 | $1.693 \times 10^{-3}$ | $3.374 \times 10^{-5}$ | $5.037 \times 10^{-7}$ | $6.005 \times 10^{-9}$ | $<10^{-10}$ | $<10^{-12}$ | $<10^{-14}$ |
| $10^{-5}$ | 0.9940 | $5.964 \times 10^{-3}$ | $1.786 \times 10^{-5}$ | $3.561 \times 10^{-8}$ | $<10^{-10}$ | $<10^{-13}$ | $<10^{-16}$ | $<10^{-19}$ | $<10^{-22}$ |

**Table 2. Output word error probabilities**

| | | Four modes of operation | | | | | | | | | | | |
|---|---|---|---|---|---|---|---|---|---|---|---|---|---|
| Input bit error probability | Probability of one or more errors | Detecting 7 errors | | | Correcting 1 Detecting 6 | | | Correcting 2 Detecting 5 | | | Correcting 3 Detecting 4 | | |
| | | A | B | C | A | B | C | A | B | C | A | B | C |
| $5 \times 10^{-3}$ | 0.95 | 0.946 | 0 | <0.004 | 0.80 | 0.15 | <0.007 | 0.57 | 0.42 | <0.02 | 0.17 | 0.62 | <0.04 |
| $10^{-3}$ | 0.45 | 0.45 | 0 | $<10^{-7}$ | 0.12 | 0.75 | $<10^{-6}$ | 0.023 | 0.95 | $<10^{-5}$ | 0.003 | 0.992 | $<10^{-4}$ |
| $10^{-4}$ | 0.06 | 0.06 | 0 | $<10^{-14}$ | 0.002 | 0.987 | $<10^{-12}$ | $3.4 \times 10^{-5}$ | 1 | $<10^{-10}$ | $5 \times 10^{-7}$ | 1 | $<10^{-8}$ |
| $10^{-5}$ | 0.006 | 0.006 | 0 | $<10^{-22}$ | $1.8 \times 10^{-5}$ | 0.994 | $<10^{-14}$ | $3.6 \times 10^{-8}$ | 1 | $<10^{-16}$ | $<10^{-10}$ | 1 | $<10^{-13}$ |

A = Probability of detected but uncorrectable error.
B = Fraction of words with detected errors that are corrected.
C = Output word error probability (these are estimates and should be regarded as upper bounds).

This $M(x)$ is then divided by $P(x) = f_1 f_3 f_5(x^3 + 1)$ where $f_1(x) = x^{10} + x^3 + 1$; $f_3 = x^{10} + x^3 + x^2 + x + 1$, $f_5 = x^{10} + x^7 + x^3 + x^2 + 1$. The remainder

$$R(x) = \sum_{i=0}^{32} b_i x^i$$

is formed, and the parity checks ($b_i$) are sent. (In order to have a nonzero modulus after division by $P(x)$, certain positions in the encoder are complemented by a polynomial $F(x)$ at the end of encoding. This is done to facilitate synchronization. We take this complementation into account by forming the correct $M(x) + R(x)$ from the received word by re-adding in the $F(x)$.) From $M + R$ we compute $S(x)$, the remainder of the division of $M + R$ by $P(x)$.

Evaluate $S(\beta^j) = S_j$, $j = 1, 3, 5$, where $\beta$ is a root of $f_1(x)$. Note that $S_j = \sum a_i \beta^{(564-i)} = 0$ for a correctly received word. Relabel $c_j = a_{459-j}$; $c_m = 0$, $j \leq 459$. Then

$$S_j = \sum_{i=0}^{1022} c_i \beta^{-ij}.$$

Thus, if $t$ errors are made in positions $j_1, j_2, \ldots, j_t$, we have

$$S_1 = \sum_{i=1}^{t} \beta^{-j_i}, \; S_3 = \sum_{i=1}^{t} \beta^{-3j_i}, \; S_5 = \sum_{i=1}^{t} \beta^{-5j_i}$$

Letting $\gamma = 1/\beta$, we have the symmetric power sums in the error positions $\gamma^{j_1}, \gamma^{j_2}, \ldots, \gamma^{j_t}$. The program is described in the next section.

*c. Decoding program*

(1) Compute $S_1, S_3, S_5$

(2) Calculate $R_3 = S_3 + S_1^3$

(3) If $R_3 = 0$, a single error has been made in the position $S_1 = \gamma^{\ell}$, $\ell > 459$. (Note: NASCOM furnishes in effect the fact that the received word has one or two errors; if it does not have errors, the entire procedure is bypassed.)

(4) If $R_3 = 0$, check if $S_5 = (S_3R_3/S_1) + S_1^5$. If so, then 2 errors have been made. These are the roots of the quadratic equation

$$x^2 + \sigma_1 x + \sigma_2 = 0; \qquad \sigma_2 = R_3/S_1.$$

The quadratic can be solved and mechanized using technique of Ref. 1.

(5) If $S_5 \neq (S_3R_3/S_1) + S_1^5$, then 3 or more errors have been made. Solve the cubic $x^3 + S_1x^2 + \sigma_3 = 0$, where $\sigma_2 = (S_1^3S_3 + S_5)\ R_3$; $\sigma_3 = (S_1S_5 + S_1^3S_3 + R_3^2)/R_3$. The roots of this cubic, which are the error positions, can be found either via a search routine or by using the method for solving cubics in Ref. 1.

(6) If the above cubic does not have three roots in the field generated over the 2-element field by $\beta$, an error has been detected which cannot be corrected, i.e., 4 or more errors have occurred.

Work is under way to find the most efficient method of implementing this decoding procedure on SFOF computers.



# E. Digital Devices Development: Nine-Channel Autocorrelator and SDS 900 Series Computer Interface Logic

*E. B. Lutz*

## 1. Introduction

The following is a description of the logic used in interfacing the nine-channel autocorrelator and the SDS 930 Computer at the Venus DSS test site. The main purpose of interfacing is to optimize the efficiency of the computer in controlling external devices (Ref. 3).

The basic setup is easily explained by means of Fig. 8, which shows a 30-ft cable connecting the autocorrelator with the SDS 930 through the POT and PIN cards which contain the interface logic. These so-called "J-Cards" are standard ZX-11 blank cable plugs which are modified to contain integrated circuit logic.

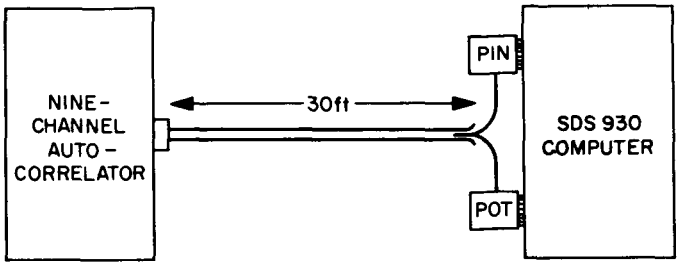


**Fig. 8. 30-ft Interface cable from nine-channel autocorrelator to SDS 930**

In controlling peripheral units, the computer transmits a 24-bit word in parallel, of which a certain number of bits is decoded to determine which of the external devices is to be selected. Other bits are decoded and used to generate specific functions inside the unit being selected. These commands are generated by the computer and transmitted through the POT card while data from the external device will be entered into the computer through the PIN card.

## 2. Functions

Table 3 shows the various functions and the corresponding octal codes for the nine-channel autocorrelator. Bits 3 through 11 describe the EOM for external units (octal 023), and bits 0 through 2 and 18 through 20 specify the class to which the nine-channel autocorrelator belongs (octal 06). In addition, the unit designation (bits 21 through 23) distinguishes between units belonging to the same class and is set to octal 0 for the nine-channel autocorrelator. The various functions such as load, precess, etc., are uniquely specified by bits 12 through 17. Whenever data is to be sent to the computer (PIN Operation), the function code assumes the octal value of 40.

## 3. Description

Figs. 9 and 10 show the logic diagrams of the POT and PIN cards, respectively. Both cards utilize Signetics integrated circuits to a large extent, in combination with passive discrete components, such as diodes, resistors, and capacitors. Those lines which carry information from the computer's C-register are designated by $C_0$, $C_1$, $C_2$, etc., and are in one-to-one correspondence with bits 0 through 23 in Table 3. In addition, such lines as $\overline{Ssc}$, Qq2, etc., perform the necessary control and timing functions which are thoroughly explained in the SDS manuals (Ref. 4). The signal lines LL1 through LL5 and PTUE transmit data to the correlator, and their functions can be found in Table 3.

**Table 3. 9-Channel autocorrelator function commands**

| Command | C-Register | | | | | | | |
|---|---|---|---|---|---|---|---|---|
| | Class | EOM | | EOM Type | Function | | Class | Unit |
| | 1st octal | 1st octal | 2nd octal | | 1st octal | 2nd octal | 2nd octal | |
| | 0 1 2 | 3 4 5 | 6 7 8 | 9 10 11 | 12 13 14 | 15 16 17 | 18 19 20 | 21 22 23 |
| Load D/A | 0 | 0 | 2 | 3 | 3 | 0 | 6 | 0 |
| Stop count — start output | 0 | 0 | 2 | 3 | 3 | 1 | 6 | 0 |
| Precess output | 0 | 0 | 2 | 3 | 3 | 2 | 6 | 0 |
| Restart count | 0 | 0 | 2 | 3 | 3 | 3 | 6 | 0 |
| Shift D/A, insert zero | 0 | 0 | 2 | 3 | 3 | 4 | 6 | 0 |
| Shift D/A, insert one | 0 | 0 | 2 | 3 | 3 | 5 | 6 | 0 |
| Lower X-Y pen | 0 | 0 | 2 | 3 | 3 | 6 | 6 | 0 |
| Raise X-Y pen | 0 | 0 | 2 | 3 | 3 | 7 | 6 | 0 |
| PIN setup | 0 | 0 | 2 | 3 | 4 | 0 | 6 | 0 |

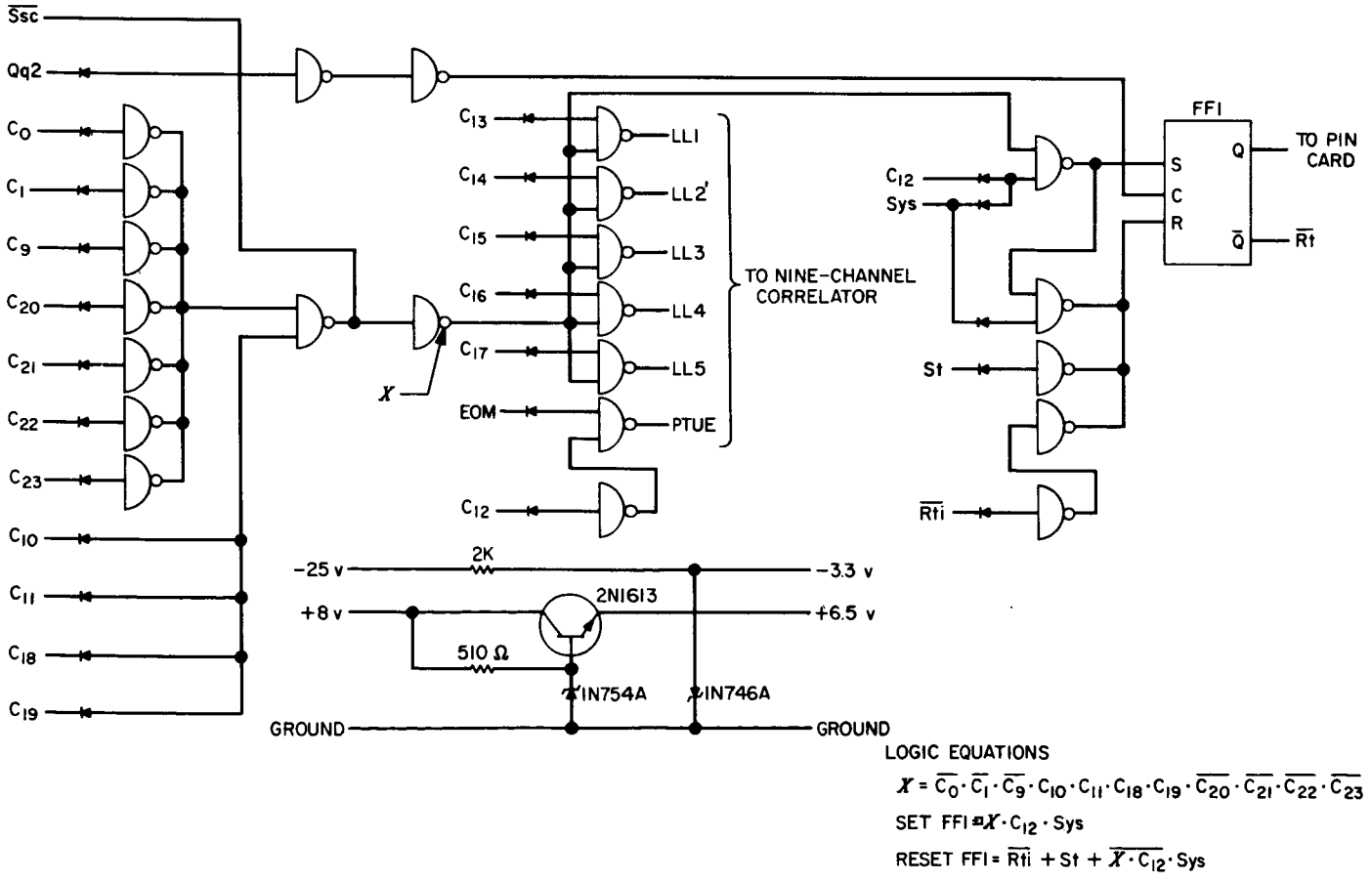


**Fig. 9. POT card logic**

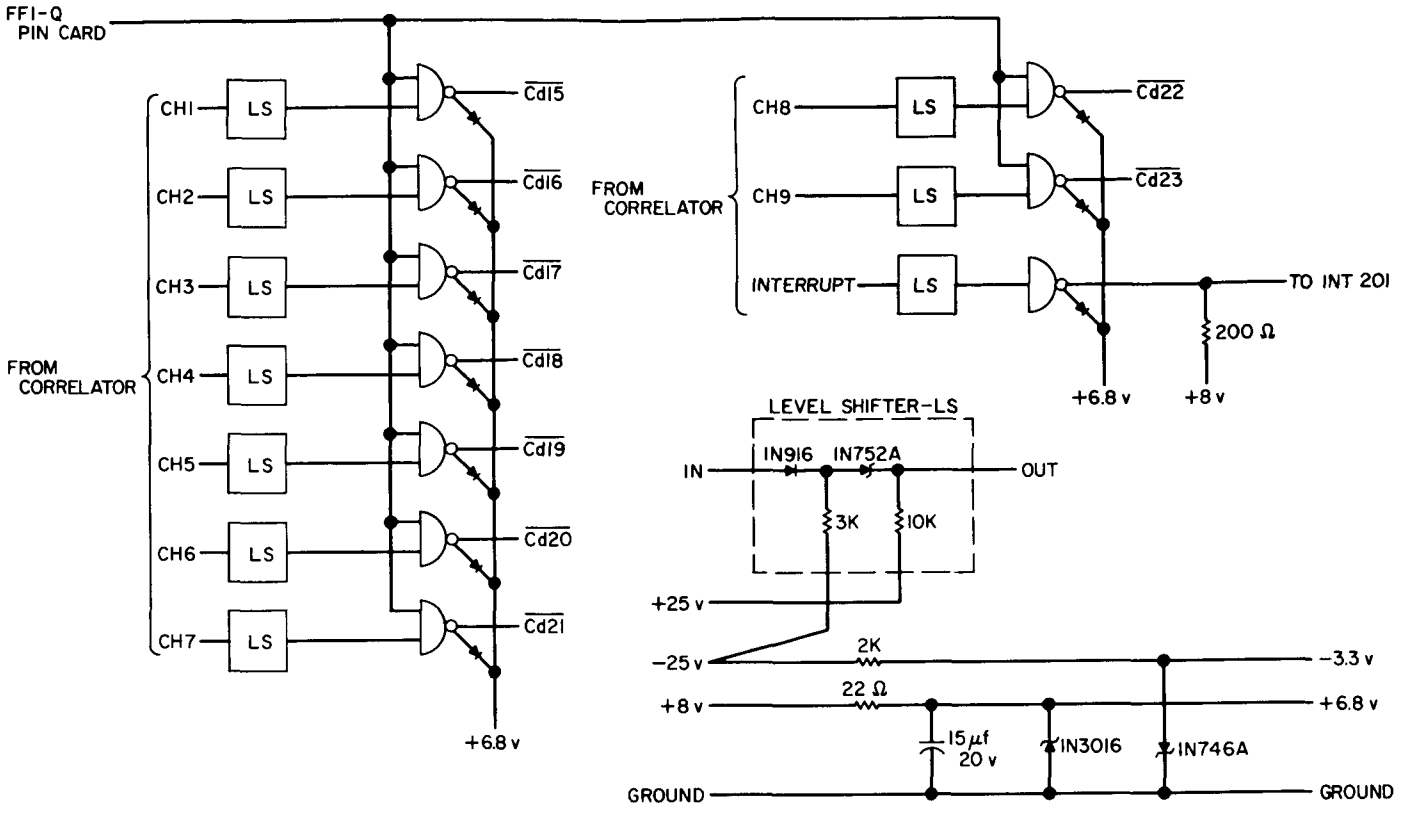


**Fig. 10. PIN card logic**

When an EOM 40 *(PIN setup)* is executed, FF1 is set, enabling the gates on the PIN card which then will recognize data sent from the correlator through the channel lines CH1, CH2, etc. Those lines then enter the C-register through Cd15, Cd16, etc. The level shifters (LS) serve the purpose of translating negative logic from the correlator into the appropriate positive levels which are standard to the SDS 930 computer. FF1, when set, also signals the computer through Rt that it must exit the *wait* phase and start receiving data. In addition, an *interrupt* line (INT 201) is derived from the PIN card logic and fed to a corresponding *interrupt* jack-mounted on a card which plugs into the same connector cage.

In order to insure reliable operation, the interface logic circuits are powered by 6.5-v supplies which are derived from the standard SDS + 8 v. This was done primarily to avoid exceeding the 8-v breakdown ratings on the integrated circuits.

### 4. Conclusion

Initial tests on the cable plus interface cards were performed at JPL on an SDS 930 computer, simulating the various logical conditions. Final tests at the Venus DSS were found to be satisfactory, and the logic is currently installed and operative.



## F. Microwave Maser Development: Extension of Klystron Tuning Range

R. Clauss

### 1. Introduction

Two tunable traveling wave masers have been delivered to Goldstone (February and June, 1966). Descriptive information and data for these amplifiers can be found in *SPS* 37-37 through 37-40, Vol. III under the heading "Microwave Maser Development." The basic difference between the new TWM's and masers previously used at the Goldstone Deep Space Stations is tunability. The new slow-wave comb structure has been

designed and loaded to give a tuning range which covers both 2295 and 2388 Mc. When the signal frequency is changed, the pump klystron frequency must also be changed. An external over-coupled cavity is used with the pump klystron to extend its electronic tuning range. No mechanical adjustments at the maser package are necessary when the signal frequency is tuned to either 2295 or 2388 Mc. This frequency change may be accomplished entirely from the maser instrumentation rack.

## 2. *Dual Frequency Klystron Package*

VA 246E and VA 246R klystrons have been used to pump S-band masers for several years. This field experience has shown that these tubes have adequate power, good stability, and reliability. These klystrons, however, do not have sufficient tuning range to cover maser operation at both 2295 and 2388 Mc. A brief survey of available klystrons has not yielded a tube suitable for the required tuning range. A change to other pump sources (such as a backward wave oscillator) might present new stability, reliability, or compatibility problems and has not been considered at this time.

Laboratory tests of a VA 246R klystron with an external overcoupled cavity have resulted in a split mode of operation with frequencies spread much more than the normal tuning range. The external cavity is formed by the use of irises and a one-half wavelength section of guide through the klystron heat sink. Fig. 11 shows the assembly sequence for the klystron and external cavity. Figs. 12 and 13 show the irises which fit a standard waveguide flange. Capacitive tuning is accomplished with a tuning screw in the heat sink. Klystron tuning range is determined by the coupling and Q of the external cavity. The iris sizes determine the loaded Q and coupling between the klystron and external cavity.

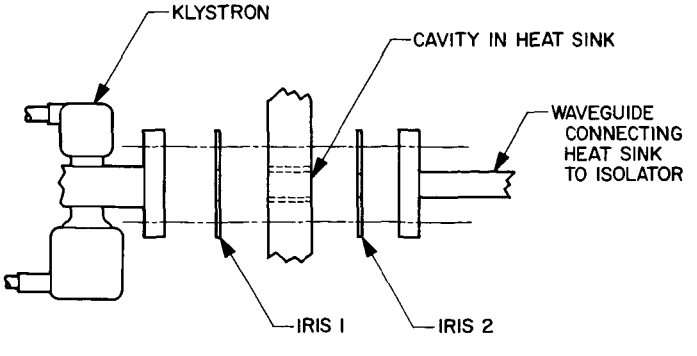


**Fig. 11. Klystron and external cavity**

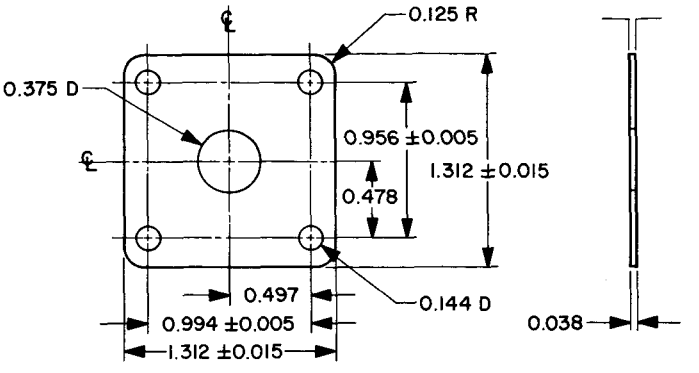


**Fig. 12. Iris 1 of Fig. 11**

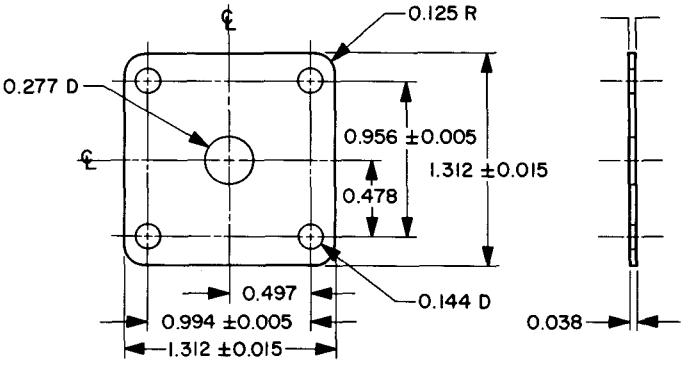


**Fig. 13. Iris 2 of Fig. 11**

Mechanical tuning adjustments are required after assembly of the dual frequency klystron package prior to installation on the maser package. A block diagram of the klystron package is shown in Fig. 14. Test equipment to be used during the tuning procedure is shown in Fig. 15. By frequency modulating the klystron a display of frequency versus power may be viewed on an oscilloscope (for initial adjustments). During normal operation with the maser the klystron is in a CW mode. The klystron frequency is determined by the reflector voltage. In Fig. 16 (a graph of frequency versus reflector voltage) it is interesting to note that a double-valued region exists. In this region (shaded on Fig. 16) the klystron frequency is dependent upon the direction of reflector voltage change. For example, if a setting of 325 v is approached from 350 v, the klystron will oscillate at 12.872 kMc. If the setting of 325 v is approached from 300 v, the klystron will oscillate at 12.724 kMc. Even in this double-valued region stability has been excellent,

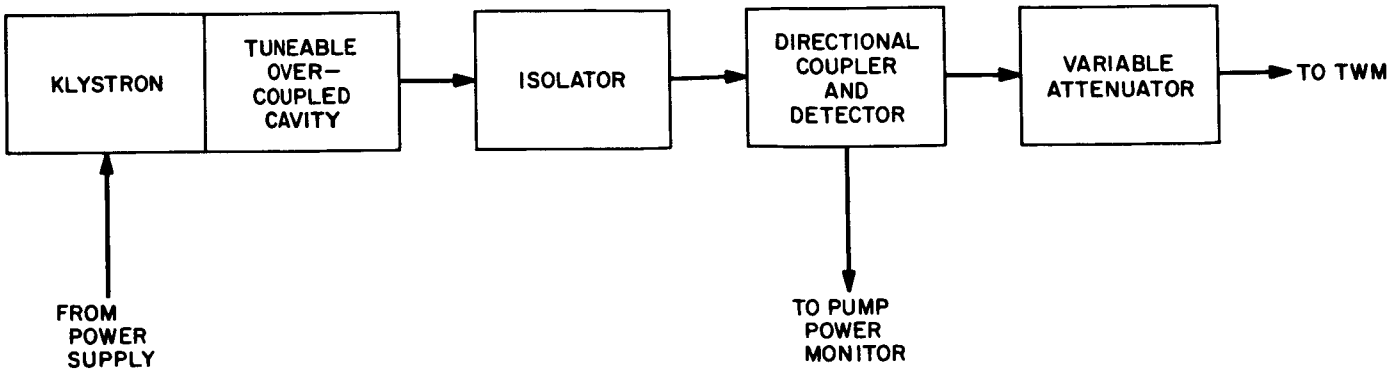


**Fig. 14. Dual-frequency klystron package block diagram**

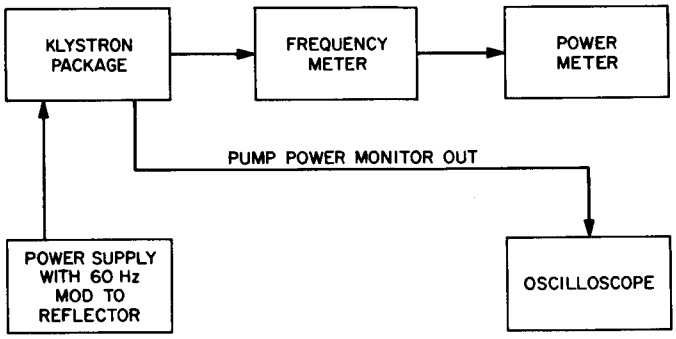


**Fig. 15. Test equipment block diagram**

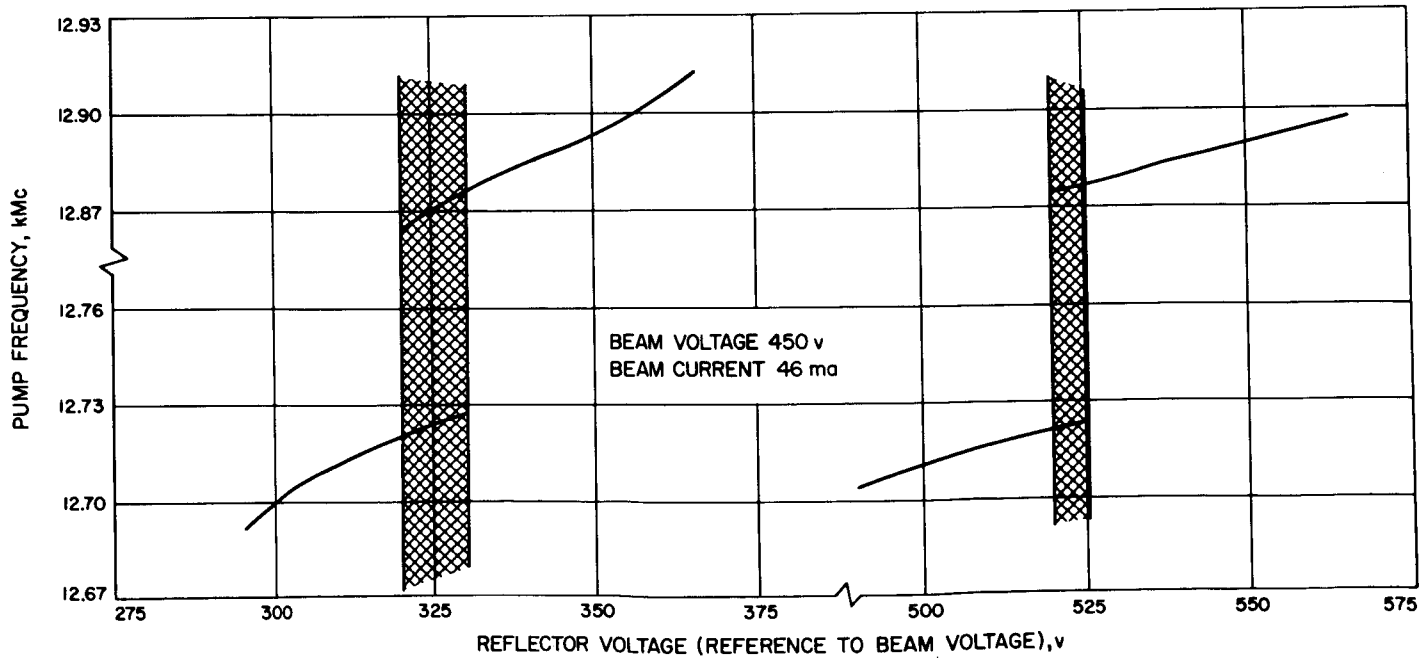


**Fig. 16. Klystron frequency versus reflector voltage**

both during laboratory testing and field operation. The TWM requires approximately 100 mw of pump power. Fig. 17 shows pump power output versus frequency. The data was taken during preparation of a dual-frequency klystron package which is now in use at the Mars DSS.

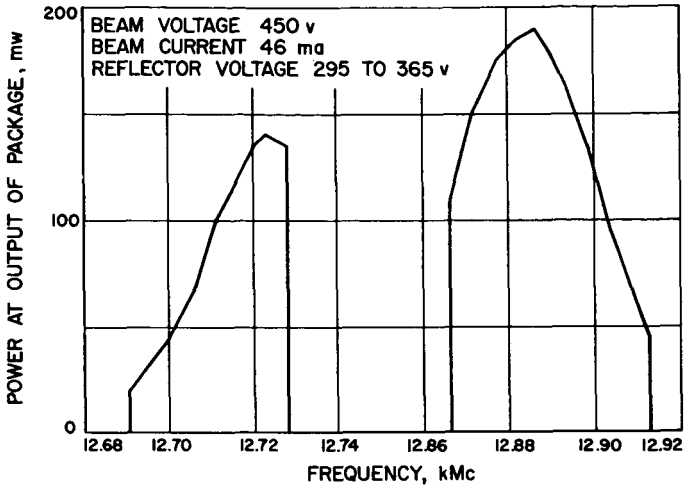


**Fig. 17. Klystron power versus frequency**

The phenomenon of "frequency pulling" due to a cavity external to the klystron is well known and is usually avoided. Here it is used to extend the tuning range of a fix-tuned klystron.



# G. Frequency Generation and Control: Atomic Hydrogen Frequency Standard Evaluation

*W. Higa*

A simple technique has been used to evaluate the stability characteristics of a traveling wave tube (TWT). In addition to providing pertinent information regarding the TWT as a possible follow-up amplifier to the atomic hydrogen maser, the experiment itself is important in establishing a method for future evaluation of the atomic frequency standard.

As shown schematically in Fig. 18 a phase bridge is used to measure the relative phase shift between two

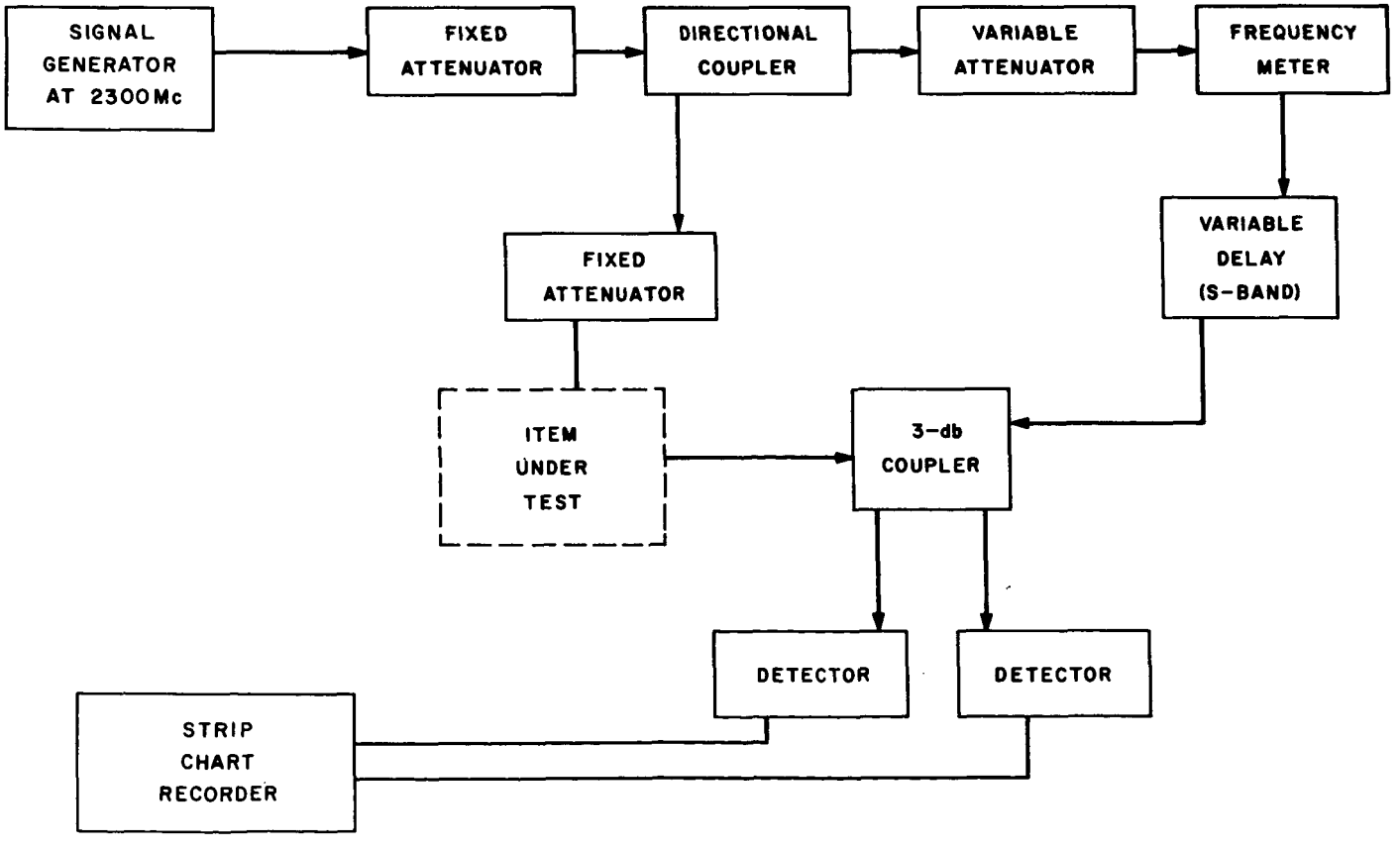


**Fig. 18. Block diagram for phase stability measurement**

signal paths with the test device (unknown) in one of the paths. A pair of matched diodes was used as synchronous detectors and provided adequate sensitivity. In order to minimize differential phase errors due to frequency excursions in the signal generator, it was necessary to equalize the electrical lengths of the two paths. This was achieved by means of a precision S-band delay line in one of the paths.

The calibrated delay line also provided the means for calibrating the sensitivity of the phase bridge. A resolution of the order of 0.05 deg was readily achieved. Fig. 19 shows a typical recording with passive elements (coaxial cable) in both paths of the phase bridge. Short-term jitter is of the order of ±0.05 deg, and the drift over the period of an hour is of the same order of magnitude.

Fig. 20 shows the stability test with the TWT (Watkins-Johnson Model WJ 268-2). The short- and long-term phase variation is seen to be increased slightly to around ±0.25 deg. The origin of the short-term jitter needs to be investigated; its regularity suggests the possibility of inadequate filtering in the built-in power supply and may be easily resolved.

The dual-channel traveling wave maser (TWM) for the hydrogen line frequency (1420 MHz) is being completed. Stability tests similar to that described here will be made before using the TWM to evaluate the short-term stability of the hydrogen maser.

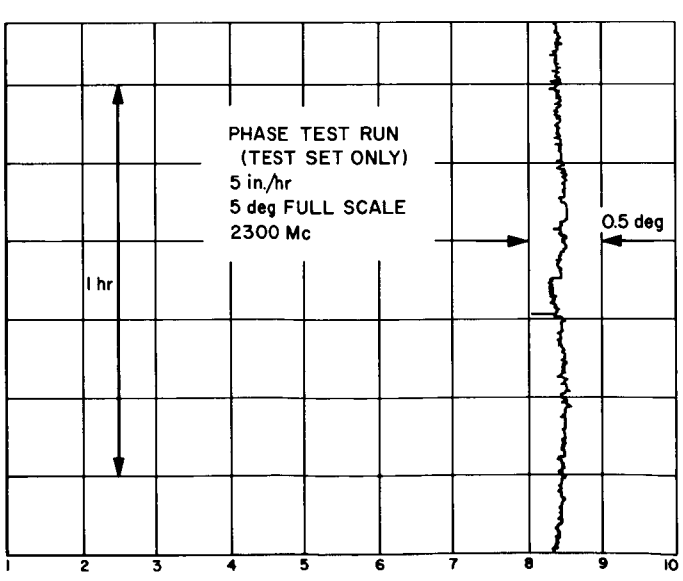


**Fig. 19. Calibration test-run for system of Fig. 18 with passive elements**

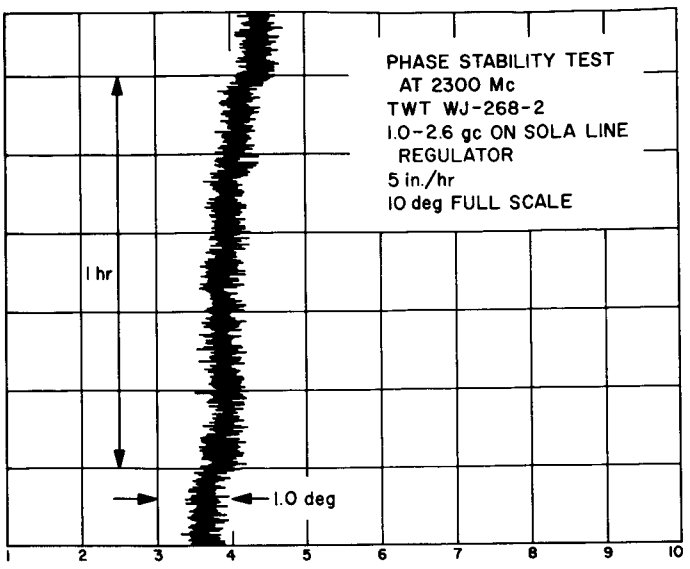


**Fig. 20. Test results for TWT (Note reduced sensitivity as compared with Fig. 2)**



# H. Improved RF Calibration Techniques: Noise Temperature Calibrations

*T. Y. Otoshi and C. T. Stelzried*

## 1. R&D Cone

Calibrations of the Venus DSS R&D cone were performed during May and June, 1966 at JPL on the roof of Bldg. 238. The calibration work basically consisted of measurements of: (1) transmission line insertion losses and reflection coefficients, (2) antenna noise temperature, (3) receiver noise temperature, and (4) high and low gas tube temperatures.

Descriptions of the RF cone instrumentation, the RF calibration system, and a tabulation of recently measured insertion losses and reflection coefficients were presented in *SPS 37-40*, Vol. III, pp. 93–100.

Noise temperature measurements were performed by the Y-factor method, which involves the use of two thermal reference noise standards and switching between the unknown and the thermal noise standards. For the cone calibrations, the two thermal standards used were a cryogenically cooled waveguide termination and an

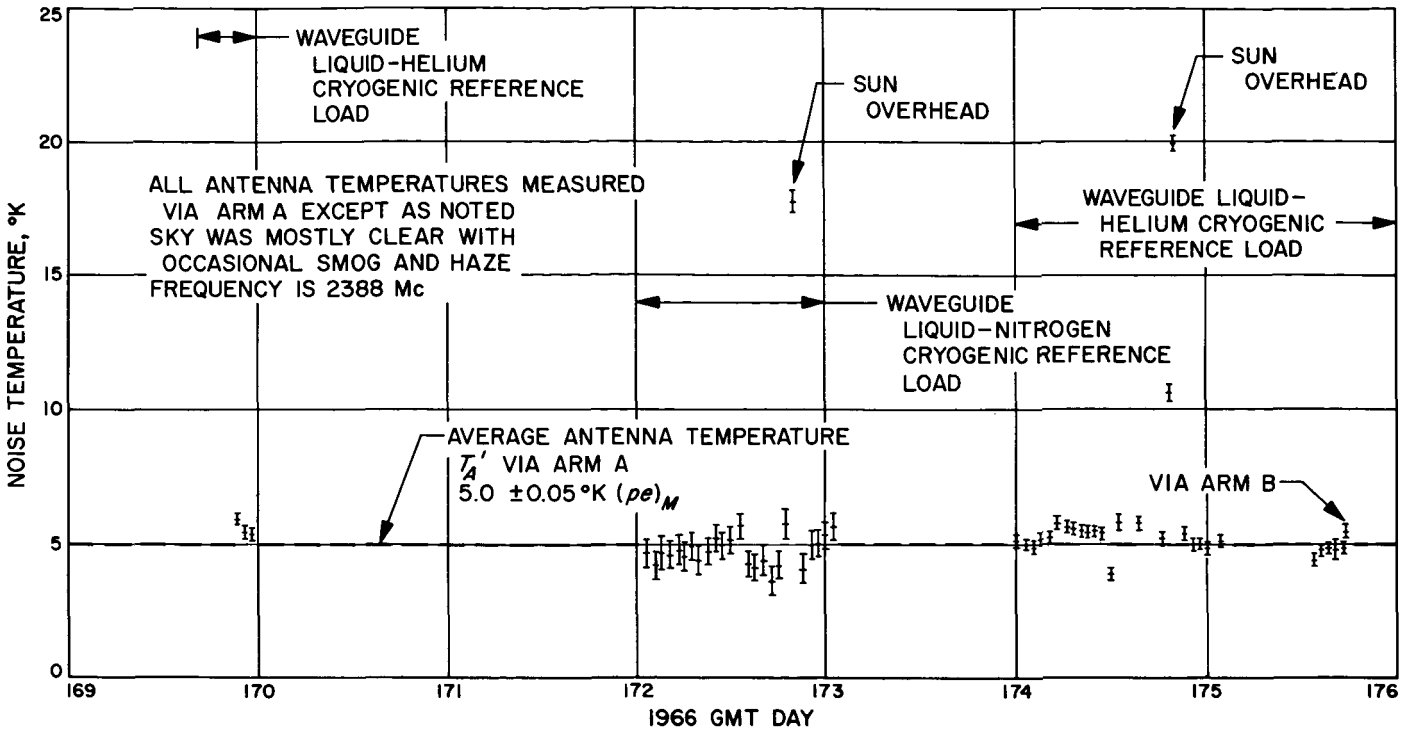


**Fig. 21. R&D cone antenna noise temperature defined at the antenna output reference flange**

ambient waveguide termination. The Y-factor equations as well as probable errors for this measurement technique are discussed in *SPS 37-39*, Vol. IV, pp. 86–91.

Fig. 21 shows the results of antenna noise temperature calibrations made at 2388 Mc for the antenna in the circular polarization mode. The antenna noise temperature in this figure is defined at the antenna output reference flange which (for this cone) is the input to the circular waveguide rotary joint preceding the turnstile junction. Each data point represents the average of 10 sets of Y-factor measurements. The probable error associated with each data point includes the probable errors of the effective cryogenic load temperature, ambient load temperature, Y-factor ratios, and the measurement precision index. The probable error, however, does not include the errors due to mismatch, which are treated separately.

A calibration run was made each hour over approximately 24-hr periods to permit study of antenna temperature variations due to weather and radio sources. The first 24-hr sequence used a liquid nitrogen-cooled waveguide load (MMC SR 8135 SN 004) as the cryogenic reference standard, and the second 24-hr sequence used a liquid helium-cooled waveguide load. Comparisons of the results from the two 24-hr runs provide a check on the consistency of the antenna temperature measurements as well as a cross check on the stability and accuracy of the cryogenic loads. In Fig. 21 it is of interest to note the periodic rise in the antenna temperature caused by the Sun passing overhead during the noon hours.

Figs. 22, 23, and 24 show plots of the 2388-Mc. line-loss temperature contribution, receiver temperature, and gas tube temperatures, respectively. The line-loss temperature contribution is the difference between antenna temperature defined at the receiver reference flange and the antenna temperature defined at the antenna output reference flange (previously defined). The receiver reference flange for this cone is defined to be the output of the 26-db directional coupler (*SPS 37-39*, Vol. III).

The overall average noise temperatures for the R&D cone at 2388 Mc are summarized in Table 4. The overall averages were computed from the data points shown in the figures, with the exception of omitting those antenna temperature data points obtained when the Sun was overhead. The probable error shown with each average is the measurement precision index of the overall average. The tabulated uncertainties due to mismatch errors are the present best estimates and are based upon the noise temperature mismatch error analysis for two port networks presented in *SPS 37-40*, Vol. IV, pp. 202–208.

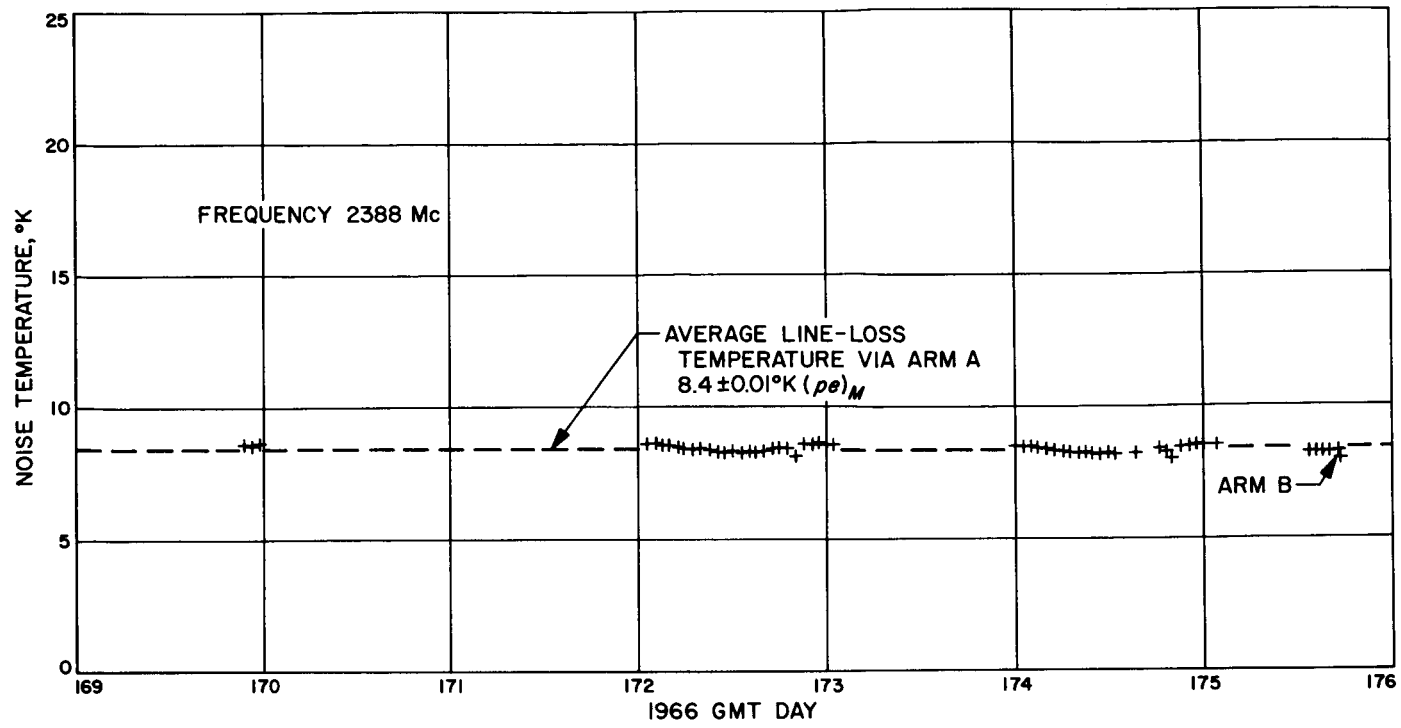


**Fig. 22. R&D cone noise temperature contributed by antenna line loss via Arm A**

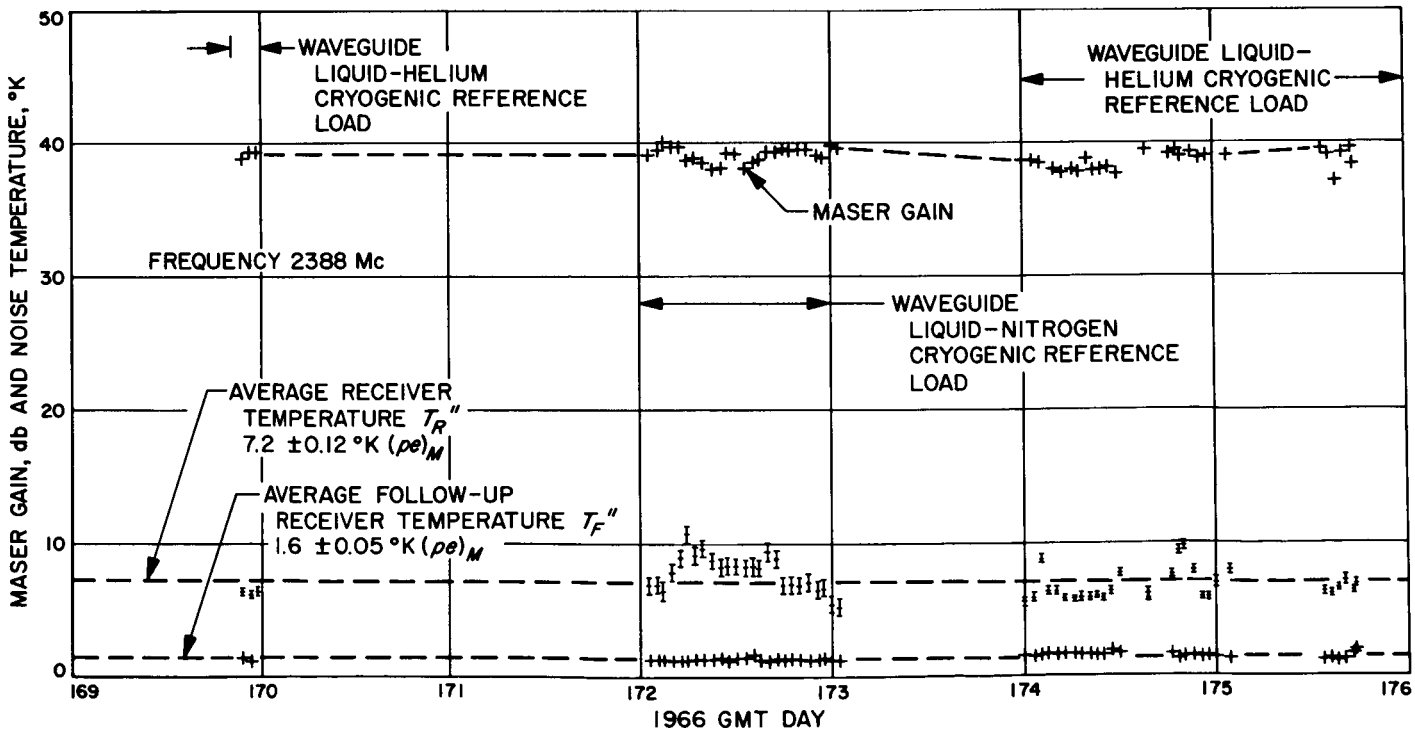


**Fig. 23. R&D cone maser gain and the receiver and follow-up noise temperatures defined at the receiver reference flange**

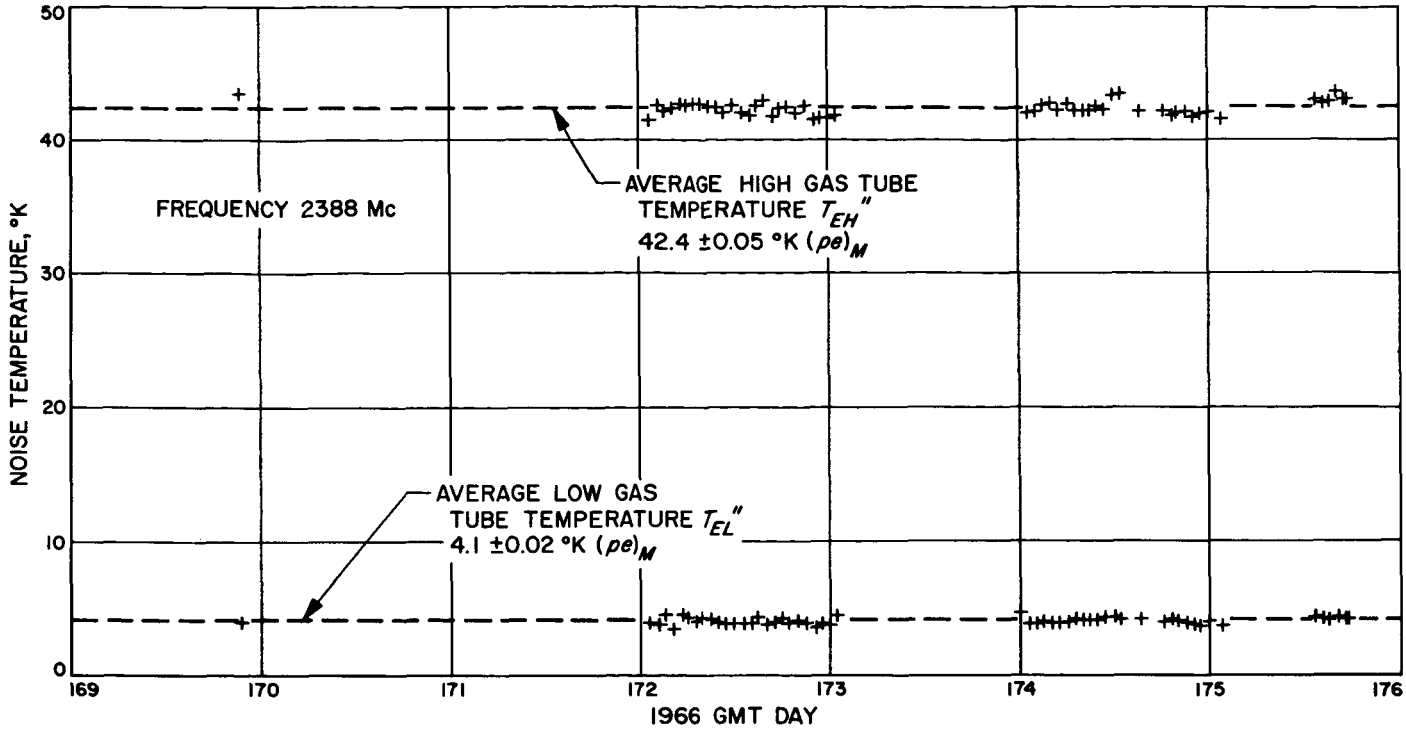


**Fig. 24. R&D cone high and low gas tube noise temperatures defined at the receiver reference flange**

**Table 4. Summary of average noise temperatures for R&D cone at 2388 Mc**

| Noise source | Reference flange | Average noise temperature, °K | Peak uncertainties due to mismatch, °K |
|---|---|---|---|
| Antenna via Arm A | Antenna output | 5.0 ± 0.05 $(pe)_M$ | ±1.0 |
| Transmission line loss contribution via Arm A | | 8.4 ± 0.01 $(pe)_M$ | |
| Receiver | Receiver | 7.2 ± 0.12 $(pe)_M$ | ±0.2 |
| System via Arm A | Receiver | 20.6 | |
| Followup receiver contribution | Receiver | 1.6 ± 0.05 $(pe)_M$ | |
| High gas tube | Receiver | 42.4 ± 0.05 $(pe)_M$ | |
| Low gas tube | Receiver | 4.1 ± 0.02 $(pe)_M$ | |

$(pe)_M$ denotes the measurement precision index of the average.

## 2. 85-Ft Dish/R&D Cone

After calibrations were completed at JPL, the R&D cone was shipped to the Venus DSS and installed on the 85-ft antenna system. The results of two weekly noise temperature calibrations of this system at 2388 Mc are shown tabulated in Table 5. These preliminary system temperature measurements of the 85-ft antenna system give approximately 22.0°K (with 0.4°K for the followup receiver) as compared to a 19.4°K system temperature measured for the R&D cone on the ground if we assume the same followup contribution for an equal-basis comparison.

The difference in system temperatures for the R&D cone on the ground and on the 85-ft dish should be due mainly to the difference in the antenna temperatures. If the system temperature difference of 2.6°K is added to the antenna temperature of 5.0°K measured for the R&D cone on the ground, then the antenna temperature measured for the R&D cone on the 85-ft dish should be 7.6°K. However, examination of the preliminary data in Table 5 reveals that the antenna temperature measured for the R&D cone on the 85-ft antenna is approximately 6.6°K. The discrepancy of 1°K is believed to be caused by uncertainties in the liquid-nitrogen–cooled load used in the measurement. Further examination of the data in Table 5 shows that the receiver temperature measured during the weekly calibrations is hotter than those measured when the cone was on the ground. A difference between the calibrated and actual value for the cryogenic load temperature can result in the measured receiver temperature being too high and the antenna temperature being too low.

**Table 5. Summary of 85-ft dish/R&D cone weekly calibrations at 2388 Mc**

| Noise source | Reference flange | Turnstile junction arm | Noise temperatures, °K | | Peak uncertainties due to mismatch, °K |
|---|---|---|---|---|---|
| | | | GMT day 198 | GMT day 205 | |
| Antenna | Antenna output | A | 6.6 ± 0.48 (p.e.) | 6.3 ± 0.48 (p.e.) | ±1.2 |
| | | B | 6.8 ± 0.48 (p.e.) | 6.6 ± 0.48 (p.e.) | ±1.1 |
| Transmission line loss contribution | | A | 8.6 | 8.4 | |
| | | B | 8.3 | 8.1 | |
| Receiver | Receiver | | 6.8 ± 0.57 (p.e.) | 7.6 ± 0.57 (p.e.) | ±0.3 |
| System | Receiver | A | 21.9[a] | 22.3 | |
| | | B | 21.9 | 22.2[a] | |
| Follow-up receiver contribution | Receiver | | 0.4 | | |
| High gas tube | Receiver | | 44.8 | 44.3 | |
| Low gas tube | Receiver | | 4.4 | 4.2 | |

[a]Difference between given system temperature and that obtained by adding contributing temperatures is due to round-off.

A study is presently being made to determine the causes of discrepancies in the cryogenic load temperature. One possible source of error being investigated is the pressure differential between the atmosphere and the gas of the cryogenic fluid inside the dewar.

Evaluation of the RF characteristics of a number of radome materials was made from data received on the Venus DSS cone. Radiometric measurements were made with and without samples of the radome material over the horn (Fig. 25), and four separate computer programs were used to reduce and evaluate the data taken.



# I. RF Techniques: Evaluation of Radome Materials for the Ascension Island DSS Antenna

*B. Seidel and C. Stelzried*

## 1. Introduction

RF characteristics of radome materials have been evaluated by the use of radiometric measurements. Computer techniques were used for the evaluation and error analysis data handling.

Unfortunately, the time available for this experiment did not allow for repeatability data on the various samples. Therefore, in some cases the tolerances on the results are of the same order of magnitude as the results themselves. It is felt, however, that the results of the experiment with a probable error of approximately 0.01 db are still useful.

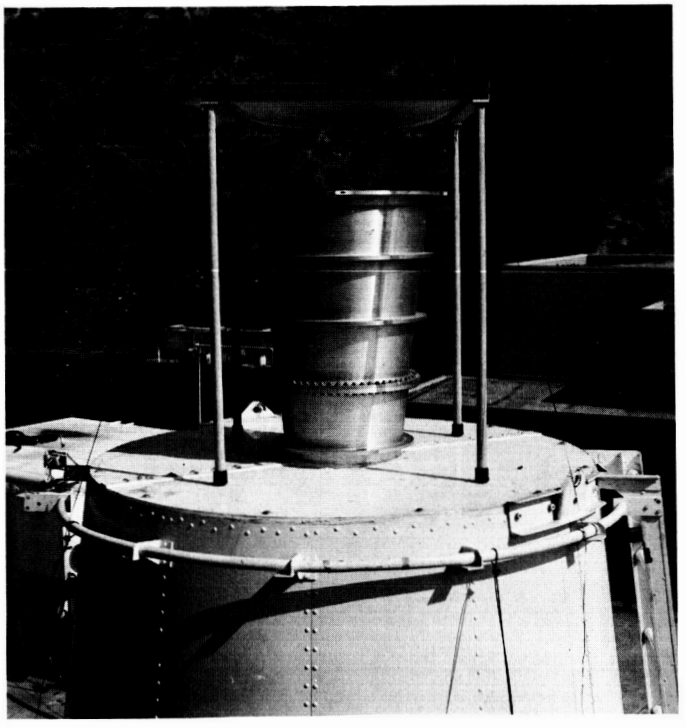

**Fig. 25. Venus DSS cone with sample of radome material over the horn**

## 2. Theory

A block diagram of the radiometer system used for the radome material evaluation is shown in Fig. 26. The loss of the material $L_R$ at an ambient temperature $T_0$ is determined from system effective noise-temperature measurements looking at the sky $(T'_{SA})_2$ and $(T'_{SA})_1$, with and without the material placed between the horn pointed at zenith and the sky. The effective noise temperatures of the sky $T'_2$ and $T_2$ with and without the material in place, are related by Ref. 5.

$$T'_2 - T_2 = (T_0 - T_2)\left(1 - \frac{1}{L_R}\right) \qquad (1)$$

The measured change in system temperature is therefore

$$(T'_{SA})_2 - (T'_{SA})_1 = (T_0 - T_2)\left(1 - \frac{1}{L_R}\right) \qquad (2)$$

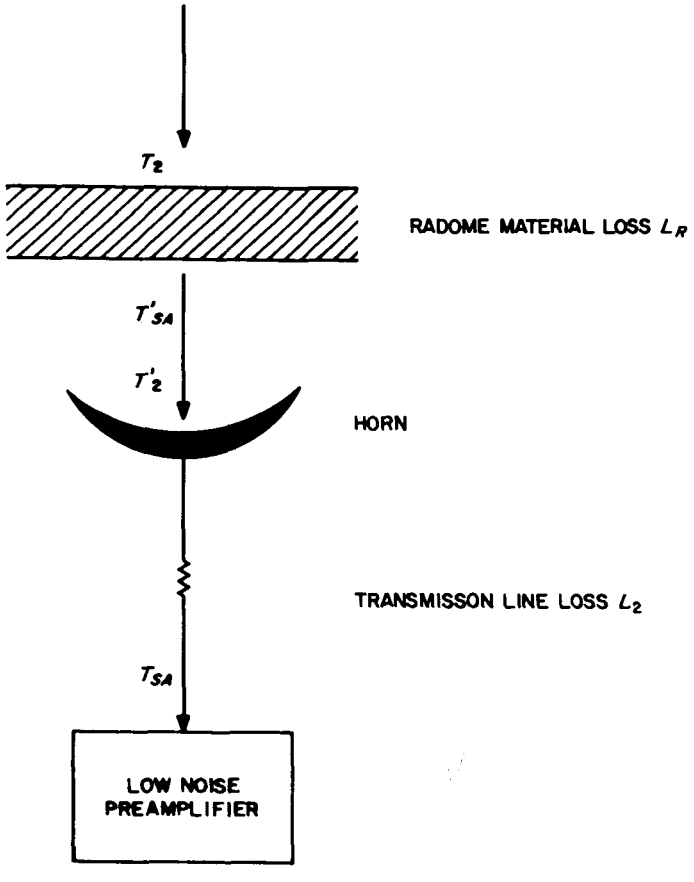


**Fig. 26. Block diagram of radiometer system for radome material evaluation**

The noise-temperature measurements are most conveniently referred to the maser input (Ref. 6, IBM 1620 computer program CTS/20B) through the transmission line loss $L_2$

$$L_2\left[(T_{SA})_2 - (T_{SA})_1\right] = (T'_{SA})_2 - (T'_{SA})_1 \qquad (3)$$

Manipulating Eqs. (2) and (3)

$$L_R = \frac{1}{1 - L_2\dfrac{(T_{SA})_2 - (T_{SA})_1}{T_0 - T_2}} \qquad (4)$$

The probable error of $L_R$ is given by Ref. 7

$$PE_{L_R} = \left[PE^2_{L_2}\left|\frac{\partial L_R}{\partial L_2}\right|^2 + \left(PE^2_{T_0} + PE^2_{T_2}\right)\left|\frac{\partial L_R}{\partial T_0}\right|^2 + \left[PE^2_{(T_{SA})_2} + PE^2_{(T_{SA})_1} + PE^2_{(T_{SA})_B}\right]\left|\frac{\partial L_R}{\partial T_{SA}}\right|^2\right]^{1/2} \qquad (5)$$

where

$$\left|\frac{\partial L_R}{\partial L_2}\right| = \frac{L_R(L_R - 1)}{L_2}$$

$$\left|\frac{\partial L_R}{\partial T_0}\right| = \frac{L_R(L_R - 1)}{T_0 - T_2}$$

$$\left|\frac{\partial L_R}{\partial T_{SA}}\right| = \frac{L_R^2 L_2}{T_0 - T_2}$$

and

$PE_{L_2}$ = probable error of the transmission line loss, $L_2$

$PE_{T_0}$ = probable error of the ambient temperature, $T_0$

$PE_{T_2}$ = probable error of the sky temperature, $T_2$

$PE_{(T_{SA})_2}$ = probable error of the system temperature measurement with radome material in place due solely to measurement scatter

$PE_{(T_{SA})_1}$ = same as $PE_{(T_{SA})_2}$ except with radome material removed

$PE_{(T_{SA})_B}$ = probable error of system temperature measurements due to instrument bias errors

The system temperature bias errors $PE\ (T_{SA})_B$ are correlated by the measurements, whereas the errors due to system temperature measurement scatter are uncorrelated and add in the usual squared manner. Eqs. (4) and (5) have been programmed for the IBM computer and designated CTS/27A.

Fig. 26 can also be used to derive the effect on system noise performance of the evaluated radome material for any receiving system. The increase in effective system temperature defined at the input of the low noise preamplifier is obtained by manipulating Eq. (4)

$$\Delta T_{SA} = \frac{(T_0 - T_2)\left(1 - \frac{1}{L_R}\right)}{L_2} \qquad (6)$$

The parameters in Eq. (6) pertain to the receiving system under evaluation. The probable error is

$$PE_{\Delta T_{SA}} = \left[ PE^2_{L_2} \left|\frac{\partial \Delta T_{SA}}{\partial L_2}\right|^2 + (PE^2_{T_0} + PE^2_{T_2}) \left|\frac{\partial \Delta T_{SA}}{\partial T_0}\right|^2 + PE^2_{L_R} \left|\frac{\partial \Delta T_{SA}}{\partial L_R}\right|^2 \right]^{1/2} \qquad (7)$$

where

$$\left|\frac{\partial \Delta T_{SA}}{\partial L_2}\right| = \frac{\Delta T_{SA}}{L_2}$$

$$\left|\frac{\partial \Delta T_{SA}}{\partial T_0}\right| = \frac{\Delta T_{SA}}{T_0 - T_2}$$

$$\left|\frac{\partial \Delta T_{SA}}{\partial L_R}\right| = \frac{\Delta T_{SA}}{I^2_R\left(1 - \frac{I}{L_R}\right)}$$

and the probable errors are as previously defined. Eqs. (6) and (7) have been programmed for the IBM 1620 computer and designated CTS/27B.

## 3. Results

Table 6 lists the pertinent results of this evaluation. Some of the samples were unaltered, some had seams, and some were soaked in brine (several days) before measurement, as indicated.

The results of the experiment indicate that, from an RF standpoint, Sample V-25306 should be selected for

**Table 6. Results of tests for various radome materials**

| Sample | $L_R$ db | $PE_{L_R}$ db | $\Delta T_{SA_1}$ °K | $PE_{(\Delta T_{SA})_1}$ °K | $\Delta T_{SA_1}$ °K | $PE_{(\Delta T_{SA})_2}$ °K | Test Conditions |
|---|---|---|---|---|---|---|---|
| 15187 | 0.0282 | 0.0095 | 1.52 | 0.511 | 1.54 | 0.520 | No seam, brine-soaked |
| 15187 | 0.0310 | 0.0079 | 1.67 | 0.425 | 1.70 | 0.432 | Seam, brine-soaked |
| 15878 | 0.0585 | 0.0090 | 3.14 | 0.482 | 3.19 | 0.491 | Seam, brine-soaked |
| 15878 | 0.0650 | 0.0092 | 3.49 | 0.493 | 3.55 | 0.501 | No seam, brine-soaked |
| V-25284 | 0.0265 | 0.0093 | 1.43 | 0.500 | 1.45 | 0.509 | Seam, brine-soaked |
| V-25306 | 0.0162 | 0.0090 | 0.87 | 0.485 | 0.89 | 0.493 | Seam, brine-soaked |
| 15878 | 0.0072 | 0.0088 | 0.38 | 0.475 | 0.39 | 0.483 | No seam |
| V-25284 | 0.0071 | 0.0084 | 0.38 | 0.454 | 0.39 | 0.461 | No seam |
| 15187 | 0.0079 | 0.0086 | 0.42 | 0.464 | 0.43 | 0.472 | Seam |
| V-25306 | 0.0128 | 0.0097 | 0.69 | 0.523 | 0.70 | 0.523 | No seam |

$L_R$ = measured insertion loss of the sample

$PE_{L_R}$ = probable error of the insertion loss measurement

$\Delta T_{SA_1}$ = expected increase in the system temperature of the Ascension Island DSS receiving system when the system is at an ambient temperature of 25°C

$\Delta T_{SA_2}$ = same as $\Delta T_{SA_1}$ except at an ambient temperature of 30°C

$PE_{(\Delta T_{SA})_1}$ = probable error of $\Delta T_{SA_1}$

$PE_{(\Delta T_{SA})_2}$ = probable error of $\Delta T_{SA_2}$

the radome material. However, since none of the materials will vastly degrade the system performance, other considerations (i.e., structural strength) may prove to be the deciding criteria on the material.



# J. Efficient Antenna Systems: Aperture Blockage and Surface Tolerance Loss Calculations for Non-Uniform Illumination and Error Distribution

A. Ludwig

If an antenna with a reasonably well-defined aperture is divided into several segments (concentric rings for example), the efficiency of the whole antenna is related to the efficiency of each segment by

$$\eta = \left[ \sum_{n=1}^{N} (a_n P_n \eta_n)^{1/2} \right]^2 \qquad (1)$$

where

$\eta$ = overall efficiency

$\eta_n$ = efficiency of the $n$th segment

$N$ = number of segments

$P_n$ = fraction of total radiated power intercepted by the $n$th segment

$a_n$ = fractional aperture area in the $n$th segment

All efficiencies are defined by

$$\eta = \frac{G}{4\pi A/\lambda^2} = \frac{G}{G_0} \qquad (2)$$

where in the case of segments

$G$ = the gain of the $n$th segment, measured in the direction of maximum gain of the whole antenna (not necessarily the maximum gain of the segment) assuming that the power incident on the segment is total radiated power (no spillover)

$A$ = physical aperture area of the $n$th segment

Eq. (1) simply expresses the summation of the field contributions of each segment, assuming that the contributions from all segments are *in phase* and normalized by total area and total radiated power. For overall efficiency, spillover is accounted for by the fact that the sum of $P_n$ is in general less than 1. Eq. (1) may be easily extended for the case of phase differences in the contributions of individual segments.

One application of Eq. (1) lies in the evaluation ot aperture blockage loss. Areas of the aperture that are shadowed by a subreflector, feed, or support structure, may be considered as one or more segments with zero efficiency, or with an estimated efficiency in the case of partial RF transparency of the obstacle. The effect of a single totally blocked segment is found to be

$$\eta' = [\,(\eta)^{1/2} - (a_n P_n \eta_n)^{1/2}\,]^2 = \eta \left[\, 1 - \left(\frac{\eta_n}{\eta} a_n P_n\right)^{1/2} \right]^2 \qquad (3)$$

where

$\eta'$ = overall efficiency with the $n$th segment totally blocked

$\eta$ = overall efficiency in the absence of blockage

$\eta_n$ = efficiency of the $n$th segment if it were not blocked

This formulation has been previously used by Gray (Ref. 8). Typically $\eta_n > \eta$, since illumination is more likely to be uniform over a segment, and since spillover is included in $\eta$ but not in $\eta_n$. For the special case of $\eta = \eta_n$, and $a_n = P_n$ (percentage of intercepted energy equals percentage of area) Eq. (3) reduces to

$$\eta' = \eta\,[1 - a_n]^2 \qquad (4)$$

which is a form frequently used for aperture blockage loss. As an example of the error introduced by using Eq. (4) instead of Eq. (3), in a recent problem subreflector blockage represented 1.1% of the aperture area, yielding a blockage loss factor of 0.978, using Eq. (4). The fractional energy in the blocked region was 2.54%, considerably higher than the fractional area, since the illumination was at a maximum in this region. The unblocked overall $\eta$ was 0.739. Assuming that $\eta_n = 1$ (the illumination is virtually uniform in the blocked region), Eq. (3) yields a blockage loss factor of 0.962 (which agrees well with a more sophisticated computer calculated value using an integral technique, Ref. 9, similar to that given in Ref. 10). In this case the difference in the two computations is only 0.07 db, but for careful efficiency calculations this is not insignificant. Also, for higher blockage the difference is amplified.

A second possible application of Eq. (1) is in determining surface tolerance loss. When surface errors are not uniformly distributed over the aperture, segments over which errors are nearly uniformly distributed may be evaluated for RMS error and the loss applied to the individual $\eta_n$ values. If each segment is individually best-fitted (as it should be), a modified version of Eq. (1), including the phase differences of the contributions of each segment, should be used. For the special case of all contributions adding in phase, efficiency would be given by

$$\eta = \left( \sum_{n=1}^{N} \left[ a_n P_n \eta_n \exp - \left( \frac{4\pi\sigma_n}{\lambda} \right)^2 \right]^{1/2} \right)^2 \qquad (5)$$

where $\sigma_n$ is the RMS error of the $n$th segment.[1] It is of interest to determine an equivalent overall $\sigma$ that would yield the same loss given by Eq. (5). This may be determined by

$$\exp - \left( \frac{4\pi\sigma}{\lambda} \right)^2 \left[ \sum_{n=1}^{N} (a_n P_n \eta_n)^{1/2} \right]^2 = \left[ \sum_{n=1}^{N} \left( a_n P_n \eta_n \exp - \frac{4\pi\sigma_n^2}{\lambda} \right)^{1/2} \right]^2 \qquad (6)$$

Defining a function

$$f(\sigma) = 1 - \exp - \frac{1}{2} \left( \frac{4\pi\sigma}{\lambda} \right)^2 = \frac{1}{2} \left( \frac{4\pi\sigma}{\lambda} \right)^2 - \frac{1}{2} \cdot \frac{1}{4} \left( \frac{4\pi\sigma}{\lambda} \right)^4 + \cdots \qquad (7)$$

It is easily found that

$$f(\sigma) = \frac{\sum_{n=1}^{N} f_n^{(\sigma)} (a_n P_n \eta_n)^{1/2}}{\sum_{n=1}^{N} (a_n P_n \eta_n)^{1/2}} \qquad (8)$$

For $\left( \frac{4\pi\sigma}{\lambda} \right) << 1$ this becomes

$$\sigma^2 \cong \frac{\sum_{n=1}^{N} \sigma_n^2 (a_n P_n \eta_n)^{1/2}}{\sum_{n=1}^{N} (a_n P_n \eta_n)^{1/2}} \qquad (9)$$

Therefore, for low surface loss, the error should be weighted by the square root of segment area, power and efficiency. For high loss, Eqs. (8) or (5) should be used to determine the equivalent $\sigma$. A weighting of error by area and power has been suggested by Mezger (Refs. 11 and 12), but he does not give a derivation, and therefore the reason for the disagreement with the above derivation is not known. It is worth noting that for uniform illumination, $\eta_n = 1.0$, $a_n = P_n$, the weighting reduces to the square root of area squared, or simply area, which is again a conventional method of weighting error.

[1]The technique of dividing an aperture into segments is independent of the method used to calculate losses for each segment; a discussion of the validity of the form used above when applied to segments of various sizes is beyond the scope of this article. However, it should be noted that one must be careful that the criteria for the validity and accuracy of a given formula are satisfied over each segment.



# K. Efficient Antenna Systems: Frequency and Size Dependence of a Subreflector Beamshaping Flange

A. Ludwig

## 1. Introduction

It has been determined that a beamshaping flange on a subreflector for a Cassegrainian antenna can appreciably improve antenna efficiency (Ref. 13). This article is primarily concerned with the effect of operating at a frequency significantly above the design frequency of the flange.

## 2. Evaluation of Frequency Dependence

The subreflectors for the 85-ft- and 210-ft-D DSIF antennas have flanges designed for S-band operation. To evaluate the performance of these subreflectors at several frequencies, the subreflector configurations and illumination were input to a JPL-developed computer program

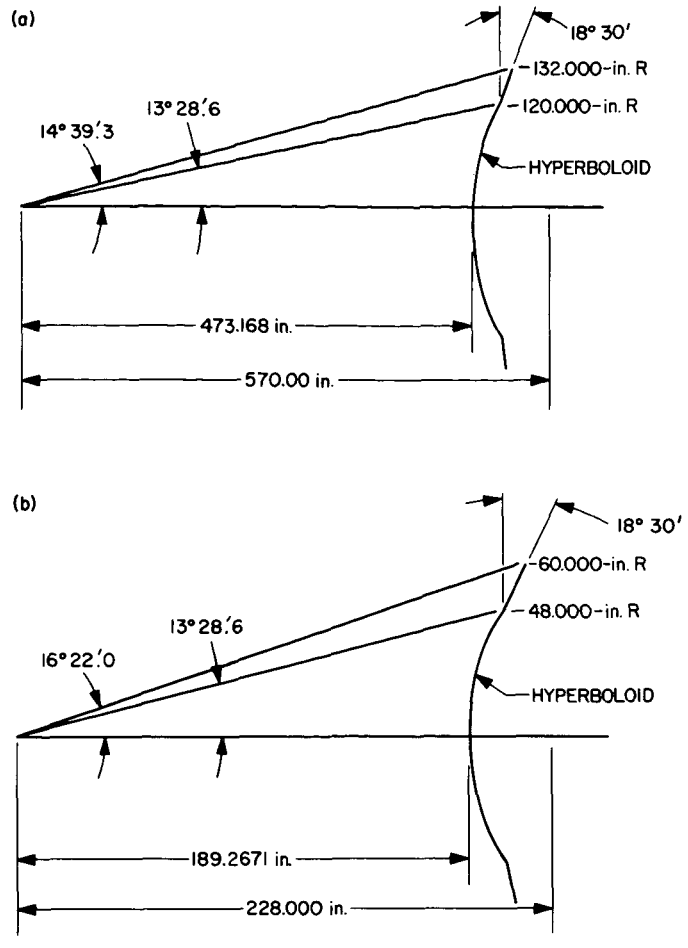


**Fig. 27. Subreflector configurations (a) 210-ft-D antenna (b) 85-ft-D antenna**

which calculates scattering from an arbitrary surface of revolution (Ref. 14). The computed scattered patterns were then input to another computer program which evaluates antenna efficiency (Ref. 15). Both subreflectors were evaluated at S, C, X, and $K_u$-band. The subreflector configurations are shown in Fig. 27. The flanges for both subreflectors are 12 in. wide, since it has been determined experimentally that the optimum flange is about two wavelengths wide, independent of the subreflector size (for large subreflector sizes in wavelengths). The subreflector illumination, which was assumed to arise from a dual mode feedhorn (Ref. 16) scaled for each frequency (such that the pattern would remain constant) is shown in Fig. 28. Several of the resulting computed scattered patterns are shown in Fig. 29. It is seen from Fig. 29 that operating above the design frequency causes substantial distortion at the edges of the patterns. The phase patterns, which are not shown, are also perturbed in this region. Scattered patterns from the subreflectors with the flange removed (pure hyperboloids) are shown in Fig. 30.

The resulting antenna efficiencies for the illumination patterns shown in Figs. 29 and 30, and for the other cases evaluated, are shown in Fig. 31. Efficiency includes losses due to spillover past subreflector and main reflector, amplitude and phase illumination losses, and cross-polarization losses. It is seen that the flange results in substantial improvement in performance at the design frequency, and has very little effect on efficiency, either positively or negatively, at the higher frequencies. However, it should be noted that the subreflectors without flanges are smaller than optimum, and the efficiencies for these cases would be 1 to 2% higher if the hyperboloids were somewhat larger.

The most interesting fact illustrated by Fig. 29 is that the flange is much more effective on the smaller subreflector. The illumination efficiency of the smaller antenna is actually greater than that of the larger antenna — a complete reversal of the normal situation as illustrated by the no-flange cases.

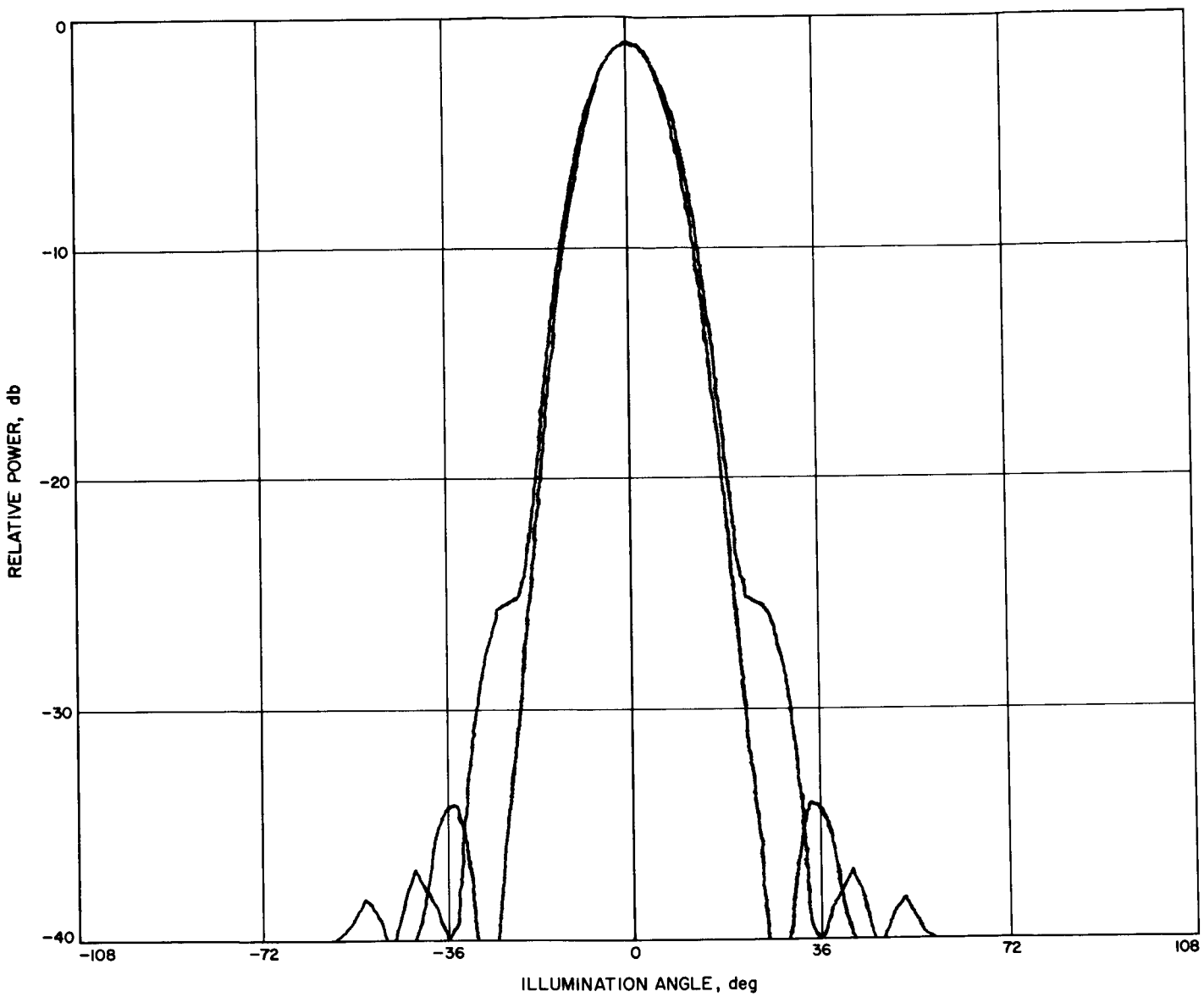


**Fig. 28 Primary feed pattern**

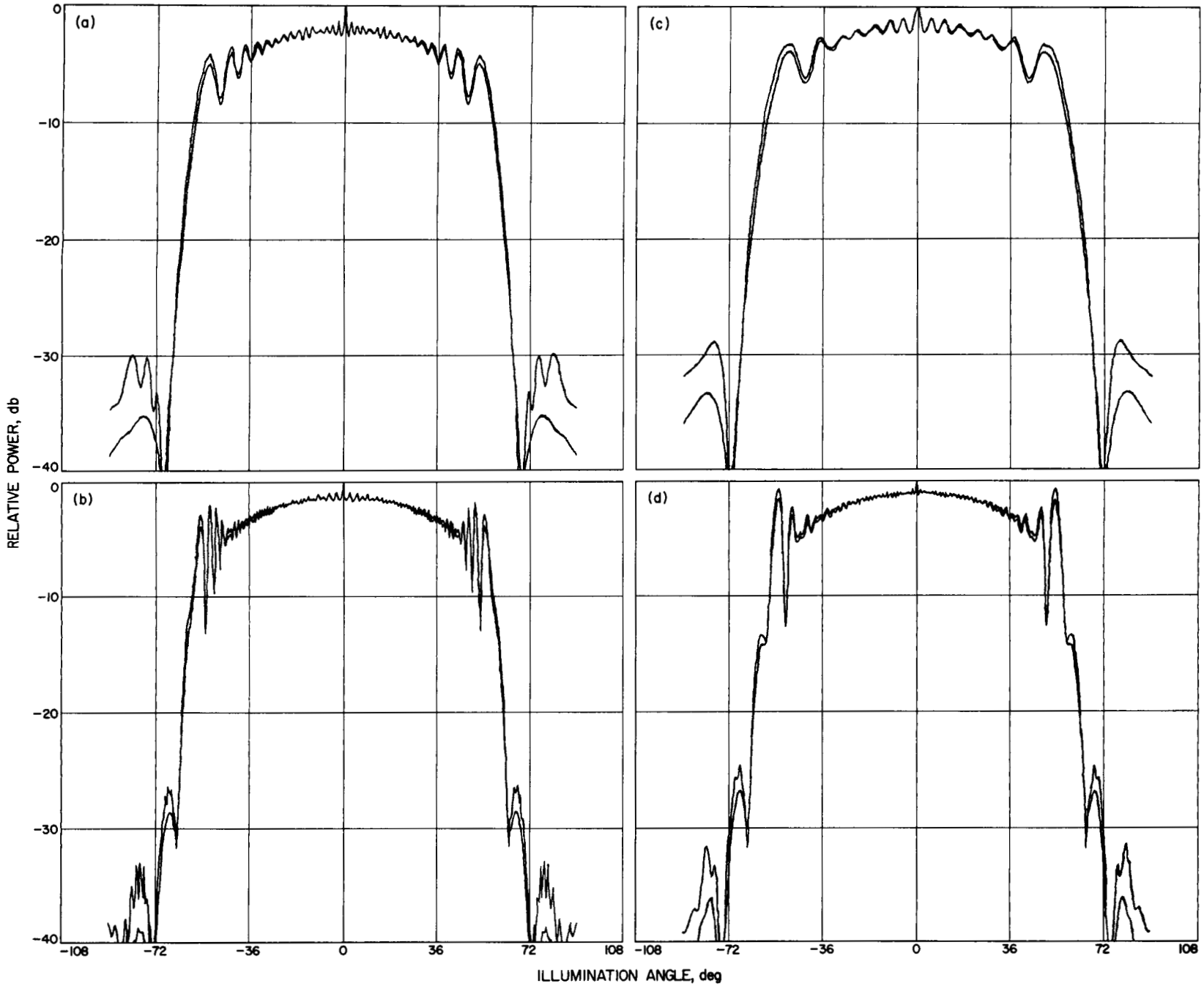


**Fig. 29. Scattered patterns of subreflectors with flange (a) 210-ft-D antenna S-Band, (b) 210-ft-D antenna X-Band (c) 85-ft-D antenna S-Band (d) 85-ft-D antenna X-Band**

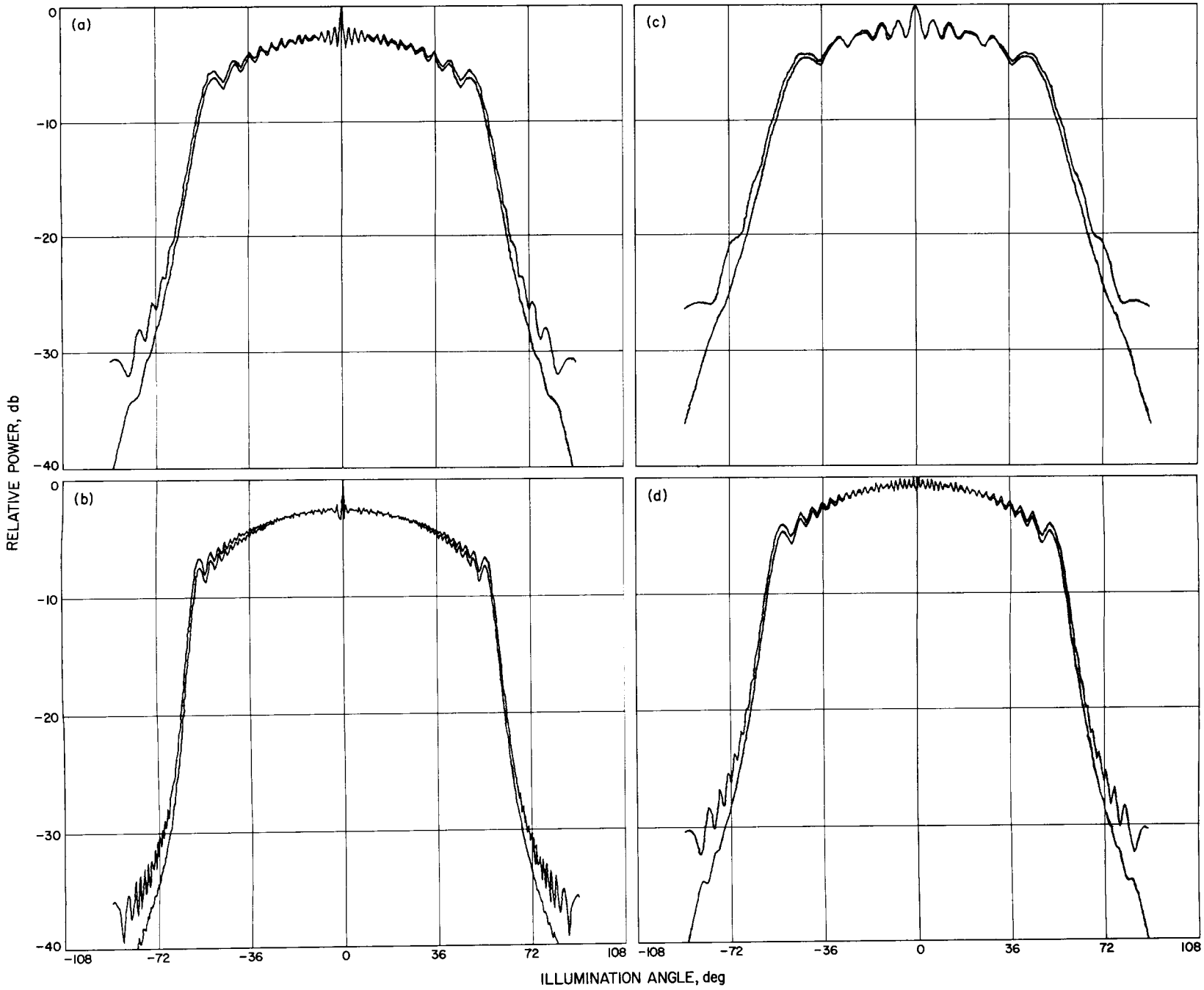


**Fig. 30. Scattered patterns of subreflectors without flange (a) 210-ft-D antenna S-Band (b) 210-ft-D antenna X-Band (c) 85-ft-D antenna S-Band (d) 85-ft-D antenna X-Band**

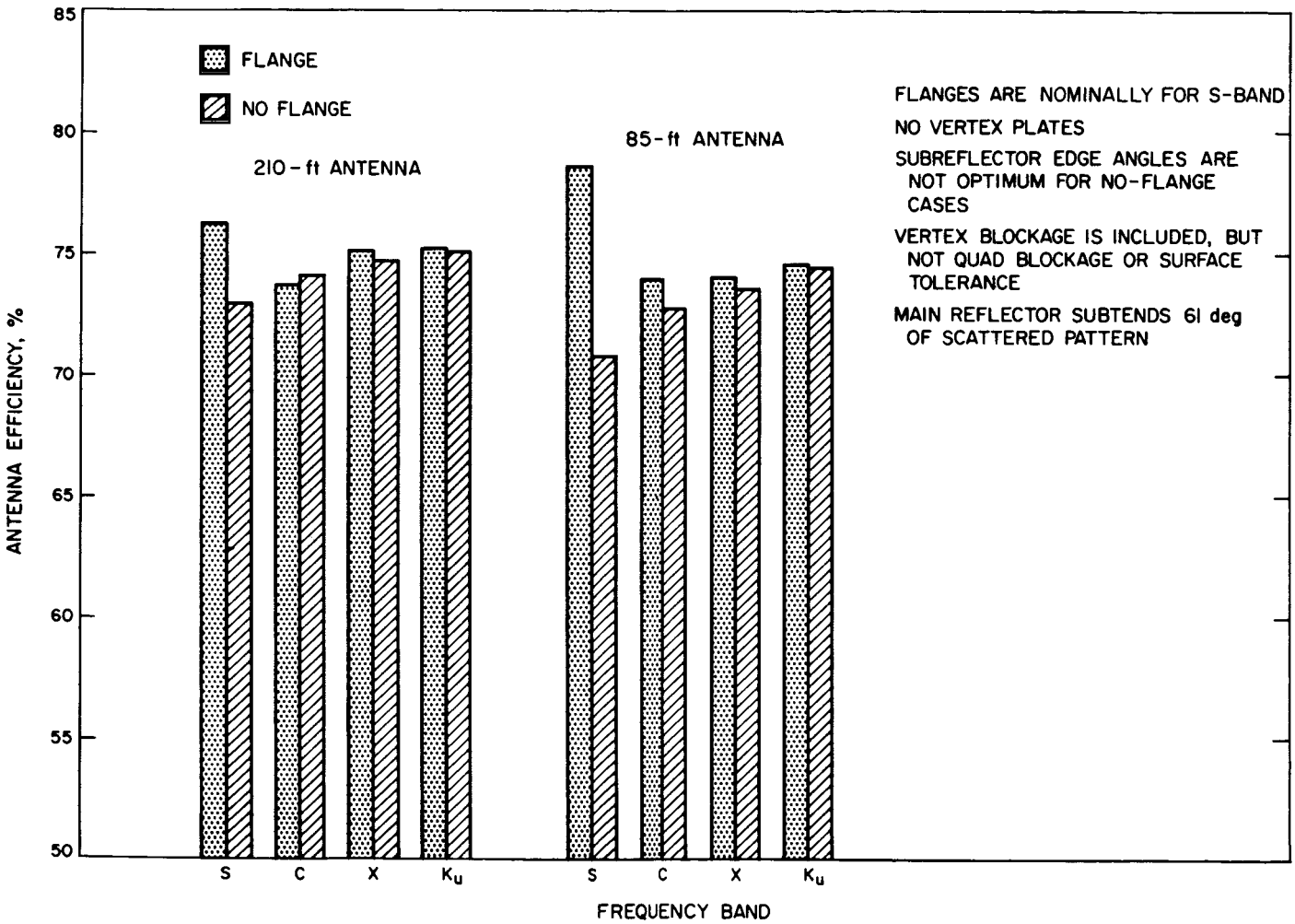


**Fig. 31. Efficiency of subreflector patterns**

This curious situation is the result of the fact that, on the smaller subreflector, the flange subtends a larger portion of the feed pattern, resulting in 3% less forward spillover. This increase more than makes up for the larger diffraction effects of the smaller subreflector. Making the flange larger for the large subreflector would result in distorted patterns similar to the higher frequency patterns, and making the hyperboloidal section larger would cause more loss due to increased illumination taper than could be gained by decreased spillover. Thus, it appears that for the hyperboloid/flange combination, smaller subreflectors are better than larger subreflectors. The difference in efficiency is small, but it indicates an area of potential improvement in the design of large subreflectors.



# I. Advanced Development of Microwave Antenna Subsystems: 100-kw SCM Cone Tests

R. W. Hartop

As part of the continuing effort to maintain state-of-the-art capability in the microwave antenna subsystem of the DSIF, advanced development has begun on the design of waveguide components capable of handling from 500- to 2000-kw CW transmitter power. *SPS 37-40*, Vol. III, p. 80, described some special tests which have been performed on present Goldstone Duplicate Standard (GSDS) components in order to determine their limitations under very high power.

During this reporting period, these tests were extended with the testing of a complete GSDS S-band Cassegrain monopulse (SCM) cone assembly at power levels up to 100 kw CW. These tests were performed at the Venus DSS, using an available 100-kw klystron. The SCM cone was mounted on one of the elevators so that the RF power radiated through the roof port, and an R&D traveling wave maser was installed in the cone with complete instrumentation to monitor system noise temperature and to detect noise bursts due to corona discharges or contaminants. In addition, a 12-channel recorder was used to monitor thermal temperatures of critical components within the cone by means of calibrated thermocouples.

Two complete power runs were made at various power levels from 20 through 100 kw. The first test used the RCP bridge circuit of the SCM feed and was completely successful. After shutting down and switching to left-handed circular polarization (LCP), 100 kw was again transmitted through the feed, but after 3 min at full power (preceded by 5 min at 75 kw) a sudden noise burst was observed on the spectrum analyzer and the chart recorder. The transmitter was manually turned off, and the power was then gradually increased in 10- to 15-kw increments as in previous runs. This time, however, noise bursts would occur every time at about 40 kw, and the tests were concluded at this point.

It had been anticipated that one of the components that might give trouble during very high-power testing was the waveguide load that is used to terminate several unused ports in the system (such as the cross-difference ports of the SCM feed). An attempt was made during the tests to monitor the temperature of these loads to prevent them from reaching their 350°F melting point. However, because of the low thermal conductivity of the load material, combined with the high conductivity of the aluminum waveguide to which the thermocouples were attached, it was difficult to estimate what the actual load material temperature was at a given time.

Thus, when the noise burst problem arose during the LCP test, it was assumed that one of the cross-difference loads had overheated and introduced contaminants into the system. However, later investigation showed this assumption to be incorrect; a load on the receiver arm of the diplexer had slightly overheated and given off enough vapor to cause the noise bursts. Fortunately, no contaminants were introduced permanently into the system, and, after replacing the load, the SCM cone passed a standard diplexing test at the Echo DSS antenna test range.

The fact that a load which is theoretically isolated by 90 db from the transmitter signal could overheat has prompted several further investigations. In one test, similar loads were power-tested to determine their capacity. Briefly, it was found that the load could tolerate about 30 w indefinitely with a load temperature reaching 215°F. After 24 min at 50 w, however, the load material began to smoke. This suggests that the load within the cone must have been exposed to a power level in excess of 50 w, which effectively proves that the signal must have been a harmonic of 2110 MHz in order to pass through the 2200 MHz cutoff sections of the diplexer. Allowing for poor impedance match of the waveguide components at the harmonic frequencies, it appears that the klystron was radiating a total harmonic power of at least 100 w. Further tests will be performed to substantiate these findings.

An anomalous result of the tests was the peculiar behavior of the system noise temperature during diplexing at high power levels. The phenomenon is being investigated in the laboratory as maser availability permits and will be discussed further in the next reporting period.

Despite the difficulty with harmonic power, the 100-kw SCM cone tests were highly successful and indicate that the design goal of 2000-kw CW microwave components may well be achieved in the relatively near future.

# References


1. Berlekamp, E., Rumsey, H., Solomon, G., "Solutions of Algebraic Equations Over Fields of Characteristic 2," *SPS 37-39*, Vol. IV, Jet Propulsion Laboratory, Pasadena, California, June 30, 1966, pp. 219—226.
2. Peterson, W. W., "Error-Correcting Codes," John Wiley & Sons, New York, N.Y. 1961.
3. Martin, W. L., "Digital Communication Tracking: Interfacing with SDS 900 Series Computers," *SPS No. 37-39*, Vol. III, Jet Propulsion Laboratory, Pasadena, California, May 31, 1966, p. 52.
4. "SDS 925/930/9300 Computers INPUT-OUTPUT," Scientific Data Systems, Santa Monica, California, January 1965.
5. Stelzried, C. T., "Temperature Calibration of Microwave Thermal Noise Sources," *IEEE Transactions on Microwave Theory and Techniques*, Vol. MTT-13, January 1965, p. 129.
6. Stelzried, C. T., Otoshi, T. Y., "R&D Listening Cone — Advanced Antenna System Daily System Noise Temperature Calibrations," *SPS 37-39*, Vol. III, pp. 86—103.
7. Worthing, A. G., Gaffner, J., "Treatment of Experimental Data," John Wiley and Sons, Inc., New York, N.Y., 9th Printing, 1960, p. 209.
8. Gray, C. L., "Estimating the Effect of Feed Support Member Blocking on Antenna Gain and Sidelobe Level," *Microwave Journal*, pp. 88—91, March 1964.
9. Ludwig, A., et al., "Computer Programs for Antenna Feed System Design and Analysis," Sect. IX, Technical Report 32-979, Jet Propulsion Laboratory, Pasadena, California (to be published).
10. Wested, J. H., "Shadow and Diffraction Effect of Spars in a Cassegrainian System," p. 2118, Microwave Laboratory, Danish Academy of Technical Sciences, Copenhagen, Denmark, March 1966.
11. Mezger, P. G., "An Experimental Check of Antenna Tolerance Theory Using the NRAO 85-Foot and 300-Foot Telescopes," 1964 PTGAP International Symposium Program and Digest, pp. 181—185, September 1964.
12. Mezger, P. G., "An Experimental Check of Antenna Tolerance Theory Using Radio Astronomical Techniques," NRAO Internal Report, April 1965.
13. Potter, P. D., "A Simple Beamshaping Device for Cassegrainian Antennas," Technical Report No. 32-214, Jet Propulsion Laboratory, Pasadena, California, January 1962.
14. Rusch, W. V. T., "Scattering of a Spherical Wave by an Arbitrary Truncated Surface of Revolution," Technical Report 32-434, Jet Propulsion Laboratory, Pasadena, California, May 1963.

# References (Cont'd)

15. Ludwig, A., "Antenna Feed Efficiency," *SPS 37-26*, Vol. III, April 1964, pp. 200–208.

16. Potter, P. D., "A New Horn Antenna With Suppressed Sidelobes and Equal Beamwidths," *Microwave Journal*, June 1963, pp. 71–78.

# IV. Communications Development Engineering



## A. Step Recovery Diode Multiplier

E. R. Caro

Development of the step-recovery diode has made possible efficient high-order frequency multiplication without the attendant circuit complexities of Varactor frequency multipliers.

A frequency multiplier has been developed for use in the planned Block IIIC modification of the DSIF tracking system local oscillator and transmitter exciter multiplier chains. In order to achieve the modification with a minimum amount of change, the physical design of the unit was made compatible with the available mounting space in the system. The existing multiplier chains in the system include a $\times 32$ module. In the modified chain, this multiplication is accomplished in two steps: a solid state $\times 4$ and amplifier module, and a step-recovery diode $\times 8$ unit. A multiplication factor of 8 was chosen in order to achieve the power output required consistent with the input power capability of presently available diodes. This also places the input frequency in the VHF region of 260 to 280 Mc where sufficiently high levels of power can be generated with transistor circuits. An added advantage of a $\times 8$ unit is the fact that the nearest sideband at the output is 260 to 280 Mc away from the center of the output bandpass. This allows sufficient suppression of undesired sidebands to tolerable levels with a minimum number of output filtering stages. Considerable effort was exerted towards making the design as simple as possible without compromising performance so that the unit would be easily reproducible and require a minimum amount of testing time.

Fig. 1 shows a photograph of the multiplier, and Fig. 2 shows a schematic diagram. The multiplier consists of a step-recovery diode mounted in a two-cavity output bandpass filter. The diode is series-fed through a low-pass filter FL-1 which isolates the input network from the output network. L1, C1, C2 and C3 form a matching section to transform the diode impedance to 50 ohms. R1 is a bias resistor.

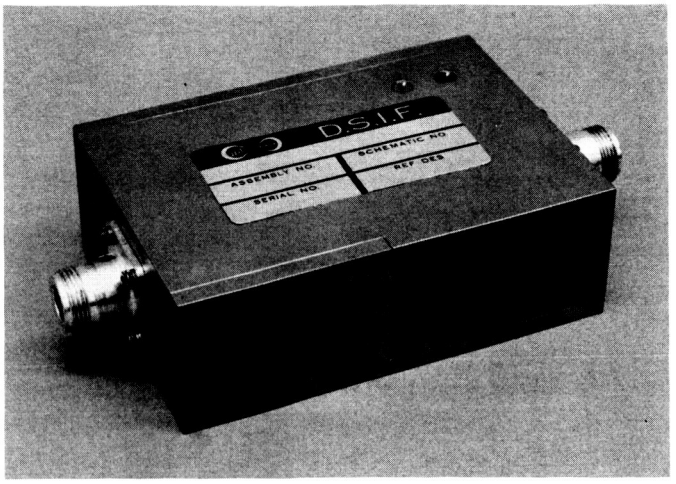


**Fig. 1. Photograph of step-recovery diode ×8 frequency multiplier**

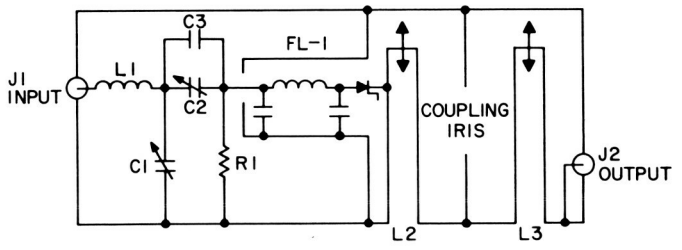


**Fig. 2. Schematic diagram of ×8 frequency multiplier**

The low-pass filter FL-1 is a 3-element Chebyshev filter designed for a 350-Mc cutoff. The filter uses distributed coaxial capacitive elements and a helical center conductor for the inductive element.

The diode taps directly into the center conductor of the first output filter cavity. The tapping point into the cavity was determined experimentally for optimum match between the diode and the output load. Tapping directly into the center conductor also serves as a convenient heat sink for the diode.

The two output cavities are coupled through an iris in the common wall between them. Output coupling is accomplished with a loop. Alignment of the unit is straightforward. An input signal is applied to the unit, and the tuning controls C1, C2 and L2, L3 are adjusted for maximum output. Since a bandpass symmetry requirement has been imposed on the unit, optimum alignment of the output cavities is more easily accomplished with a swept input signal. Tuning of the output cavities is accomplished by varying the length of the center conductors.

It was discovered during temperature testing (0 to 50°C) that variations in the length of the center conductors due to a change in temperature were enough to detune the output cavities and cause a shift in the bandpass response of the unit. To correct the condition, the adjustable portion of the center conductors was made out of Invar.

Fig. 3 shows the bandpass response of the unit at three different temperatures, 0, 25 and 50°C, after incorporating the Invar center conductors. As can be seen, very little detuning ($< \pm 0.25$ Mc) occurred over this temperature range.

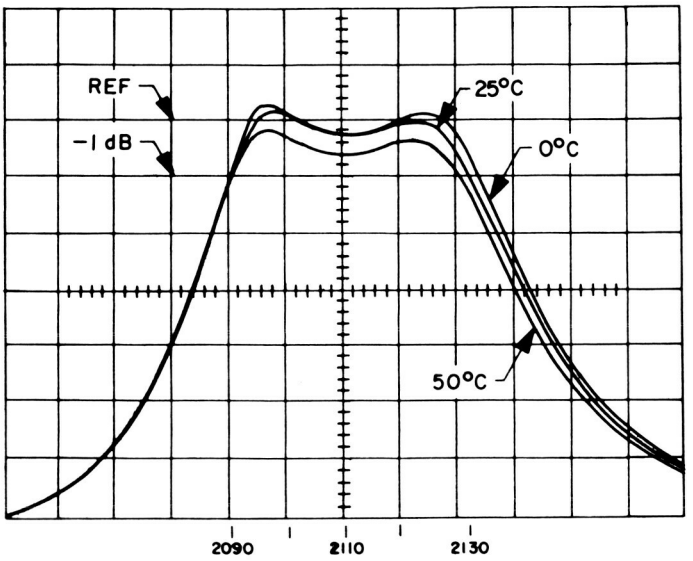


**Fig. 3. Bandpass response of ×8 frequency multiplier at 0, 25, and 50°C**

Performance of the unit is presented in Table 1. Fig. 4 shows input versus output curves for four typical diodes tested. Note that the output increases with the input until saturation occurs at about 4 W of drive power.

Tests made on 20 diodes of the same type purchased in three different batches indicate that the uniformity of the diodes is very good. Very little retuning was required after mounting each diode into the module. For the exciter ×8, where 500 MW of output power is required, with an input drive level of 4 W, the yield of usable diodes was 75%. However, for the lower level ×8 used in the local oscillator, where only 200 MW of output is required, all of the diodes tested were acceptable.

Table 1. Performance of ×8 frequency multiplier[a]

| | Exciter X8 $f_o$ = 2110 Mc | LO X8 $f_o$ = 2235 Mc |
|---|---|---|
| Input power, dBm | +36 | +33 |
| Output power, dBm | +27 | +24 |
| Bandwidth (−1 dB), Mc | 40 | 40 |
| Input impedance, Ω | 50 | 50 |
| Spurious signal level below desired signal | | |
| 6th harmonic, dB | >40 | >40 |
| 7th harmonic, dB | >40 | >40 |
| 9th harmonic, dB | >40 | >40 |
| 10th harmonic, dB | >40 | >40 |

[a] Input dynamic range, see Fig. 4.

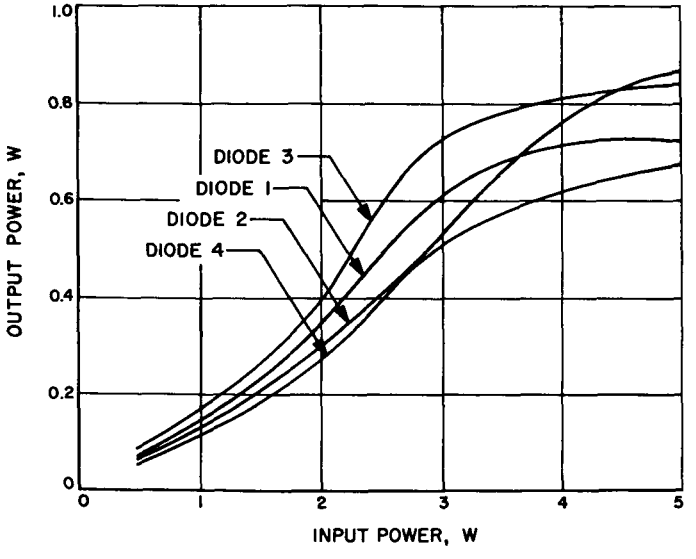


Fig. 4. Input versus output curves of ×8 frequency multiplier for four different diodes

The tuning range of the multiplier was made sufficiently wide (1900 to 2300 Mc) to allow the use of the same unit for both exciter and local oscillator application by applying the appropriate input signal and tuning the output cavities to the corresponding output signal.

Conversion efficiency of the ×8 multiplier averages 12.5%, with some diodes exhibiting as high as 25% efficiency at below saturation levels.

This same basic unit was also operated as a ×16 multiplier (140 Mc to 2240 Mc) by redesigning the low-pass filter for a lower cutoff frequency. Performance of the unit as a ×16 was quite satisfactory with a corresponding decrease in efficiency because of the higher multiplication factor.

## B. MSFN Transmitters

*R. L. Leu*

Implementation of the DSN/MSFN dual transmitter was started at the Pioneer Station. Testing of the first 20 kW transmitter was interrupted by the *Pioneer B* tracking commitment after approximately 90% of the tests were completed. The tests will be completed on a non-interference basis with the tracking commitments. With the exception of incidental amplitude modulation (IAM), the transmitter meets or exceeds the design specification for all tests which have been accomplished. The IAM tests were inconclusive.

The measurement of IAM showed the Klystron complied with the specification (−60 dB below the carrier) from 2 kHz on up. From 200 Hz to 2 kHz the test equipment had a dynamic range of only 53 dB. A better test setup will be needed to measure −60 dB below the carrier from 200 Hz to 2 kHz.

The ripple on the output of the high-voltage power supply (20 kV, 3 A) was measured at 25 V peak-to-peak. Using the measured value, the incidental phase modulation (IPM) contributed by the Klystron was calculated at 1.5 deg, peak-to-peak. The measured value, using the test setup of Fig. 5, was 1.2 deg, peak-to-peak. The measured results are shown in Fig. 6.

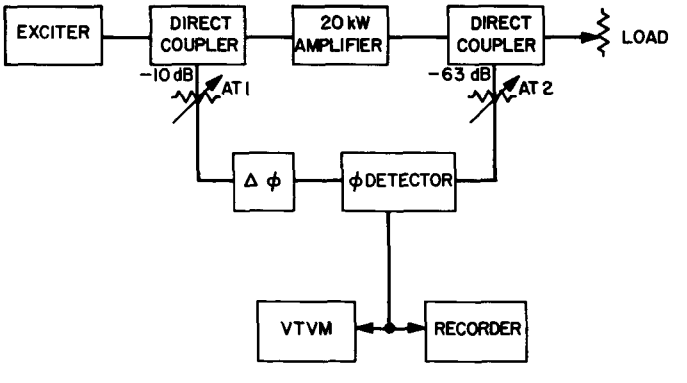


Fig. 5. Incidental phase modulation test setup

With the exception of the heat exchanger, all equipment for the second transmitter has been delivered and is being installed. The second transmitter is to be tested on a non-interference basis with the *Pioneer B* mission. The installation and testing of the dual transmitter configuration is scheduled for completion in September 1966.

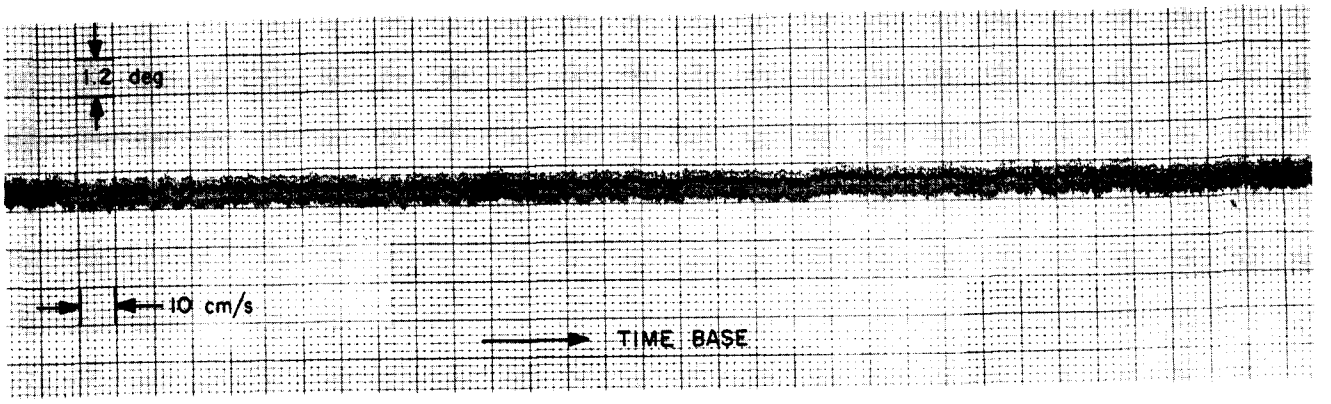


Fig. 6. Incidental phase modulation across 5K70SG Klystron



## C. Klystron Protective Device

E. J. Finnegan

### 1. Introduction

The mercury pool Ignitron crowbar reported on in *SPS 37-40*, Vol. III, was tested during this reporting period. The triggered spark gap crowbar will be compared to the Ignitron in this report.

### 2. Ignitron Crowbar

A mercury pool Ignitron is a cold cathode tube. Mercury is vaporized by a high current pulse applied to the

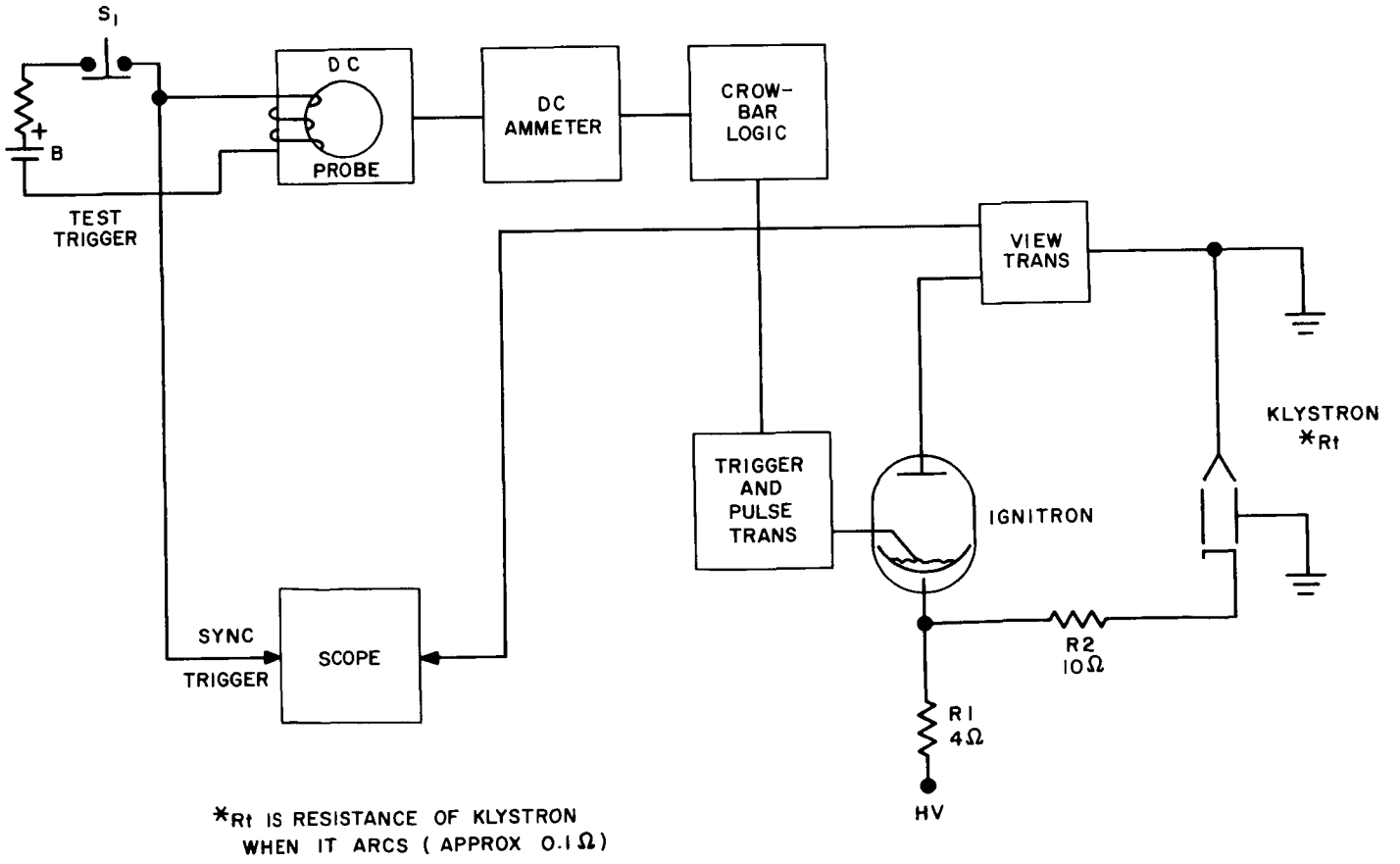


Fig. 7. Test setup for measuring crowbar response

ignitor immersed in the mercury pool, thus making it a mercury gas tube. This type of device is ideal for use as a crowbar due to its capability of handling very high current pulses (thousands of amperes) for short durations without any damage.

The circuit used to test the Ignitron is shown in Fig. 7. In the first test, the Ignitron was connected in parallel with the spark gap crowbar to test its effectiveness. The spark gap alone gives a loud sharp discharge. With the Ignitron operating in parallel with it, one sees only a very faint arc, thus indicating the effectiveness of the Ignitron.

Fig. 8(a) shows the current discharge wave form as viewed when discharging the spark gap only. The spark gap takes approximately 3000 $\mu$s to dissipate the energy from the 1 $\mu$F capacitor in the power supply.

Fig. 8(b) shows the current wave form as viewed when the Ignitron is used in place of the spark gap crowbar.

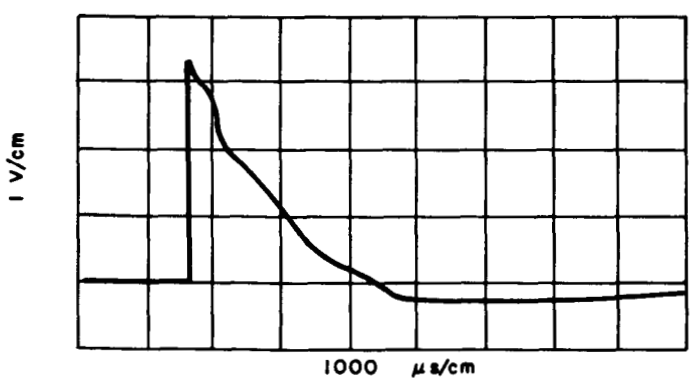


(a) SPARK GAP CROWBAR

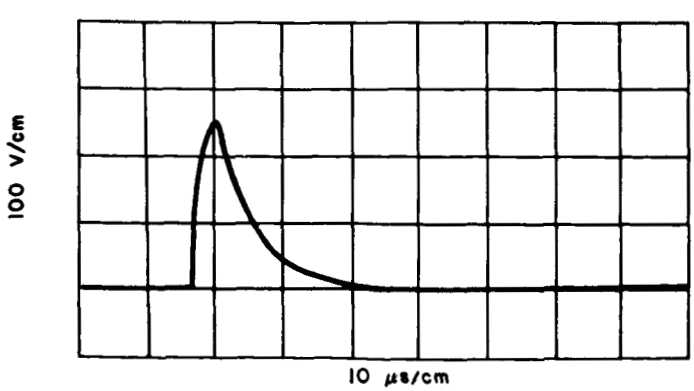


(b) IGNITRON CROWBAR

**Fig. 8. Spark gap crowbar and Ignitron crowbar**

By comparing Fig. 8(a) with Fig. 8(b), it can be seen that the surge current of the Ignitron is approximately 100 times greater and the discharge time is approximately 100 times faster than the spark gap. The Ignitron clears the line of dangerously high currents considerably faster than the spark gap. This should give greater protection to the Klystron, since the high current is shunted from the arcing Klystron at a faster rate. The energy that reaches the tube may be expressed by

$$\text{Energy} = \tfrac{1}{2}cv^2\left(\frac{R_t}{R_1 + R_2}\right)$$

(see Fig. 7); $R_t$ is approximately 0.1 Ω when the Klystron arcs. The energy reaching the tube with a crowbar and operating at 20 kV as it was in the test would be about 1.4 Joules; this would be adequate protection for the Klystron.

Further testing and modifications are necessary before final conclusions may be drawn; however, the test data obtained seems to indicate that there is an advantage to the use of an Ignitron tube as a protective device.



# D. Advanced Transmitter Development

R. E. Arnold

## 1. Introduction

During this reporting period, tests were conducted on the 1-MW high-voltage power supply at the Goldstone Venus Station, and a linear exciter was implemented and tested for amplitude-modulating the *Mariner* 100-kW transmitters. This report summarizes the results of the tests.

## 2. The 1-MW High-Voltage Power Supply Tests

Tests were performed on the 1-MW power supply installed at the Goldstone Venus Station in order to substantiate the conclusions resulting from previous tests described in *SPS 37-38*, Vol. III, pp. 56–61. The conclusion from those tests was that the high-voltage ripple and noise could be reduced by replacing the Amplidyne exciting the field of the 400-Hz generator with a faster responding programmable solid-state power supply. The substantiating tests consisted of first breadboarding a simple 400-Hz, 3-phase full-wave bridge silicon control

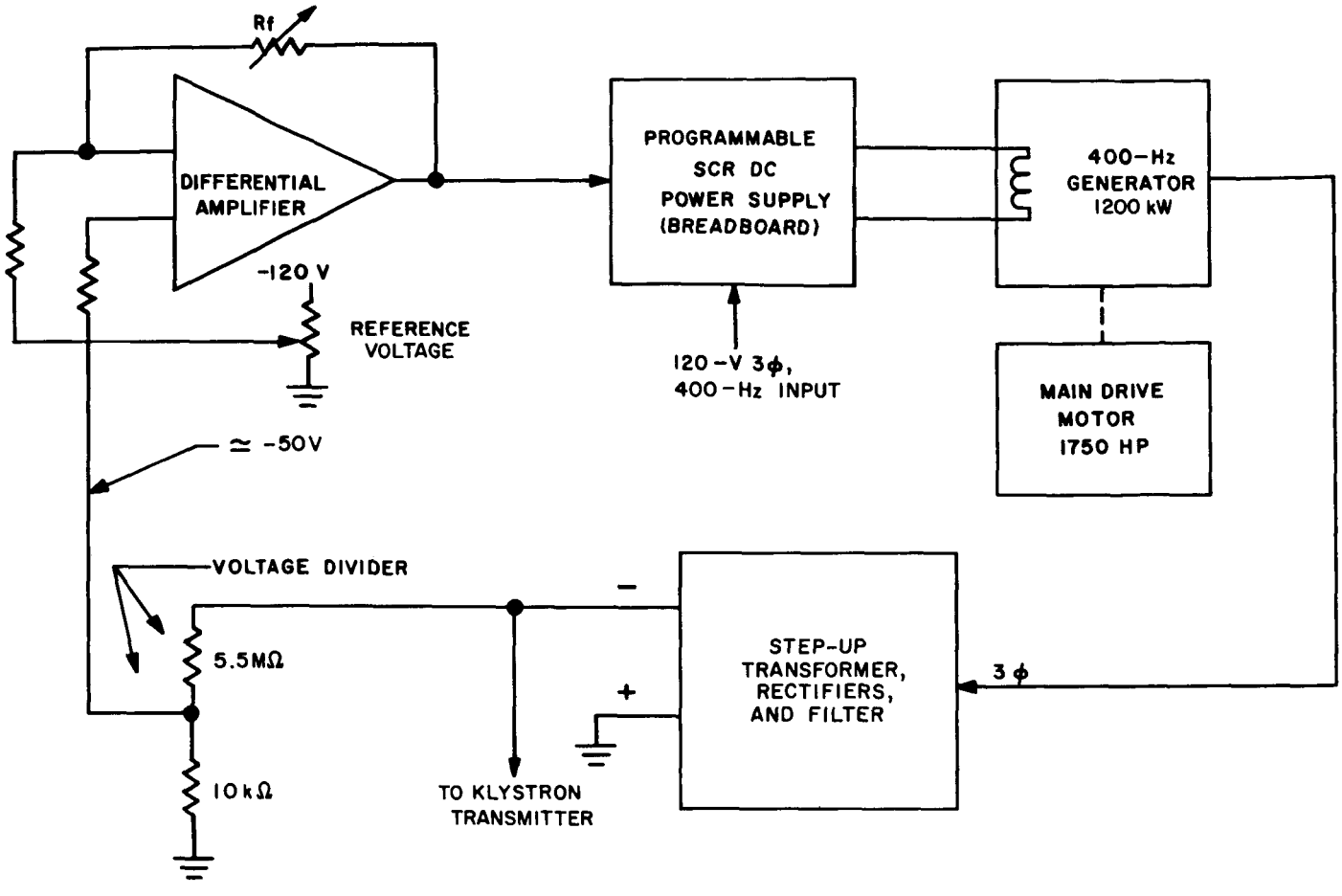


**Fig. 9. Simplified SCR system test diagram**

rectifier (SCR) power supply at JPL and then temporarily installing it in the 1-MW power supply system at Goldstone. Fig. 9 shows the test setup in which the SCR power supply replaced the Amplidyne and a solid-state differential amplifier replaced the vacuum tube regulator amplifier normally used in the system.

Fig. 10(a) depicts a recording of the high-voltage ripple during normal operation at Goldstone before the temporary test setup was installed. The test was run at a nominal 28-A generator field current, producing a Klystron beam voltage of 30 kV at 7.4 A.

Fig. 10(b) is a recording of the high-voltage ripple using the SCR power supply and differential amplifier. The test was run at a nominal 23-A generator field current (the near-maximum output of the breadboard SCR power supply) for a Klystron beam voltage of 26.5 kV at 6.4 A. The low-frequency noise and ripple has been almost entirely eliminated. The recording also shows a marked increase in 60-Hz ripple, which is thought to be due to the instrumentation. The test did fully demonstrate that the beam voltage's low-frequency ripple characteristics can be significantly improved by replacing the Amplidyne with a faster responding SCR power supply.

Because of the encouraging results of the above tests and those described in *SPS 37-38*, Vol. III, pp. 56–61, a specification for a programmable 175-V, 100-A solid-state power supply was written. Subsequently, a contract was awarded to build two units; one unit to excite the 1200 kW 400-Hz generator, and the other unit to excite the 1750 HP drive motor. They are currently being fabricated by a vendor, and delivery of the first unit is expected in September 1966.

### 3. Mariner *Transmitter Noise Modulation*

On 8/5/66, as part of the regular once-a-month 100-kW *Mariner* transmitter support, the 100-kW transmitter was noise amplitude modulated during radio contact with

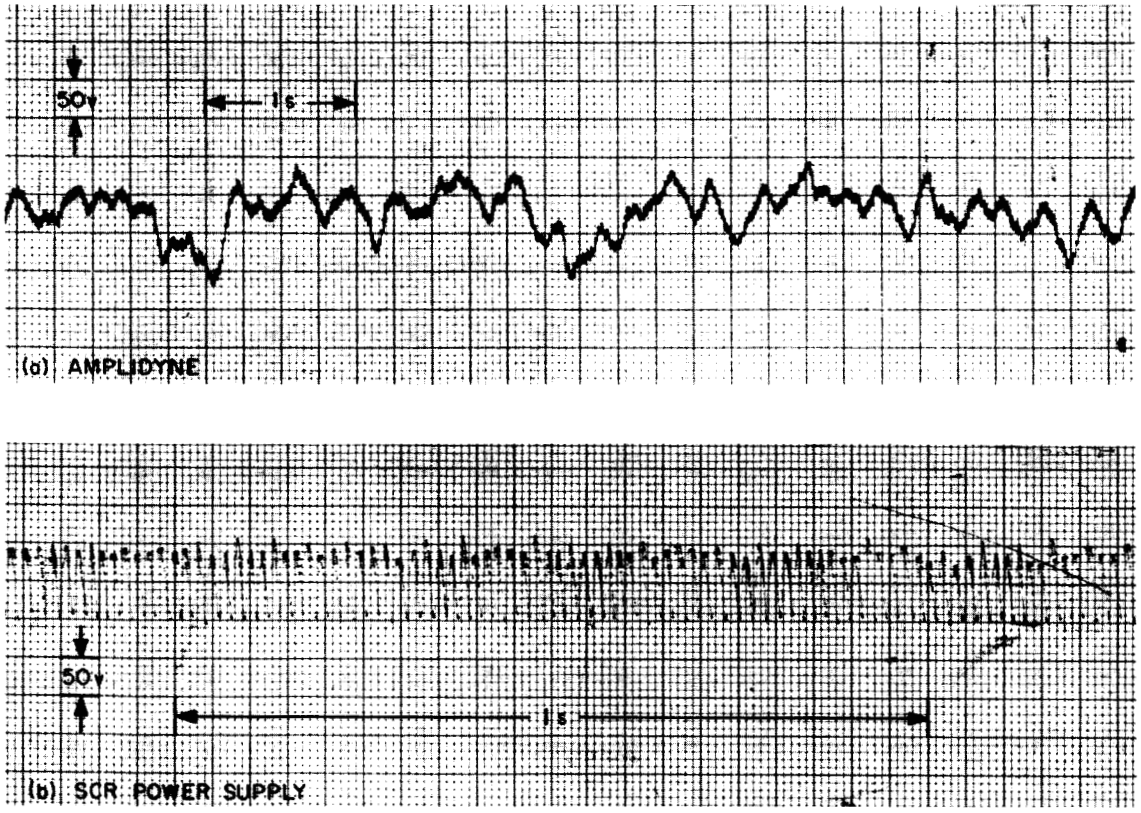


Fig. 10. High-voltage ripple of Amplidyne and of SCR power supply

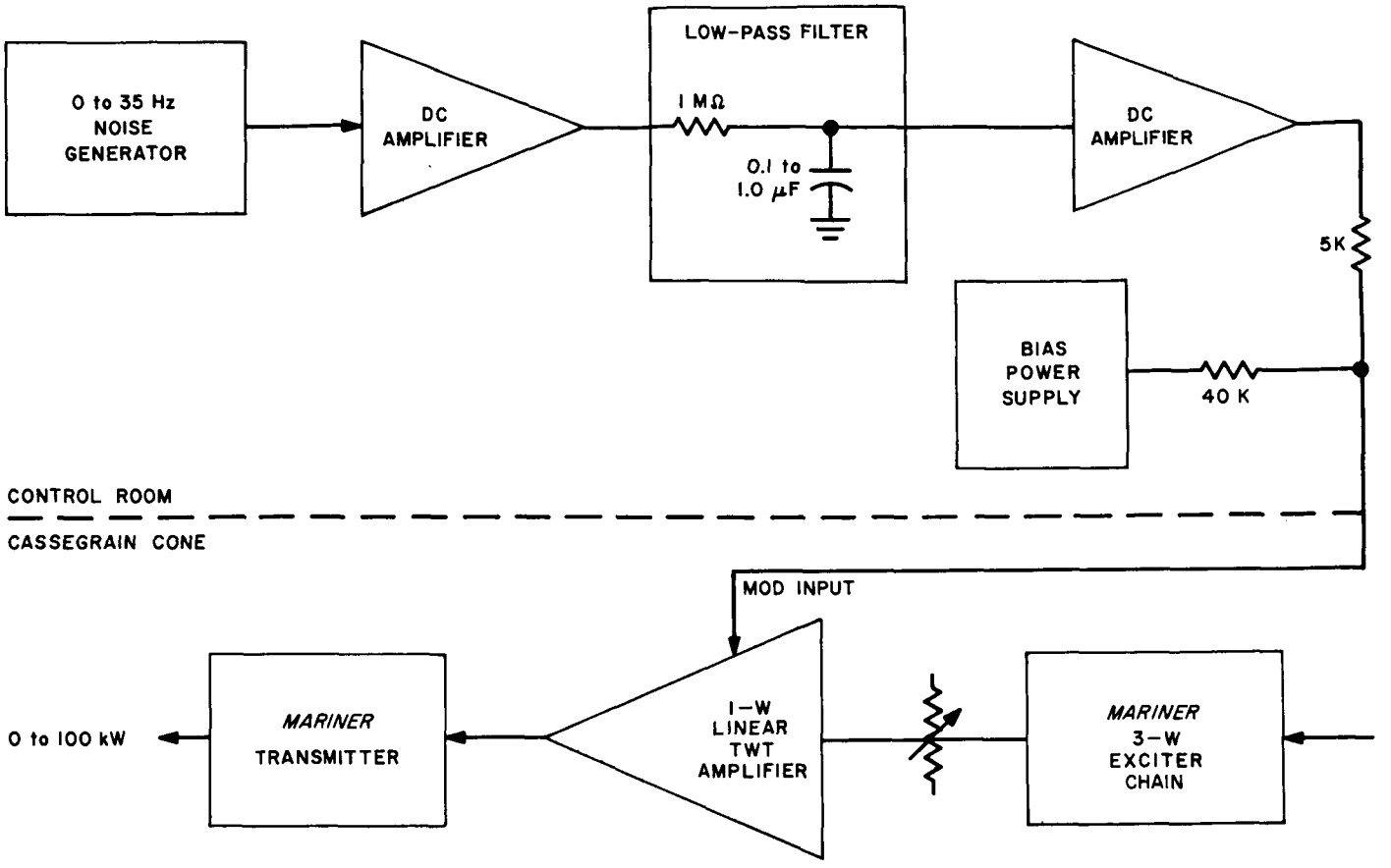


**Fig. 11. *Mariner* noise modulation experiment, block diagram**

the *Mariner IV* spacecraft. The intent of the experiment was to determine the ability of the spacecraft's transponder to return the noise; no commands were sent.

The amplitude modulation was obtained by modulating a 1-W traveling wave tube amplifier (TWT) placed between the 3-W buffer amplifier of the *Mariner* exciter multiplier chain and the Klystron transmitter. The DC-coupled modulation input jack, a feature of the particular TWT used, was employed to obtain the required modulation. The block diagram of the experimental setup is shown in Fig. 11. The combined Klystron/TWT output power characteristics versus TWT modulation input voltage are shown in Fig. 12. The non-linearities at low output powers are due to the TWT modulation characteristics. The beam voltage of the Klystron was raised slightly during the experiment to obtain peak powers of 100 kW.

The low-frequency modulating signal was obtained from a 0- to 35-Hz white-noise generator located in the

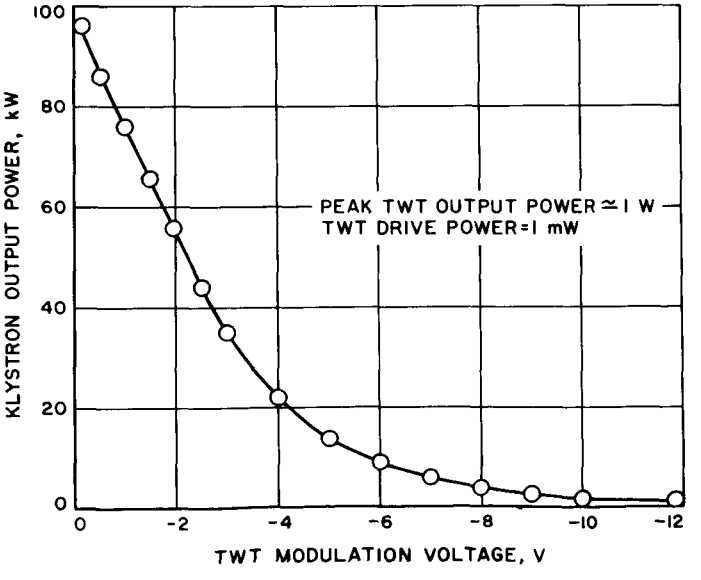


**Fig. 12. Transmitter output power versus TWT modulation voltage**

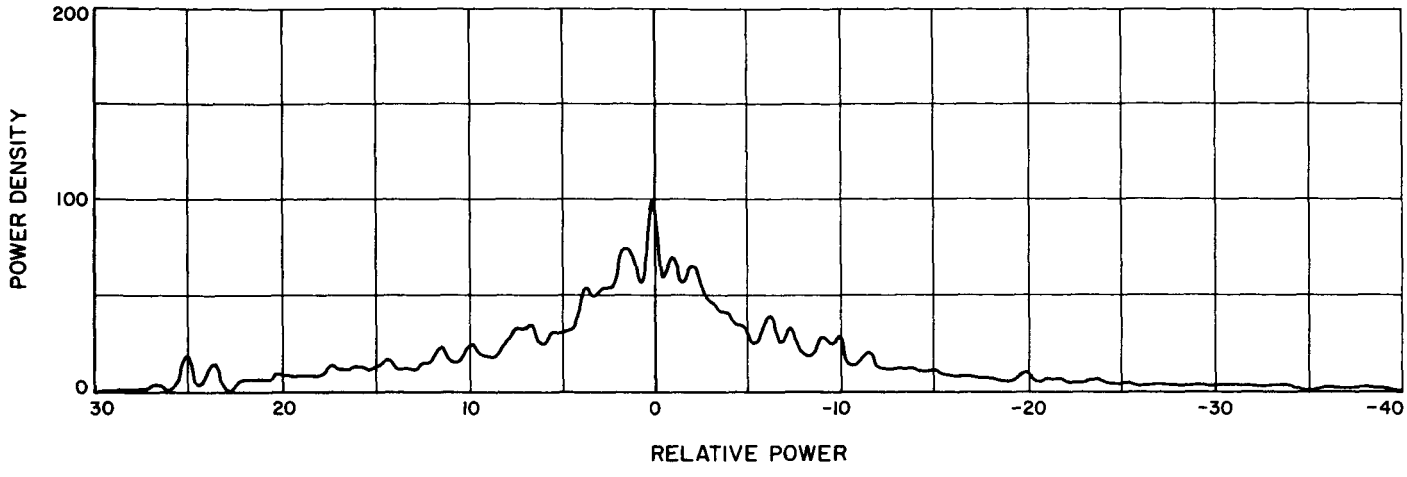


**Fig. 13. Transmitter total spectrum**

Venus Station control room. The experiment requirements necessitated that the noise bandwidth be reduced by the filter shown in Fig. 11.

Fig. 13 shows the transmitter total spectrum as recorded by the Venus Station's autocorrelator. The TWT was biased for 50-kW transmitter average power, the filter RC time constant was 0.5 s, and the amplitude modulation was 100%.

The next *Mariner* transmitter support will require suppressed-carrier double-sideband transmitter modulation. Preparations are currently being made to provide such a modulator.



# E. S-Band Planetary Radar Receiver Development

C. F. Foster

## 1. Introduction

During this reporting period, the construction and installation of the 2388-MHz bistatic radar receiver was completed. This receiver will be used for the Mercury and Venus planetary radar experiments.

## 2. System Description and Implementation

The 2388-MHz bistatic radar receiver (see Fig. 14) consists of several subsystems: (1) The 2388-MHz to 30-MHz converter, or first converter, (2) the 30-MHz to 455-kHz converter, or second converter, (3) the 2388-MHz test transmitter, (4) the Mars Station programmed oscillator, described in *SPS 37-38*, Vol. III, pp. 54–63, (5) the Mars-to-Venus Station microwave link, described in *SPS 37-39*, Vol. III, pp. 106–108, (6) a portion of the Mod IV receiver, described in *SPS 37-38*, Vol. III, pp. 66–71, and (7) the Venus Station correlator, described in *SPS 37-25*, Vol. III, pp. 33–38. The first converter (see Fig. 15) is contained in a standard antenna box mounted in the 3A section of the Mars Station cone (see Fig. 16). It has the following specifications: Input and output impedance is 50 Ω, the single-sideband noise figure is 9.25 dB, the conversion gain is +59.6 dB, the mixer balance is 21 dB, and the 1-dB bandwidth is 10 MHz. The second converter is also contained in a standard antenna box mounted in the 3A section of the Mars Station cone (see Fig. 17). It has the following specifications: Input impedance is 50 Ω, output impedance is 75 Ω, the conversion gain is selected by means of a manual gain control system (*SPS 37-40*, Vol. III), and has a maximum gain of +55 dB. The converter bandwidth is 400 kHz. This bandwidth was established by the use of a 30-MHz center frequency crystal filter having a 400-kHz 3-dB bandwidth. The 30-MHz signal is mixed down to 455-kHz and amplified by a video amplifier. A plot of the final system bandwidth is shown in Fig. 18. The output of the second converter is sent via the microwave link to the Venus Station Mod IV receiver where it is divided between the 455-kHz doppler loop (*SPS 37-38*, Vol. III, pp. 54–63) and the AM spectrum channel. The 400-kHz bandwidth is reduced to 27.3 kHz in the Mod IV AM channel for the Mercury experiments. The output of the AM channel is then sent to the correlator for signal processing.

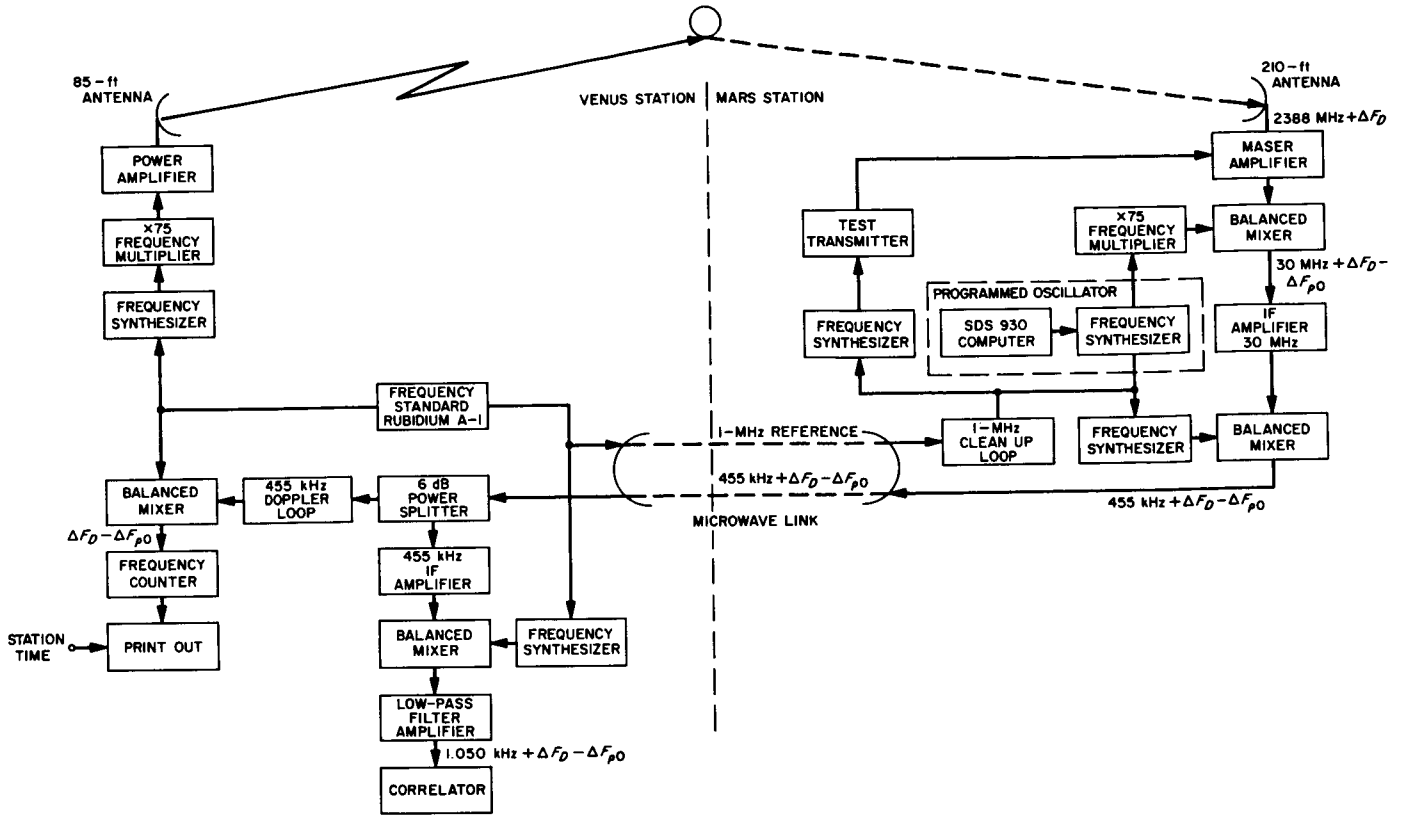


**Fig. 14. Bistatic radar block diagram**

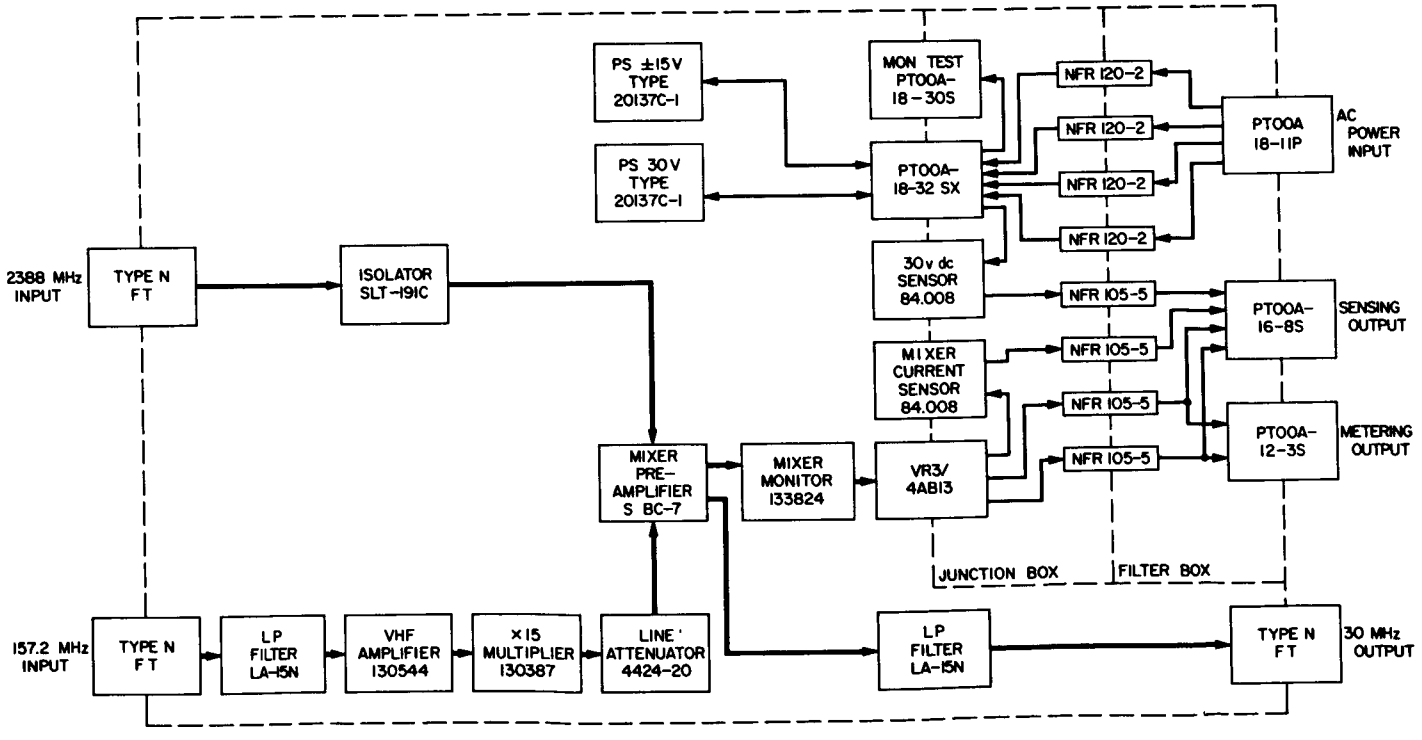


**Fig. 15. 2388-MHz to 30-MHz converter block diagram**

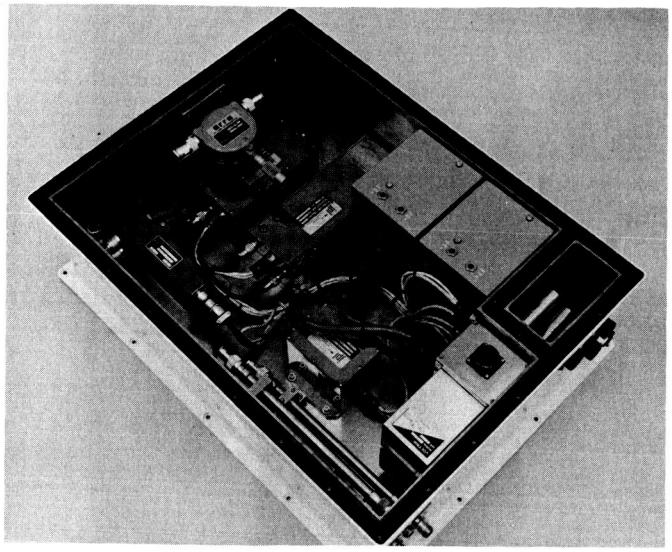

Fig. 16. Photo of 2388-MHz to 30-MHz converter

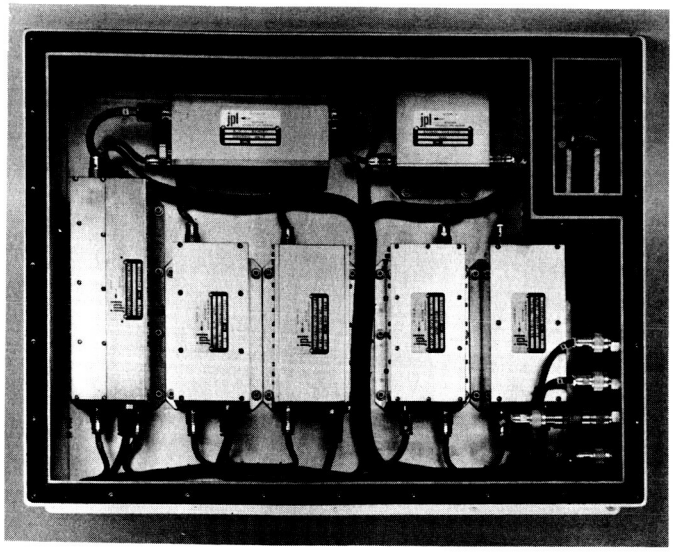

Fig. 17. Photo of 30-MHz to 455-kHz converter

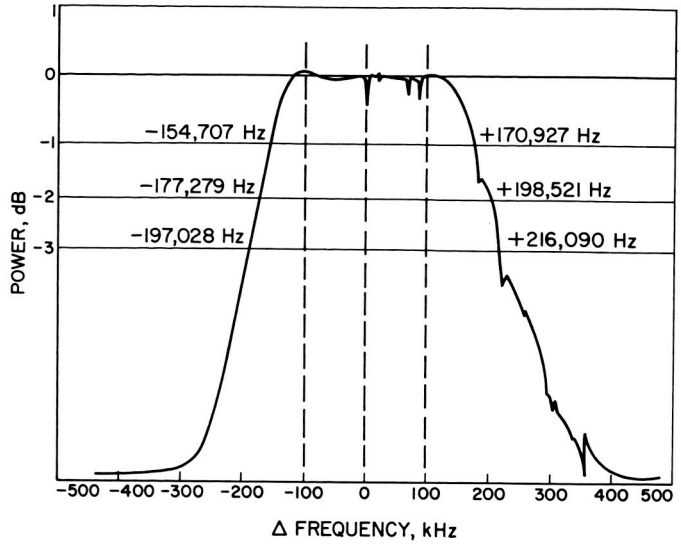


Fig. 18. Bistatic radar converter passband plot

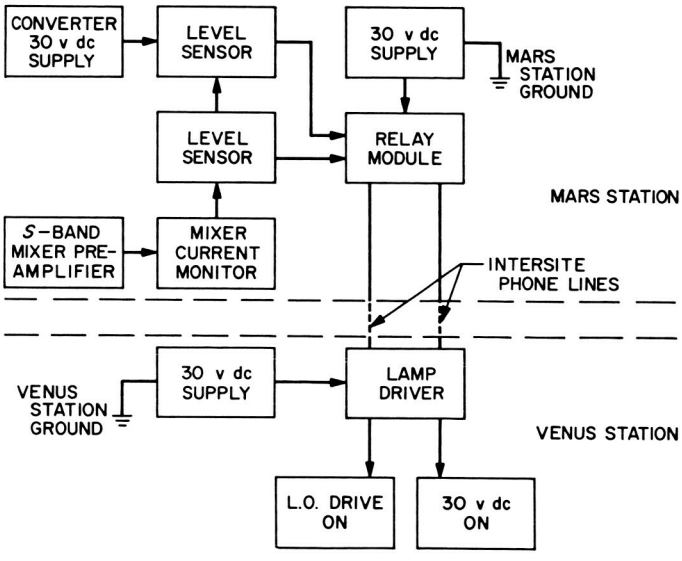


Fig. 19. 2388-MHz bistatic subsystem monitoring diagram

Monitoring of the Mars Station converter condition (local oscillator drive and power supply voltage) is accomplished by using preset high- and low-level detectors adjusted to sense nominal system levels. Their outputs are transmitted to the Venus Station via intersite phone lines and displayed at the Mod IV receiver (see Fig. 19).

The programmed oscillator, the maser, and the reference frequency generators at the Mars Station have to be shared by the 2388-MHz bistatic radar receiver and the Mars Station 2295-MHz experimental receiver. Because of this fact, and the remoteness of the various subsystems at the Mars Station, the several cable and frequency changes necessary when changing from one system to the other are accomplished by coax switches operated from a single front panel selector on the Mars Station 2295-MHz experimental receiver (see Fig. 20). This provides instant change-over from one receiver to the other.

The signal of the 2388-MHz coherent test transmitter, which in past systems had been injected into the maser by way of the maser instrumentation box, was provided

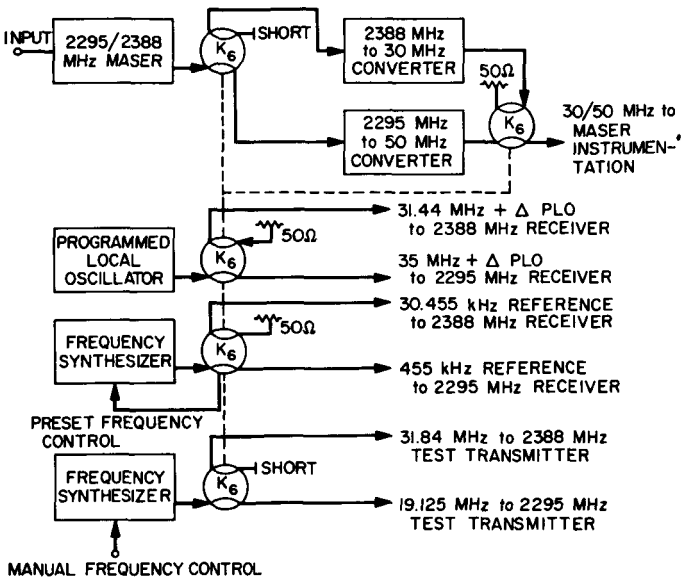


**Fig. 20. 2388/2295-MHz receiver change-over switch**

with another injection point (see Fig. 21). This was done because, in the past, whenever a noise tube or a coax switch was changed in the maser instrumentation box, the path loss between the maser and the test transmitter required recalibration. The 2388-MHz and the 2295-MHz test transmitters are both located in the alidade room to allow receiver calibrations to be made by a single operator. The test transmitter was calibrated using the CW power method (*SPS 37-38*, Vol. III, pp. 41–51).

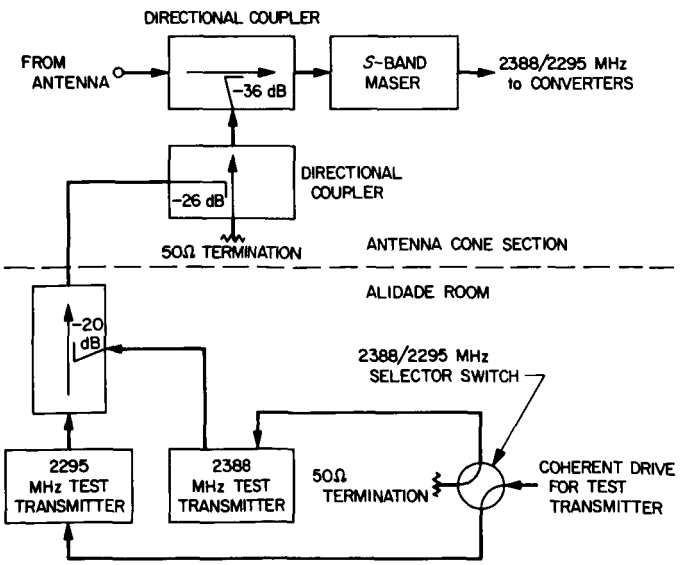


**Fig. 21. 2388/2295-MHz test transmitter maser input path**

The 2388-MHz bistatic radar receiver installation is successful and is being used to support the Mercury radar experiment.



# F. Resistive Loop Directional Coupler Calibration

*R. C. Chernoff*

## 1. Introduction

The resistive loop type directional coupler presently used as a reflected power monitor on high-power transmitters was calibrated by two different methods. The results agree to within experimental error. The frequency variation of directivity was also measured and was found to be small (1.5%) but adequate for the application.

## 2. General

Resistive loop waveguide directional couplers are used as reflected power monitors on all JPL high-power S-band transmitters currently in DSN or planetary radar service. Although this type of coupler is generally inferior to the multi-hole type in directivity and bandwidth, it does have the advantage of compactness. This type of coupler consists of a loop which protrudes into the waveguide through the *E*-wall and which is terminated by coaxial lines on each end (see Fig. 22). One of the lines is terminated in a detector, while the other is terminated in a tuner and a coaxial load. Directivity in this device results essentially from the "right hand rule" for the

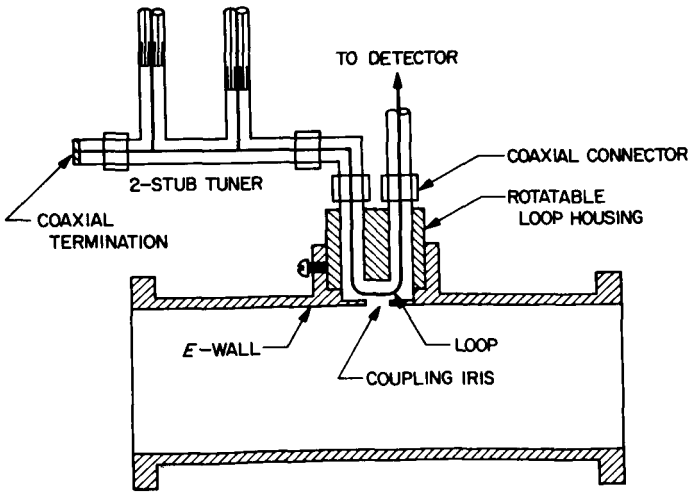


**Fig. 22. Resistive loop waveguide directional coupler**

propagation of electromagnetic waves. According to this rule, the orientation of the magnetic vector with respect to the electric vector in the reflected wave is opposite to that in the incident wave. The device simultaneously couples to both the magnetic field (via the loop) and the electric field (via the coaxial termination); and by judicious adjustment of the magnetic coupling, high directivity can be achieved. (See Refs. 1 and 2 for quantitative discussions of the device.)

For reflected power monitoring in high-power transmitters, the directivity required will depend upon the maximum allowable reflected power. This is typically about 1% (−20 dB) of the forward (incident) power, so that the required directivity is at least 30 dB if the full-scale error in indicated reflected power is to be held to less than 10%. The resistive loop coupler is capable of this directivity, although over quite small bandwidths (see Fig. 23), if carefully adjusted. If, as is usually the case, the transmitter is required to operate only in a narrow frequency band, the frequency sensitivity is not a serious handicap. However, the initial adjustment is tedious, and the device, at least in its present form, is easily put out of adjustment by even moderately careless handling. Moreover, there is some question as to the temperature stability of the device. Temperature instability, if appreciable, would seriously affect the performance at high CW power levels.

### 3. Calibration Procedures

A resistive loop coupler in use as a reflected power monitor in the 100-kW transmitter test bed was recently removed and recalibrated in an attempt to improve its somewhat erratic performance. The coupler was adjusted for approximately 35 dB directivity at 2113 Mc. Directivity was optimized first by rotating the loop and then by adjusting the double stub tuner. The purpose of the tuner is not, as might be supposed by analogy with directional couplers of the coupled transmission line type, to match out the residual VSWR of the termination. Its primary purpose in this device is to cancel the self-inductance of the loop. Directivity was measured by two methods. In the first, a sliding short terminated the waveguide system as shown in Fig. 24. Assuming that the coupler is inserted in the waveguide system in the "normal" manner, i.e., as if the sliding short were the antenna (or dummy load) and the slotted section were the Klystron, the RF voltage at the detector (SWR meter) would be

$$|E_D| = |DCE_1 + CE_1 e^{j\beta l}| = |CE_1| \cdot |D + e^{j\beta l}| \quad (1)$$

where $E_1$ = amplitude of the incident wave,

$C$ = voltage coupling coefficient,

$\beta = 2\pi/\lambda_g$,

$l$ = distance from coupling loop to short,

$D$ = directivity,

$\lambda_g$ = guide wavelength.

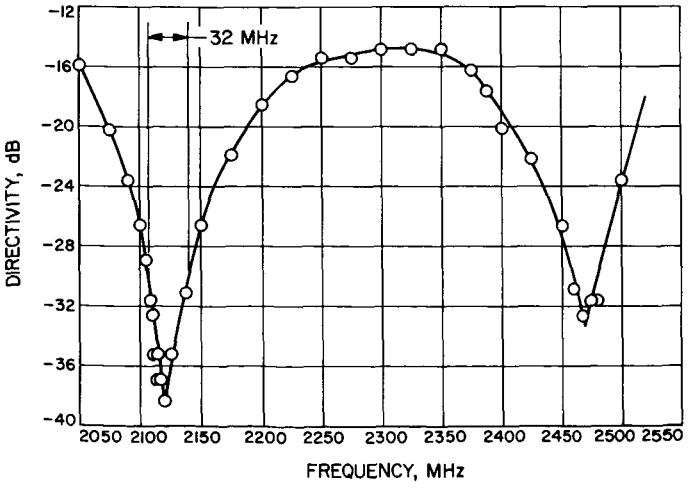


**Fig. 23. Directivity of resistive loop type directional coupler**

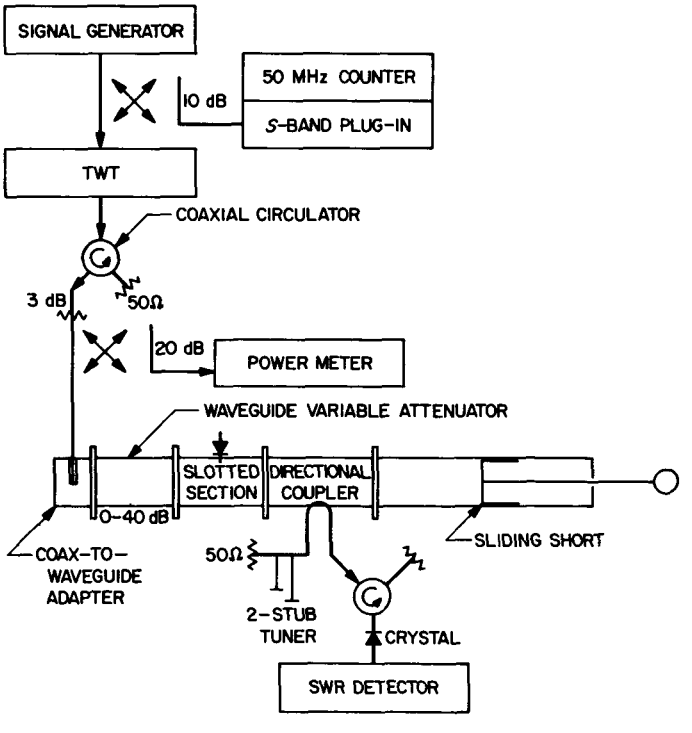


**Fig. 24. Setup for directivity measurements**

We assume, because the correction is small, that $|\rho| = 1$ for the sliding short. From Eq. (1) we see that if $D = 0$ (infinite directivity), $|E_D| = |CE_1|$. As the short is moved toward or away from the coupler, the phase of $e^{j\beta l}$ changes while the phases of $D$, $C$, and $E_1$ do not. Therefore, the resultant, $E_D$, is the vector sum of a rotating and a constant vector. Optimizing the directivity, therefore, consists of attaining the smallest possible fluctuation of $E_D$ as the short is moved in and out. Moreover, from the observed fluctuation in $E_D$ we can calculate $D$ in the following manner: First, we assume that our detector is square-law, as would be the case for the crystal detector used in Fig. 24. The power absorbed by the detector (which we assume to be well-matched) is

$$P_D = |E_D|^2 G_L$$

where $G_L$ is the detector impedance.

$$\text{Thus, Max } P_D = (\text{Max } |E_D|)^2 G_L$$

$$= [|CE_1| \cdot (1 + |D|)^2 G_L]$$

$$\text{and Min } P_D = (\text{Min } |E_D|)^2 G_L$$

$$= [|CE_1| (1 - |D|)^2 G_L]$$

The "wiggle," $W$, observed on the dB scale of the square-law detector, is

$$W = 10 \log \left( \frac{\text{Max } P_D}{\text{Min } P_D} \right)$$

$$= 20 \log \left( \frac{1 + |D|}{1 - |D|} \right) \qquad (2)$$

Solving for the directivity in dB,

$$\text{Directivity} = 20 \log D = 20 \log \left( \frac{10^{W/20} - 1}{10^{W/20} + 1} \right) \qquad (3)$$

The above derivation assumed that $E_1$ remained constant as the short is moved in and out. This will be true only if the system of Fig. 24 is perfectly matched looking from the coupler toward the generator. The waveguide attenuator serves as a pad to isolate the system from the coax-to-waveguide transition mismatch. The slotted section is used to check the constancy of $|E_1|$ as the short is moved. While this arrangement worked reasonably well, the match could have been improved by substituting a waveguide tuner for the slotted section, which would in turn be inserted on the load side of the coupler in order to adjust the tuner for the best attainable match.

Another assumption used in the above derivation, viz., that the coupler is connected in the waveguide system in the "normal" manner, is by no means essential; the method works equally well if the coupler is reversed. Eq. (1) becomes

$$|E_D| = |CE_1| \cdot |1 + De^{j\beta l}| \qquad (4)$$

but all the subsequent equations stay the same.

While probably the simplest and quickest method of measuring directivity, the above method is not the most accurate. For very small $W$ (and $D$), one can derive the simple error formula.

$$d\,[\text{Directivity (dB)}] \approx \frac{8.7\,dW}{W}$$

where $W$ is in dB. Thus, if $W = 0.3$ dB, corresponding to Directivity = 35 dB, an error of 0.05 dB in $W$ causes a 1.5 dB error in directivity. In order to improve upon this, it was necessary to substitute a sliding load for the sliding short in the setup shown in Fig. 24. In this measurement, the coupler must first be connected in the usual manner, as if the sliding load were the antenna. The load is then moved toward or away from the coupler until at least one pair of maxima-minima are observed. The dB difference between them, $W$, and the relative power level (square-law detector reading) of the minimum (or maximum) are recorded. The coupler is now reversed and the new power level, which of course is higher than the first by the order of magnitude of the directivity, is recorded; or, preferably, an accurately calibrated waveguide attenuator is used to reduce the incident power level to yield the same relative power indication as that of the minimum (or maximum) previously observed. Suppose

$\text{Max } P_{L1}$ = the maximum relative power indication observed as the sliding load is moved with the coupler normally connected,

$P_{L2}$ = the relative power indication with the coupler reversed,

$$\text{and } W = 10 \log \left( \frac{\text{Max } P_{L1}}{\text{Min } P_{L1}} \right).$$

Then

$$\text{Directivity} = 20 \log D = \begin{cases} 10 \log \left( \dfrac{\text{Max } P_{L1}}{P_{L2}} \right) + 20 \log \left( \dfrac{1 + 10^{-W/20}}{2} \right), \text{for } \mid D \mid > \mid \rho \mid \\ 10 \log \left( \dfrac{\text{Max } P_{L1}}{P_{L2}} \right) + 20 \log \left( \dfrac{1 - 10^{-W/20}}{2} \right), \text{for } \mid D \mid \leq \mid \rho \mid \end{cases} \tag{5}$$

[See Sect. 5 for the derivation of Eq. (5).] The above described method avoids the "perfect" termination requirement of some methods of directivity measurement, but it does, unlike the first (sliding short) method, require either reversing the coupler, or interchanging the source and detector, in order to measure the coupling coefficient ($C$). The second (sliding load) method has the additional disadvantage that one must know in advance whether $\mid D \mid > \mid \rho \mid$ or $\mid D \mid \leq \mid \rho \mid$. A more refined method of directivity measurement (Ref. 3) uses a sliding load with adjustable $\rho$ so that $\mid \rho \mid$ is made equal to $\mid D \mid$. (The Min $P_{L1}$ is a null, $W = \infty$, and the second term in Eq. (5) is simply 6 dB.) This device, however, is not commercially available. A similar procedure is described in Ref. 4, the only difference being that the $\rho$ of a conventional low-VSWR sliding load is adjusted by home-made methods (paper clips or adhesive foil) to maximize $W$.

## 4. Calibration Results

By the sliding short method the measured directivity at 2113 Mc is 32.5 dB, and by the sliding load method it is 32.7 dB. Each of these is the average of three readings. The frequency variation of directivity was measured by the sliding short method and is shown in Fig. 23. The bandwidth for 30 dB or greater directivity is 1.5% which is of of the same order of magnitude as that reported in the literature (Ref. 1). The smaller directivity maximum at 2470 Mc was not expected, and it is not known at present if there is any way in which directivity can be maximized at two or more selected frequencies.

The high-power performance of the coupler will be evaluated in future work. This will consist of (1) simultaneous low-power measurements of the waveguide plus termination (water load or feed horn) reflection coefficient by both the coupler and a slotted line, and (2) remeasurement of the coupler directivity at high temperature (60 to 100°C) to simulate high-power operation.

## 5. Derivation of Eq. (5)

The voltage detected by the coupler when terminated by a sliding short of reflection coefficient $\rho$ is

$$E_{L1} = (CE_1)(D + \rho e^{j\beta l})$$

using the same notation as in Eq. (1). Therefore, as the load is moved in and out we observe

$$\text{Max} \mid E_{L1} \mid = \mid CE_1 \mid (\mid D \mid + \mid \rho \mid)$$
$$\text{Min} \mid E_{L1} \mid = \mid CE_1 \mid \cdot (\mid D \mid - \mid \rho \mid).$$

Since our detector is square law, we actually measure

$$\text{Max } P_{L1} = \mid CE_1 \mid^2 (\mid D \mid + \mid \rho \mid)^2 G_L$$
$$\text{Min } P_{L1} = \mid CE_1 \mid^2 (\mid D \mid - \mid \rho \mid)^2 G_L$$

If $\mid D \mid > \mid \rho \mid$,

$$\mid DCE_1 \mid (G_L)^{1/2} = \tfrac{1}{2} [(\text{Max } P_{L1})^{1/2} + (\text{Min } P_{L1})^{1/2}]. \tag{6}$$

Let $W = 10 \log \dfrac{\text{Max } P_{L1}}{\text{Min } P_{L1}}$. Then

$$(\text{Min } P_{L1})^{1/2} = 10^{-W/20} (\text{Max } P_{L1})^{1/2} \tag{7}$$

With the coupler reversed, the power input to the detector is

$$P_{L2} = \mid CE_1 \mid^2 G_L. \tag{8}$$

Substituting from (7) into (6) and dividing (6) by (8) gives

$$\text{Directivity} = 10 \log \frac{\text{Max } P_{L1}}{P_{L2}} + 20 \log \frac{1 + 10^{W/20}}{2} \tag{9}$$

The result for $\mid D \mid \leq \mid \rho \mid$ follows almost immediately by changing (6) to

$$\mid DCE_1 \mid (G_2)^{1/2} = \tfrac{1}{2} [(\text{Max } P_{L1})^{1/2} - (\text{Min } P_{L1})^{1/2}]. \tag{10}$$

# References

1. Harvey, A. F., *Microwave Engineering,* Academic Press, p. 109, 1963.

2. Allan, H. R., and Curling, C. D., "The Reflectometer," *Proceedings, IEE.,* Vol. 96, Part III, p. 25, 1949.

3. Schafer, G. E., and Beatty, R. W., "A Method for Measuring the Directivity of Directional Couplers," *Transactions of the I.R.E. for Microwave Theory and Technique,* MTT-6, p. 419, Oct. 1958.

4. Sucher, M., and Fox, J., *Handbook of Microwave Measurements,* 3rd ed., Vol. II, pp. 653–658, Polytechnic Press, 1963.

# V. Deep Space Station Engineering and Operations



## A. Flight Project Support

*J. Orbison and W. J. Kinder*

### 1. Lunar Orbiter I Mission

The *Lunar Orbiter I* spacecraft was launched from Cape Kennedy on Wednesday, 10 August 1966. After the launch and upon confirmation of lunar injection, Echo DSS secured the station for preparation of the first view period, 11 August. Commands for the first orbital engine de-boost firing were transmitted from the Echo DSS during the early portion of the fourth view period, Sunday, 14 August.

Successful reception and video photographic processing of the spacecraft picture readouts were accomplished for the original high orbit and the final low orbit picture taking sequences, and continued through 31 August. In addition to the successful mission function, Time Synchronization Correlations were performed between stations Echo, Madrid, and Woomera using the Mark I Ranging Subsystem. The latter was augmented by a team from the National Bureau of Standards at Boulder, Colorado, who brought a Cesium Atomic Time Standard for a time comparison with the Echo DSS Rubidium Atomic Frequency Standard. The NBS time correlations were performed during the Earth-lunar cruise mode; preliminary data indicates an accuracy with WWV of 156.4 $\mu$s.

### 2. Pioneer VII Mission, *J. Orbison*

The *Pioneer VII* spacecraft was launched on Wednesday, 17 August 1966. The Pioneer DSS, acting as backup to the Echo DSS for *Pioneer VI*, was designated the Prime Station for the launch and early tracking of *Pioneer VII*. The overlap of the *Lunar Orbiter* and *Pioneer VII* view periods were such that the Echo DSS could only have tracked a portion of either spacecraft's passes for any given day. The nature of the early passes of both spacecraft made it imperative that full view periods be observed.

Prior to the launch of *Pioneer VII*, NASA/AMES personnel arrived at Goldstone to direct a series of spacecraft Type II Orientation Tests. From the *Pioneer* Ground Operational Equipment (*SPS 37-35*, Vol. III, pp. 15–16)

located in the Echo DSS control building, commands are first entered and verified through the TCP computer, and stored in the command encoder awaiting transmit time. Actuation of the transmit function, microwaved the command from the Echo DSS to the Pioneer DSS transmitter and from there to the spacecraft. The spacecraft's telemetry is received at the Pioneer DSS and microwaved to the Echo DSS where it is processed through the *Pioneer* GOE demodulator/synchronizer and into the TCP computer for teletype routing to the Space Flight Operations Facility in Pasadena.

During the Pioneer DSS second pass of *Pioneer VII*, Thursday, 18 August, the Type II Orientation aligned the spacecraft high-gain antenna with the Earth. A daily tracking schedule was thereafter maintained through the end of August.

Two TCP computers, designated Alpha and Beta, are the basic units for the Telemetry and Command Processing (TCP-II) subsystem (*SPS* 37-38, Vol. III, p. 102). Included are the transfer racks allowing rapid interchange between *Lunar Orbiter* and *Pioneer* mission functions, the NASCOM High-Speed Data Line equipment and the associated teletype printers. Normal operation provides for *Lunar Orbiter* data processing through the Alpha computer and *Pioneer* data processing through the Beta computer. In the event of a computer failure during overlap tracking, the spacecraft priority at that time would determine use of the operational computer. Transfer between the computers is accomplished nominally within 5 min, resulting in minimal loss of data.

### 3. Pioneer VI Mission, J. Orbison

The *Pioneer VI* spacecraft is in the 9th month of its flight. The Mars DSS assumed the prime tracking of the *Pioneer VI* beginning with Pass 196, 29 June 1966, with telemetry and command processing being accomplished at the Echo DSS via microwave in a manner similar to that described for the Echo/Pioneer DSS arrangement.

Until Pass 234, 6 August, the Echo DSS also provided a transmitter and command function for the Mars DSS. Because of prime power difficulties with the diesel generators, the Mars DSS delayed testing the 20-kw transmitter installation on the 210-ft antenna until additional prime power was provided. Beginning with Pass 235, 7 August, the Mars DSS assumed the command transmission to the *Pioneer VI*, freeing the Echo DSS for the approaching *Lunar Orbiter* Operation. Telemetry and command processing and prime magnetic tape recording continues to be performed at the Echo DSS.

### 4. Mariner IV Mission, J. Orbison

Twenty-two months after its launch on 28 November 1964, the *Mariner IV* spacecraft is being tracked for several hours on a one-day-a-month schedule. During the last scheduled tracking period on 5 August 1966, two-way lockup was established using the 85-ft antenna and the 100-kw transmitter at the Venus DSS and the 210-ft antenna of the Mars DSS for receiving. Commands were transmitted to the spacecraft low gain omni-antenna, and resultant spacecraft telemetry was recorded.

### 5. Surveyor B Mission, J. Orbison

The *Surveyor I* Mission was officially terminated in July, and the Pioneer DSS began station preparation for the *Surveyor B* Mission scheduled for a September launch from Cape Kennedy, Florida. In general, the *Surveyor* equipment and the S-band system have remained unchanged. Except for equipment relocation in the S-band control room to permit installation of the Multiple Mission Support Area (MMSA), only minor assembly modifications have been performed. Inter-area compatibility tests were performed, and the equipment has been maintained in operational readiness for the launch.

### 6. MSFN Apollo Implementation at DSS 11, 42 and 61, W. J. Kinder

Should a failure or serious degradation of performance occur at the *Apollo* Prime station, mission requirements commit the co-located DSN *Apollo* Backup station to be fully capable of substituting for the Prime station within a short interval of time. The co-located DSN stations (Ref. 1) normally will participate in the *Apollo* lunar missions and their simulations on a full-time basis from launch minus 2 weeks to the end of the mission and at other times on a scheduled basis.

The 85-ft antenna Backup station will have a dual capability, thereby permitting communication with two *Apollo* spacecraft simultaneously (Ref. 2). Different frequencies will be assigned to the dual functions; however, only a single DSN 85-ft antenna will be used. Dual tracking, including data formatting, is accomplished at the DSN site and will employ separate NASCOM circuits to the computers at MSC's Mission Control Center (MCC-H) providing full redundancy to the Prime station. Two-way voice is shared between the Prime and Backup sites in that while the transmitter and receiver are located at the Backup site, the "downlink" voice demodulators are located at the Prime station, with the latter's NASCOM circuits used to relay voice to and from

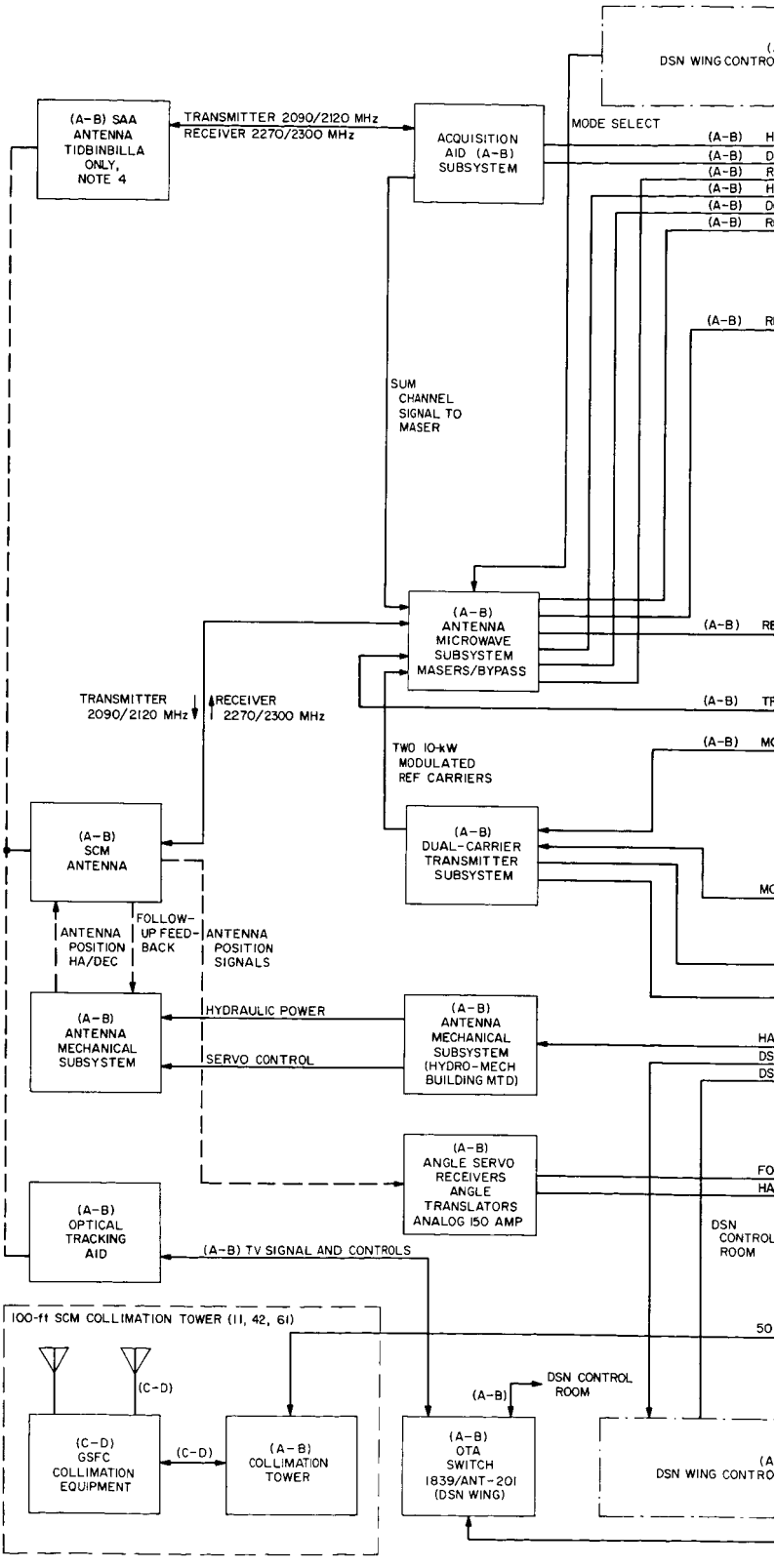
DSN WING CONTRO
(A-B) SAA ANTENNA TIDBINBILLA ONLY, NOTE 4
TRANSMITTER 2090/2120 MHz
RECEIVER 2270/2300 MHz
ACQUISITION AID (A-B) SUBSYSTEM
MODE SELECT
(A-B) H
(A-B) D
(A-B) R
(A-B) H
(A-B) D
(A-B) R
(A-B) R
SUM CHANNEL SIGNAL TO MASER
(A-B) ANTENNA MICROWAVE SUBSYSTEM MASERS/BYPASS
(A-B) RE
TRANSMITTER 2090/2120 MHz
RECEIVER 2270/2300 MHz
(A-B) TF
TWO 10-kW MODULATED REF CARRIERS
(A-B) MC
(A-B) SCM ANTENNA
(A-B) DUAL-CARRIER TRANSMITTER SUBSYSTEM
MC
ANTENNA POSITION HA/DEC
FOLLOW-UP FEED-BACK
ANTENNA POSITION SIGNALS
(A-B) ANTENNA MECHANICAL SUBSYSTEM
HYDRAULIC POWER
SERVO CONTROL
(A-B) ANTENNA MECHANICAL SUBSYSTEM (HYDRO-MECH BUILDING MTD)
HA
DS
DS
(A-B) ANGLE SERVO RECEIVERS ANGLE TRANSLATORS ANALOG 150 AMP
FO
HA
(A-B) OPTICAL TRACKING AID
(A-B) TV SIGNAL AND CONTROLS
DSN CONTROL ROOM
100-ft SCM COLLIMATION TOWER (11, 42, 61)
50
(C-D)
(A-B)
DSN CONTROL ROOM
(C-D) GSFC COLLIMATION EQUIPMENT
(C-D)
(A-B) COLLIMATION TOWER
(A-B) OTA SWITCH 1839/ANT-201 (DSN WING)
(A
DSN WING CONTRO

117-1

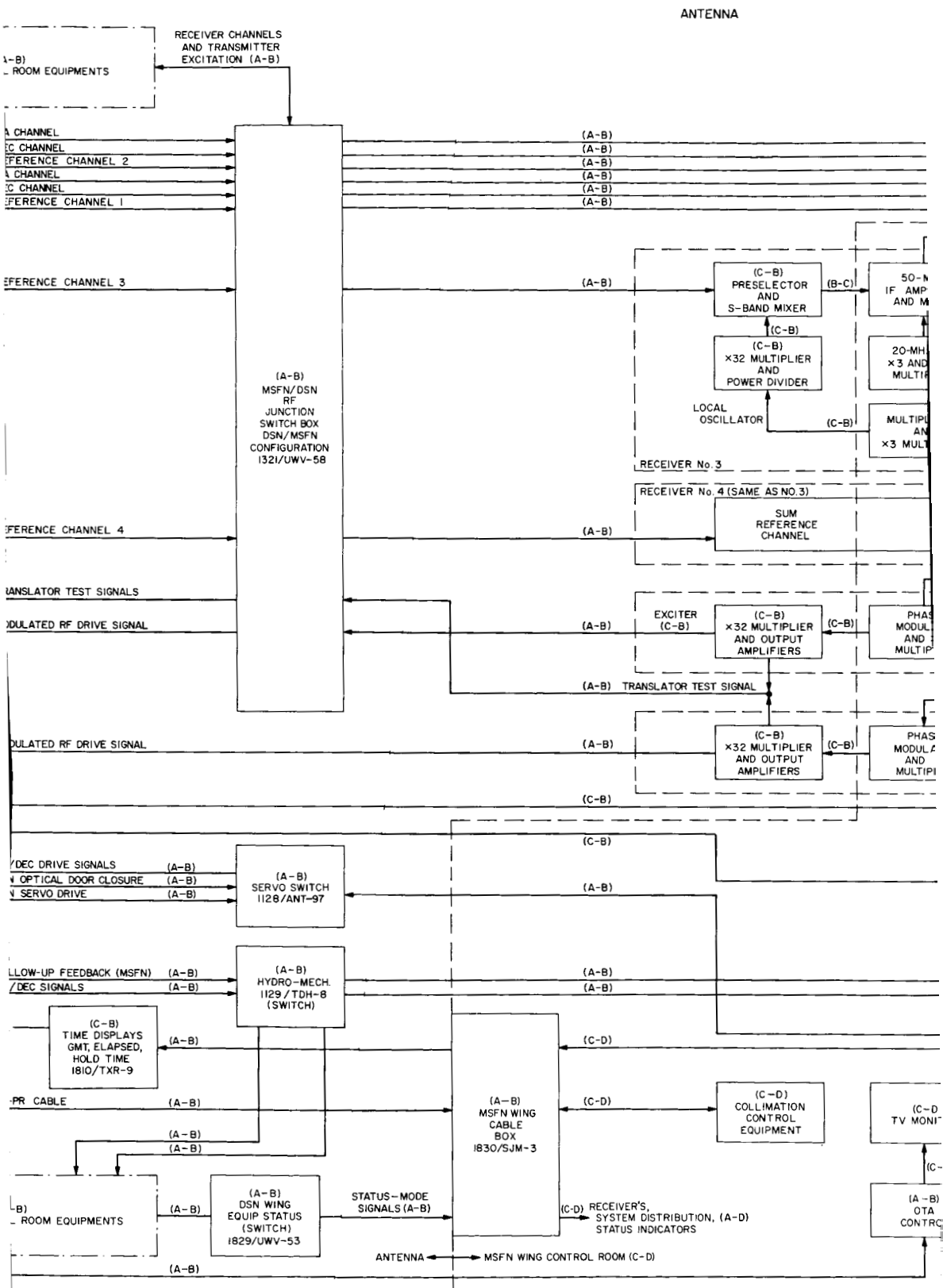
ANTENNA
RECEIVER CHANNELS AND TRANSMITTER EXCITATION (A-B)
ROOM EQUIPMENTS
CHANNEL
CHANNEL
FERENCE CHANNEL 2
CHANNEL
CHANNEL
FERENCE CHANNEL 1
FERENCE CHANNEL 3
FERENCE CHANNEL 4
RANSLATOR TEST SIGNALS
ODULATED RF DRIVE SIGNAL
ODULATED RF DRIVE SIGNAL
(A-B)
MSFN/DSN RF JUNCTION SWITCH BOX DSN/MSFN CONFIGURATION 1321/UWV-58
(C-B) PRESELECTOR AND S-BAND MIXER
(B-C)
(C-B) ×32 MULTIPLIER AND POWER DIVIDER
LOCAL OSCILLATOR
RECEIVER No. 3
RECEIVER No. 4 (SAME AS NO. 3)
SUM REFERENCE CHANNEL
EXCITER (C-B)
(C-B) ×32 MULTIPLIER AND OUTPUT AMPLIFIERS
TRANSLATOR TEST SIGNAL
(C-B) ×32 MULTIPLIER AND OUTPUT AMPLIFIERS
/DEC DRIVE SIGNALS
OPTICAL DOOR CLOSURE
SERVO DRIVE
(A-B) SERVO SWITCH 1128/ANT-97
LLOW-UP FEEDBACK (MSFN)
/DEC SIGNALS
(A-B) HYDRO-MECH. 1129/TDH-8 (SWITCH)
(C-B) TIME DISPLAYS GMT, ELAPSED, HOLD TIME 1810/TXR-9
PR CABLE
(A-B) MSFN WING CABLE BOX 1830/SJM-3
(C-D) COLLIMATION CONTROL EQUIPMENT
ROOM EQUIPMENTS
(A-B) DSN WING EQUIP STATUS (SWITCH) 1829/UWV-53
STATUS-MODE SIGNALS (A-B)
(C-D) RECEIVER'S, SYSTEM DISTRIBUTION, (A-D) STATUS INDICATORS
ANTENNA
MSFN WING CONTROL ROOM (C-D)
(A-B) OTA CONTRO
7-1
117-2

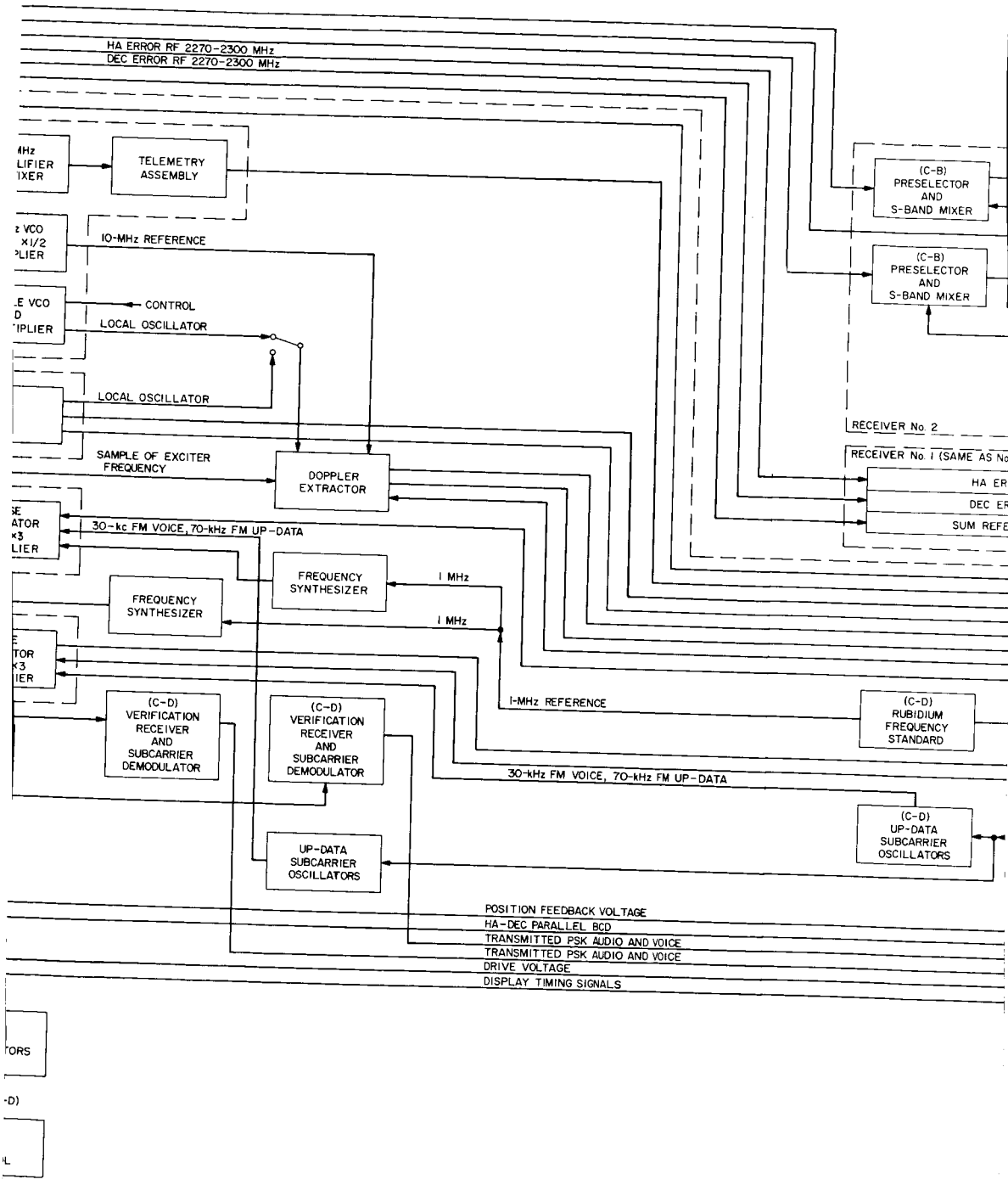
HA ERROR RF 2270-2300 MHz
DEC ERROR RF 2270-2300 MHz
TELEMETRY ASSEMBLY
(C-B) PRESELECTOR AND S-BAND MIXER
(C-B) PRESELECTOR AND S-BAND MIXER
10-MHz REFERENCE
CONTROL
LOCAL OSCILLATOR
LOCAL OSCILLATOR
RECEIVER No. 2
RECEIVER No. 1 (SAME AS No
HA ER
DEC ER
SUM REFE
SAMPLE OF EXCITER FREQUENCY
DOPPLER EXTRACTOR
30-kc FM VOICE, 70-kHz FM UP-DATA
FREQUENCY SYNTHESIZER
1 MHz
FREQUENCY SYNTHESIZER
1 MHz
1-MHz REFERENCE
(C-D) RUBIDIUM FREQUENCY STANDARD
(C-D) VERIFICATION RECEIVER AND SUBCARRIER DEMODULATOR
(C-D) VERIFICATION RECEIVER AND SUBCARRIER DEMODULATOR
30-kHz FM VOICE, 70-kHz FM UP-DATA
(C-D) UP-DATA SUBCARRIER OSCILLATORS
UP-DATA SUBCARRIER OSCILLATORS
POSITION FEEDBACK VOLTAGE
HA-DEC PARALLEL BCD
TRANSMITTED PSK AUDIO AND VOICE
TRANSMITTED PSK AUDIO AND VOICE
DRIVE VOLTAGE
DISPLAY TIMING SIGNALS

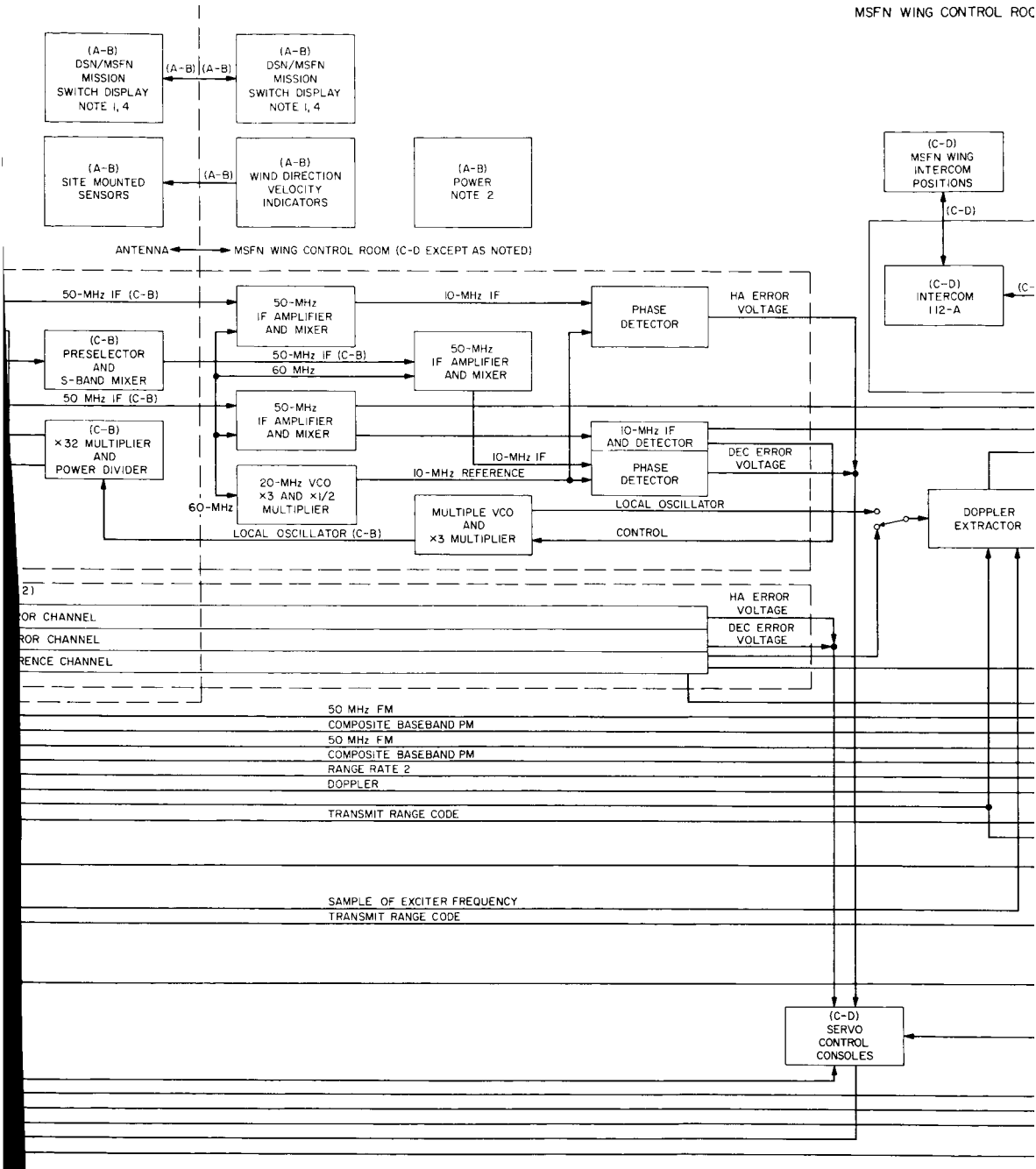
MSFN WING CONTROL ROO
(A-B) DSN/MSFN MISSION SWITCH DISPLAY NOTE 1, 4
(A-B)
(A-B) DSN/MSFN MISSION SWITCH DISPLAY NOTE 1, 4
(A-B) SITE MOUNTED SENSORS
(A-B)
(A-B) WIND DIRECTION VELOCITY INDICATORS
(A-B) POWER NOTE 2
(C-D) MSFN WING INTERCOM POSITIONS
(C-D)
(C-D) INTERCOM 112-A
ANTENNA
MSFN WING CONTROL ROOM (C-D EXCEPT AS NOTED)
50-MHz IF (C-B)
50-MHz IF AMPLIFIER AND MIXER
10-MHz IF
PHASE DETECTOR
HA ERROR VOLTAGE
(C-B) PRESELECTOR AND S-BAND MIXER
50-MHz IF (C-B)
60 MHz
50-MHz IF AMPLIFIER AND MIXER
50 MHz IF (C-B)
50-MHz IF AMPLIFIER AND MIXER
10-MHz IF AND DETECTOR
DEC ERROR VOLTAGE
(C-B) ×32 MULTIPLIER AND POWER DIVIDER
10-MHz IF
10-MHz REFERENCE
PHASE DETECTOR
20-MHz VCO ×3 AND ×1/2 MULTIPLIER
60-MHz
LOCAL OSCILLATOR
DOPPLER EXTRACTOR
MULTIPLE VCO AND ×3 MULTIPLIER
CONTROL
LOCAL OSCILLATOR (C-B)
2)
OR CHANNEL
ROR CHANNEL
RENCE CHANNEL
HA ERROR VOLTAGE
DEC ERROR VOLTAGE
50 MHz FM
COMPOSITE BASEBAND PM
50 MHz FM
COMPOSITE BASEBAND PM
RANGE RATE 2
DOPPLER
TRANSMIT RANGE CODE
SAMPLE OF EXCITER FREQUENCY
TRANSMIT RANGE CODE
(C-D) SERVO CONTROL CONSOLES

-2

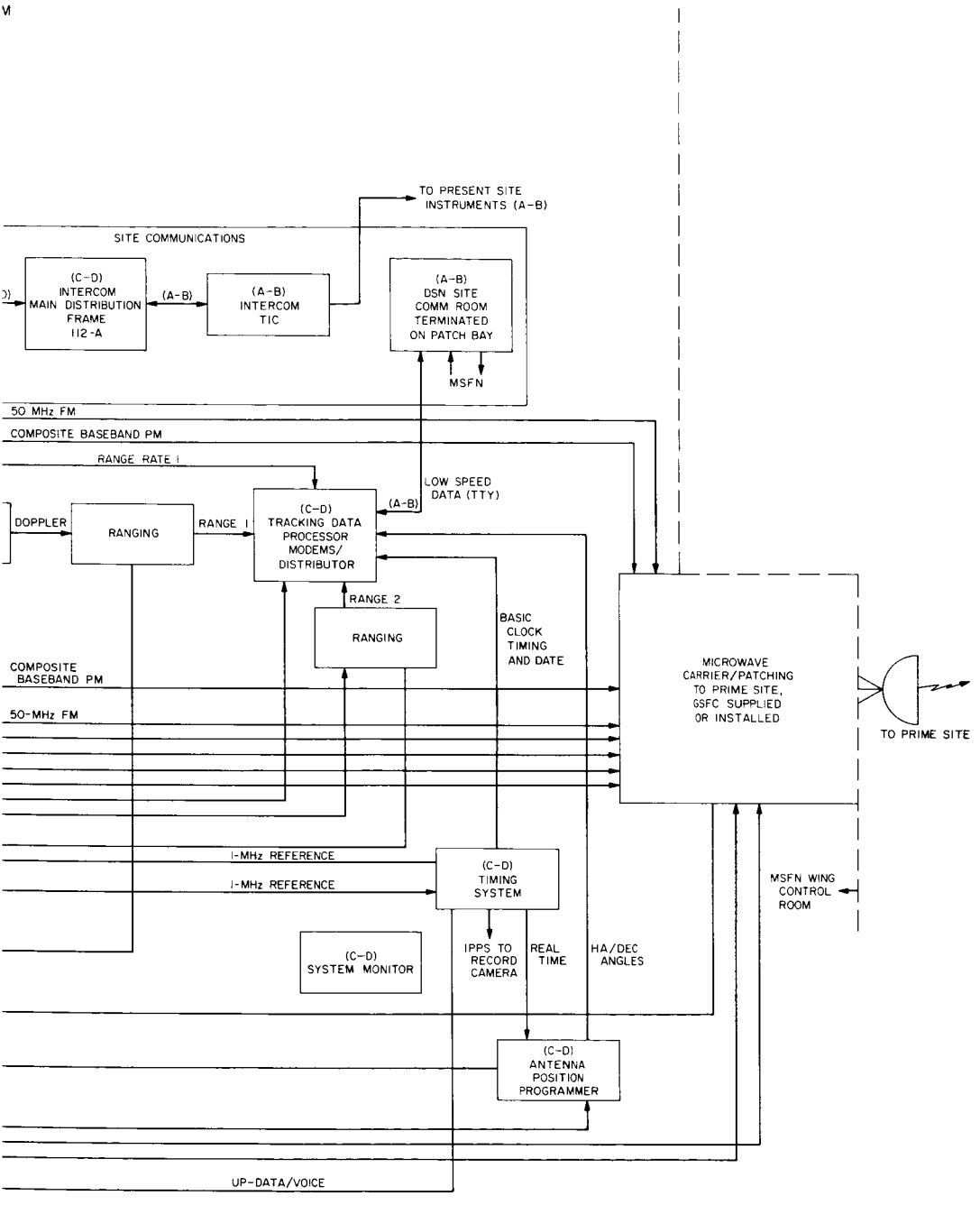


NOTES:

1. BOTH KEY OPERATED MISSION SWITCHES MUST BE ENGAGED, MODE MAINTAINED AFTER SELECTION
2. EXISTING FACILITIES, POWER PLANT AND DISTRIBUTION TO BE ENLARGED TO COMPENSATE FOR ADDITIONAL MSFN SITE REQUIREMENTS
3. J-BOXES REQUIRING SWITCHING ARE LABELED-ACTIVATED BY DSN/MSFN MISSION SWITCH
4. ACQUISITION AID SUBSYSTEM (DSS 42) TEST CONTROLS IN DSN WINGS ONLY

LEGEND
(A) JPL SUPPLIED
(B) JPL INSTALLED
(C) GSFC SUPPLIED
(D) GSFC INSTALLED

**Fig. 1. MSFN/DSS *Apollo* Backup station system interface diagram**

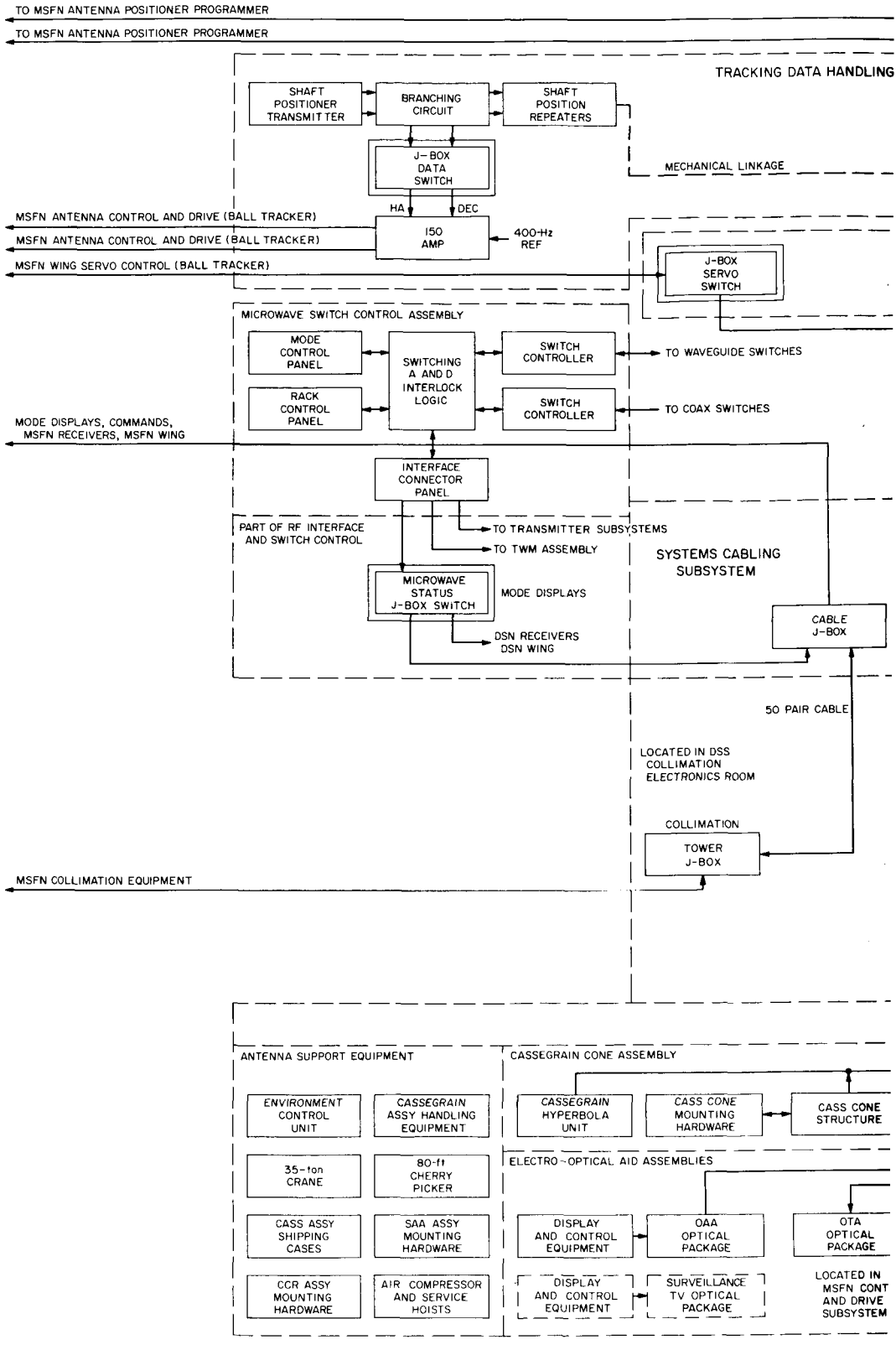


**Fig. 2. MSFN/DSS *Apollo* Backup station conversion diagram; DSN equipments**

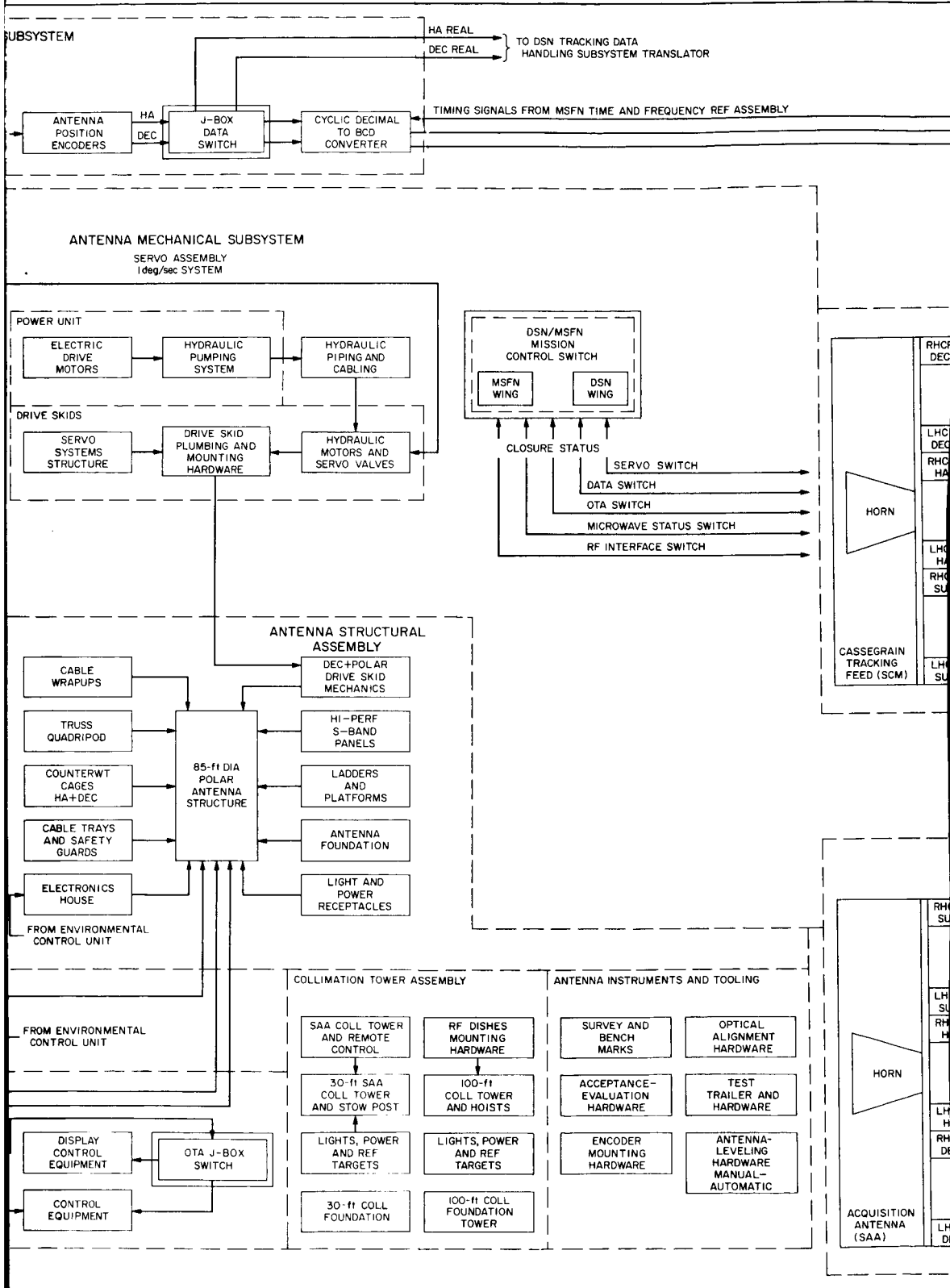
SUBSYSTEM
HA REAL
DEC REAL
TO DSN TRACKING DATA HANDLING SUBSYSTEM TRANSLATOR
ANTENNA POSITION ENCODERS
HA
DEC
J-BOX DATA SWITCH
CYCLIC DECIMAL TO BCD CONVERTER
TIMING SIGNALS FROM MSFN TIME AND FREQUENCY REF ASSEMBLY
ANTENNA MECHANICAL SUBSYSTEM
SERVO ASSEMBLY
1deg/sec SYSTEM
POWER UNIT
ELECTRIC DRIVE MOTORS
HYDRAULIC PUMPING SYSTEM
HYDRAULIC PIPING AND CABLING
DRIVE SKIDS
SERVO SYSTEMS STRUCTURE
DRIVE SKID PLUMBING AND MOUNTING HARDWARE
HYDRAULIC MOTORS AND SERVO VALVES
DSN/MSFN MISSION CONTROL SWITCH
MSFN WING
DSN WING
CLOSURE STATUS
SERVO SWITCH
DATA SWITCH
OTA SWITCH
MICROWAVE STATUS SWITCH
RF INTERFACE SWITCH
HORN
CASSEGRAIN TRACKING FEED (SCM)
ANTENNA STRUCTURAL ASSEMBLY
CABLE WRAPUPS
TRUSS QUADRIPOD
COUNTERWT CAGES HA+DEC
CABLE TRAYS AND SAFETY GUARDS
ELECTRONICS HOUSE
FROM ENVIRONMENTAL CONTROL UNIT
85-ft DIA POLAR ANTENNA STRUCTURE
DEC+POLAR DRIVE SKID MECHANICS
HI-PERF S-BAND PANELS
LADDERS AND PLATFORMS
ANTENNA FOUNDATION
LIGHT AND POWER RECEPTACLES
COLLIMATION TOWER ASSEMBLY
ANTENNA INSTRUMENTS AND TOOLING
FROM ENVIRONMENTAL CONTROL UNIT
SAA COLL TOWER AND REMOTE CONTROL
RF DISHES MOUNTING HARDWARE
30-ft SAA COLL TOWER AND STOW POST
100-ft COLL TOWER AND HOISTS
LIGHTS, POWER AND REF TARGETS
LIGHTS, POWER AND REF TARGETS
30-ft COLL FOUNDATION
100-ft COLL FOUNDATION TOWER
SURVEY AND BENCH MARKS
OPTICAL ALIGNMENT HARDWARE
ACCEPTANCE-EVALUATION HARDWARE
TEST TRAILER AND HARDWARE
ENCODER MOUNTING HARDWARE
ANTENNA-LEVELING HARDWARE MANUAL-AUTOMATIC
DISPLAY CONTROL EQUIPMENT
OTA J-BOX SWITCH
CONTROL EQUIPMENT
HORN
ACQUISITION ANTENNA (SAA)

118-2

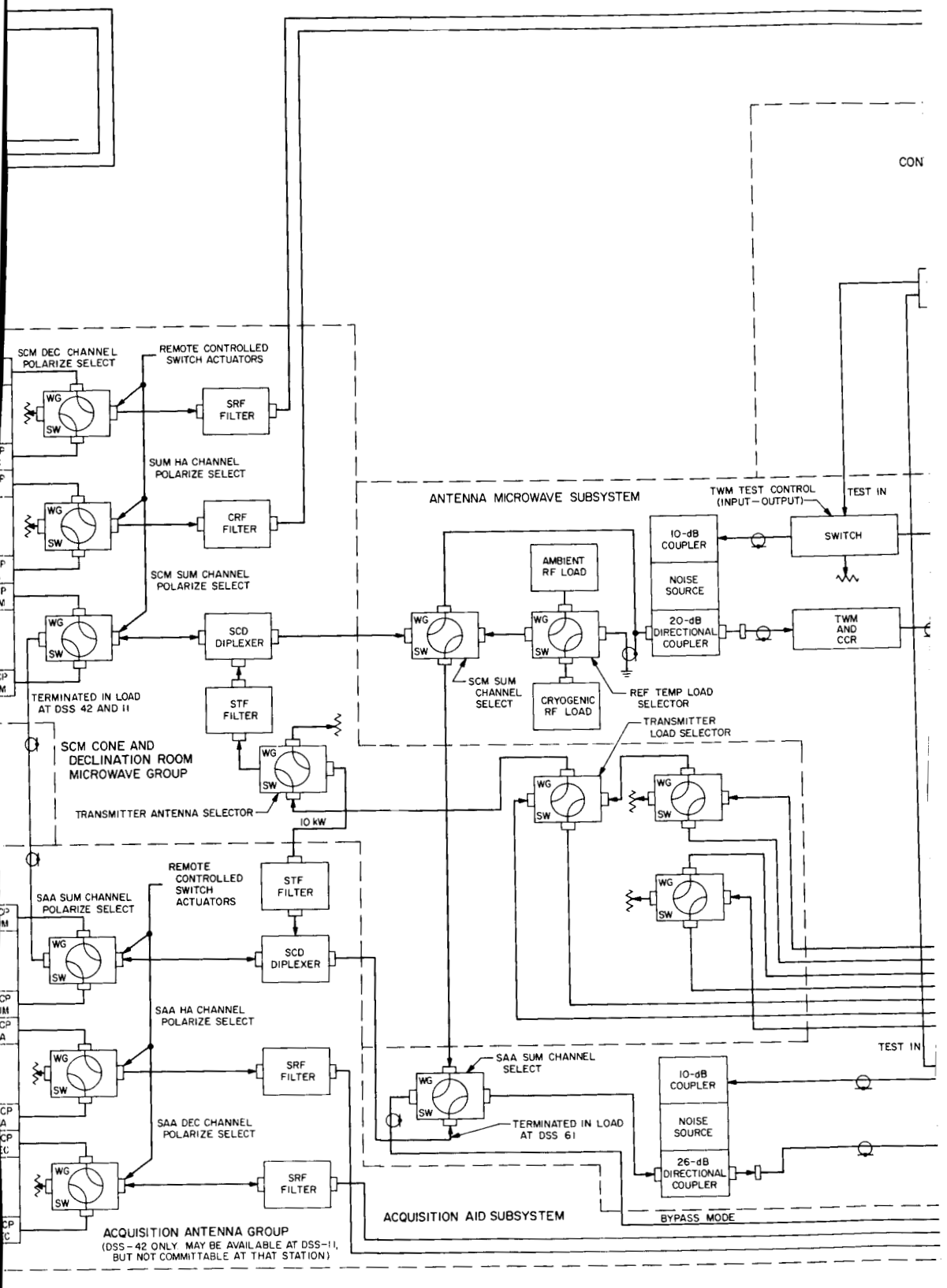
SCM DEC CHANNEL POLARIZE SELECT
REMOTE CONTROLLED SWITCH ACTUATORS
WG
SW
SRF FILTER
SUM HA CHANNEL POLARIZE SELECT
CRF FILTER
SCM SUM CHANNEL POLARIZE SELECT
SCD DIPLEXER
STF FILTER
TERMINATED IN LOAD AT DSS 42 AND 11
SCM CONE AND DECLINATION ROOM MICROWAVE GROUP
TRANSMITTER ANTENNA SELECTOR
10 kW
ANTENNA MICROWAVE SUBSYSTEM
TWM TEST CONTROL (INPUT–OUTPUT)
TEST IN
10-dB COUPLER
SWITCH
AMBIENT RF LOAD
NOISE SOURCE
20-dB DIRECTIONAL COUPLER
TWM AND CCR
SCM SUM CHANNEL SELECT
CRYOGENIC RF LOAD
REF TEMP LOAD SELECTOR
TRANSMITTER LOAD SELECTOR
REMOTE CONTROLLED SWITCH ACTUATORS
SAA SUM CHANNEL POLARIZE SELECT
STF FILTER
SCD DIPLEXER
SAA HA CHANNEL POLARIZE SELECT
SRF FILTER
SAA DEC CHANNEL POLARIZE SELECT
SRF FILTER
SAA SUM CHANNEL SELECT
TERMINATED IN LOAD AT DSS 61
10-dB COUPLER
NOISE SOURCE
26-dB DIRECTIONAL COUPLER
TEST IN
BYPASS MODE
ACQUISITION AID SUBSYSTEM
ACQUISITION ANTENNA GROUP
(DSS-42 ONLY. MAY BE AVAILABLE AT DSS-11, BUT NOT COMMITTABLE AT THAT STATION)

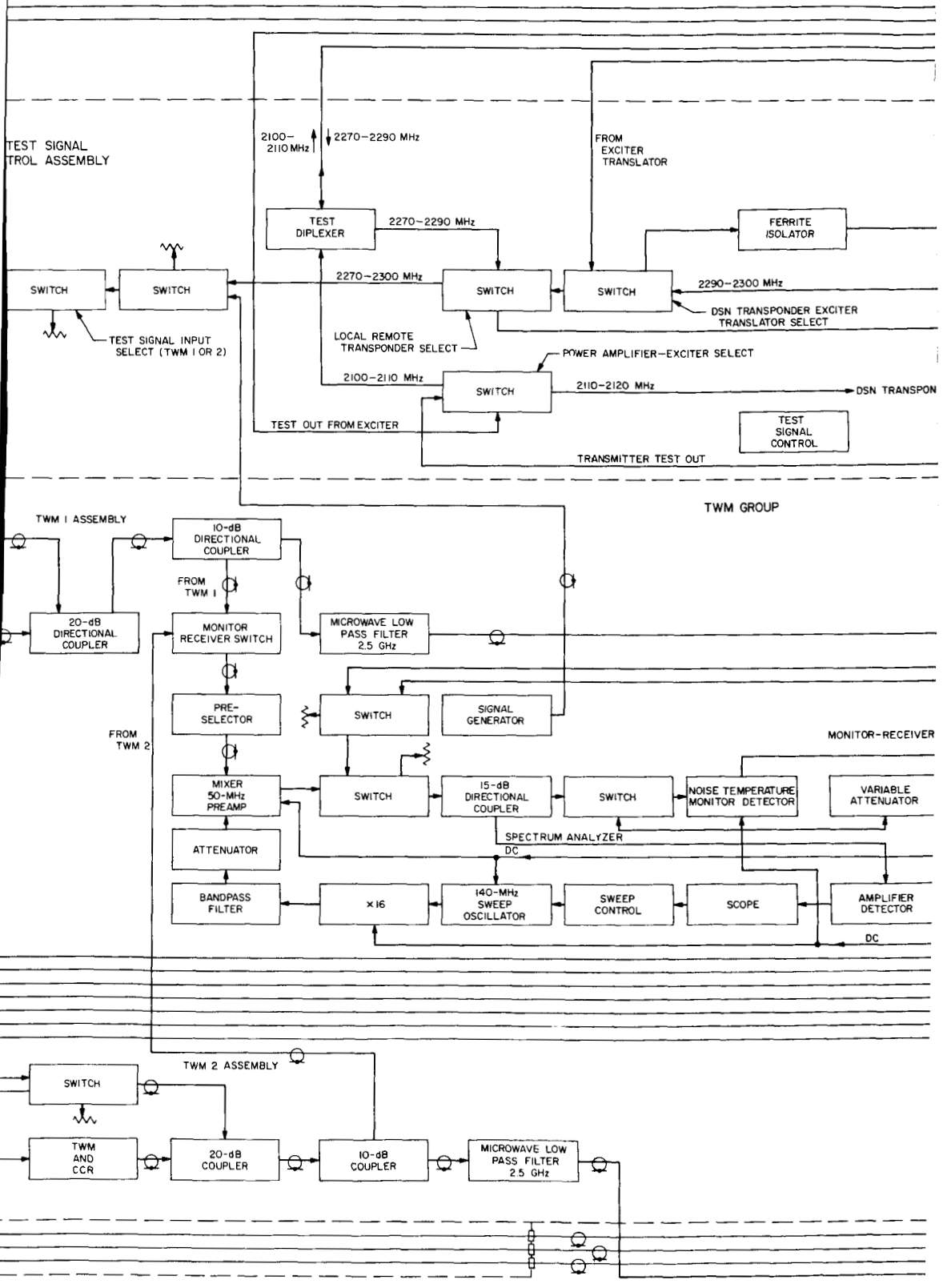
TEST SIGNAL
TROL ASSEMBLY
2100–
2110 MHz
2270–2290 MHz
FROM
EXCITER
TRANSLATOR
TEST
DIPLEXER
2270–2290 MHz
FERRITE
ISOLATOR
SWITCH
SWITCH
2270–2300 MHz
SWITCH
SWITCH
2290–2300 MHz
DSN TRANSPONDER EXCITER
TRANSLATOR SELECT
TEST SIGNAL INPUT
SELECT (TWM 1 OR 2)
LOCAL REMOTE
TRANSPONDER SELECT
POWER AMPLIFIER–EXCITER SELECT
2100–2110 MHz
SWITCH
2110–2120 MHz
DSN TRANSPON
TEST OUT FROM EXCITER
TEST
SIGNAL
CONTROL
TRANSMITTER TEST OUT
TWM GROUP
TWM 1 ASSEMBLY
10-dB
DIRECTIONAL
COUPLER
FROM
TWM 1
20-dB
DIRECTIONAL
COUPLER
MONITOR
RECEIVER SWITCH
MICROWAVE LOW
PASS FILTER
2.5 GHz
PRE-
SELECTOR
SWITCH
SIGNAL
GENERATOR
FROM
TWM 2
MONITOR-RECEIVER
MIXER
50-MHz
PREAMP
SWITCH
15-dB
DIRECTIONAL
COUPLER
SWITCH
NOISE TEMPERATURE
MONITOR DETECTOR
VARIABLE
ATTENUATOR
SPECTRUM ANALYZER
DC
ATTENUATOR
BANDPASS
FILTER
×16
140-MHz
SWEEP
OSCILLATOR
SWEEP
CONTROL
SCOPE
AMPLIFIER
DETECTOR
DC
TWM 2 ASSEMBLY
SWITCH
TWM
AND
CCR
20-dB
COUPLER
10-dB
COUPLER
MICROWAVE LOW
PASS FILTER
2.5 GHz

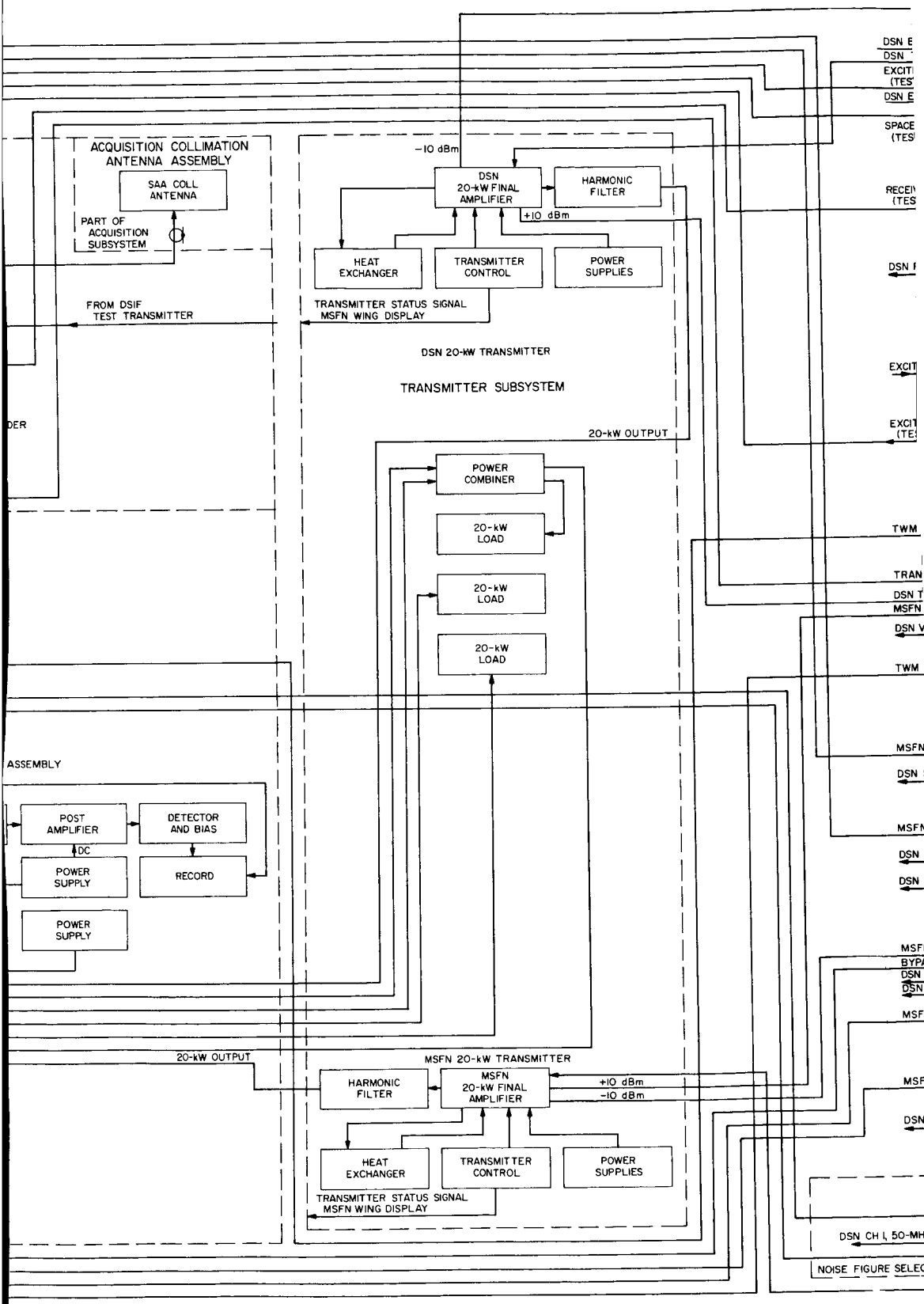
ACQUISITION COLLIMATION ANTENNA ASSEMBLY
SAA COLL ANTENNA
PART OF ACQUISITION SUBSYSTEM
FROM DSIF TEST TRANSMITTER
-10 dBm
DSN 20-kW FINAL AMPLIFIER
HARMONIC FILTER
+10 dBm
HEAT EXCHANGER
TRANSMITTER CONTROL
POWER SUPPLIES
TRANSMITTER STATUS SIGNAL MSFN WING DISPLAY
DSN 20-kW TRANSMITTER
TRANSMITTER SUBSYSTEM
20-kW OUTPUT
POWER COMBINER
20-kW LOAD
20-kW LOAD
20-kW LOAD
ASSEMBLY
POST AMPLIFIER
DETECTOR AND BIAS
DC
POWER SUPPLY
RECORD
POWER SUPPLY
20-kW OUTPUT
MSFN 20-kW TRANSMITTER
HARMONIC FILTER
MSFN 20-kW FINAL AMPLIFIER
+10 dBm
-10 dBm
HEAT EXCHANGER
TRANSMITTER CONTROL
POWER SUPPLIES
TRANSMITTER STATUS SIGNAL MSFN WING DISPLAY
DSN CH I, 50-MH
NOISE FIGURE SELEC

118-5

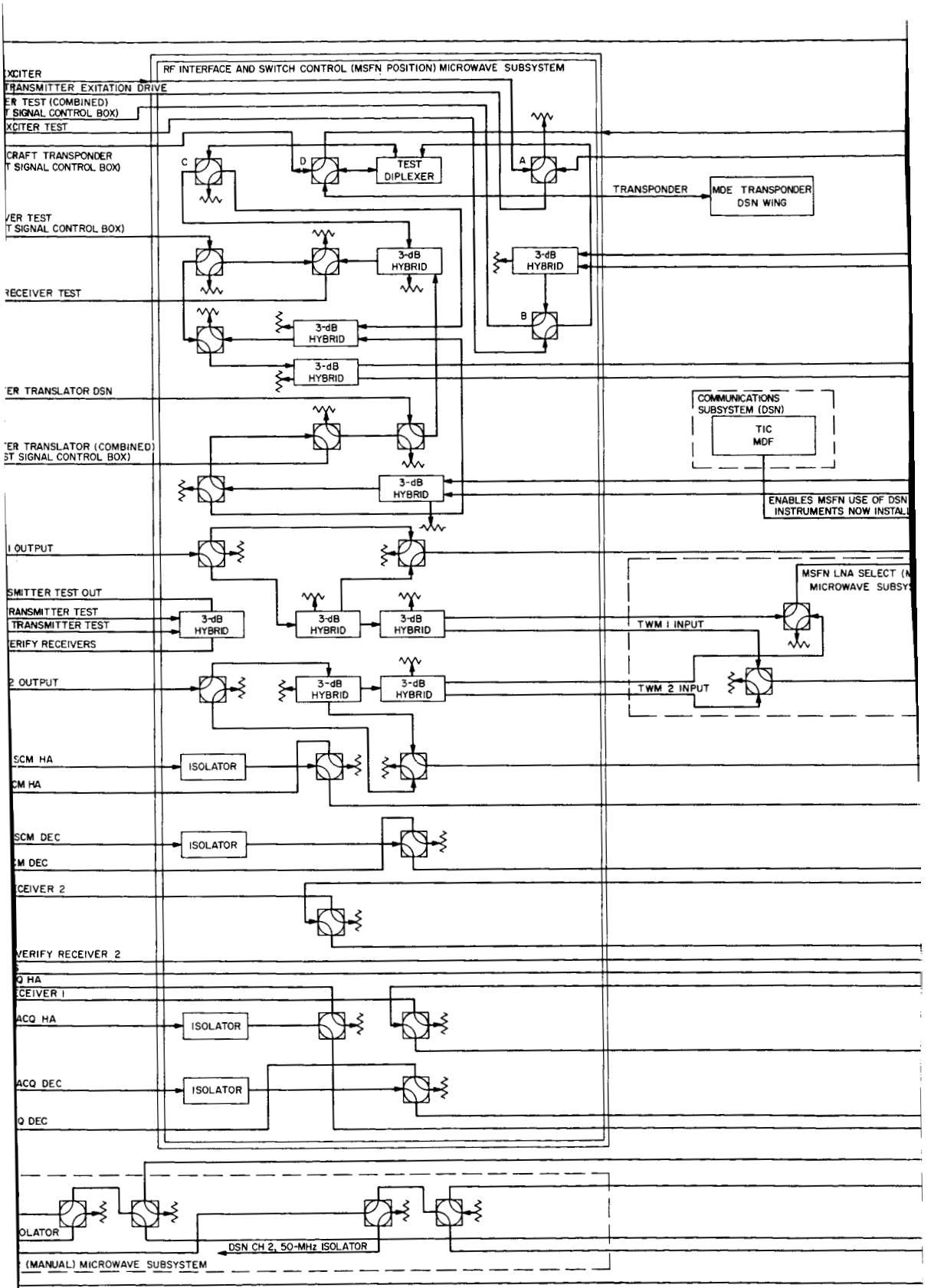
RF INTERFACE AND SWITCH CONTROL (MSFN POSITION) MICROWAVE SUBSYSTEM
XCITER
TRANSMITTER EXITATION DRIVE
ER TEST (COMBINED)
T SIGNAL CONTROL BOX)
XCITER TEST
CRAFT TRANSPONDER
T SIGNAL CONTROL BOX)
VER TEST
T SIGNAL CONTROL BOX)
RECEIVER TEST
ER TRANSLATOR DSN
ER TRANSLATOR (COMBINED)
ST SIGNAL CONTROL BOX)
I OUTPUT
SMITTER TEST OUT
RANSMITTER TEST
TRANSMITTER TEST
ERIFY RECEIVERS
2 OUTPUT
SCM HA
CM HA
SCM DEC
M DEC
CEIVER 2
VERIFY RECEIVER 2
Q HA
CEIVER I
ACQ HA
ACQ DEC
Q DEC
OLATOR
(MANUAL) MICROWAVE SUBSYSTEM
C
D
TEST DIPLEXER
A
TRANSPONDER
MDE TRANSPONDER DSN WING
3-dB HYBRID
3-dB HYBRID
3-dB HYBRID
B
3-dB HYBRID
3-dB HYBRID
3-dB HYBRID
3-dB HYBRID
3-dB HYBRID
3-dB HYBRID
3-dB HYBRID
ISOLATOR
ISOLATOR
ISOLATOR
COMMUNICATIONS SUBSYSTEM (DSN)
TIC MDF
ENABLES MSFN USE OF DSN
INSTRUMENTS NOW INSTALL
MSFN LNA SELECT (N
MICROWAVE SUBSYS
TWM 1 INPUT
TWM 2 INPUT
DSN CH 2, 50-MHz ISOLATOR

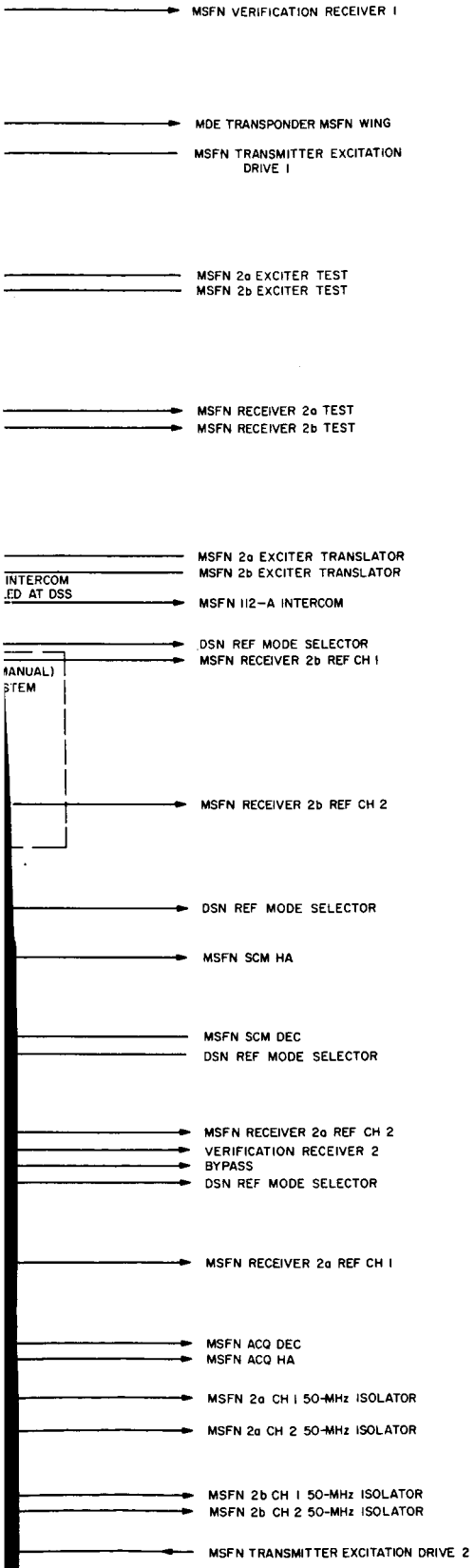
MSFN VERIFICATION RECEIVER 1
MDE TRANSPONDER MSFN WING
MSFN TRANSMITTER EXCITATION DRIVE 1
MSFN 2a EXCITER TEST
MSFN 2b EXCITER TEST
MSFN RECEIVER 2a TEST
MSFN RECEIVER 2b TEST
MSFN 2a EXCITER TRANSLATOR
MSFN 2b EXCITER TRANSLATOR
INTERCOM
ED AT DSS
MSFN 112-A INTERCOM
DSN REF MODE SELECTOR
MSFN RECEIVER 2b REF CH 1
ANUAL)
STEM
MSFN RECEIVER 2b REF CH 2
DSN REF MODE SELECTOR
MSFN SCM HA
MSFN SCM DEC
DSN REF MODE SELECTOR
MSFN RECEIVER 2a REF CH 2
VERIFICATION RECEIVER 2
BYPASS
DSN REF MODE SELECTOR
MSFN RECEIVER 2a REF CH 1
MSFN ACQ DEC
MSFN ACQ HA
MSFN 2a CH 1 50-MHz ISOLATOR
MSFN 2a CH 2 50-MHz ISOLATOR
MSFN 2b CH 1 50-MHz ISOLATOR
MSFN 2b CH 2 50-MHz ISOLATOR
MSFN TRANSMITTER EXCITATION DRIVE 2

MCC-H. Two-way data (commands, telemetry, TV, etc.) is handled similar to two-way voice. However, for both of these functions, the DSN *Apollo* stations will be implemented with subcarrier modulators. Subcarrier demodulation and decommutation will be performed at the Prime sites using composite spectra from the DSN *Apollo* station's carrier phase demodulators and/or the 50 MHz IF (FM) output. Selected spacecraft telemetry (e.g., transponder phase error and AGC) is routed back to the DSN site after processing by the Prime station. A microwave carrier two-way communication system links the co-located *Apollo* Prime and Backup stations.

Selected DSN stations to be modified for *Apollo* support are as follows:

| | |
|---|---|
| Goldstone-Pioneer | MSFN/DSS 11 |
| Canberra-Tidbinbilla | MSFN/DSS 42 |
| Madrid-Robledo | MSFN/DSS 61 |

Table 1 summarizes the major *Apollo* functional requirements.

**Table 1. Functions of the MSFN *Apollo* Backup station system**

(1) Acquire and track spacecraft signals through an integral acquisition subsystem.

(2) Transmit voice, data, and ranging signals to spacecraft.

(3) Transfer track from the acquisition subsystem to the main receiving subsystem.

(4) Determine range and range rate parameters of spacecraft and transfer this information to recorders and/or the NASA Communications Network.

(5) Receive video, voice and telemetry information from the spacecraft, and transfer this information to recorders and/or the NASA Communications Network.

(6) Accept pointing information from specified sources (drive tapes, manual) and utilize this information to drive the antenna.

(7) Maneuver or position the antenna according to any manual drive inputs within the specified maximum rate and acceleration.

(8) Operate in programmed search modes.

(9) Follow a second antenna in slaved mode.

(10) Provide slaving signals for driving other antennas.

(11) Provide visual readout of antenna pointing angle, record this information, and/or transfer this information to the NASA Communications Network.

A Master Mission control switch automatically changes the DSS equipment configuration to either MSFN or DSN mission support. Except for the site intercom/communication manual patches and transmitter/maser retuning, the DSN/MSFN station will be in one configuration or the other, by the activation of the Master Mission control switch featuring the following singularities:

(1) Single activation; requiring the simultaneous operation of two identical keys—one in each control room.

(2) Dual location; DSN and MSFN control room.

(3) Mission mode maintained after selection.

After key operation, four indicator lamps will signify switching center closures, i.e., the microwave subsystem; the angle encoder interface; and servo interface; and the Optical Tracking Assembly. A remote wind velocity and direction display will be furnished to the MSFN servo console from the common site mounted sensors.

Initial considerations in the JPL approach to the mission requirements were to perturb the present DSN S-band installation as little as possible and to assess or utilize existing GSFC Prime site engineering. In Fig. 1, the MSFN/DSS *Apollo* Backup station system interface diagram delineates the responsibilities in both equipment and installation shared between JPL and GSFC. Only the JPL equipment engineering conversion will be discussed and is shown in Fig. 2.

The 85-ft antenna microwave subsystem equipment includes two traveling wave maser (TWM) low-noise amplifiers and associated closed-cycle refrigeration; S-band cassegrain monopulse cone; test signal control assembly; monitor receiver assembly; and required microwave hardware, cables, and waveguide.

A microwave switch junction box, operated by the master mission switch and installed in the antenna electronics room, permits either the MSFN or DSN use of the common antenna-mounted microwave equipments. Similarly, located in the DSN control plenum, a status signal switch junction box routes DSN microwave configuration status signals and receiver IF attenuator commands to either network. Accidental radiation from the MSFN collimation tower equipment will be prevented by an interlock controlled by the status signal switch. Either the MSFN or DSN wing can be in a total operational system configuration simultaneously with the other network's system in a partial or independent test configuration mode. The common test signal control assembly

will permit test signals from either of the two test sources, i.e., transponders or exciter translators, to be injected into the MCFN crystal mixer input circuits of the multiple receiver reference and angle channels.

For simultaneous transmission of two separate carrier signals, two 20-kW transmitters will provide MSFN S-band frequency power amplification (*SPS 37-38*, Vol. III, p. 72). Combining two signals at high level, each 20-kW transmitter will dissipate 50% of its power in a 3-dB hybrid combiner waterload with the remaining power being radiated. The two transmitters will be controlled from a new transmitter rack placed in the DSN control room adjacent to the microwave subsystem. Status signals, indicative of transmitter operation, showing beam voltage applied to the power amplifiers are routed to the MSFN control room for monitoring purposes.

GSFC will use the existing GSDS Optical Tracking Aid (OTA) consisting of cameras, filters, lenses, *J*-boxes, cables, and control panels with camera controls and aperture door operation available to either network monitor via the mission switch-operated optical tracking and switching junction box located in the DSN control room. This arrangement assures only one optical reference system to align the mechanical axes. The Optical Acquisition Aid (OAA) assembly will remain unchanged.

Structural modifications to the antenna electronics room to accommodate the additional MSFN equipments consist of a new catwalk and guard rail to facilitate servicing of the antenna junction box and installation of new floor beams. Additional antenna cable trays and wrapup drums are also required. Three spare SCM cones complete with microwave components (less maser) will be furnished. One cone will be stored at each individual DSN *Apollo* site in its original shipping container under an environment of pressurized dry nitrogen.

The GSDS S-Band Acquisition Aid Subsystem (SAA) requires modifications to accommodate both MSFN and DSN frequencies. This will be accomplished by broadbanding present waveguide components. Modifications will be accomplished at Goldstone and Tidbinbilla only, since no Acquisition Aid is available at the Madrid station.

An angle encoder switch junction box routes antenna angle data digital signals to either the DSN Tracking Data Handling Subsystem or GSFC's Antenna Position Programmer. Analog angle data signals for the GSFC servo system ball tracker are circuited through isolation amplifiers. This switching center will be located in the present TDH rack in the Hydro-mechanical building.

To permit the antenna drive signals originating in either control room to control the common antenna hydraulic drive assembly, a servo switch junction box, located in the Hydro-mechanical building pump room is required. All three antenna sites will be retrofitted with new DC tachometers.

A new SCM collimation tower 50-pair cable will be installed adjacent to the existing DSIF collimation tower cable for MSFN use.

Low-speed TTY data telephone pair cables connect the GSFC Tracking Data Processor and the DSS communication room. The JPL Tactical Intercom and Communication Assembly (TIC) will also be interfaced with the GSFC 112-A intercom subsystem via a cable to the latter's vertical distribution frame and by appropriate pre-mission manual telephone patches. This arrangement will allow GSFC to use the presently installed DSS telephone instruments.

JPL-provided facilities will include floor space for the MSFN configuration at the selected sites. Utilities, comprising power, air conditioning and water in amounts required by GSFC for proper operation of the MSFN equipment, will also be provided.



## B. Facility Construction and Equipment Installation

*J. Orbison and H. L. Richter*

### 1. Mars Deep Space Station, J. Orbison

The installation of the S-band system continues concurrently with the Mars DSS operation. Originally, the operation was performed using the JPL R&D receiver and maser, and the Station Digital Instrumentation Subsystem. The transmitting to the tracked spacecraft was performed by the Venus DSS and the Echo DSS when required. Both of the latter stations also provided the necessary recording and processing via microwave from the Mars DSS.

Essentially, the Mars DSS has received the total S-band system and is currently completing the installation. The major exception is the use of the JPL R&D maser with the DSIF receiver for current tracking of the *Pioneer VI* spacecraft. The 20-kW transmitter was placed in operation on 7 August. The high-voltage power supply for the transmitter currently is located in the large service area on the first floor of the pedestal (Fig. 3). Eventually it will be relocated to its permanent position in the main equipment room on the alidade.

The master equatorial assembly was positioned in the room atop the central instrument tower early in June. Currently it is in the installation and checkout phase of leveling and alignment.

The diesel generators, which provide the present power to the Mars DSS, experienced excessive torque effects in the rotors and required disassembly for rework. An 1126-kW diesel generator unit (Fig. 4) was temporarily installed near the generator building to provide station power while the three generators were undergoing repairs. The No. 2 generator is in operational standby for emergencies and will itself be reworked when the other two become operational.

Construction of a commercial power line from the recently completed Southern California Edison substation, 5 miles east of the Venus DSS, to the Mars DSS was begun in late July. Scheduled for a fall completion, it will provide adequate power requirements for planned

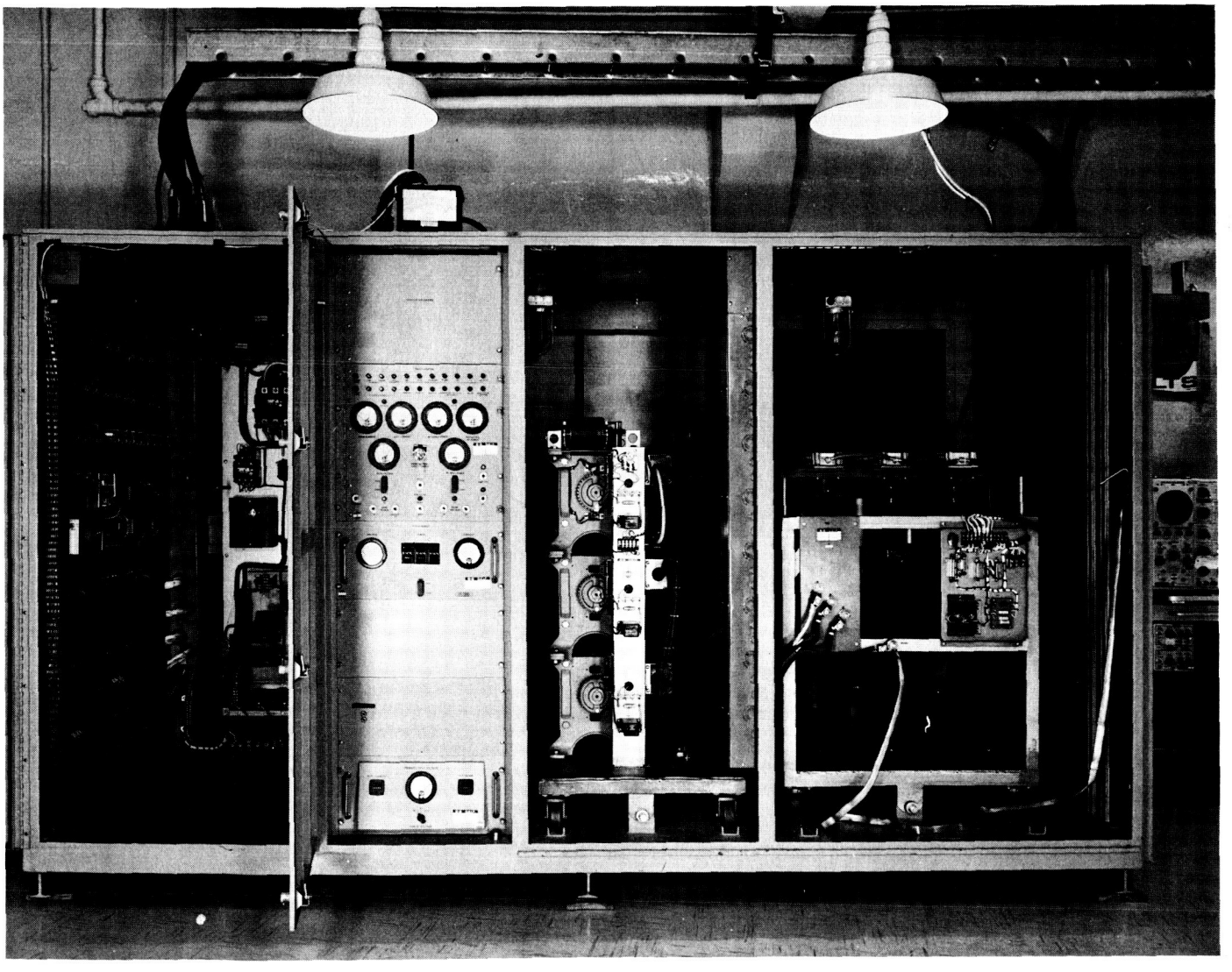

**Fig. 3. Mars DSS transmitter high-voltage power supply**

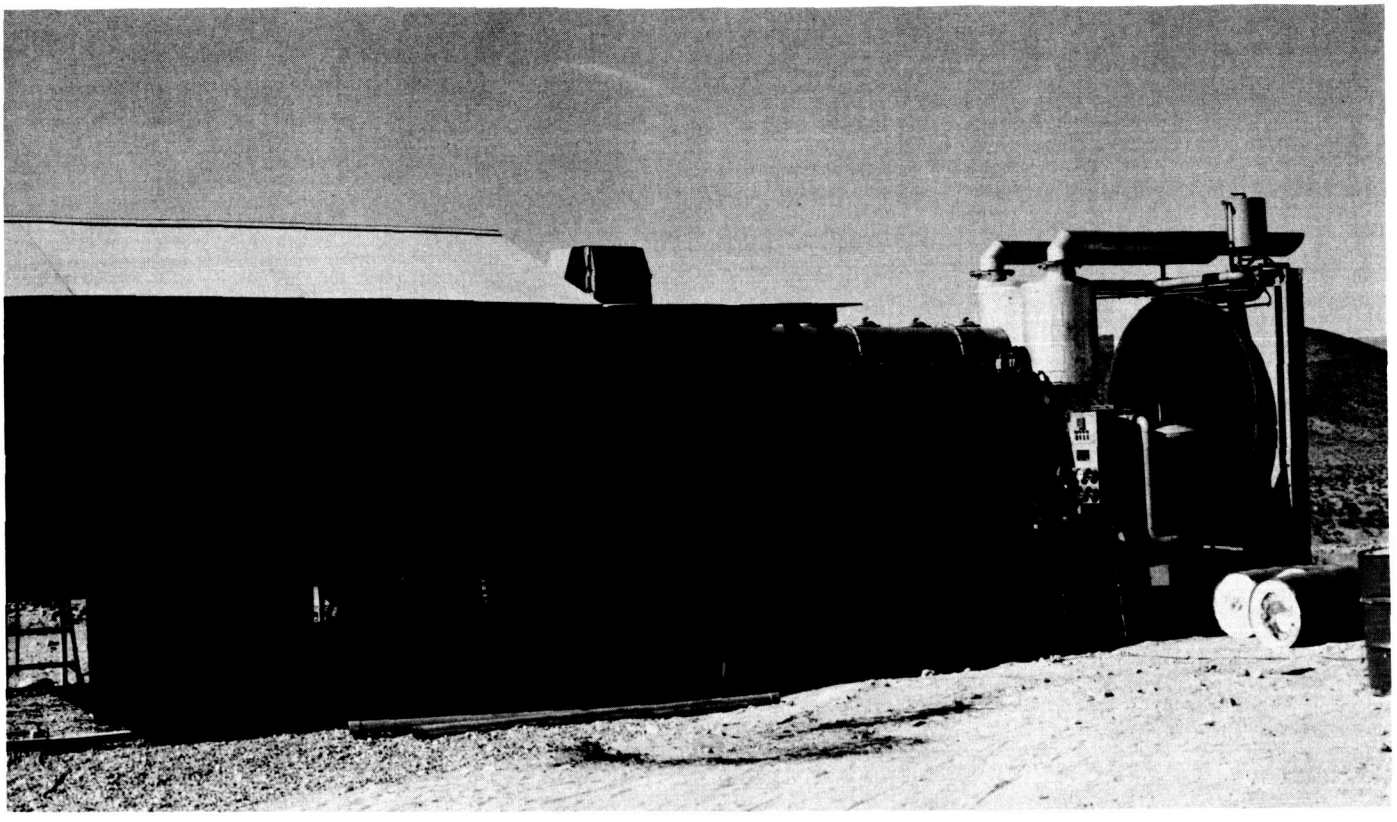

**Fig. 4. Temporary 1126-kW diesel generator at Mars DSS**

station operations, and will also serve as backup to the Station's diesel power which is used during mission-critical periods. The pole line will terminate approximately 1 mile south of the 210-ft antenna, and the cabling will proceed underground to the substation site near the diesel generator building.

## 2. *Pioneer Deep Space Station,* J. Orbison

The Pioneer DSS requirements to maintain support to the normal DSN missions, and also help in the implementation of the MSFF, required extensive station changes. Initially, these dual requirements began with an enlargement of the Control Building (*SPS 37-27*, Vol. III, p. 5; *37-28*, Vol. III, pp. 13–15; *37-29*, Vol. III, pp. 10–11). Two opposed identical wings were constructed with equal tunnel access to the hydro-mechanical building, and the 85-ft antenna.

Installation of the MSFF S-band system began in July 1966 and is in progress in the west wing of the control building (Fig. 5). Equipment installation to date includes the receiver and transmitter exciter, antenna servo electronics, antenna position programmer, tracking data processor, and portions of the telemetry equipment. Subsystem power-on tests, preliminary interfacing and basic operational tests are in progress.

The additional weight of the second transmitter and the maser assemblies requirements of the MSFF on the antenna required the addition of 4900 lb of counterweights to the west side of the hour angle gear. Equipment relocations, new cable trays, and other changes to the declination room and the antenna were also made. A cable wrap-up, patterned after the one developed on the Echo DSS 85-ft antenna (*SPS 37-35*, Vol. III, p. 17) has been installed and tested.

The original 10-kW Klystron power amplifier was changed to a 20-kW unit, necessitating modifications to the high-voltage power supply located in the hydro-mechanical building to provide the additional power. The MSFF 20-kW Klystron power amplifier and associated equipment were also installed in the declination room, while the high voltage power supply was installed adjacent to the original unit. Near the base of the northeast leg of the antenna are the two heat exchangers for the transmitter power amplifiers, with a newly fabricated header permitting either unit to be used with either transmitter.

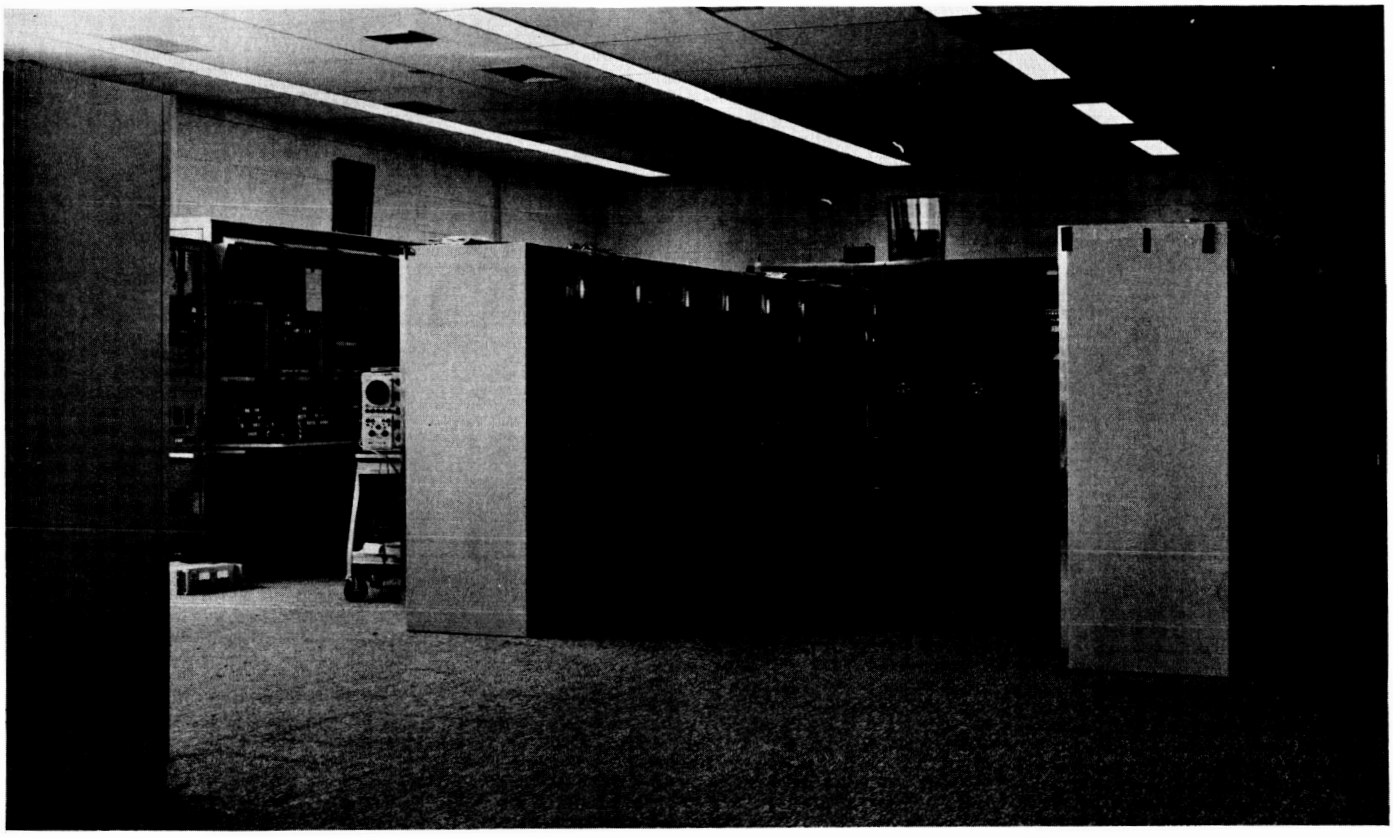

**Fig. 5. Manned space flight facility control room installation**

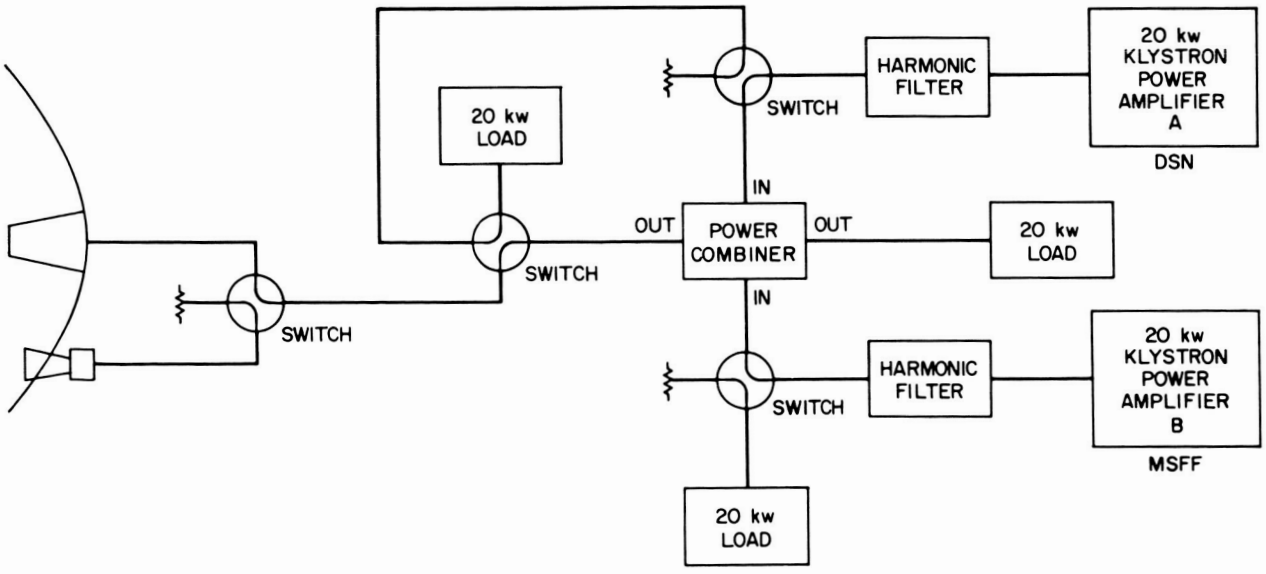


**Fig. 6. Dual 20-kW transmitter simplified waveguide switching**

A simplified block diagram of the dual transmitter installation is illustrated in Fig. 6. The switching arrangement permits either transmitter to be coupled to the Cassegrain Tracking Feed or the Acquisition Aid antenna. Through the use of the power combiner, both transmitters can feed the antenna simultaneously.

The parametric amplifier was removed to provide space for mounting the MSFF maser in the declination shaft room. By using a locally fabricated DSN/MSFF RF switching assembly, complete flexibility between the two systems is possible. Either system can control the antenna drive, use either or both masers with the respective receivers, transmit individually or simultaneously, and perform the system transfer quickly, when needed.

Equipment relocations were performed in the DSN control room to provide space for the Multiple Mission Support Area, and the dual capability needed for the DSN/MSFF function. Relocated were the Analog Instrumentation subsystem and the Antenna Microwave ground control racks. An additional Analog Instrumentation subsystem, recorders, and the TCP computers for the Telemetry and Command Processing subsystem will be installed at a later date.

### 3. Echo Deep Space Station, J. Orbison

*Lunar Orbiter* and *Pioneer VII* equipment freezes delayed the installation of the second Analog Instrumentation Subsystem delivered just prior to the final testing and launch of the *Lunar Orbiter*. The equipment racks were placed in position in the control room and readied for interrack and interface cabling. Two Ampex FR-1400 magnetic tape recorders for the second system arrived in late June and were installed and placed in operation for *Pioneer* spacecraft recording, a function they are currently performing for *Pioneers VI* and *VII*.

### 4. Venus Deep Space Station, J. Orbison

Construction of the Laboratory and Office Building, G-60, is in progress (Fig. 7). The outside walls, and roof are in the final stage of construction, and the interior features installations are in process.

### 5. DC Tachometer Installation on DSIF 85-ft Polar Antennas, H. L. Richter

In order to improve the interface of rate feedback signals with MSFN servo electronics and to upgrade the rate loops of the standard DSIF 85-ft diameter polar tracking antennas, it was decided to replace the presently used 400-Hz AC tachometers with DC tachometers. The DC tachometer offers a number of advantages over the AC machine when used in a basically DC servo system as the DSIF employs. These advantages manifest themselves in the fact that the need for field excitation and demodulation is eliminated thereby making the system simpler. By elimination of the above, the noise level of the feedback signal is decreased to that of pickup and any phase shifting because of noise is eliminated. The DC tachometer also provides better feedback sensitivity at

**Fig. 7. Laboratory and office building, G-60, at Venus DSS**

low rates because the signal is not degraded by the demodulator. Finally the DC tachometer, in the size used, is much less expensive, costing approximately 25% as much as the comparable AC machine.

The DC tachometer chosen was the Servo-Tek model SB-740B-1. This machine is a standard DC permanent magnet tachometer generator with built-in temperature compensation and a nominal gain of 20.8 V/1000 rpm. This tachometer was chosen on the recommendation of Collins Radio Company, who supplied the MSFN system and who have gained experience on a number of antennas. The tachometer was laboratory tested for gain and life characteristics. The machine tested was found to be linear at approximately 21 V/1000 rpm from 0.5 to 3000 rpm with a signal-to-noise ratio of 0.5 at 1 rpm and a ratio of 1 at 25 rpm, increasing steadily upward from there. The tachometer was life-tested for 1000 hr at a nominal rate of 2000 rpm and showed no visible loss of gain or increase of noise. Catalog life on the tachometer brushes is given as 100,000 hr, and bearings are assumed to exceed this.

The testing and trial installation of the tachometers was performed on the DSS-12 antenna declination drive. The declination axis was chosen because it could be modified without jeopardizing any tracking commitments of that station since the declination axis does not move to any appreciable extent when tracking deep space targets and because the theoretical models of the hour angle and declination rate loops are nearly identical. The only difference between the two is that the hydraulic poles are slightly different in location, this being due to different line lengths between the servo valve and the motors. The difference can be considered negligible, however.

The modification to the servo group electronics involves removal of all demodulators, which demodulated the 400-Hz rate signal, and installation of new wiring for the additional tachometers added to motors not so equipped in the old configuration and designing the proper compensation for the loops to obtain maximum gain and bandwidth.

The low-speed rate loop was compensated with a 9:1 lead-lag compensator with lead corner at 40 rad/s and a 10:1 lag-lead compensator with lag corner at 0.63 rad/s for additional phase margin and DC gain, respectively. The final Bode diagrams for the low-speed rate loop are shown in Fig. 8. The final open-loop DC gain constant is 800. For the high-speed rate loop, it was necessary to

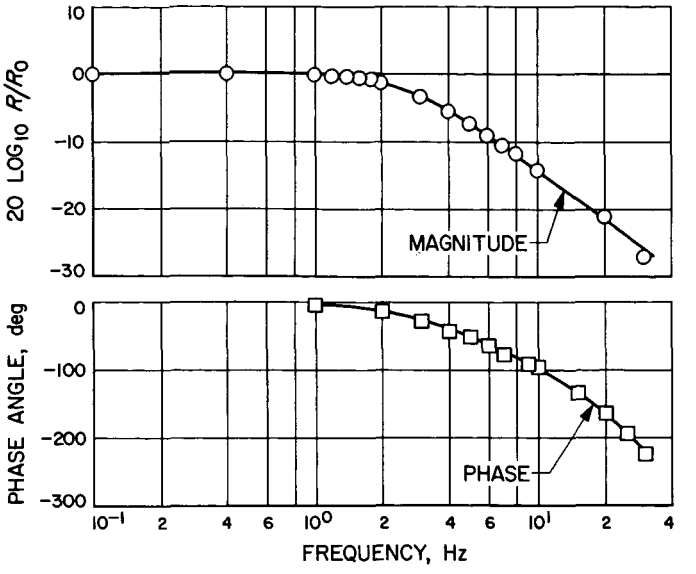


**Fig. 8. Declination low-speed closed-rate loop**

close the pressure loop around the servo valve in order to obtain additional phase margin and hydraulic damping. The high-speed pressure loop was compensated with a 12:1 lead-lag compensator, the lead corner at 28 rad/s, resulting in the closed pressure loop transfer function shown in Fig. 9. After closing the pressure loop as indicated, the high-speed rate loop was closed using

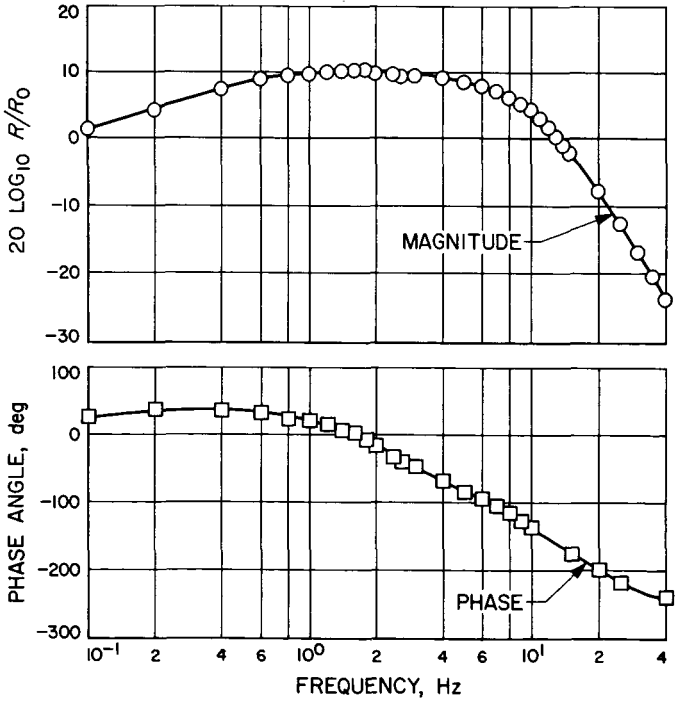


**Fig. 9. Declination high-speed closed-pressure loop**

a 10:1 lag-lead compensator with the lag corner at 0.63 rad/s. This resulted in the Bode diagram of Fig. 10. The final open rate loop DC gain is 230.

Response curves were obtained from magnitude and phase data measured on a Boonshaft and Fuchs transfer function analyzer.

The physical change to the servo amplifier chassis was planned so that no mechanical modifications to the chassis or front panel were required. Sockets formerly used for demodulators were rewired to become sockets for the compensation and summing networks for the new and existing feedback signals. Planning the modification in this manner allowed the change to be made without any visible change to the equipment. Detailed installation procedures are set forth in JPL Procedure DZA-1026-IP.

The DC tachometer modification is now being readied for installation on all DSIF 85-ft diameter antennas.

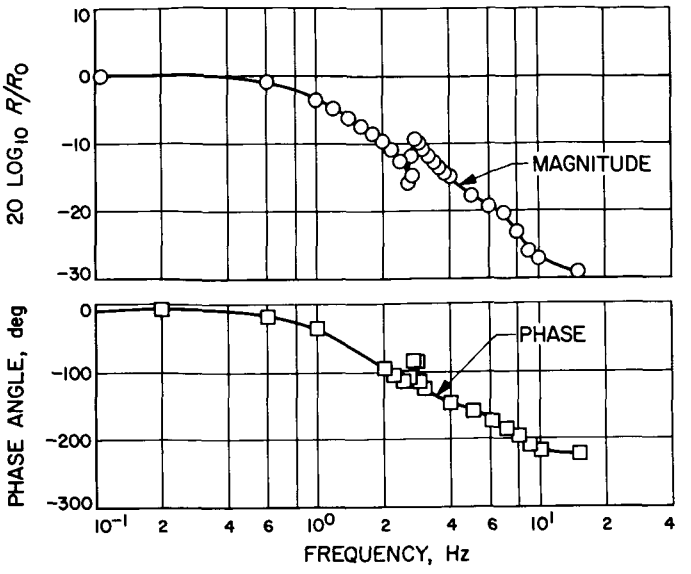


**Fig. 10. Declination high-speed closed-rate loop transfer function**



# C. DSIF Station Control and Data Equipment

*R. Flanders, G. Jenkins, A. Burke, H. Baugh, and W. Frey*

## 1. Introduction

The DSIF Station Control and Data Equipment (SCDE) is to be implemented to provide increased support for the flight projects as a part of the DSIF station equipment. In the performance of this objective, the equipment is to provide the capability for processing spacecraft telemetry and command data in direct support of the mission, and for station monitoring, time and frequency tagging, and antenna pointing as a part of the mission independent functions. The specific subsystems involved with these tasks are the Antenna Pointing Subsystem (APS), Digital Instrumentation Subsystem (DIS), Station Monitor and Control Console (SMC), Telemetry and Command Processor (TCP), and the Frequency and Timing Subsystem (FTS). The function of each of these subsystems, together with the current status, is described in the following paragraphs.

## 2. Antenna Pointing Subsystem

The Antenna Pointing Subsystem (APS) provides the DSIF stations with the capability to point antennas under computer control in addition to the existing automatic tracking and manual control modes of operation. The primary function of the subsystem is to point an antenna toward a spacecraft or celestial body ephemeris that is either derived internally based on parameter inputs or supplied by external data contained on precomputed drive tapes. The subsystem consists of an SDS 910 computer with associated peripheral equipment, interface equipment and a subsystem control panel. The APS operates in conjunction with the servo assembly of the Antenna Mechanical Subsystem and the antenna angle readouts of the Tracking Data Handling Subsystem. The APS will add the following capabilities to the DSIF: (1) Rapid acquisition time. (2) Tracking when there is no RF signal or the received signal strength is too low for automatic tracking operations. (3) More flexibility and precision in control of antenna movement.

The Antenna Pointing Subsystem is being implemented in two steps. The first step, the Interim Antenna Pointing Subsystem, meets the flight project antenna pointing requirements on an interim capability basis. The second implementation step will provide a full capability Antenna Pointing Subsystem (APS 1). The interim APS utilizes existing equipment to perform its function, while the APS 1 requires the addition of new computer interface equipment to operate. Both the interim and full capability APS are described in detail in *SPS 37-38*, Vol. III.

The Interim APS has been implemented in DSIF Stations 12, 14, 41, 42, and 61. Station 11 will be implemented in September 1966, and Stations 62 and 72 will be installed in the last quarter of this year. The Interim APS is presently providing antenna pointing support for the *Lunar Orbiter* Flight Project at Stations 12, 41, and 61.

The first implementation of the APS 1 equipment will be during October 1966 at Station 14. Stations 11, 12, 41, 42, 51, 61, 62, and 72 will be implemented in 1-month intervals beginning in May 1967. At the present time, hardware evaluation and program checkout are being conducted on the prototype APS 1 which is located at the Laboratory.

### 3. Digital Instrumentation Subsystem, Phase II

The Digital Instrumentation Subsystem Phase II (DIS II), together with the Station Monitor and Control Console Phase II (SMC II) provides the facility for system monitoring at each station in the DSIF. The DIS/SMC II performs the following functions: (1) Station performance and status monitoring. (2) Alarm monitoring of critical station parameters. (3) Preparation of a permanent record of station performance and failure data for real time and post-mission analysis. The DIS II provides for the acquisition, processing, recording, and communication of station data.

The DIS II is implemented with the major elements of the DIS I configuration (*SPS 37-16, -20, -21,* and *-34,* Vol. III), with the exception of the Communications Buffer which has been assigned to the Telemetry and Command Processor (TCP), and the SDS 910 computer and peripheral equipment which is being utilized as part of the Antenna Pointing Subsystem (APS). The DIS II utilizes the SDS 920 computer, peripheral equipment, magnetic tape transports, and data gathering equipment from the DIS I. To this is added the following elements: (1) Y-Buffer interlace. (2) Memory expansion of 8,192 words of magnetic core memory to increase memory capacity to 16,384 words. (3) Monitor Page Printer and Coupler. (4) Line Printer and Coupler. (5) Cartridge Loading Magnetic Tape Unit. (6) Communications Buffer with full duplex teletype and high-speed data line communications capability.

A prototype of the DIS II is being procured and will be utilized for: (1) evaluation of the configuration and performance prior to procurement of production quantities, (2) verification of the subsystem documentation, (3) checkout of the operational programs and diagnostics, and (4) establishing interface compatibility with the mating subsystems in the stations. Completion of the prototype evaluation is scheduled for the fourth quarter of 1966. Subsequent to the completion of the evaluation, a production quantity of the DIS II will be implemented. This will require the retrofit of the existing DIS I at each of the stations involved. The initial installations will be performed at DSS 11, 12, 61, 62, and 71 and are scheduled for operation during the first quarter of 1967. The remaining stations are scheduled to be updated to the DIS II configuration during the latter part of 1967. Supporting documentation is to be prepared, for completion simultaneously with the hardware availability.

The program for the DSIF System Monitor function is being prepared to replace the Interim Monitor Program currently used at the stations. The Interim Monitor Program is presently operating with the DIS I and performs limited monitoring functions. The permanent System Monitor Program will be available for use at selected stations when the DIS II becomes operational, and will provide a full monitoring capability, including performance and alarm monitoring, data gathering and processing, and station report preparation and communication.

### 4. Station Monitor and Control Console

The primary objectives of the Station Monitor and Control Console Phase I (SMC I) are: (1) to provide the facility for the display and control of station performance at a central location, for use by the station manager at each site, and (2) to display information to indicate nonstandard system or subsystem operation. SMC Phase II will add the capability of: (1) displaying selected station parameters, (2) an English text printout of station performance and status, (3) system alarm monitoring under control of the DIS to indicate station failures, and (4) a teletype page printer. SMC I is essentially complete with exception of the countdown clock. Procurement of the clock is in process and should be complete by May 1967.

Procurement of a prototype Program Alarm and Control Panel has been initiated and is scheduled for completion by September 1966. An order for six additional panels will follow upon completion of the prototype evaluation. The prototype line printer has been procured and will be shipped to DSS 11 for testing and evaluation. Thereafter, five stations will be equipped with line printers as part of SMC II.

A graphical recorder will be mounted in the station monitor console to provide the facility for displaying

actual data versus predicted performance data on an X-Y plot. Procurement of a prototype graphical recorder has been initiated, for evaluation of the recorder prior to procurement of an additional quantity. The X-Y recorder will be evaluated at JPL and at DSS 11 to verify proper performance, establish interface compatibility with companion equipment, and assure the validity of the supporting documentation. Prototype evaluation is to be completed during the fourth quarter of 1966, with operation at five stations scheduled for the first quarter of 1967.

## 5. Telemetry and Command Processors, Phase II

The Telemetry and Command Data Processors Phase II (TCP II) are the major assemblies in the Telemetry and Command Data Handling Subsystem Phase II (TCD II). A description of the TCP II has been presented in *SPS 37-38*, Vol. III, Sect. VI-C. The major changes in TCP II during this period are as follows:

(1) The TCP II-A configuration has been eliminated and the stations formerly configured; namely DSS 11, 42, and 62, will now be implemented with the standard TCP II configuration. Table 2 shows the modified TCP II configuration.

**Table 2. DSIF TCP II configuration**

| DSIF identification | TCP configuration | Operational date |
|---|---|---|
| 11 | II | December 1966 |
| 12 | II | February 1966 |
| 41 | II | March 1966 |
| 42 | II | November 1966 |
| 51 | II-B | October 1965 |
| 61 | II | March 1966 |
| 62 | II | December 1966 |
| 71 | II | March 1966 |
| 72 | II | April 1966 |

(2) The TCP II-A scheduled for installation into DSIF 11 in December has temporarily been installed in the Spacecraft Assembly Facility (SAF) at JPL for support of the *Mariner 67* Project. This unit will be returned to the DSIF in January 1967.

(3) TCP II has been participating in Flight Project Support at four stations. DSS 12, 41, 61, and 71 have operational TCP II assemblies, and these stations have been utilizing the TCP II in providing support to the *Lunar Orbiter* and *Pioneer* flight projects. At the present time, not enough data has been processed by the TCP II for a quantitative analysis.

## 6. Frequency and Timing Subsystem, Phase II

*a. Background.* The present Frequency and Timing Subsystems (FTS I) has some serious deficiencies in the areas of reliability, resolution and accuracy, and drive capability. Increasingly stringent mission requirements have indicated the need for a new subsystem, FTS II, which can correct these difficulties.

*b. Reliability.* In order for the FTS to provide correct time information, all elements must operate essentially error-free for long periods of time. The digital elements in the present subsystem can not do this satisfactorily, since the modules are of an older design and the logical structure makes no provision for error detection or correction.

FTS II will be implemented with redundant assemblies using Hi-Rel Modules so that the probability of a module failure is greatly reduced and the subsystem can continue to operate correctly even if failures do occur. An example of this type of structure is the divider chain which produces 1 pps from a 1 MHz input. This assembly will consist of three identical divide-by $10^6$ counters with triplicate majority logic voters operating on the 1 pps signals. If two of the signals agree and one disagrees, the good outputs will be used, the dissenting signal suppressed, and an alarm indication given. The offending element may be "locked out," requiring operator intervention, or it may be automatically synchronized to the two and re-connected.

*c. Resolution and accuracy.* The present FTS digital clock has provision for advancing or retarding to set the clock to the proper time in relation to WWV, but the changes can only be made in increments of 100 $\mu$s, so the time can not be set to closer than $\pm 50$ $\mu$s. The timing pulses out of the unit have considerable phase jitter in view of present requirements, so there is a need for improvement in this area.

In FTS-II, it is planned that the clock-setting resolution be 1 $\mu$s, as there are an increasing number of tracking operations where this order of resolution is important.

The phase jitter of the timing pulses from FTS-I is a consequence of the use of slow-speed digital modules

and unclocked logic for the generation of the key pulses. FTS-II modules will have much shorter delay times, and all key pulses will be directly clocked by the basic frequency source so that the phase jitter should be less than a few tens of nanoseconds.

The absolute accuracy of the timing information is a function of the basic input frequency. FTS-I uses rubidium frequency standards, which can nominally provide the necessary accuracy, but they have presented some reliability problems. FTS-II will use similar standards, initially, although some work is being done by the vendors to improve the reliability of the units.

*d. Capability.* As the tracking stations grow in complexity, there is a continual demand for additional services and additional driving capability on existing signals. This generally leads to overloaded drivers and little or no isolation between subsystems. Overloading in some cases has caused malfunctions in the station clock.

The digital dividers in FTS-II will be completely isolated from all output circuits by short-circuit-proof amplifiers, so that no external activity can upset the basic timing chains. Similarly, the digital clocks will be isolated from their customers by amplifiers which also provide the level-shifts required by the different systems of logical elements used in other subsystems. Key timing pulses and frequencies will have individual distribution amplifiers for each customer, to aid in preventing interaction between subsystems.

An additional capability to be provided by FTS-II is that of flexibility. In the checkout and simulation area there are requirements for switching the sources of timing signals so that one project may be checking its equipment with tape playback signals while another project may be tracking with real-time signals. All combinations of timing sources and customers should be available by suitable switching, without requiring that the FTS-II digital clock itself be interfered with in any way.

*e. Status.* At the present writing, all the functional requirements for FTS-II have been established, and the basic design philosophy has been defined. Procurements have been initiated for the digital modules for the prototype unit, and for the documentation. Investigations have been started in the area of long-term stability of frequency standards, and in the area of techniques for synchronizing overseas stations to a central timing system to be established at Goldstone as a portion of FTS-IIA and FTS-IIB.

### 7. Summary

A limited quantity of the Station Control and Data Equipment has been operational in support of recent flight projects. Use of the equipment during these missions has provided experience for the station personnel, as well as an indication of expected performance when implementation of the final configuration is complete. As a result, some improvements have been incorporated into the development. For the most part, the performance has been favorable.



## D. Venus Station Operations

M. A. Gregg, E. B. Jackson, and A. L. Price

### 1. Experimental Activities

During the period 14 June to 30 June, the Venus Station was not in an operational configuration; instead, it was conducting maintenance, modifications, upgrading, and station cleanup. The monthly cooperative (with the Mars Station) experimental track of the *Mariner IV* spacecraft took place on 1 July, and full operational status with a return to 24-hr/day operation started on 5 July.

The cooperative, with the Mars Station, tracks of the *Mariner IV* spacecraft (on 1 July and 8 August) returned one- and two-way telemetry data (recorded on magnetic tape at the Mars Station), spectograms (via microwave to the Venus Station), and some two-way doppler data to be utilized in orbit analysis. The spacecraft transmitted power and frequency in the two-way mode appear to be nominal; however, the spacecraft in the one-way mode is being received at a frequency of approximately 600 Hz (at carrier frequency) different from predictions. The exact amount of difference and possible reasons are still under study.

During the period of 12 July to 5 August, a bistatic planetary radar experiment with Mercury as the target was conducted at the Venus Station. The transmitting antenna was the Venus 85-ft Az-El, and the receiving antenna was the Mars 210-ft Az-El. The signal was fed to Venus at 455 kHz via the intersite microwave link,

with both ranging and total spectrum data being collected. The round-trip range to Mercury was found to be initially some 5000 $\mu$s less than predicted. However, it moved into closer agreement with prediction until, at the end of the experiment, the range error was only 2200 $\mu$s less than predicted. This range error must be corrected by additional system delay between the Mars and Venus Stations via the microwave link. This delay is still undergoing measurement but is on the order of 150 $\mu$s. Thus, at the end of the experiment, the actual round-trip range was less than the predicted round trip range by approximately 2350 $\mu$s, or approximately 438 miles.

The Mercury bistatic planetary radar experiment was complicated by the present errors associated with the 210-ft antenna pointing system which, at a maximum, approximate one-half of the 3-dB beamwidth in both elevation and azimuth axes. A day of experimental time was utilized to obtain offset data by which the nominal pointing data could be modified. This data was obtained by taking signal strength measurements, integrated over a 5-min period, from Mercury. These measurements were taken in groups of three arbitrary offsets in both axes and then a parabola was fitted through the three points thus obtained. The resulting offsets versus indicated azimuth and elevation are illustrated in Fig. 11.

## 2. Subsystem Performance

*a. 100-kW transmitting systems.* The R&D transmitter for this reporting period has been operated only during the month of July in conjunction with the Mercury bistatic experiments. During this time the transmitter has operated a total of 358.5 filament hours and 192.6 beam hours. Some internal arcing and outgassing of the tube were experienced after the shut-down period.

For this period, the *Mariner* 100-kW transmitter has operated a total of 61.8 filament hours and 38.4 beam hours. However, during testing of the system the *Mariner* Klystron developed a short from the cathode to body,

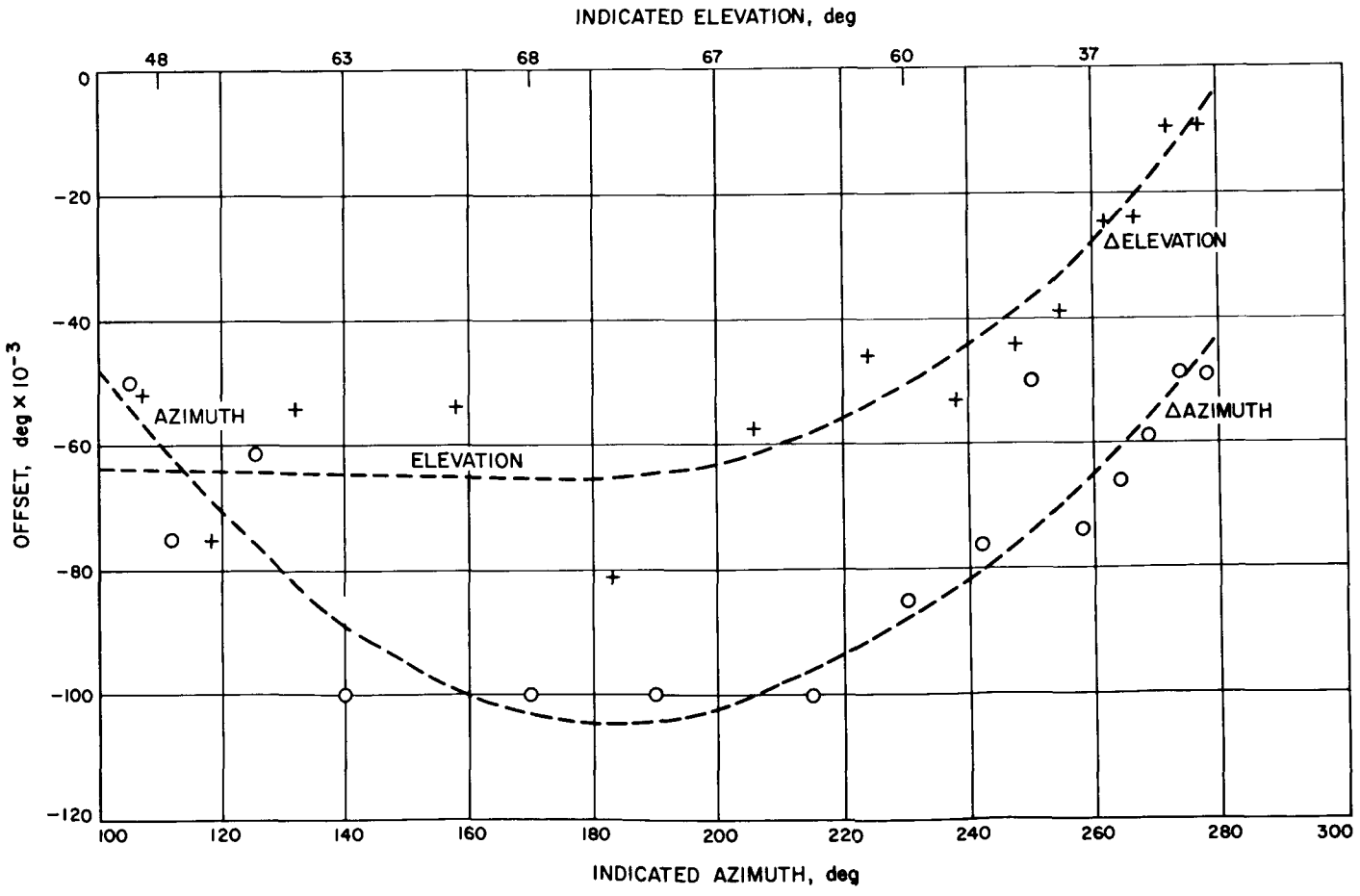


**Fig. 11. Empirically determined offsets, Mars 210-ft antenna, for use on the planet Mercury**

and on 20 June S/N 5 was removed and replaced with S/N 4. During these hours of tracking and testing, only one other failure occurred, which was the waveguide switching at the start of a *Mariner* track. A total of 2 min of tracking time was lost. During this period the system has also been used in evaluation of the design for the solid-state regulator and exciter for the 1 MW synchronous motor and generator.

The testing of the new X-3060 Eimac 100-kW Klystrons has been in progress during this period. A leak developed in S/N H5-30 beyond the normal pumpdown capability after 77.3 filament hours and 16.1 beam hours, and the tube was returned to Eimac.

Support was given to testing the standard DSN diplexing cone at 100 kW.

***b. Receiving systems.*** The *X*-band system 8448 MHz was used in a lunar radar experiment. One module failure, a radio frequency keyer module, occurred. This was repaired at the Laboratory and re-installed in the receiver.

The Venus Station *Mariner* receiver was not used during this period. *Mariner* spacecraft reception was accomplished by feeding the 455 kHz signal from the Mars Station *Mariner* receiver, via the microwave link, into the AM channel of the Venus Station Mod IV receiver.

Reception of signals during the Mercury bistatic experiment was handled similarly. The 455 kHz signal from the Mars Station 2388 MHz receiver was fed, via the microwave link, into the AM channel and the main loop channel of the Mod IV receiver.

The 30 MHz portion of the Mod IV receiver was used in obtaining spectrograms of the Venus Station *Mariner* transmitter transmitted signal. This was accomplished by feeding 30 MHz from the RWV receiver into the Mod IV receiver. The Mod IV receiver's third conversion oscillator, a frequency synthesizer, was used to center the spectrum within the passband of the digital processing equipment.

A failure in the programmed local oscillator, resulting in large doppler errors in the digital subsystems, occurred. It was found that by substituting an external frequency synthesizer for the one used in the PLO, the trouble was corrected. A new synthesizer was installed in the PLO, and the operation is now normal. The old synthesizer was returned to the Laboratory for repair. Some tape reader problems have occurred. Corrective work is underway.

### 3. System Improvements

***a. Transmitting systems.*** The Owens Lab 500-V power supplies which were purchased for the new R&D exciter antenna-mounted equipment have both failed in less than 48 hr of operating time.

New control circuitry associated with the operation and protection of the pumps for the 400 kW system was designed, installed, and documented.

***b. Receiving systems.*** The installation of all the Venus Station receiving systems has been completed during this period.

The *X*-band digital phase modulator has been modified to facilitate its proper adjustment. The modification involved the removal of one of the external adjustable controls, thus simplifying the setup procedure.

The 30 MHz leakage problem in the Mod IV receiver has been corrected. This was accomplished by rerouting the AM channel 30 MHz mixer AGC cable.

The system checkout of the new central frequency synthesizer (CFS), by the Laboratory Project Engineer, has been completed. The unit has now been turned over to the station for operation and maintenance. The old interim CFS has been returned to the Laboratory.

# References

1. Stevens, R., *DSIF Implementation Plan for MSFN Backup Wings at DSS 11, 42, and 61*, EPD 344, Jet Propulsion Laboratory, Pasadena, Calif., April 15, 1966.

2. Schiffman, F., *Functional Specification DSIF Apollo Backup System Configuration, 85-ft*, DOW-1198-FNC, Jet Propulsion Laboratory, Pasadena, Calif., June 10, 1966.